Modelling Reactive Transport in Sedimentary Rock Environments - Phase II

MIN3P code enhancements and illustrative simulations for a glaciation scenario

NWMO TR-2011-13 **December 2011**

Sergio Andres Bea Jofré[1], K. Ulrich Mayer[1] and Kerry T. B. MacQuarrie[2]

[1]Department of Earth and Ocean Sciences, University of British Columbia
[2]Department of Civil Engineering, University of New Brunswick

nwmo
NUCLEAR WASTE MANAGEMENT ORGANIZATION
SOCIÉTÉ DE GESTION DES DÉCHETS NUCLÉAIRES

Nuclear Waste Management Organization
22 St. Clair Avenue East, 6th Floor
Toronto, Ontario
M4T 2S3
Canada

Tel: 416-934-9814
Web: www.nwmo.ca

Modelling Reactive Transport in Sedimentary Rock Environments - Phase II
MIN3P code enhancements and illustrative simulations for a glaciation scenario

NWMO TR-2011-13

December 2011

Sergio Andres Bea Jofré[1], K. Ulrich Mayer[1] and Kerry T. B. MacQuarrie[2]

[1]Department of Earth and Ocean Sciences, University of British Columbia
[2]Department of Civil Engineering, University of New Brunswick

ABSTRACT

Title: **Modelling Reactive Transport in Sedimentary Rock Environments - Phase II. MIN3P code enhancements and illustrative simulations for a glaciation scenario**
Report No.: **NWMO TR-2011-13**
Author(s): Sergio Andres Bea Jofré[1], K. Ulrich Mayer[1] and Kerry T. B. MacQuarrie[2]
Company: [1]Department of Earth and Ocean Sciences, University of British Columbia
[2]Department of Civil Engineering, University of New Brunswick
Date: December 2011

Abstract
Canada's plan for the long-term care of used nuclear fuel is containment and isolation in a Deep Geologic Repository (DGR) constructed in a suitable sedimentary or crystalline rock formation. In sedimentary basins fluid migration and geochemical conditions may be impacted by multiple interacting processes including density-dependent groundwater flow, solute transport, heat (energy) transport, mechanical loading, and rock-water interactions. Understanding the interactions among these processes is important when assessing the long-term hydrodynamic and geochemical stability of sedimentary basins during glaciation/ deglaciation events. To improve the capability to investigate these processes, an enhanced version of the reactive transport code MIN3P (i.e. MIN3P-NWMO) was developed and tested. The key code enhancements included: fluid density and activity coefficient formulations for high ionic strength solutions; inclusion of one-dimensional hydromechanical coupling to account for fluid pressure changes due to ice sheet loading; and coupling with heat (energy) transport. The new capabilities of MIN3P-NWMO were verified and tested for selected problems by making comparisons with the results of other similar models and available analytical solutions.

The MIN3P-NWMO code was used to simulate flow and reactive transport in a hypothetical two-dimensional sedimentary basin subjected to a simplified glaciation scenario consisting of a single cycle of ice sheet advance and retreat. The simulation provided an illustrative example of the hydrogeological and geochemical stability of the sedimentary basin over a time period of 32,500 years. The sedimentary basin was approximately 400 km in width, 4 km thick at its deepest point, and comprised of 12 individual sedimentary rock units including sandstones, shales, evaporites, and carbonates. Fluid pressures were shown to increase in low hydraulic conductivity units during ice sheet advance due to hydromechanical coupling. During the period of deglaciation, specific discharge increased in the shallow aquifers and deeper high-hydraulic conductivity units (e.g. sandstones) as a result of the infiltration of glacial meltwater below the warm-based glacier. These changes, however, had a negligible effect on the fluid density distribution below depths of approximately 300 m. From a geochemical perspective, the simulation revealed that dedolomitization occurred during the deglaciation period. However, dedolomitization was mainly restricted to the shallow aquifers and, as a consequence of the low flow rates in the sedimentary basin, the net rates of dedolomitization were practically negligible for time scales on the order of 10,000 years. Although dissolution of halite (NaCl) was more significant locally (i.e. at the margins of the evaporite units), it was not as widespread as dedolomization. Slight porosity enhancement was predicted as a result of halite dissolution in the evaporite unit. A series of alternative scenarios was also investigated in which individual model assumptions or processes were varied with respect to the base case. In general, the simulation results indicate a high degree of geochemical stability for this hypothetical basin.

TABLE OF CONTENTS

LIST OF TABLES

Page

LIST OF FIGURES

Page

1. INTRODUCTION

The Canadian Nuclear Waste Management Organization (NWMO) is responsible for implementing Adaptive Phased Management (APM), Canada's plan for the long-term care of used nuclear fuel produced by Canada's nuclear reactors. The goal of APM is containment and isolation of used nuclear fuel in a Deep Geologic Repository (DGR) constructed in a suitable sedimentary or crystalline rock formation. A key objective of the APM Geoscience research program is to further understanding of geosphere evolution and stability, including potential geosphere responses to future glaciations.

In sedimentary basins fluid migration and geochemical conditions may be impacted by a variety of interacting physical and chemical processes, including density-dependent groundwater flow, heat transport, mass transport, mixing of waters of different geochemical compositions, water-rock interaction, and mechanical loading. Understanding the interactions among these processes is important when assessing the long-term hydrogeological and geochemical stability of sedimentary basins (Mayer and MacQuarrie, 2007), and is thus relevant for the safety evaluation of deep geologic repositories for used nuclear fuel (e.g. Sykes et al., 2011; Park et al., 2009).

In North America, sedimentary basins have been subjected to a series of periodic glaciation-deglaciation events (e.g. Grasby et al., 2000; Grasby and Chen, 2005; McIntosh and Walter, 2005, 2006; McIntosh et al., 2011). In the future, it is therefore expected that a DGR located within a sedimentary rock setting in Canada will be subject to glaciation events associated with long-term climate change (e.g., Peltier, 2011). The regional buildup of significant fluid pressures below melting glaciers (e.g. Bense and Person, 2008) may provide the driving force for meltwater infiltration into sedimentary basins, leading to geochemical disequilibrium between the infiltrating meltwater and the rock formations. Present day geochemical evidence confirms that glacial waters have entered shallow aquifers in the past. For example, McIntosh and Walter (2005) provided evidence that meltwater recharged through confined Silurian-Devonian aquifers at the margins of both the Illinois and Michigan basins. Using elemental and isotopic geochemistry of groundwaters in Silurian-Devonian carbonate and glacial drift aquifers, McIntosh and Walter (2005) suggested that groundwater geochemistry had been altered by incongruent dissolution of carbonate minerals, dissolution of halite and anhydrite, cation exchange, microbial processes and mixing with brines.

The findings of McIntosh and Walter (2005) demonstrate that the ingress of glacial waters into sedimentary rock sequences is not a conservative process. Solutes interact with the solid phase, adsorb onto clays or oxides, and mineral dissolution-precipitation reactions affect the groundwater and rock composition. Mineral dissolution and precipitation may also result in modifications to media properties (e.g. porosity and permeability), possibly providing a feedback to fluid flow. Such modifications may be insignificant at human timescales but may be more substantial over geological timescales (Person et al., 1996). Hanor (2001) simulated the effects of advective-dispersive mixing of fluids of differing chlorinity on mass transfer in rock-buffered systems. This work demonstrated that reactive transport should occur in any porous medium where there is a chlorinity gradient, even where molecular diffusion is the sole solute transport mechanism. In theory, large volumes of individual mineral phases could be dissolved or precipitated as a result of such mixing, without the need for substantial fluid migration, because fluid-mineral reactions will tend to maintain fluid compositions and concentration gradients. Despite the fact that rock-water interactions affect the geochemical evolution in sedimentary

basins, very little work has been performed to quantitatively assess these interactions using numerical simulations. To fill this gap, this report focuses on developing modelling capabilities for simulating reactive transport in sedimentary rock formations. In addition, illustrative numerical simulations are conducted that explore the magnitude and rate of change of geochemical conditions within a sedimentary groundwater system influenced by glacial events.

2. OBJECTIVES AND SCOPE

This work focuses on the numerical simulation of groundwater flow and reactive transport in sedimentary rock basins with three main objectives:

1. Enhancement and verification of a numerical model for conducting flow and reactive transport simulations (i.e. density-dependent flow and solute transport, geochemical reactions, hydromechanical coupling, and energy transport) in sedimentary basins affected by glaciation/deglaciation;

2. An evaluation of the feasibility of using the new code for simulating the response of a hypothetical large-scale sedimentary basin to ice sheet advance and retreat over time periods greater than 30,000 years; and

3. Conducting a preliminary sensitivity analysis of geochemical stability in the hypothetical sedimentary basin as a function of selected model processes and parameters.

To address the first objective, the code MIN3P-NWMO was developed based on the original version of MIN3P (Mayer et al., 2002) and a more recent version that had been modified to include the density coupling between groundwater flow and solute transport (MIN3P-D, Henderson et al., 2009). Several code enhancements have been made as part of the present work, including:

- Calculation of ion activity corrections in high ionic strength solutions using the Harvie-Möller-Weare model (HMW, Harvie et al., 1984) based on the Pitzer (1973) equations;
- Fluid density calculations based on fluid volumetric predictions derived from the Pitzer (1973) equations according to Monnin (1994);
- One-dimensional hydromechanical coupling (Neuzil, 2003) due to ice sheet advance and retreat; and
- A numerical formulation to couple energy (heat) transport (following Voss and Provost, 2008) with fluid and solute transport (i.e. density-driven flow controlled by thermohaline convection).

These additions were chosen because a) many sedimentary basins are known to contain brines of high ionic strength, b) glaciation is the single largest perturbation influencing the stability of a deep-seated sedimentary environment that may host a DGR, and c) the substantial thickness of many sedimentary basins (on the order of several km) is likely to result in thermal gradients.

The existing capabilities of MIN3P and MIN3P-D relevant to this work were verified and re-tested after each of the code modifications. In addition, the new capabilities of MIN3P-NWMO were verified and tested in relation to other similar models cited in the literature and available analytical solutions.

Concerning the second objective, a simulation for a two-dimensional cross-section of a generic sedimentary basin was carried out with the MIN3P-NWMO code. The base case simulation included the following processes:

- Coupling between density-driven groundwater flow and reactive transport;
- Water-rock interaction including mineral dissolution-precipitation (predominantly dedolomitization and evaporite dissolution) and ion exchange;
- Fluid pressure changes induced by ice sheet loading (hydromechanical coupling);
- Porosity and permeability decline with depth; and
- Transient boundary conditions for flow and transport due to the advance and retreat of a continental ice sheet over the sedimentary basin.

To address the third objective, several variations of the base case were simulated to illustrate the influence of different conceptual models and model parameters. Simulations were conducted to evaluate the following aspects:

- Permafrost formation in front of the ice sheet, resulting in reduced hydraulic conductivity at the leading edge of the ice sheet;
- Presence of fractures in shallow aquitards, effectively resulting in an increase in vertical hydraulic conductivity;
- An increased initial depth of freshwater;
- No depth variation of rock unit porosities and permeabilities;
- Inclusion of thermal convection and conduction;
- Exclusion of ion exchange; and
- Exclusion of mineral dissolution-precipitation and ion exchange (conservative multicomponent solute transport).

3. MODEL FORMULATION AND DEVELOPMENT

The MIN3P-D code (Henderson et al., 2009) simulates groundwater flow, solute transport, and geochemical reactions under variable density conditions for solutions with maximum ionic strengths similar to seawater. However, this code is not suitable for simulating processes in more concentrated solutions and brines. Thermal effects, for example resulting from a geothermal gradient or ingress of cold meltwater, are not considered. In addition, the feedback between glacial loading and groundwater flow, induced during ice sheet advance and retreat, is not included in MIN3P-D. In order to more adequately simulate processes in sedimentary basins it was necessary to implement these additional processes into MIN3P-D, resulting in MIN3P-NWMO. This section describes the mathematical formulation of the new MIN3P-NWMO code, with an emphasis on the additions made as part of the current work.

3.1 GOVERNING EQUATIONS FOR GROUNDWATER FLOW

MIN3P-NWMO is designed to simulate the movement of variable density fluids and energy, as well as reactive transport. The physical properties of groundwater, including density and viscosity, are computed as a function of the solute concentration (e.g. Total Dissolved Solid, TDS) and temperature (T). The dependence of fluid density on solute concentrations results in the coupling between the movement of fluids and the migration of dissolved species (Voss and

Souza, 1987; Oldenburg and Pruess, 1995; Diersch and Kolditz, 2002) and temperature (Voss and Provost, 2008). The density-driven formulation implemented in MIN3P-NWMO is partially based on MIN3P-D (Henderson et al., 2009).

One-dimensional hydromechanical coupling is implemented following the formulation of Neuzil (2003), and its derivation is detailed in Appendix A. If surface loading is homogeneous and spatially extensive, then a one-dimensional vertical formulation for stress and strain is appropriate. Neuzil (2003) has reviewed the potential errors arising from ignoring lateral strains resulting from non-uniform loads (e.g. spatially varying ice sheet thickness), and noted that although assessing the errors is difficult, they are probably modest in the context of other uncertainties involved in simulating large-scale hydrogeologic systems. The assumption of purely vertical stress has also been invoked previously to simulate groundwater flow in hydrogeologic systems affected by large-scale ice sheet loading and unloading (e.g. Bense and Person, 2008; Lemieux et al., 2008; Normani, 2009).

Similar to recent work (e.g., Lemieux et al., 2008; Normani, 2009), in MIN3P-NWMO the fluid mass conservation in fully-saturated porous media is described by:

$$\frac{\partial \phi \rho}{\partial t} = \rho \frac{S_s}{\rho_f g}\left(\frac{\partial P_a}{\partial t} - \zeta \frac{\partial \sigma_{zz}}{\partial t}\right) + \phi \frac{\partial \rho}{\partial t} = \nabla \cdot \rho \mathbf{q_a} + \rho Q \qquad \text{Equation 3-1}$$

$$\mathbf{q_a} = \frac{\mathbf{k}}{\mu}\left(\nabla P_a + \rho g\right) \qquad \text{Equation 3-2}$$

where $\mathbf{q_a}$ is the specific discharge (Darcy velocity) [L T^{-1}], ρ and ρ_f are the fluid and freshwater densities, respectively [M L^{-3}], g is the gravity constant [L T^{-2}], ϕ is the porosity [-], S_S is the one-dimensional specific storage [L^{-1}], P_a is the fluid pressure [M L^{-1} T^{-2}], ζ is the one-dimensional loading efficiency [-], σ_{zz} is the vertical stress [M L^{-1} T^{-2}], μ is the dynamic fluid viscosity [M L^{-1} T^{-1}], $\mathbf{k}$ is the permeability tensor [L^2], and Q is the volumetric fluid source/sink term [T^{-1}]. As discussed by Normani (2009), the hydromechanical coupling term $\rho \frac{S_s}{\rho_f g}\left(\zeta \frac{\partial \sigma_{zz}}{\partial t}\right)$ in Equation 3-1 effectively links fluid pressure changes with temporal changes in the vertical stress and the porous medium properties S_S and ζ. Geometric deformation of the computational domain to account for land surface movements resulting from vertical stress changes (i.e. lithosphere deflection because of the weight of ice) is not currently considered.

3.1.1 Fluid density and viscosity

The relationship between fluid density and solute concentrations has been determined for mixtures of brines, seawater, and freshwater (Millero, 1982), and is typically modelled using empirical relationships (e.g. Frind, 1982; Voss, 1984; Kharaka et al., 1988; Guo and Langevin, 2002; Oldenburg and Pruess, 1995; Frolkovic and Schepper, 2001).

The fluid density (ρ) in Equation 3-1 and Equation 3-2 is computed as a function of temperature and concentrations using:

$$\rho = \rho_0 + \Delta\rho_C + \Delta\rho_T \qquad \text{Equation 3-3}$$

where ρ_0 is the reference density (e.g. density of pure water at 25 ^{o}C) [M L^{-3}], and $\Delta\rho_C$ and $\Delta\rho_T$ are the density changes due to concentration and temperature, respectively [M L^{-3}].

A commonly employed approach treats fluid density change as a linear function of TDS (Frind, 1982; Voss, 1984; Kharaka et al., 1988; Guo and Langevin, 2002, Henderson et al., 2009):

$$\Delta\rho_C = \frac{\partial\rho}{\partial \mathrm{TDS}}\mathrm{TDS} \qquad \text{Equation 3-4}$$

where $\partial\rho/\partial\mathrm{TDS}$ [-] is assumed to be constant. Reported values for the constant $\partial\rho/\partial\mathrm{TDS}$ are 0.688 and 0.714 for geochemical modelling of seawater-freshwater interactions (Kharaka et al., 1988; Guo and Langevin, 2002). TDS [M L^{-3}] is computed as:

$$\mathrm{TDS} = \sum_{j=1}^{N_c} T_j^a \mathrm{PM}_j \qquad \text{Equation 3-5}$$

where N_C is the number of aqueous components, T_j^a is the total aqueous component concentration for the *j*th aqueous component [mol L^{-3}], and PM_j is the molecular weight of the *j*th master species [M mol^{-1}].

The linear relationship between density and TDS is typically assumed when NaCl dominates the salinity (e.g. seawater). However, the presence of $CaCl_2$-enriched brines in many sedimentary basins requires a more sophisticated model for density calculations because density will depend on the elemental composition of the fluids (e.g. McIntosh et al., 2011). MIN3P-NWMO allows for the computation of $\Delta\rho_C$ in Equation 3-3 using a non-linear relationship with respect to concentrations. For instance, $\Delta\rho_C$ can be computed as the difference between a reference density and a density calculated based on Pitzer's equations according to Monnin (1994), implemented following Bea et al. (2010). In this case, density calculations are based on the total volume of the solution that contains 1 kg of water (V) (Monnin, 1994):

$$V = V_{id} + V_{ex} = 1000\upsilon_W + \sum_i m_i \overline{V}_i^o + V_{ex} \qquad \text{Equation 3-6}$$

where V_{id} is the ideal volume based on the molar volume of solutes and V_{ex} represents the total excess volume of a multicomponent electrolyte solution. υ_W is the specific volume of pure water (L^3 M^{-1}), m_i is the molality of the ith aqueous species [mol M^{-1}], and $\overline{V}_i^o$ is the standard

partial volume of the solute i (L^3 mol^{-1}). The term V_{ex} in Equation 3-6 can be expressed as a virial expansion of the solute molalities:

$$\frac{V_{ex}}{RT} = f^{v}_{DH}(I) + 2\sum_{c}\sum_{a} m_c m_a \left(B^{v}_{ca} + \left(\sum_{c} m_c z_c \right) C^{v}_{ca} \right) \qquad \text{Equation 3-7}$$

In this expression, R is the ideal gas constant, T the absolute temperature, m_c the molality of cation c (of charge z_c), and m_a that of anion a. $f^{v}_{DH}(I)$ is the Debye-Hückel term that is a function of the ionic strength, and B^{v}_{ca} and C^{v}_{ca} are the second virial coefficients for the volume that accounts for the interactions among ions. A detailed description of the formulation for fluid density as a function of solution composition is provided in Appendix B.4.

In MIN3P-NWMO the dependence of density on temperature, $\Delta\rho_T$ in Equation 3-3, can be computed using linear or non-linear relationships. For instance, a linear approximation can be expressed as:

$$\Delta\rho_T \approx \frac{\partial\rho}{\partial T}\Delta T \qquad \text{Equation 3-8}$$

where $\partial\rho/\partial T$ [M L^{-3} Θ^{-1}] is a constant, and ΔT is the temperature change with respect to the reference temperature of the reference density ρ_0. Alternatively, $\partial\rho/\partial T$ in Equation 3-8 can be computed based on a non-linear relationship.

Groundwater flow as described by the pressure-based form of Darcy's equation (Equation 3-2) is a function of dynamic viscosity (μ), which also depends on concentration and temperature according to:

$$\mu = \mu_f f^{\mu}_{T} f^{\mu}_{C} \qquad \text{Equation 3-9}$$

where μ_f is the viscosity [M L^{-1} T^{-1}] of a reference water with temperature T_f [Θ] and concentration C_f [M L^{-3}], and f^{μ}_{T} [-] and f^{μ}_{C} [-] are the correction terms to account for deviations from reference conditions. These terms are empirically defined and can be computed as (e.g. see Lever and Jackson, 1985; Diersch and Kolditz, 2002):

$$f^{\mu}_{C} = \frac{1 + 1.85\omega - 4.1\omega^2 + 44.5\omega^3}{1 + 1.85\omega_f - 4.1\omega_f^2 + 44.5\omega_f^3} \qquad \text{Equation 3-10}$$

$$f_T^{\mu} = \frac{1 + 0.7063\sigma_f - 0.04832\sigma_f^3}{1 + 0.7063\sigma - 0.04832\sigma^3} \qquad \text{Equation 3-11}$$

where ω and ω_f are the solute mass fractions in the fluid for the actual and reference viscosities, respectively, and $\sigma = (T - 150)/100$, with T provided in units of ^{o}C. Alternatively, the viscosity-temperature dependence (f_T^{μ}) can be computed based on the expression presented by Voss and Provost (2008):

$$f_T^{\mu} = \frac{10^{\left(\frac{248.37}{T_f + 133.15}\right)}}{10^{\left(\frac{248.37}{T + 133.15}\right)}} \qquad \text{Equation 3-12}$$

where T_f is the temperature [Θ] of the reference water, with T provided in units of ^{o}C. The temperature corrections presented in Equations 3.11 and 3.12 are both implemented in MIN3P-NWMO. If viscosity is assumed constant, then f_T^{μ} and f_C^{μ} in Equation 3-9 are approximated as unity.

3.2 GOVERNING EQUATIONS FOR ENERGY TRANSPORT

Energy is transported in the water-solid system by the flow of groundwater and by thermal conduction from higher to lower temperatures through both the fluid and solids. The governing equation for energy transport implemented in MIN3P-NWMO represents the balance between energy fluxes and the time rate of change of the amount of energy stored in the solid matrix and fluid. This balance is expressed as follows (Voss and Provost, 2008):

$$\frac{\partial \phi \rho S_a c_w T}{\partial t} + \frac{\partial (1-\phi)\rho_s c_s T}{\partial t} = \nabla \cdot \phi \rho c_w \mathbf{q_a} T - \nabla \cdot \boldsymbol{\lambda} \nabla T + \\ - \nabla \cdot \phi \rho c_w \mathbf{D_a} \nabla T + \rho^* Q c_w T^* \qquad \text{Equation 3-13}$$

where S_a is the water saturation (here set to 1 for a fully-saturated system), c_W and c_S are the specific heat capacity for the water and solid phases, respectively [$L^2\ T^{-2}\ \Theta^{-1}$], ρ_S is the solid density [$M\ L^{-3}$], $\boldsymbol{\lambda}$ is the thermal conductivity tensor for the porous medium [$LM\ T^{-3}\ \Theta^{-1}$], and T and T^* are the temperatures for the porous medium and external water, respectively [Θ].

The time derivative expresses the total change in energy stored in both the solid matrix and fluid per unit total volume. The term involving $\mathbf{q_a}$ [$L\ T^{-1}$] describes energy transport by convection

with the flowing groundwater. The term involving bulk thermal conductivity, $\boldsymbol{\lambda}$, accounts for heat conduction through groundwater and solids, and the term involving the dispersion tensor, $\mathbf{D_a}$ [$L^2\ T^{-1}$], approximates the contributions of irregular flows and diffusive mixing, which are not accounted for in the convection term. The term involving Q [T^{-1}], the fluid mass source, accounts for the energy added by a fluid source with temperature T^* and density ρ^*.

MIN3P-NWMO employs a weighted arithmetic mean for bulk thermal conductivity $\boldsymbol{\lambda}$ [$M\ L\ T^{-3}\ \Theta^{-1}$]:

$$\boldsymbol{\lambda} = \phi S_a \boldsymbol{\lambda_w} + (1-\phi)\boldsymbol{\lambda_s} \qquad \text{Equation 3-14}$$

where $\boldsymbol{\lambda_W}$ and $\boldsymbol{\lambda_S}$ are the fluid and solid thermal conductivities [$M\ L\ T^{-3}\ \Theta^{-1}$], respectively.

Energy production or consumption due to exothermic and endothermic chemical reactions is not implemented in the present version of MIN3P-NWMO and is not expected to significantly affect the energy balance in sedimentary basin simulations. In addition, changes in material properties at near-freezing temperatures (e.g. hydraulic conductivity, thermal conductivity) because of ice formation or melting within the porous medium are currently not coupled with energy transport. Therefore when simulating the impact of permafrost on groundwater flow the hydraulic conductivity of predetermined regions of the model domain is independently set to a low value (see Section 9.1).

3.3 GOVERNING EQUATIONS FOR REACTIVE TRANSPORT

Modelling the movement of variable density fluids requires concurrent simulation of the spatial distribution of solutes that affect fluid density. The mass conservation equations for N_c aqueous components are given by:

$$\frac{\partial \phi T_j^a}{\partial t} + \frac{\partial T_j^s}{\partial t} = -\nabla \cdot \left[\mathbf{q_a} T_j^a\right] + \nabla \cdot \left[\phi \mathbf{D_a} \nabla T_j^a\right] + Q_j^{a,a} + Q_j^{a,m} + Q_j^{a,ext} \qquad j = 1, N_c \qquad \text{Equation 3-15}$$

where T_j^a is the total aqueous component concentration for the j^{th} component [$M\ L^{-3}\ H_2O$], and T_j^s is the total concentration [$M\ L^{-3}$ porous medium] of the j^{th} aqueous component on the exchanger. $Q_j^{a,a}$ [$M\ L^{-3}\ T^{-1}$] and $Q_j^{a,m}$ [$M\ L^{-3}\ T^{-1}$] are internal source and sink terms from intra-aqueous kinetic reactions and kinetically controlled dissolution-precipitation reactions, and $Q_j^{a,ext}$ [$M\ L^{-3}\ T^{-1}$] is an external source and sink term (Mayer et al., 2002).

To complete the system of governing equations, an additional set of mass conservation equations has to be defined, which describes the change of mineral quantities over time (Mayer et al., 2002):

$$\frac{\partial V_{f,j}^{m}}{\partial t} = V_j^m R_j^m \qquad \text{Equation 3-16}$$

where $V_{f,j}^{m}$ [L^3 mineral L^{-3} porous medium] is the volumetric fraction for the *j*th mineral species, V_j^m is its molar volume [L^3 mineral M^{-1}], and R_j^m is the overall dissolution-precipitation rate for the *j*th mineral [$M\ L^{-3}\ T^{-1}$].

Total concentrations in Equation 3-15 are defined as:

$$T_j^a = c_j + \sum_{i=1}^{N_X} \nu_{ij}^x c_i^x \qquad \text{Equation 3-17}$$

$$T_j^s = \sum_{i=1}^{N_S} \nu_{ij}^s c_i^s \qquad \text{Equation 3-18}$$

where N_X and N_S are the number of aqueous complexes and ion-exchange complexes, respectively. ν_{ij}^x and ν_{ij}^s are the stoichiometric coefficients for the j^{th} aqueous component in the i^{th} aqueous complexation and ion exchange reaction, respectively. c_j is the concentration of the j^{th} primary species, and c_i^x and c_i^s are the concentrations of the *i*th aqueous complex and ion-exchanged species, respectively.

Hydrodynamic dispersion in Equation 3-15 is modelled as a Fickian process, resulting in dispersive chemical fluxes proportional to the gradient in solute concentrations. This approach is consistent with recent models developed by Frolkovic (1999) and Guo and Langevin (2002).

3.3.1 Geochemical reactions

The geochemical reactions included in MIN3P-NWMO are the same as those implemented in the original version of MIN3P (Mayer et al., 2002). The relevant reactions can be summarized as:

- Kinetic dissolution/precipitation of mineral phases, including oxidative mineral dissolution (can be surface-controlled or diffusion-controlled reactions);
- Intra-aqueous reactions that are equilibrium or kinetically controlled (e.g. oxidation of Fe(II) by dissolved oxygen); and
- Cation-exchange processes.

For a full description of the formulation of these reactions the reader is referred to Mayer et al. (2002).

3.3.2 Thermodynamic model for brines: Pitzer model

Ion interactions are neglected in dilute solution models, such as Debye-Hückel and its variants which are appropriate for dilute solutions with ionic strengths up to 0.7 mol l^{-1}. However, the interaction between individual ions cannot be neglected in highly saline solutions and brines, found for example in Canadian sedimentary basins (e.g. Hobbs et al., 2011). Simulating geochemical processes under these conditions requires a model based on virial expansions that account for ionic interactions. The most popular approaches are based on the Pitzer equations (Pitzer, 1973), which entail summation of all possible binary and ternary short-range interaction terms as well as mixing terms. Parameters have been derived for major ions (e.g. Harvie et al., 1982; Reardon, 1988; Haung, 1989; Christov and Möller, 2004). The Pitzer model is appropriate for solutions with ionic strengths up to 20 mol l^{-1} and has been applied successfully to simulate geochemical reactions in brines in various hydrogeologic settings (e.g. Eugster et al., 1980; He and Morse, 1993; Ayora et al., 1994; Krumgalz, 2001; Marion, 2002; Marion et al., 2003; Tosca et al., 2005).

The Pitzer equations have been implemented previously in a number of geochemical modelling codes including: PHREEQC (Parkhurst and Appelo, 1999), TEQUIL (Greenberg and Möller, 1989), EQL/EVP (Risacher and Clement, 2001) and EQ3/6 (Wolery and Jarek, 2003). These programs are designed to solve speciation and reaction path problems such as evaporation trends, mixing of waters, and titration. Reactive transport codes have also been formulated to employ the Pitzer equations; examples include UNSATCHEM-2D (Simunek and Suarez, 1994), SCALE2000 (Azaroual et al., 2004), PHAST (Parkhurst et al., 2005), FRACHEM (Bachler and Kohl, 2005), and BIO-CORE (Zhang et al., 2005).

To extend the applicability of MIN3P to high ionic strength solutions, the Pitzer formulation developed by Bea et al. (2010) has been implemented. This module was developed using object-oriented programming (OOP), which allowed for an efficient implementation into the MIN3P-NWMO code. Details of the mathematical and numerical formulations of the Pitzer equations are described in Appendices B.2 and B.3.

The Pitzer database developed for use with the chemical modelling code EQ3/6, as part of the Yucca Mountain project (USDOE, 2007), was used in the simulations presented here (see Appendix B.5, Appendix B.6 and Benbow et al., 2008).

3.4 NUMERICAL IMPLEMENTATION AND SOLUTION STRATEGY

The governing equations are implemented using a finite volume technique for spatial discretization and implicit time weighting for the temporal discretization. The flow and energy transport equations are solved simultaneously using Newton's method. Subsequently, the reactive transport equations are solved using the global implicit approach, also employing Newton's method for linearization. The density coupling between flow, energy and reactive transport is provided via a Picard iteration loop. A detailed presentation of the discretized equations and solution method is provided in Appendix C.

3.5 MODEL VERIFICATION

This section briefly summarizes the approach for verification of the MIN3P-NWMO code. Verification in this context refers to benchmarking the solutions obtained for selected problems with independently derived solutions, or intercomparison with comparable simulation codes. The suite of benchmark examples chosen covers the range of physical and chemical processes that are of importance to the simulations conducted in this report. The various verification examples, including input parameters and results, are described in detail in the appendices.

For verification of one-dimensional hydromechanical coupling, a comparison with the exact analytical solution presented by Lemieux et al. (2008) was conducted (Appendix D.1). The implementation of the Pitzer equations for computing activity coefficients in concentrated solutions was evaluated based on the speciation of Dead Sea water in comparison with the results obtained using two alternative geochemical speciation models (Appendix D.2).

For density-driven flow and conservative solute transport, four benchmarking problems were included following the work of Henderson et al. (2009) (Appendix D.3). Where applicable, the model results were compared to semi-analytical solutions or to literature data. The following problems were considered:

- Hydrostatic box problem (Diersch and Kolditz, 2002);
- Hydrodynamic box problem (Voss and Souza, 1987);
- Elder problem (Voss and Souza, 1987); and
- Modified Henry problem (Henry, 1964; Simpson and Clement, 2004).

For the verification of the energy balance equation, five additional benchmark problems were simulated (Appendix D.4):

- Radial flow with energy transport (comparison with analytical solution presented by Gelhar and Collins, 1971 and modified by Voss and Provost, 2008);
- Density-dependent flow and energy transport (aquifer thermal energy storage example); results are compared with SUTRA (Voss and Provost, 2008);
- Density-dependent flow and solute transport (Henry-Hilleke problem, Henry and Hilleke, 1972); results are compared with SUTRA-MS (Hughes and Sanford, 2004);
- Thermohaline convection (Oldenburg and Pruess, 1999; Geiger et al., 2006); and
- The salt dome problem (Diersch and Kolditz, 1998).

For verification of reactive transport, three examples developed by Calderhead and Mayer (2004) are presented. For these examples the MIN3P-NWMO results were compared with PHAST (Parkhurst et al., 2005) (Appendix D.5). The following problems were included because they represent important classes of reactions (i.e. homogeneous and heterogeneous; equilibrium and kinetic) that may be relevant in sedimentary rock settings:

- Dedolomitization;
- Cation-exchange; and
- Aerobic degradation of dissolved organic carbon (represented by toluene).

For verification of reactive transport in highly saline solutions, the reactive transport equations coupled with the HWM model (Harvie et al., 1984) were compared with results from the PHAST

model (Appendix D.6) for a problem that focused on the replacement of gypsum by polyhalite (Bea et al., 2010).

For all benchmark examples, good agreement was observed when comparing MIN3P-NWMO results to the reference solutions, as documented in Appendices D.1 through D.6. All benchmark problems were periodically repeated, whenever code modifications and updates were performed. This approach ensured that possible errors introduced during code development were recognized immediately and remedied.

4. CONCEPTUAL MODEL AND PARAMETERS FOR THE ILLUSTRATIVE BASE-CASE SIMULATION

The conceptual model used for the illustrative reactive transport simulations is a generic model that includes the key regionally-extensive features of several sedimentary basins located in eastern North America. Many of these key hydrogeologic features are depicted in the cross sections of the Illinois, Michigan, and Appalachian basins shown in Figure 1.

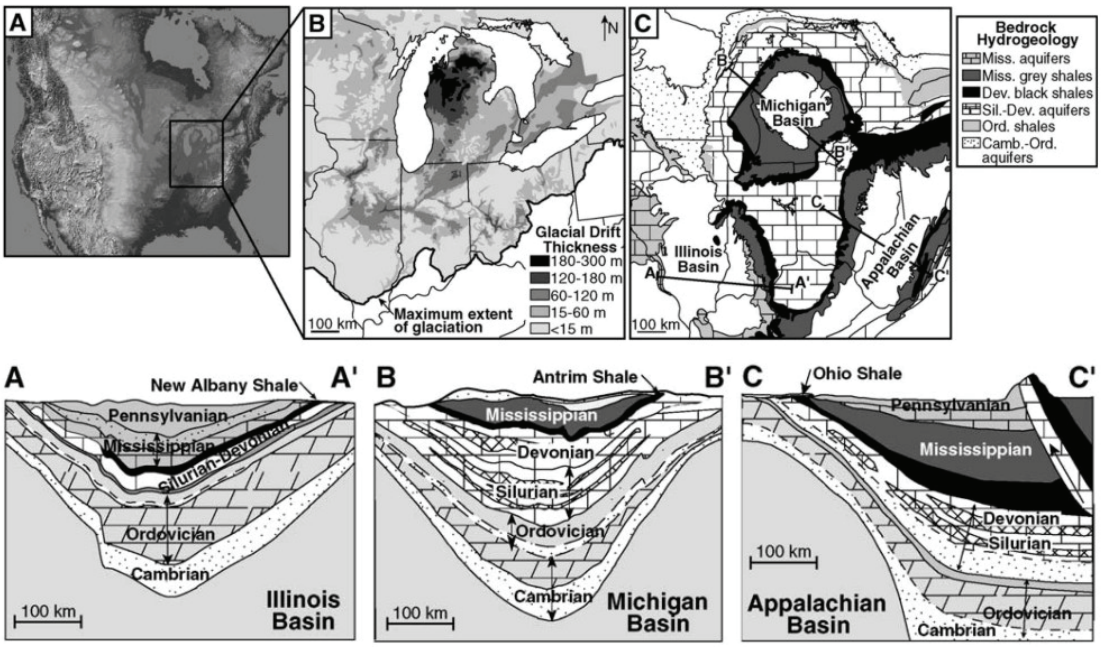

Figure 1: Location and main geological features for the intracratonic Illinois, Michigan and Appalachian sedimentary basins (from McIntosh and Walter, 2005)

These sedimentary basins are all characterized by Paleozoic sequences of limestones/ dolostones interbedded with shales and sandstones. Carbonates and sandstones constitute the main aquifers. The Silurian-Devonian and Cambrian-Ordovician aquifer systems subcrop along the margins of the Illinois, Michigan, and Appalachian basins. The basal Cambrian-Ordovician aquifers in all three basins are principally comprised of sandstones and carbonates (dolomite and limestone), confined by shales (McIntosh and Walter, 2006). The Silurian carbonates in the Michigan and Appalachian basins contain thick sequences (approximately 1 km) of bedded

halite and anhydrite, which are relatively impermeable. Overlying Devonian carbonates also contain localized halite and anhydrite (McIntosh and Walter, 2006). Deposition of relatively impermeable clays and tills during the Pleistocene helped to preserve the highly soluble evaporite minerals at shallow depths along the basin margins. Silurian-Devonian aquifers are primarily composed of dolomite and limestone. These carbonate aquifers are confined by the overlying Upper Devonian black shales, and Mississippian grey shales and siltstones. These confining units separate the Silurian-Devonian aquifer system from the overlying Mississippian clastic and carbonate aquifers (McIntosh and Walter, 2006).

The geometry and rock sequence for the hypothetical sedimentary basin used in this study are shown in Figure 2. The symmetrical sedimentary basin is about 400 km in width and has a maximum depth of 4 km. It contains a sequence of carbonates (dolostone and limestone, Dol1, Dol2, Dol3 and Lim1) interbedded with sandstone (Sand1, Sand2, Sand3 and Sand4, constituting the main aquifers) and shale (Sh1, Sh2, Sh3, constituting the main confining units). The sedimentary formations overlay the Pre-Cambrian basement (G). A weathered zone in the basement crystalline rock (Gw) is in direct contact with the lowest sedimentary unit, and noncontiguous evaporites (Ev) in dolostone unit Dol1 are also considered to provide a more comprehensive scenario. Unconsolidated glacial drift is not considered in the current conceptual model.

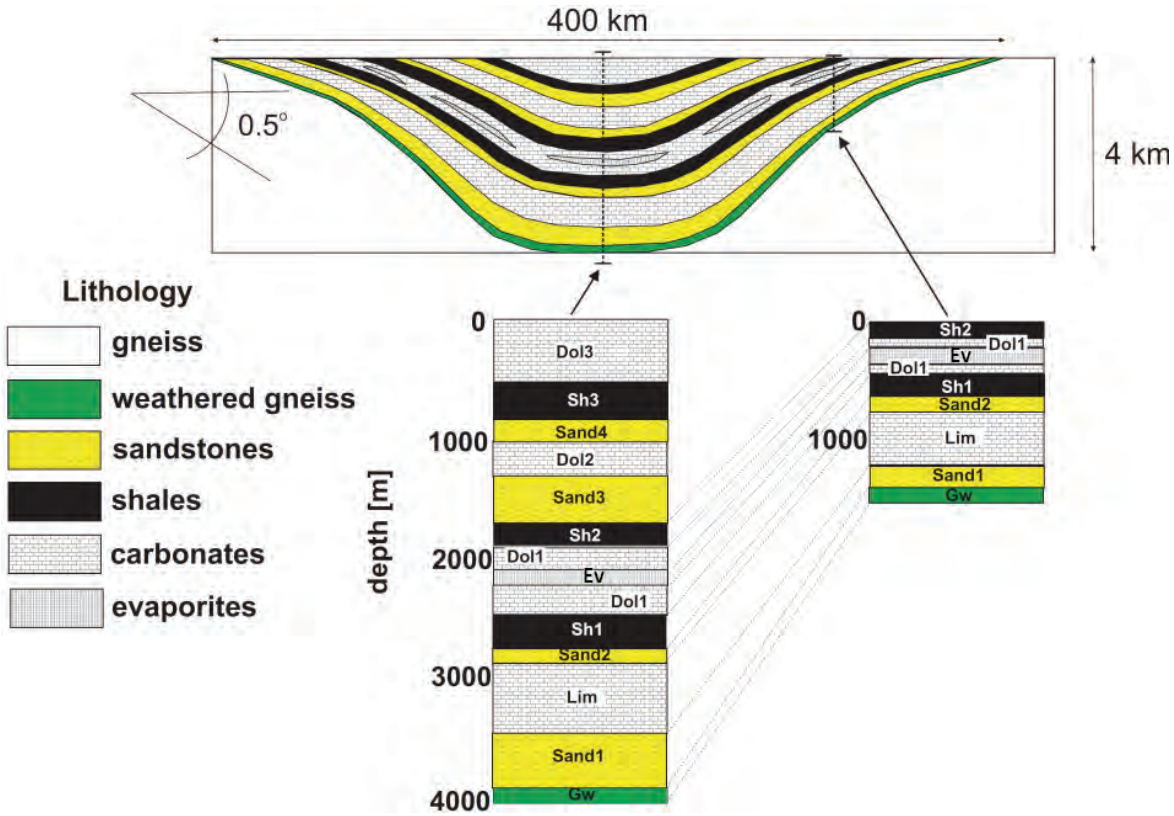

Figure 2: Geometry and main hydrogeologic units considered in the present hypothetical sedimentary basin. The basin contains a sequence of carbonates (Dol1, Dol2, Dol3 and Lim1) interbedded with sandstones (Sand1, Sand2, Sand3 and Sand4) and shales (Sh1, Sh2, Sh3), overlying a Pre-Cambrian basement (G). A weathered zone in the basement (Gw) and interbedded evaporites (Ev) are also considered

Hydrogeologic properties for the rock units are derived from a literature review and incorporate data reported for several sedimentary basins in North America (Westjohn and Weaver, 1998; Raven et al., 1992; Sykes et al., 2008; Avis et al., 2009; Birkholzer and Zhou, 2009; Harrison et al., 2009; Normani, 2009; McIntosh et al., 2011; Medina et al., 2011). Representative values for several key hydrogeologic properties are provided in Table 1. Because the value of the vertical component of hydraulic conductivity (K_V) is typically not reported, K_v is assumed to be one order of magnitude less than the horizontal component (e.g. Bense and Person, 2008; McIntosh et al., 2011). However, for the upper sandstone units, isotropic conditions are assumed, similar to the approach of McIntosh et al. (2011), who used an anisotropy factor of less than 2 for selected sandstone units.

Many physical parameters (e.g. porosity and hydraulic conductivity) in a sedimentary basin are expected to vary with depth as overlying sediments compress the underlying materials. However, variations in material properties of real sediment sequences are further complicated by variable sedimentation rates and deposit composition, diagenesis, and other processes that create heterogeneous porosity profiles. In this work we do not attempt to replicate the hydrogeologic properties of a particular sedimentary rock sequence in detail, but rather capture the general trends that are known to exist in the compacted sedimentary rocks (e.g. Bahr et al., 2001). The depth dependence of hydrogeologic properties is therefore described by an exponential or power-law porosity relationship, similar to previous investigations (e.g. Person et al., 1996; Bahr et al., 2001; Mednia et al., 2011). This approach is well suited for the illustrative large-scale simulations conducted for this study. Details regarding the calculation of hydrogeologic parameters (e.g. porosity, hydraulic conductivity, specific storage, etc.) are described in the following subsections.

Table 1: Hydrogeologic Parameters Used in BASE-CASE Simulation. Values Are for a Location Corresponding to the Center of the Sedimentary Basin

Unit	Lithology	Depth [m]	ϕ [-]	$Log_{10} K_H$ [m s^{-1}]	$Log_{10} K_v$ [m s^{-1}]	S_S [m^{-1}]
Dol3	Dolostone	200	0.027	-6.3	-7.3	3.1×10^{-7}
Sh3	Shale	700	0.102	-11.0	-12.0	1.1×10^{-6}
Sand4	Sandstone	900	0.124	-5.7	-5.7	9.2×10^{-7}
Dol2	Dolostone	1100	0.016	-7.0	-8.0	2.6×10^{-7}
Sand3	Sandstone	1500	0.100	-6.0	-6.0	8.1×10^{-7}
Sh2	Shale	1800	0.057	-11.8	-12.8	8.9×10^{-7}
Dol1	Dolostone	2000	0.009	-12.7	-13.7	2.3×10^{-7}
Ev	Evaporites	2150	0.019	-14.9	-15.9	4.5×10^{-7}
Sh1	Shale	2500	0.039	-14.4	-15.4	8.1×10^{-7}
Sand2	Sandstone	2800	0.063	-6.4	-7.4	6.5×10^{-7}
Lim	Limestone	3200	0.005	-13.7	-14.7	1.9×10^{-7}
Sand1	Sandstone	3700	0.045	-6.8	-7.8	5.7×10^{-7}
Gw	Weathered Gneiss	3950	0.002	-12.9	-13.9	5.4×10^{-7}
G	Gneiss	4000	0.002	-13.4	-14.5	1.6×10^{-7}

4.1 POROSITY

Sediment porosities will typically decrease with depth as discussed previously (e.g. Mount Simon sandstones in the Illinois Basin, Medina et al., 2011). Here, we consider that porosity ($\phi(z)$, [-]) varies with depth (z, [L]) according to Bahr et al. (2001):

$$\phi(z) = \frac{e^{-cg(\rho_S - \rho_W)z}}{e^{-cg(\rho_S - \rho_W)z} + k_1} \qquad \text{Equation 4-1}$$

where

$$k_1 = \frac{(1-\phi(0))}{\phi(0)} \qquad \text{Equation 4-2}$$

c is the compaction rate [M^{-1} L T^2] and depends on lithology, ρ_S and ρ_W are the solid and water densities, respectively [M L^{-3}], g is the gravity constant [L T^{-2}], and $\phi(0)$ is the porosity at the surface [-]. It should be noted that the fluid density will also vary with depth due to changes in the chemical composition of the groundwater. Compaction rates were assumed based on lithology and the values used for estimating porosity variations are provided in Table 2.

Table 2: Compaction Rates and Mechanical Parameters Used in the BASE-CASE Simulation. Values Are for a Location Corresponding to the Center of the Sedimentary Basin. All Values are Estimated Based on Lithology Except for the One-Dimensional Loading Coefficient, ζ, Which Is Calculated. The Parameters c, E, and ν Are Not Depth Dependent

Unit	Lithology	Depth [m]	c [Pa^{-1}]	E [GPa]	ν [-]	ζ [-]
Dol3	Dolostone	200	3.7×10^{-8}	50	0.15	0.61
Sh3	Shale	700	4×10^{-8}	15	0.1	0.59
Sand4	Sandstone	900	2.5×10^{-8}	25	0.14	0.41
Dol2	Dolostone	1100	3.7×10^{-8}	50	0.15	0.73
Sand3	Sandstone	1500	2.5×10^{-8}	25	0.14	0.46
Sh2	Shale	1800	4×10^{-8}	15	0.1	0.72
Dol1	Dolostone	2000	3.7×10^{-8}	50	0.15	0.82
Ev	Evaporites	2150	5.1×10^{-8}	16.5	0.35	0.81
Sh1	Shale	2500	4×10^{-8}	15	0.1	0.79
Sand2	Sandstone	2800	2.5×10^{-8}	25	0.14	0.58
Lim	Limestone	3200	3.7×10^{-8}	45	0.3	0.87
Sand1	Sandstone	3700	2.5×10^{-8}	25	0.14	0.65
Gw	Weathered Gneiss	3950	3.7×10^{-8}	15	0.25	0.99
G	Gneiss	4000	3.7×10^{-8}	55	0.24	0.95

Equation 4-1 implies that the porosity decreases linearly at shallow burial depths and exponentially for greater depths. In particular, for large depths, the constant k_1 will dominate the exponential term in the denominator of Equation 4-1. Values for additional hydromechanical parameters (Young's modulus, E [M L^{-1} T^{-2}]; Poisson's ratio, ν [-]) required to calculate the depth dependence of specific storage and the one-dimensional loading coefficient are also given in Table 2 (see also section 4.3).

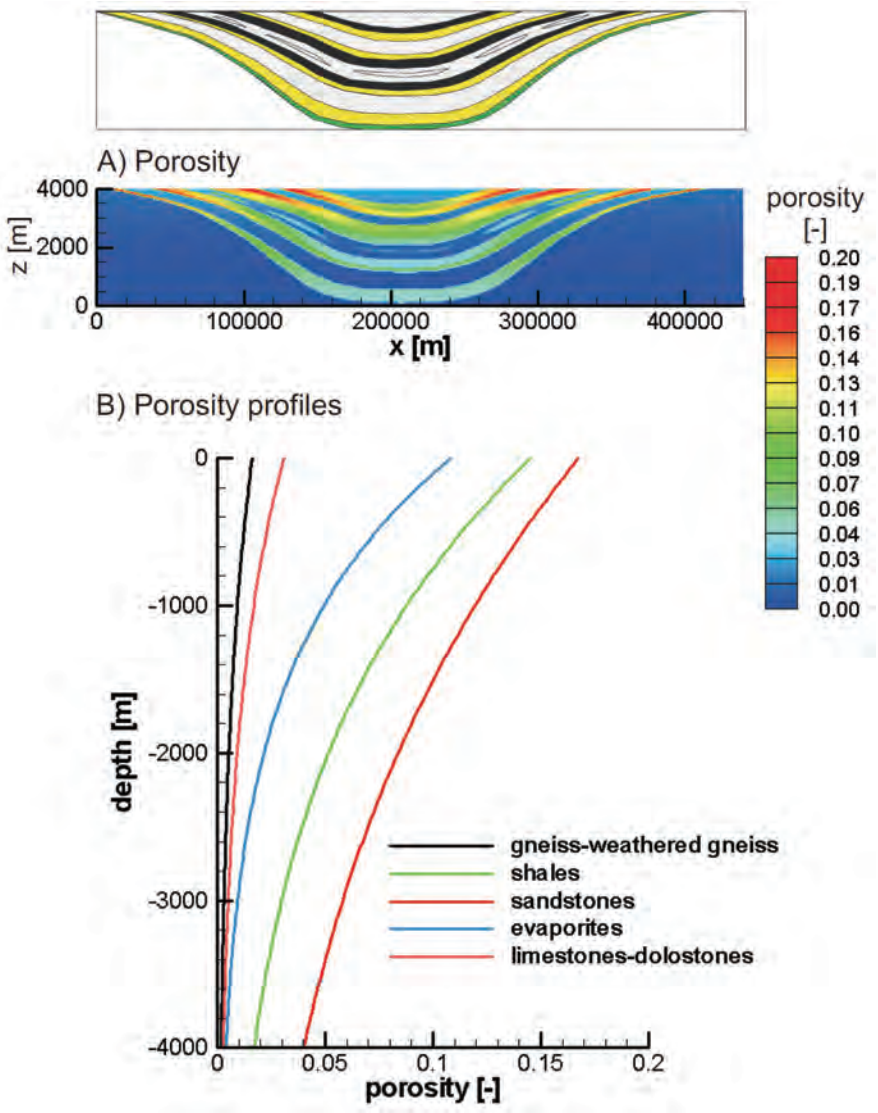

Figure 3: Initial porosity values: A) Spatial distribution. B) Vertical profiles based on lithology

The porosity field used in the simulations was computed according to Equation 4-1 and Equation 4-2. If the porosity value at the surface ($\phi(0)$) for a particular hydrogeologic unit was unknown, it was obtained from Equation 4-2 and Equation 4-1 using the reference porosity ($\phi(z_{ref})$, [-]) and reference depth (z_{ref}, [L]):

$$\phi(0) = \frac{1}{k_1 + 1}$$ Equation 4-3

where

$$k_1 = \frac{e^{-cg(\rho_s - \rho_w)z_{ref}}}{\phi(z_{ref})} - e^{-cg(\rho_s - \rho_w)z_{ref}}$$ Equation 4-4

The reference depth is the depth at which the porosity was reported in the literature. The spatial porosity distribution and depth profiles for the various rock units are shown in Figure 3A and Figure 3B, respectively (see previous page).

4.2 HYDRAULIC CONDUCTIVITY

The hydraulic conductivity tensor is also considered to vary with depth ($\mathbf{K}(z)$, [L T^{-1}]) and as a function of fluid density and viscosity. Its dependence on depth is captured by defining the permeability tensor $\mathbf{k}(z)$ as a function of the porosity field and is calculated based on the Carman-Kozeny expression:

$$\mathbf{k}(z) = \frac{\phi(z)^3}{(1-\phi(z))^2} \frac{(1-\phi(z_{ref}))^2}{\phi(z_{ref})^3} \mathbf{k_{ref}}$$ Equation 4-5

where $\mathbf{k_{ref}}$ is the reference permeability tensor [L T^{-1}], and $\phi(z_{ref})$ [-] is its associated reference porosity.

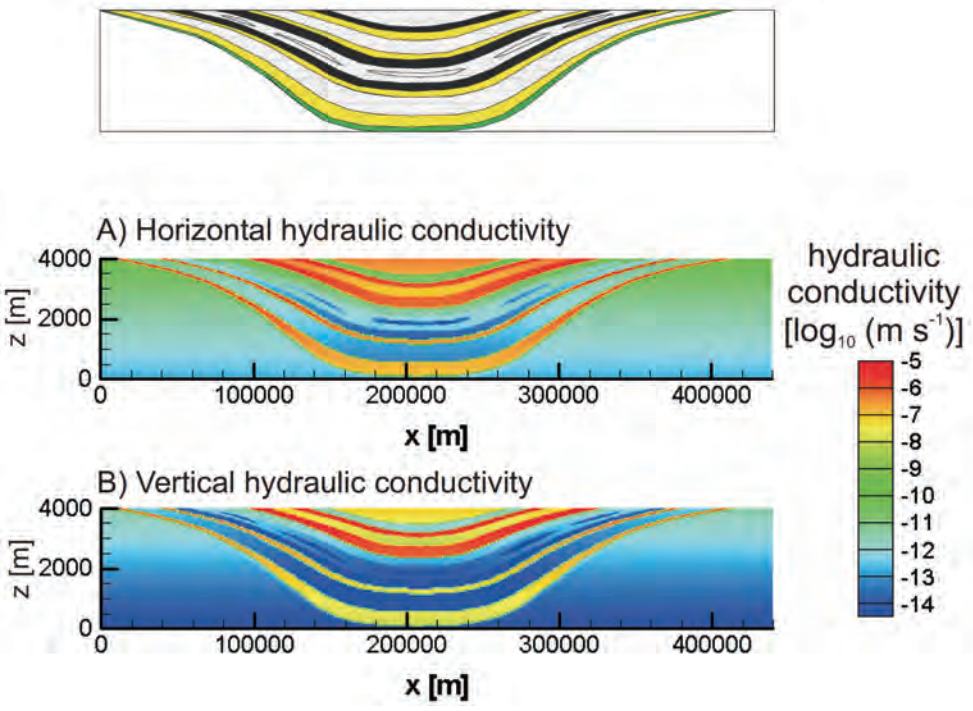

Figure 4: Hydraulic conductivity distribution: A) Horizontal component. B) Vertical component

The hydraulic conductivities are then calculated locally (when solving Equation 3-1) accounting for the fluid density and viscosity, as defined by Equation 3-3 and Equation 3-9, respectively. Horizontal and vertical hydraulic conductivity distributions for the base case simulation are shown in Figure 4A and Figure 4B, respectively (see previous page).

4.3 HYDROMECHANICAL PARAMETERS

As was discussed above, porosity changes induced by mechanical deformation of the porous medium depend on the specific storage (S_S, [L^{-1}]) and the one-dimensional loading efficiency coefficient (ζ, [-]) (see Equation 3-1). Both are computed as a function of the mechanical properties of the porous medium as (e.g. see Neuzil, 2003):

$$S_s = \rho_f g\left(\left(\frac{1}{K_b}-\frac{1}{K_s}\right)(1-\lambda)+\phi\left(\frac{1}{K_f}-\frac{1}{K_s}\right)\right) \qquad \text{Equation 4-6}$$

$$\lambda = \frac{2\alpha(1-2\nu)}{3(1-\nu)} \qquad \text{Equation 4-7}$$

$$\alpha = 1-\frac{K}{K_S} \qquad \text{Equation 4-8}$$

$$K_b = \frac{E}{3(1-2\nu)} \qquad \text{Equation 4-9}$$

where K_b is the drained bulk modulus of the porous medium [M L^{-1} T^{-2}], K_f is the bulk modulus of pore fluid [M L^{-1} T^{-2}], K_S is the bulk modulus of solids in the porous medium [M L^{-1} T^{-2}], E is Young's modulus [M L^{-1} T^{-2}], and ν is Poisson's ratio [-].

Young's modulus is the modulus of elasticity representing the stiffness of a rock material. It is defined, for small strains, as the ratio of the change of stress with strain. Poisson's ratio measures the ratio of lateral strain to axial strain, in the linearly-elastic region. For most rocks the Poisson's ratio is between 0.15 and 0.4 (e.g. Normani, 2009). Representative values for Young's modulus, E, and Poisson's ratio, ν, for the base case simulation are provided in Table 2. The one-dimensional loading efficiency coefficient (ζ) is computed as:

$$\zeta = \frac{\beta(1+\nu)}{3(1-\nu)-2\alpha\beta(1-2\nu)} \qquad \text{Equation 4-10}$$

where β is Skempton's coefficient [-], computed according to:

$$\beta = \frac{\left(\frac{1}{K_b} - \frac{1}{K_s}\right)}{\left(\frac{1}{K_b} - \frac{1}{K_s}\right) + \phi\left(\frac{1}{K_f} - \frac{1}{K_s}\right)}$$

Equation 4-11

Following Normani (2009), the rock formations were assumed incompressible in this context ($K_s = \infty$). The bulk modulus of the pore fluid was set to that of seawater (K_f = 3x10^9 Pa (kg m^{-1} s^{-2})), independent of fluid composition and pore water pressure. Distributions of computed specific storage and one-dimensional loading efficiency coefficient are shown in Figure 5A and Figure 5B, respectively. Both parameters vary with depth. The variations are more obvious for the one-dimensional loading coefficient because the parameter range is limited (0-1) and identical for all units, while the specific storage coefficient varies from unit to unit and with depth.

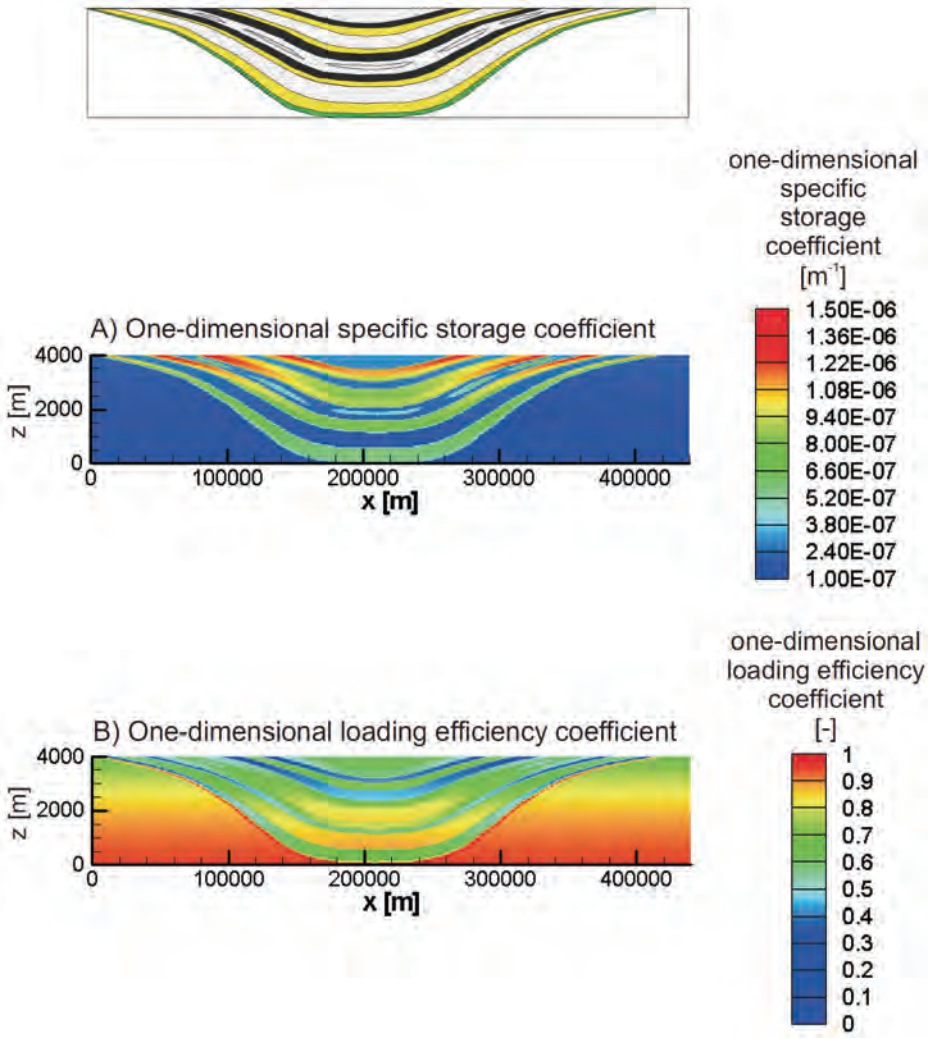

Figure 5: Spatial variation of porous medium storage parameters: A) One-dimensional specific storage coefficient. B) One-dimensional loading efficiency coefficient

4.4 GENERAL WATER COMPOSITION AND GEOCHEMICAL SYSTEM

The chemical composition of sedimentary basin formation waters differs considerably from meteoric water and is often considered to have evolved from evaporated sea water (e.g. Brennan and Lowenstein, 2002; McIntosh and Walter, 2006; Hobbs et al., 2011). Thus, major chemical components for sea water were considered in this study. Aqueous species considered in the reactive transport simulations included: Ca^{2+}, $CaOH^{+}$, $CaCl^{+}$, Mg^{2+}, $MgOH^{+}$, Na^{+}, K^{+}, SO_4^{2}, HSO_4^{-}, Cl^{-}, Br^{-}, HCO_3^{-}, CO_3^{2-}, $MgHCO_3^{+}$, H^{+}, OH^{-}, H_2O, $CaCO_3$(aq), $MgCO_3$(aq), $CaSO_4$(aq), CO_2(aq) and O_2(aq). The activity of aqueous species was computed using the HWM model (Harvie et al., 1984) implemented according to Bea et al. (2010). Virial coefficients for most of the ions were taken from the database by Benbow et al. (2008) (Appendix B.6). Reactions considered in the geochemical system are listed in Table 3.

Table 3: Geochemical Reactions Considered (BASE-CASE)

Homogeneous reactions	
$HSO_4^- \Leftrightarrow H^+ + SO_4^{2-}$	(1)
$MgOH^+ + H^+ \Leftrightarrow H_2O + Mg^{2+}$	(1)
$CaOH^+ + H^+ \Leftrightarrow H_2O$	(1)
$OH^- + H^+ \Leftrightarrow H_2O$	(1)
$HCO_3^- \Leftrightarrow CO_3^{2-} + H^+$	(1)
$CO_2(aq) + H_2O \Leftrightarrow CO_3^{2-} + 2H^+$	(1)
$CaCO_3(aq) \Leftrightarrow CO_3^{2-} + Ca^{2+}$	(1)
$MgCO_3(aq) \Leftrightarrow CO_3^{2-} + Mg^{2+}$	(1)
$CaSO_4(aq) \Leftrightarrow SO_4^{2-} + Ca^{2+}$	(1)
$CaCl^+ \Leftrightarrow Ca^{2+} + Cl^-$	(1)
$MgHCO_3^+ \Leftrightarrow Mg^{2+} + H^+ + CO_3^{2-}$	(1)
Cation-Exchange reactions	
$MgX_2 + 2Na^+ \Leftrightarrow 2NaX + Mg^{2+}$	(2)
$CaX_2 + 2Na^+ \Leftrightarrow 2NaX + Ca^{2+}$	(2)
$KX + Na^+ \Leftrightarrow NaX + K^+$	(2)
Dissolution/precipitation reactions	
$\text{Halite} \Leftrightarrow Na^+ + Cl^-$	(1)
$\text{Calcite} \Leftrightarrow CO_3^{2-} + Ca^{2+}$	(1)
$\text{Anhydrite} \Leftrightarrow SO_4^{2-} + Ca^{2+}$	(1)
$\text{Dolomite} \Rightarrow 2CO_3^{2-} + Ca^{2+} + Mg^{2+}$	(1)

(1) Equilibrium constant taken from Benbow et al. (2008).
(2) Selectivity coefficient taken Appelo and Postma (1993).

Homogeneous intra-aqueous reactions are assumed to be in equilibrium. On the time scales of interest, the concentrations of most aqueous components in shallow crustal waters are controlled by mineral solubilities. Thus, most mineral dissolution-precipitation reactions are considered to be thermodynamically-controlled. Equilibrium mineral phases include halite (NaCl), calcite ($CaCO_3$), and anhydrite ($CaSO_4$) (Table 3). Anhydrite is chosen as the Ca-SO_4 mineral phase because it is reported to be geochemically significant in several sedimentary basins (e.g. the Michigan and Appalachian basins, McIntosh and Walter, 2006); gypsum was not included in the current simulations because the presence of both anhydrite and gypsum would cause a Gibbs' phase rule violation.

Water-rock interaction involving dolomite is restricted to the process of dolomite dissolution, i.e. dedolomitization. Preliminary simulations indicated that dolomitization (i.e. dolomite formation) was occurring in the transition zone between fresh and brackish waters in the shallow aquifers. However, the highly ordered structure of dolomite complicates its precipitation from aqueous solutions at low temperatures (i.e. under near-surface conditions) and the formation of dolomite is still a matter of debate (e.g. Magaritz and Goldenberg, 1980; Baker and Kastner, 1981; Hardie, 1987). Although recent dolomite formation was observed in the mixing zone between fresh water and sea water, suggesting that dolomite formation may be more common than previously believed (Magaritz and Goldenberg, 1980), dolomitization was not considered in the present simulations.

Calcite and dolomite are assumed to be initially present in all sedimentary units. Halite and anhydrite are assumed to be initially present only in evaporite units (see also Section 7.3 below).

The cation exchange reactions considered in the BASE-CASE model are shown in Table 3, while the Cation Exchange Capacity (CEC) for the different hydrogeologic units is presented in Table 4. The CEC values were estimated by assuming that the clay content (mainly illite and chlorite) varied with lithology; the clay content for all shale units was assumed to be the same as for Upper Ordovician shales (Mazurek, 2004).

Table 4: Bulk Density and Cation Exchange Capacity Used in the BASE-CASE Simulation

		Chemical parameters	
Unit	**Lithology**	**Bulk density [kg m^{-3}] (1)**	**CEC [meq $100g^{-1}$] (2)**
Dol3, Dol2 & Dol1	Dolostone	2900	2.5
Sh3, Sh2 & Sh1	Shale	2650	5
Sand4 to Sand1	Sandstone	2800	1
Ev	Evaporite	2900	2.5
Lim	Limestone	2700	2.5
Gw	Weathered Gneiss	2750	1
G	Gneiss	2750	1

(1) Côté and Konrad (2005).
(2) Estimated.

4.5 TRANSPORT PARAMETERS

A solute diffusion coefficient of 1 x 10^{-9} m^2 s^{-1} was assumed for all dissolved species. Effective diffusion coefficients were calculated locally as a function of porosity and tortuosity based on the Millington formulation (see Mayer et al., 2002 and references therein). This implies that diffusion coefficients vary among hydrogeologic units and decrease with depth for the cases with depth-dependent porosity. The effect of dispersion was neglected for all simulations.

5. GLACIATION SCENARIO AND BOUNDARY CONDITIONS

In order to illustrate the potential hydrogeologic and geochemical perturbations generated by ice sheet movement over the sedimentary basin described above, a simplified glaciation scenario is applied. The scenario consists of a single cycle of cold-based ice sheet advance, followed by a stable glacial maximum, with subsequent warm-based ice sheet retreat. The scenario is subdivided into four stages following the approach presented by Bense and Person (2008). The scenario is depicted in Figure 6 and consists of:

- Stage I, linear ice sheet accumulation, i.e. ice sheet advance (12500 years);
- Stage II, constant ice sheet thickness (5000 years);
- Stage III, melting, i.e. ice sheet retreat (5000 years); and
- Stage IV, no ice sheet present.

The maximum ice sheet thickness and extent used in the current study are 2 km and 440 km, respectively, implying complete ice coverage of the basin during the Stage II glacial maximum.

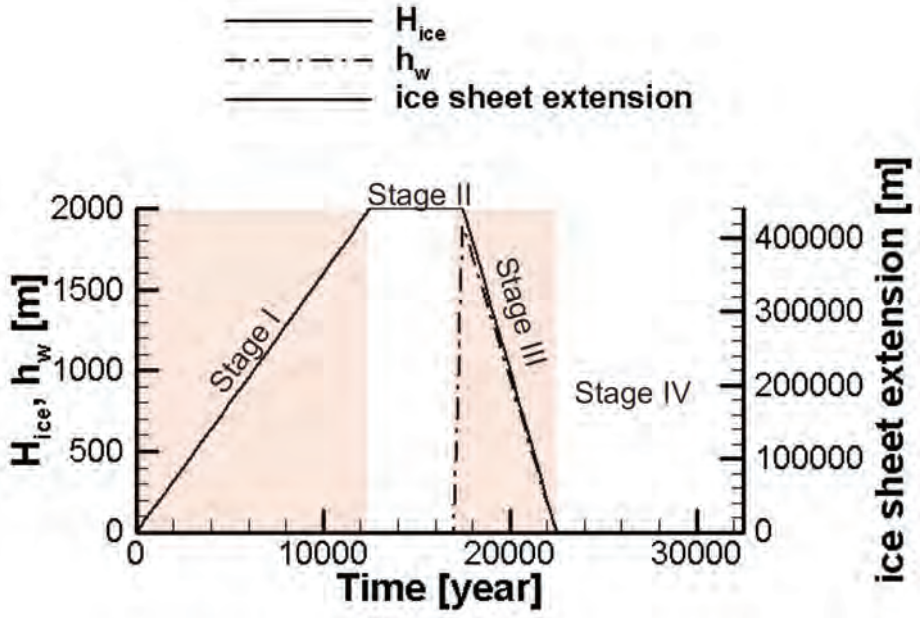

Figure 6: Glaciation scenario used to specify boundary conditions at the surface of the sedimentary basin domain, where: H_{ice} is the maximum ice sheet thickness at the right-hand edge of the domain; the ice sheet extension is measured from the right-hand edge of the domain; and h_w is the hydraulic head imposed at the right-hand edge of the domain during warm-based conditions (Stage III)

The boundary conditions for flow and solute transport are shown in Figure 7. Prescribed hydraulic head boundary conditions representing topographically-driven flow are imposed on the upper boundary of the model domain where ice is not present, with the hydraulic head varying linearly from zero to a maximum of 100 m at the center of the basin (e.g. Figure 7C). When the terminus of the ice sheet is located within the sedimentary basin the hydraulic head at the terminus is set equal to the value obtained from the linear head distribution (e.g. h1 during Stage I, Figure 7A).

The recharge boundary conditions for solute transport on the upper ice-free domain boundary are computed based on the water flux and chemical composition of meteoric water. For discharge conditions, a free exit boundary is specified for mass fluxes based on the chemical composition of the resident pore water, respectively.

During the stages of accumulation and constant ice sheet thickness (Stages I and II, Figure 6), a cold-based condition is assumed and no flux of water or solute is permitted beneath the ice sheet (i.e. $Q = Q_C = 0$ in Figure 7A). During ice sheet retreat (Stage III, Figure 6), a warm-based condition is assumed below the ice sheet and the imposed hydraulic head (Figure 7B) depends on the ice thickness. Similar to Bense and Person (2008), the thickness of the ice sheet ($h_{ice}(x,t)$, [L]) and the imposed hydraulic head beneath the ice sheet ($h_w(x,t)$, [L]) are computed as a function of distance and time according to Van der Veen (1999):

$$h_{ice}(x,t) = H_{ice}(t)\left[1-\left(\frac{x}{L(t)}\right)^{a}\right]^{1/b} \qquad \text{Equation 5-1}$$

$$h_w(x,t) = \alpha h_{ice}(x,t) \qquad \text{Equation 5-2}$$

where $H_{ice}(t)$ [L] is the specified maximum ice sheet thickness at the right-hand edge of the domain (Figure 6), L(t) [L] is the corresponding length of the ice sheet (labeled as ice sheet extension in Figure 6), x [L] is the distance from the ice sheet origin, a and b are constants [-], and α defines the ratio between the hydraulic head at the base of the ice sheet and the ice sheet thickness (in this case set to 0.95). Solute fluxes beneath the ice sheet during Stage III (Figure 7B) are computed based on the water flux and specified meltwater chemical composition.

For Stage IV, the boundary conditions for flow and solute transport are controlled by the assumed linear hydraulic head distribution, and the chemical conditions of meteoric water recharge or groundwater discharge (Figure 7C). For flow and solute transport, impervious boundaries are assumed along the two sides and bottom of the domain (Figure 7).

These boundary conditions are used in the BASE CASE simulation and in all alternative simulations. Figure 7 also includes additional thermal boundary conditions for the alternative scenario that considers non-isothermal conditions (see Section 9.5).

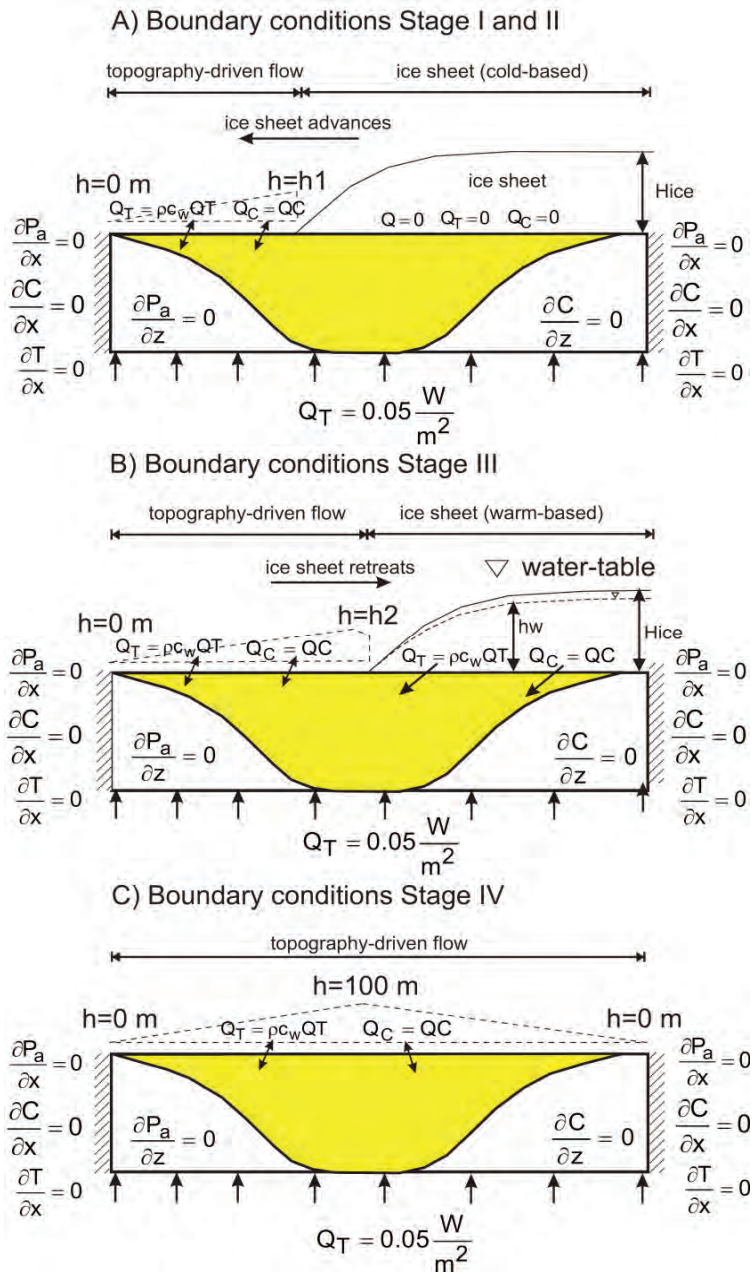

Figure 7: Boundary conditions imposed in the simulations: A) Stage I (i.e. ice sheet accumulation) and Stage II (i.e. constant ice sheet thickness). B) Stage III (i.e. ice sheet retreat). C) No ice present (i.e. present day conditions). Q **is the volumetric recharge or discharge per unit area [L** T^{-1}**],** Q_C **is the solute mass flux per unit area [M** L^{-2} T^{-1}**],** C **is solute concentration [M** L^{-3}**],** h **is the hydraulic head in ice-free areas [L],** H_{ice} **is the maximum ice sheet thickness [L], and** hw **is the hydraulic head beneath the ice sheet [L] Additional boundary conditions for the scenario that accounts for non-isothermal conditions (see Section 9.5) are also shown:** Q_T **is the energy flux per unit area [M** T^{-3}**],** T **is the water temperature [Θ], and** c_w **is the specific heat capacity of water [**L^2 T^{-2} $Θ^{-1}$**].**

6. SPATIAL DISCRETIZATION AND COMPUTATION REQUIREMENTS

The computational domain was discretized using 45,000 cells - 450 cells evenly distributed in the x (horizontal) direction and 100 cells distributed in the z (vertical) direction; the upper part of the model was refined in order to capture the processes occurring in the shallow units (see Figure 8). The fluid mass and energy conservation equations are solved simultaneously, which required the solution of a system with about 90,000 unknowns (i.e. 2 unknowns per cell, fluid pressure and temperature).

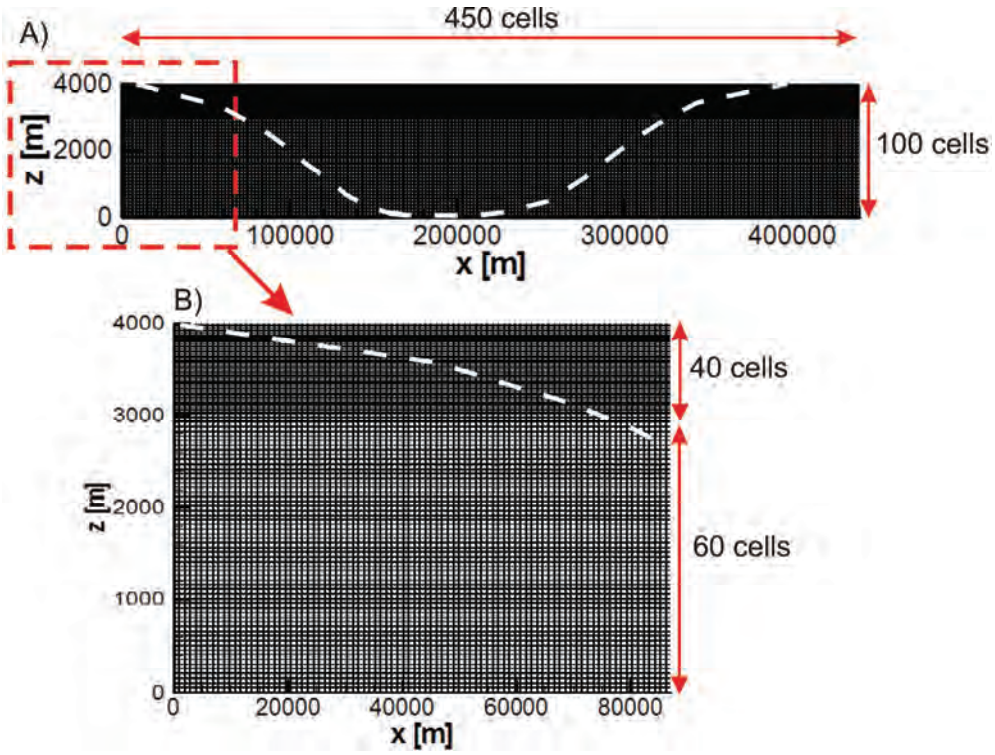

Figure 8: Spatial discretization used in the simulations: A) Entire finite volume mesh consisting of 45000 cells. B) Magnified view of the left portion of the finite volume mesh

The reactive transport calculations are the most memory-intensive portion of the simulation because of the large number of chemical components and their nonlinear interactions. MIN3P-NWMO uses the Direct Substitution Approach (DSA) in order to solve the reactive transport equations, and its memory requirements depend on the number of chemical components defined in the geochemical system (e.g. Saaltink et al., 2001; Calderhead and Mayer, 2004). The geochemical system defined in the present model includes 10 chemical components (H_2O, Cl^-, Br^-, Na^+, K^+, H^+, CO_3^{2-}, Ca^{2+}, Mg^{2+}, SO_4^{2-}). Including pressure head and temperature, there are 12 primary unknowns per cell, which results in a substantial computational demand. Runtimes for the simulations conducted during this research were on the order of 1 to 2 weeks on a state-of-the-art work station.

7. INITIAL CONDITIONS FOR ILLUSTRATIVE BASE-CASE SIMULATION

The initial conditions for flow and geochemistry for the BASE-CASE simulation are shown in Figure 9 and Figure 10, respectively.

7.1 INITIAL CONDITIONS FOR FLOW

The pressure head distributions resulting from all simulations are presented in terms of point pressure head (h(z), [L]), defined according to Post et al. (2007) as:

$$h(z) = \frac{P(z)}{g\rho(z)} \qquad \text{Equation 7-1}$$

where $P(z)$ is the pressure [M L^{-1} T^{-2}] at elevation z (L), g is the gravity constant [L T^{-2}], and $\rho(z)$ is the fluid density [M L^{-3}] at elevation z (L).

Computed initial distributions of point pressure head are shown in Figure 9B and Figure 9C. Steady state topographically-driven boundary conditions (i.e. similar to the conditions depicted in Figure 7C) were used in a 30000 year simulation to generate these initial conditions. As shown in Figure 9B and Figure 9C, the initial point pressure heads increase in an essentially linear manner with increasing depth.

7.2 INITIAL AQUEOUS GEOCHEMISTRY

In sedimentary basins, fresh to brackish waters are predominant in shallow groundwater flow systems. However, more concentrated fluids, including saline waters and brines, are present at greater depths (e.g. Hanor, 1987; McIntosh and Walter, 2005, Hobbs et al., 2011). The chemical compositions of the brines considered in the present study were initially based on data compiled by Hobbs et al. (2011). When defining initial conditions for the model, the chemical compositions of the brines were modified to be in equilibrium with the mineral phases present in the corresponding sedimentary units. For instance, as shown in Table 5 total concentrations of Mg and TIC (Total Inorganic Carbon) were specified to yield equilibrium conditions with dolomite ($CaMg(CO_3)_2$) and calcite ($CaCO_3$). Speciation and saturation indices for mineral phases were computed using Pitzer equations based on Harvie et al. (1984) and implemented according to Bea et al. (2010). The thermodynamic database described in Appendix B.6 was employed (see also Benbow et al., 2008) and fluid densities were determined using Equation 3-6 (Monnin, 1994).

The recharge in this simulation was provided by meteoric water. The composition of meteoric water shown in Table 5 was taken from Bea et al. (2004) and was equilibrated with present-day atmospheric $CO_2(g)$ (about 3.4×10^{-4} atm).

Table 5: Chemical Composition of Brines and Meteoric Water Used in the BASE-CASE Simulation

	Formation and boundary water compositions				
	(1)	**(2)**	**(3)**	**(4)**	**(5)**
pH	6	6	6	6	6
Ca [mol l^{-1}]	1.50	0.77	0.20	0.19	$6.2x10^{-4}$
Mg [mol l^{-1}]	$6.5x10^{-2}$	$4x10^{-2}$	$8.6x10^{-3}$	10^{-2}	$8.2x10^{-4}$
Cl [mol l^{-1}]	6.00	4.15	6.24	3.61	$2.9x10^{-3}$
SO_4 [mol l^{-1}]	$5.4x10^{-4}$	$4x10^{-3}$	$1.1x10^{-2}$	$5.2x10^{-5}$	$2.6x10^{-4}$
K [mol l^{-1}]	$3.4x10^{-2}$	$5.7x10^{-2}$	0.07	0.12	$6.4x10^{-5}$
TIC* [mol l^{-1}]	$1.2x10^{-4}$	$3.2x10^{-4}$	$5.2x10^{-4}$	$1.8x10^{-3}$	$1.7x10^{-5}$
Na [mol l^{-1}]	2.85	2.49	5.77	3.00	$5.2x10^{-4}$
Br [mol l^{-1}]	$1.8x10^{-2}$	$9.7x10^{-3}$	$7.4x10^{-3}$	$5.6x10^{-3}$	$4.0x10^{-5}$
Chemical signature	Ca-Na-Cl	Na-Cl	Na-Cl	Na-Cl	Ca-Mg-Cl
Ionic strength [mol l^{-1}]	7.60	4.97	6.48	3.82	$5.2x10^{-3}$
TDS [kg l^{-1}]	0.34	0.24	0.37	0.21	$2.0x10^{-4}$
Density [kg m^{-3}]	1211	1150	1204	1128	997
SI_{Hal}	-0.22	-0.71	0	-0.78	-7.47
SI_{Cal}	0	0	0	0	-4.44
SI_{Dol}	0	0	0	0	-7.64
SI_{Anhy}	-0.82	-0.25	0	-2.62	-2.76

(1) Units G, Gw, Sand1 and Sand2.
(2) Units Lim,Sh1 and Dol1.
(3) Unit Ev.
(4) Units Sh2, Sand3, Sand4, Sh3, Dol2 and Dol3.
(5) Meteoric water.
* Total Inorganic Carbon

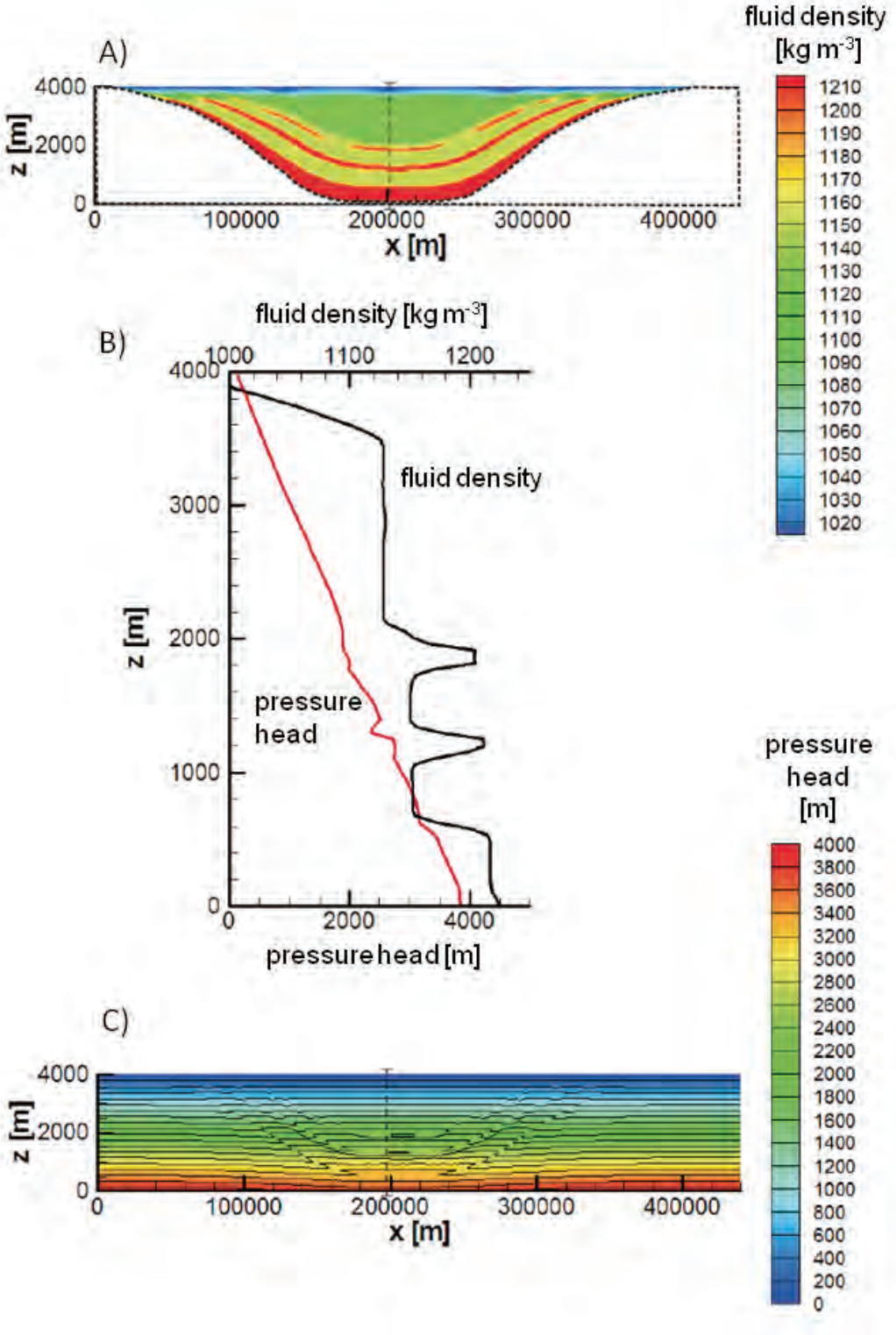

Figure 9: Initial conditions for the BASE-CASE simulation: A) Fluid density distribution. B) Vertical point pressure head and fluid density distributions in the center of the sedimentary basin. C) Spatial distribution of point pressure head

The imposed initial density distribution and a depth profile of density near the center of the basin are shown in Figure 9A and Figure 9B, respectively. Relatively fresh water (density ~ 1000 kg m^{-3}) initially exists in the upper 100 m of the domain. The fluid density then increases with depth similar to the initial conditions used in other studies of sedimentary basin fluid flow (e.g. McIntosh et al., 2011); however, the fluid density does not increase continuously with depth due to the influence of the different chemical compositions assigned for the formation brines. For example in the middle of the basin, the density reaches a local maximum of nearly 1204 kg m^{-3} (Table 5, water composition 3) at an elevation of approximately 1850 m (Figure 9B) because the evaporite unit is located between elevations 1780 m and 1900 m. Below the evaporites are dolostone (Dol1; elevation 1580 to 1780 m, Figure 2) and shale (Sh1; elevation 1290 to 1580 m, Figure 2) units and the density within this segment of the sequence drops to approximately 1150 kg m^{-3} (Table 5, composition 2). The density then again increases to 1211 kg m^{-3} between elevations 1130 and 1290 m (Figure 9B) because of the higher salinity associated with sandstone unit Sand2 (Table 5, composition 1). For gneiss, freshwater was specified in the upper 100 m of the domain; composition 1 (Table 5) was used between a depth of 100 m and the bottom of the solution domain.

7.3 INITIAL DISTRIBUTION OF MINERALOGY AND CATION EXCHANGE CAPACITY

The initial mineral volumetric contents that have been assigned to the different hydrogeologic units are shown in Figure 10A and are tabulated in Table 6.

Table 6: Mineral Volumetric Contents (%) Used in the BASE-CASE Simulation. Percentages are Assumed

Mineral	G & Gw	Sand1 to Sand4	Lim	Sh1, Sh2 & Sh3	Dol1, Dol2 & Dol3	Ev
Calcite	0	1	90	9	10	4
Dolomite	0	9	10	1	90	36
Halite	0	0	0	0	0	50
Anhydrite	0	0	0	0	0	10
Non-reactive Minerals	100	90	0	90	0	0

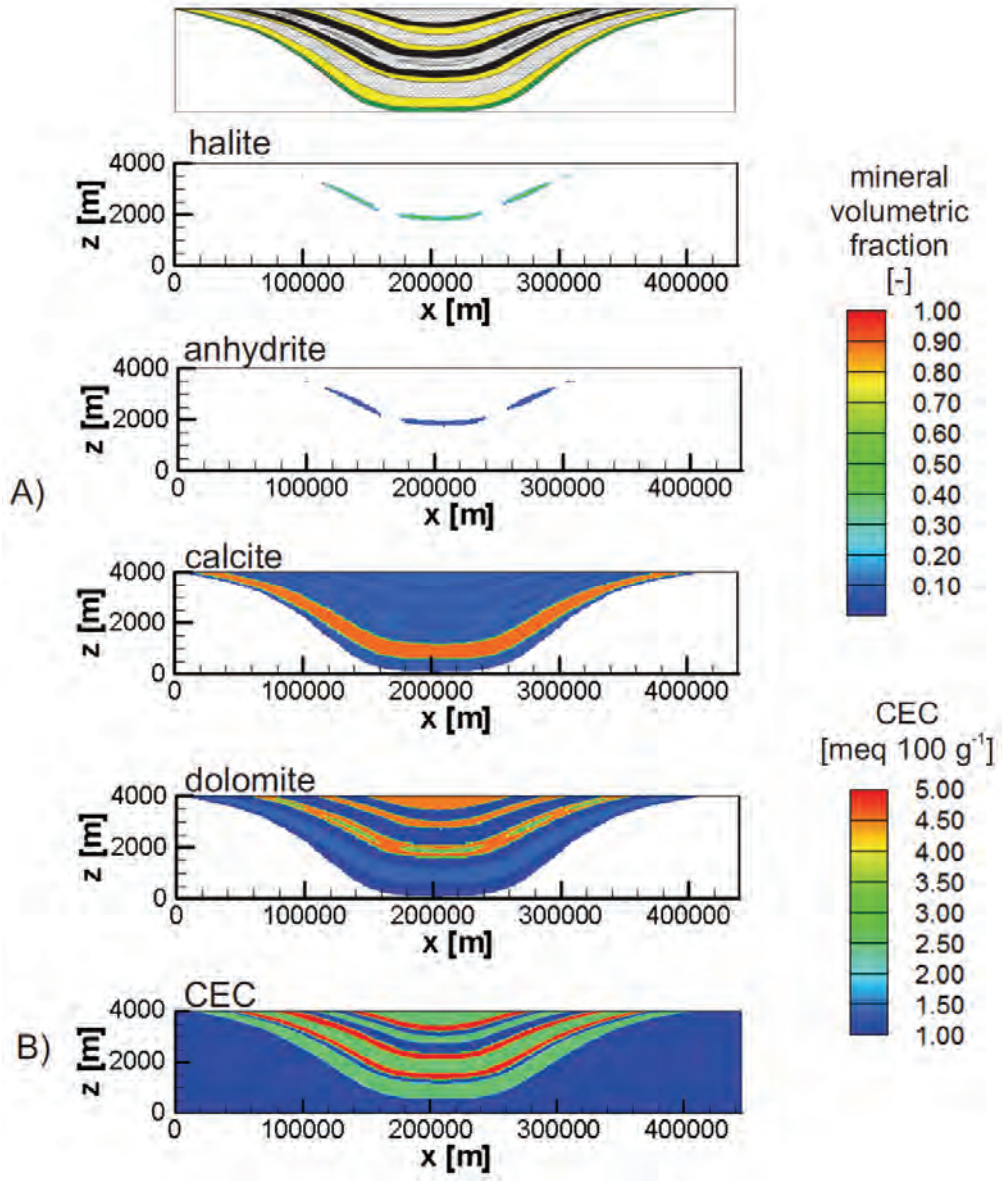

Figure 10: Initial reactive mineral and cation exchange distribution for the BASE-CASE simulation: A) Mineral volume fractions. B) Cation-exchange capacity (CEC). It was assumed that dissolution-precipitation reactions in the bedrock (Gneiss) are negligible

As discussed above, the mineral phases considered in the illustrative BASE-CASE simulation are halite (NaCl), anhydrite ($CaSO_4$), calcite ($CaCO_3$) and dolomite ($CaMg(CO_3)_2$). The mineral volumetric fraction for the i^{th} mineral phase (v_i, [-]) is computed as:

$$v_i = \frac{\%v_i}{100}(1-\phi) \qquad \text{Equation 7-2}$$

where $\%v_i$ is the volume percentage of the i^{th} mineral phase [-] in the rock and ϕ is the porosity [-]. Note that Equation 7-2 must satisfy:

$$\sum_{i=1}^{N_m} v_i = 1 - \phi \qquad \text{Equation 7-3}$$

where N_m is the total number of mineral phases present in the matrix of the porous medium. v_i, as defined in Equation 7-2 and Equation 7-3, is related to the porosity of the medium, which also varies with depth.

The CEC spatial distribution, which is assumed not to vary within individual hydrogeologic units (Table 4), is also shown in Figure 10B. Shale aquitards are characterized by relatively high CEC values, compared to limestone-dolostone aquifers and evaporite aquitards.

8. RESULTS OF THE ILLUSTRATIVE BASE-CASE SIMULATION

8.1 FLOW RESULTS

The temporal evolution of the point pressure heads and the fluid density distributions are shown in Figure 11 and Figure 12, respectively. Vertical profiles of point pressure head and density at the center of the basin at different times are shown in Figure 13. The magnitude and the horizontal and vertical components of specific discharge (Darcy velocity) at different times are depicted in Figure 14, Figure 15 and Figure 16, respectively. The temporal evolution of recharge and discharge, for the entire basin cross-section, is shown in Figure 17.

At the beginning of the simulation (i.e. in the absence of an ice sheet), groundwater flow occurs primarily at the margins of the shallow, more permeable aquifers and is driven solely by topography (i.e. Sand3, Sand4 and Dol3, see Figure 2 and Figure 15A). Recharge and discharge are essentially balanced at this time (Figure 17). Horizontal Darcy velocities in the center of the basin in Sand1 and Sand2 (Figure 2), which are the deepest high permeability units, are 2.5 x 10^{-4} and 1.1 x10^{-3} m yr^{-1}, respectively, at the beginning of the simulation (Figure 15). The vertical components of Darcy velocity at corresponding locations in Sand1 and Sand2 are on the order of 8 x 10^{-8} and 3 x 10^{-5} m yr^{-1}, respectively (Figure 16).

During Stage I (i.e. ice sheet advance), point pressure heads throughout the majority of the basin increase due to ice sheet loading (Figure 11B). The magnitude of the pressure head changes depends primarily on the hydraulic conductivity, specific storage, and loading coefficient assigned to the various hydrogeological units. The spatial variability of these parameters (e.g. Figure 4 and Figure 5B) means that the hydromechanically-induced pressure head modifications are not uniformly distributed in the basin. For example in the vertical profile at the centre of the basin at a time of 10000 yr (Figure 13A), larger pressure head differentials are induced in the intervals between 2200 and 1400 m, and between 700 and 1100 m; these intervals contain the units Dol1, Ev, and Sh1, and Lim, respectively (Figure 2). The reason for the relatively large pressure head increases in these units is that they possess some of the lowest hydraulic conductivities (approximately 10^{-13} to 10^{-15} m s^{-1}; Table 1) and highest loading coefficients (approximately 0.8 to 0.9; Table 2) in the hypothetical sedimentary rock sequence. In comparison, the Sand2 unit, which is present between 1130 and 1290 m, has a relatively high horizontal hydraulic conductivity of $10^{-6.4}$ m s^{-1} and a loading coefficient of 0.58; this parameter

combination results in a relatively small pressure differential at 10000 yr (compared to the initial conditions) as seen in Figure 13A.

The results for Stage 1 suggest that the pressure head increases in low hydraulic conductivity units (i.e. aquitards) could induce some groundwater flow from the aquitards toward adjacent aquifers of higher hydraulic conductivity. Person et al. (2007) have also predicted, for a cold-based ice sheet overriding a sedimentary basin containing a sequence of aquifers and aquitards, that vertical leakage could occur out of confining units into adjacent aquifers. For the results obtained here, an initial assessment of the impact of such leakage on water composition during the first 10000 yr of Stage I can be made by examining the simulated fluid density changes, which are a reflection of TDS and thus general water composition. It is seen that the density distribution at 10000 yr is essentially identical to the initial conditions (e.g. Figure 12A and B; Figure 13A). However, it must be noted that because the base case is a reactive transport simulation, fluid density can also be affected by geochemical processes in additional to solute transport.

The other basin-scale result of significance during Stage I is the change in specific discharge in the more permeable hydrogeologic units. For example, flow in the shallow aquifers (i.e. Sand3, Sand4 and Dol3) decreases as the cold-based ice sheet advances (Figure 14A and Figure 14B) because this effectively cuts off the meteoric recharge to these units. Conversely, at 10000 yr the specific discharge in the Sand1 and Sand2 aquifers, which extend to greater depths (Figure 2), increases relative to the initial conditions (Figure 14A and Figure 14B). At 10000 yr the horizontal component of specific discharge in Sand1 and Sand 2, at the center of the basin, (Figure 15C) is 1.4×10^{-2} m yr^{-1} and 2.9×10^{-2} m yr^{-1}, respectively. For Sand1 this represents almost two orders of magnitude increase relative to the initial conditions at this location. Because there is no glacial meltwater recharge during Stage I, the increase in specific discharge in the deeper confined aquifers must result from leakage of water from the lower permeability units (i.e. hydromechanical effects) or release from storage as a consequence of mechanical loading.

During Stage I the recharge to the basin progressively decreases (Figure 17) as more of the ground-surface boundary is covered by ice. However discharge from the basin, which results primarily from the flow caused by hydromechanical loading effects, continues until complete ice coverage at 12500 yr. During Stage II (complete ice coverage) the basin is a closed system (Figure 17). This condition arises because of the assumptions inherent in the conceptual model: i.e. a two-dimensional basin, and complete ice coverage during glacial maximum.

Results for Stage III are presented at two simulation times, 18000 yr and 20000 yr, in order to better visualize processes during the period of rapid glacial retreat and high subglacial hydraulic heads (Figure 6). These high hydraulic heads cause relatively large recharge and discharge fluxes during the period of glacial retreat (Figure 17).

Near the beginning of Stage III (i.e. 18000 yr), pressure heads increase in shallow permeable units (Figure 11C and Figure 13B) as a consequence of the re-established hydraulic connection between the now warm-based melting ice sheet and these sedimentary units. Some of the highest Darcy velocities are generated in the shallow aquifers during the early stages of glacial retreat (e.g. Figure 14C, Figure 15C, Figure 16C). At 18000 yr the horizontal Darcy velocities in the deepest section (i.e. center of basin) of the Sand1 and Sand2 aquifers are also increased to 4.3×10^{-2} m yr^{-1} and 2.3×10^{-1} m yr^{-1}, respectively. These pressure head and specific discharge changes are not; however, significant enough to perturb the fluid density in the vast majority of the basin (e.g. Figure 12C, Figure 13B). The only regions of notable meltwater ingress are in the

shallow aquifers Dol2 (x=133000 m; Figure 12C) and Sand4 (x=278000 m; Figure 12C) where isolated plumes of fresh water reach depths of approximately 350 m and 320 m, respectively.

By 20000 yr the ice sheet has retreated past the center of the basin and the point pressure heads exhibit a general decline at this location (Figure 13C). Specific discharge also exhibits a general decline, relative to 18000 yr, throughout the basin (e.g. Figure 14D); the horizontal flow direction continues to be from right to left, with the highest Darcy velocities focused in shallow permeable units that sub-crop beneath the toe of the retreating ice sheet (Figure 15D, Figure 16D). The horizontal specific discharge in Sand1 and Sand2 at the center of the basin at 20000 yr is still elevated relative to the initial conditions (Figure 15D), at 2.2×10^{-2} m yr^{-1} and 1.2×10^{-1} m yr^{-1}, respectively. Declines in fluid density at 20000 yr relative to the initial conditions are again restricted to approximately the upper 300 m of the shallow permeable aquifers (Figure 12D), with a minor density increase noted at the bottom of the Sh1 shale unit (elevation 1290 m to 1580 m, Figure 13C). The unit immediately underlying Sh1 is Sand2, which has higher fluid density and, at 20000 yr, a higher fluid pressure; the slight increase in density noted for the bottom of Sh1 is likely related to transport of solutes upward from Sand2 or to the geochemical reactions.

During Stage IV (i.e. inter-glacial period), the recharge and discharge from the basin are again balanced and the values of each have stabilized close to those assigned as the initial conditions (Figure 17). Specific discharge remains slightly elevated in the shallow permeable aquifers (Figure 14D), while horizontal specific discharge in the center of the basin in the deep units Sand1 and Sand2 is about a factor of two to three greater than initially (Figure 14A). Point pressure heads in the center of the basin have essentially returned to the initial conditions (Figure 13D), with some lower than initial pressures occurring in the Dol1, Ev, Sh1 sequence that occurs between elevations 1290 and 2090 m. As discussed previously, these units have relatively low hydraulic conductivity and this causes these units to take longer to equilibrate to changes in hydraulic boundary conditions. The fluid density distribution below a depth of approximately 300 m is essentially the same as the initial distribution (Figure 12E, Figure 13D).

The maximum horizontal Darcy velocity in the Sand2 unit, which at mid-basin occurs at a depth of approximately 2800 m and has a horizontal hydraulic conductivity of $10^{-6.4}$ m s^{-1} (Table 1), was obtained during Stage III at 18000 yr. The horizontal Darcy velocity in Sand2 at this time was 2.3×10^{-1} m yr^{-1}. Person et al. (2007) also provide results for the maximum horizontal Darcy velocity in their aquifer unit “a3”, which in their hypothetical sedimentary basin occurs at a depth of approximately 2800 m (mid-basin) and has a horizontal hydraulic conductivity of 10^{-6} m s^{-1}. Person et al. report (their Figure 16) a maximum horizontal Darcy velocity of 9.5×10^{-2} m yr^{-1} for aquifer unit “a3”, which occurs at 10000 yr when their assumed warm-based ice sheet reaches its stationary phase. Although we have used a different glacial loading scenario (i.e. cold-based during the advance phase), and different simplifying assumptions and mathematical formulations, the similarity (within a factor of 2.5) between the maximum horizontal Darcy velocities in what are essentially equivalent hydrogeologic units provides support for the BASE-CASE groundwater flow results obtained in this study.

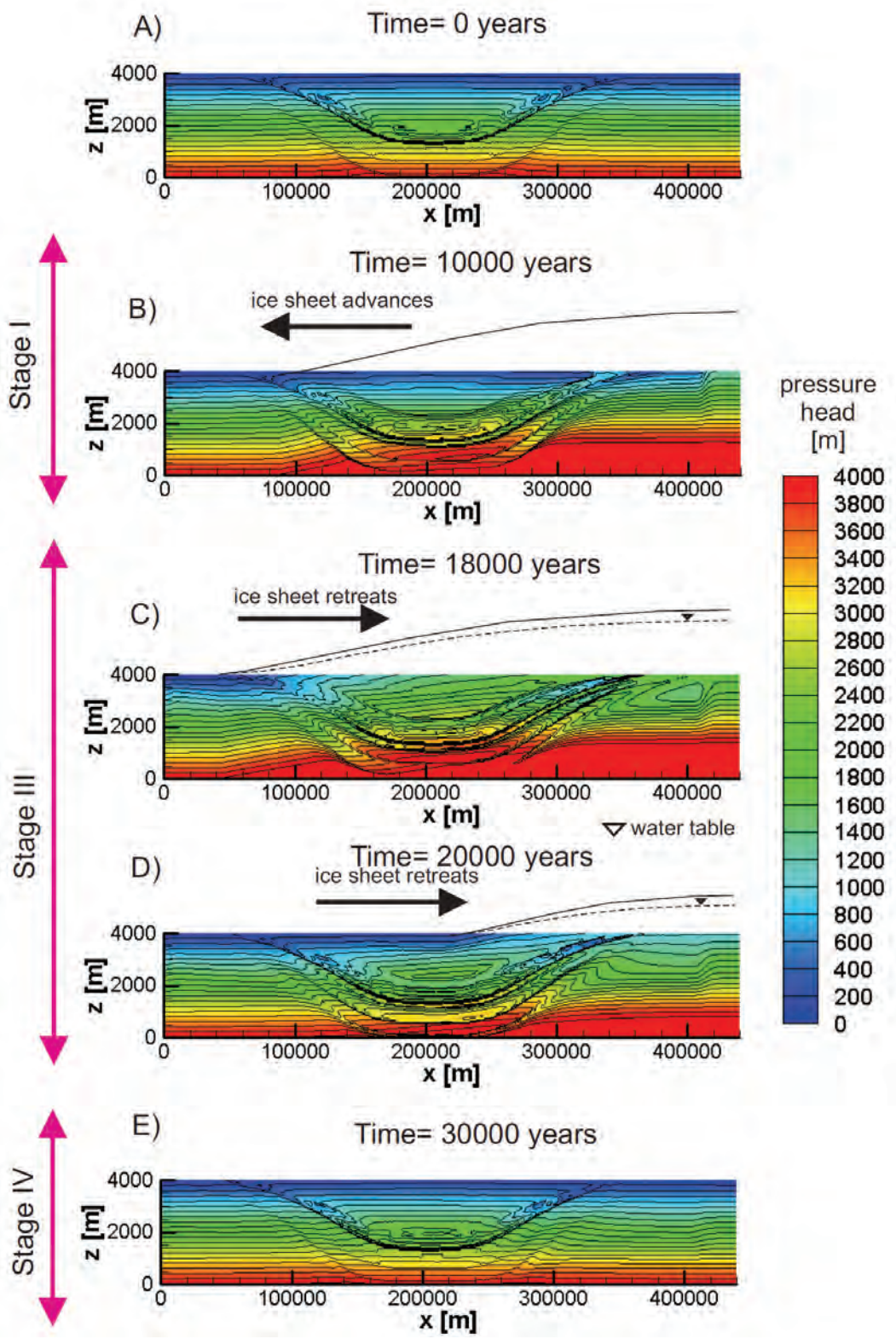

Figure 11: BASE-CASE simulation results - spatial distribution of point pressure heads: A) Initial condition. B) 10000 years (Stage I). C) 18000 years (Stage III). D) 20000 years (Stage III). E) 30000 years (Stage IV)

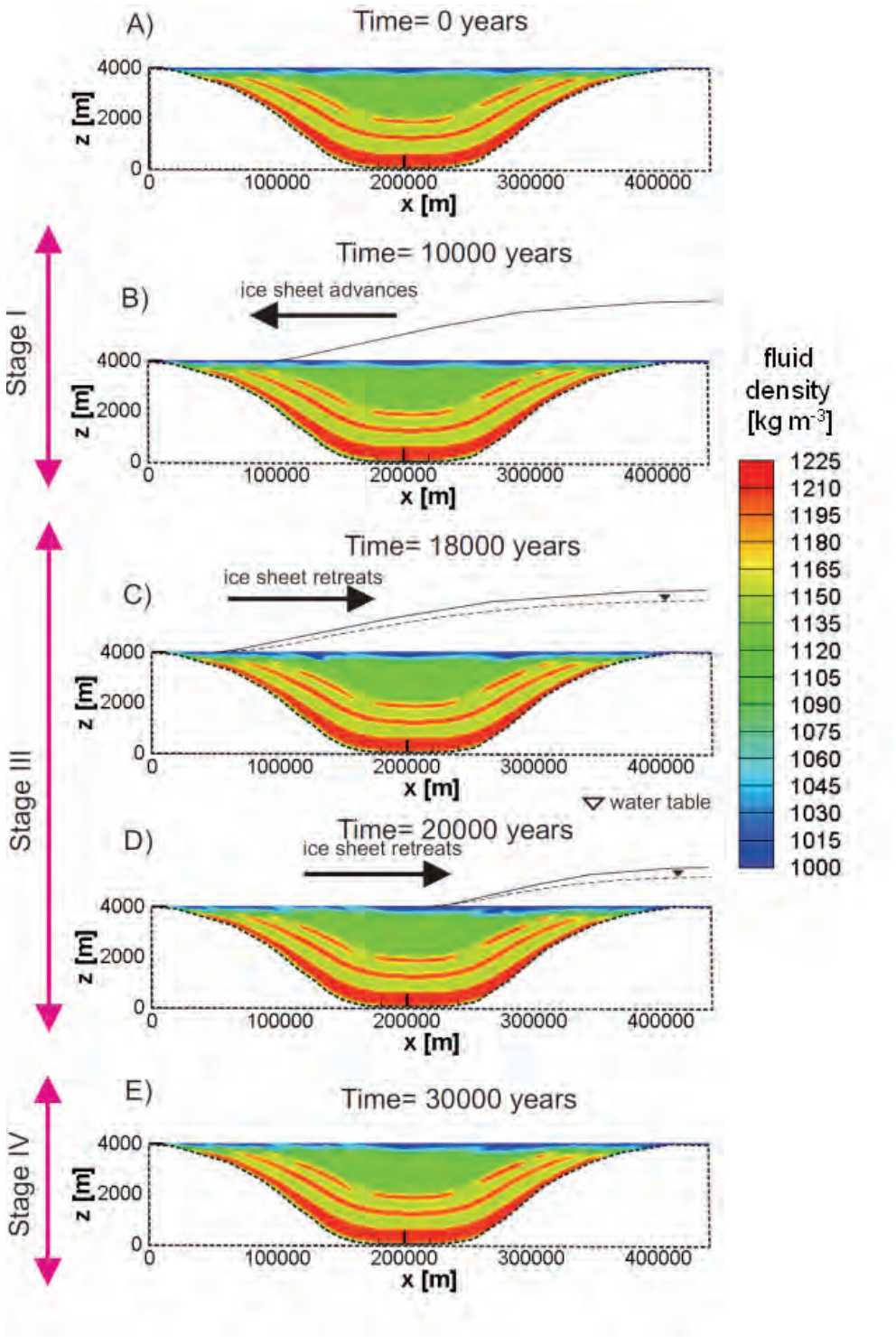

Figure 12: BASE-CASE simulation results - spatial distribution of fluid density: A) Initial condition. B) 10000 years (Stage I). C) 18000 years (Stage III). D) 20000 years (Stage III). E) 30000 years (Stage IV), results for crystalline basement rock (gneiss) removed for clarity

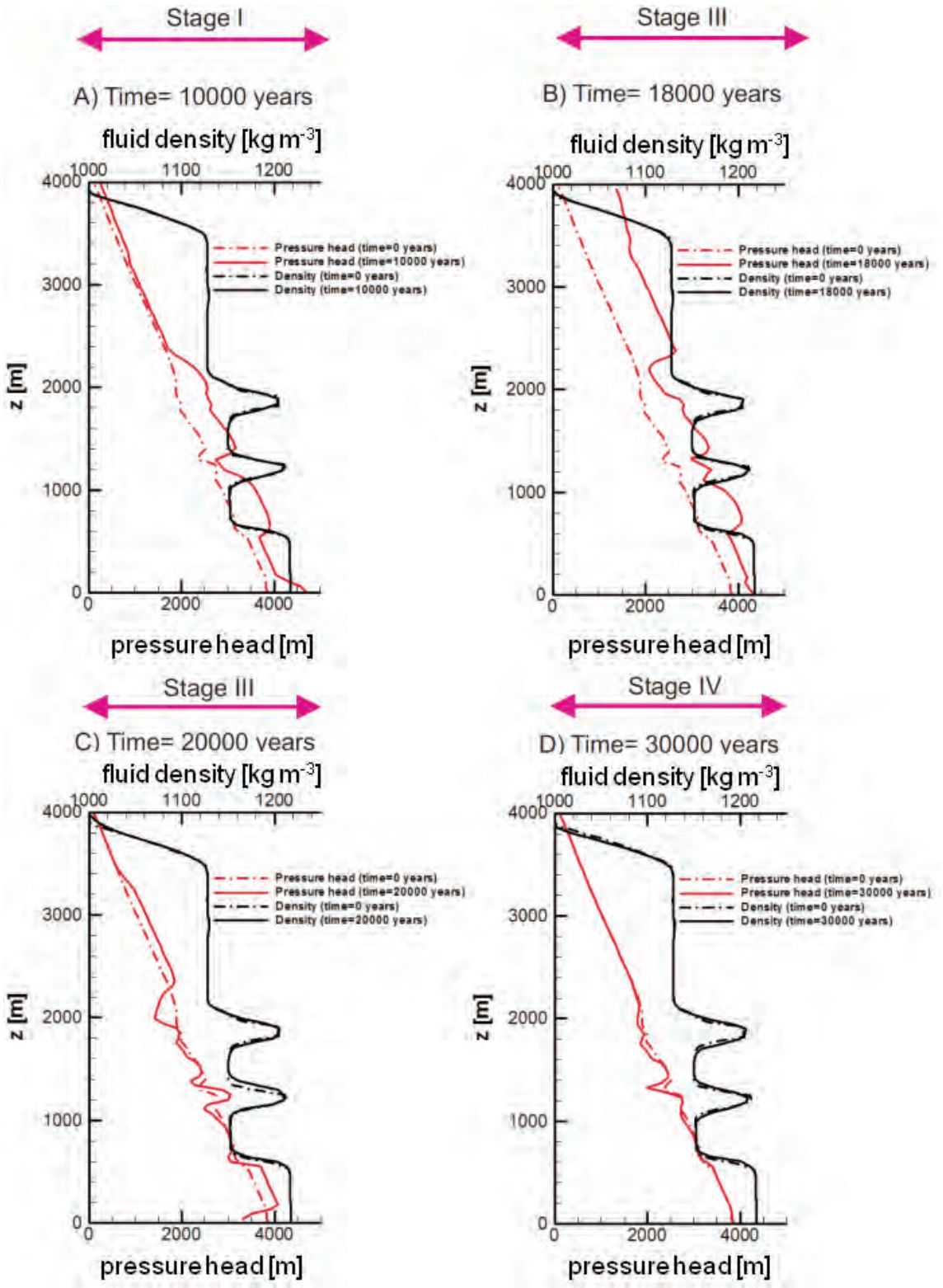

Figure 13: BASE-CASE simulation results - vertical point pressure head and fluid density distributions in the center of the sedimentary basin: A) 10000 years (Stage I). B) 18000 years (Stage III). C) 20000 years (Stage III). D) 30000 years (Stage IV)

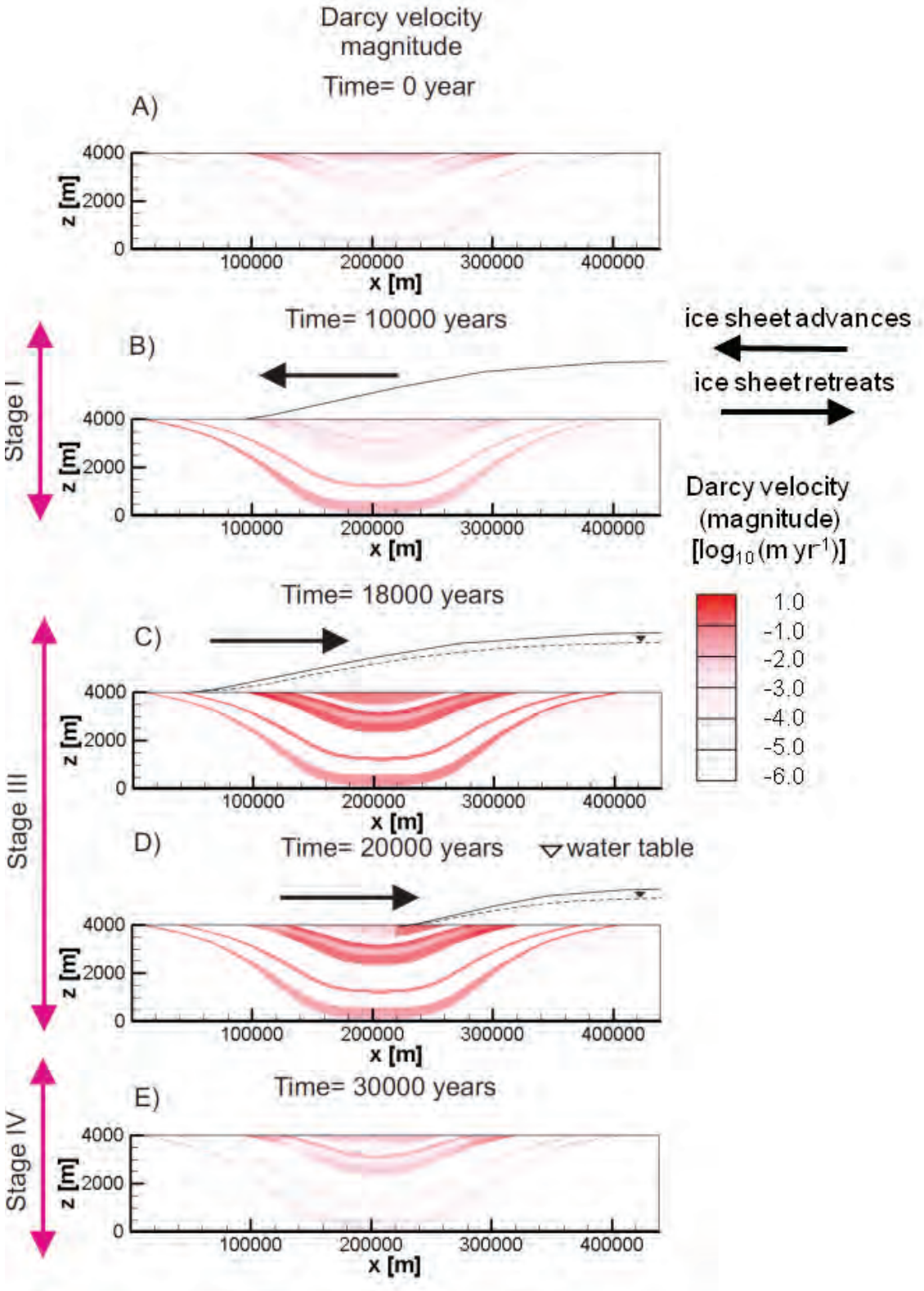

Figure 14: BASE-CASE simulation results - magnitude of specific discharge (Darcy velocity) at different times: A) Initial condition. B) 10000 years. C) 18000 years. D) 20000 years. E) 30000 years

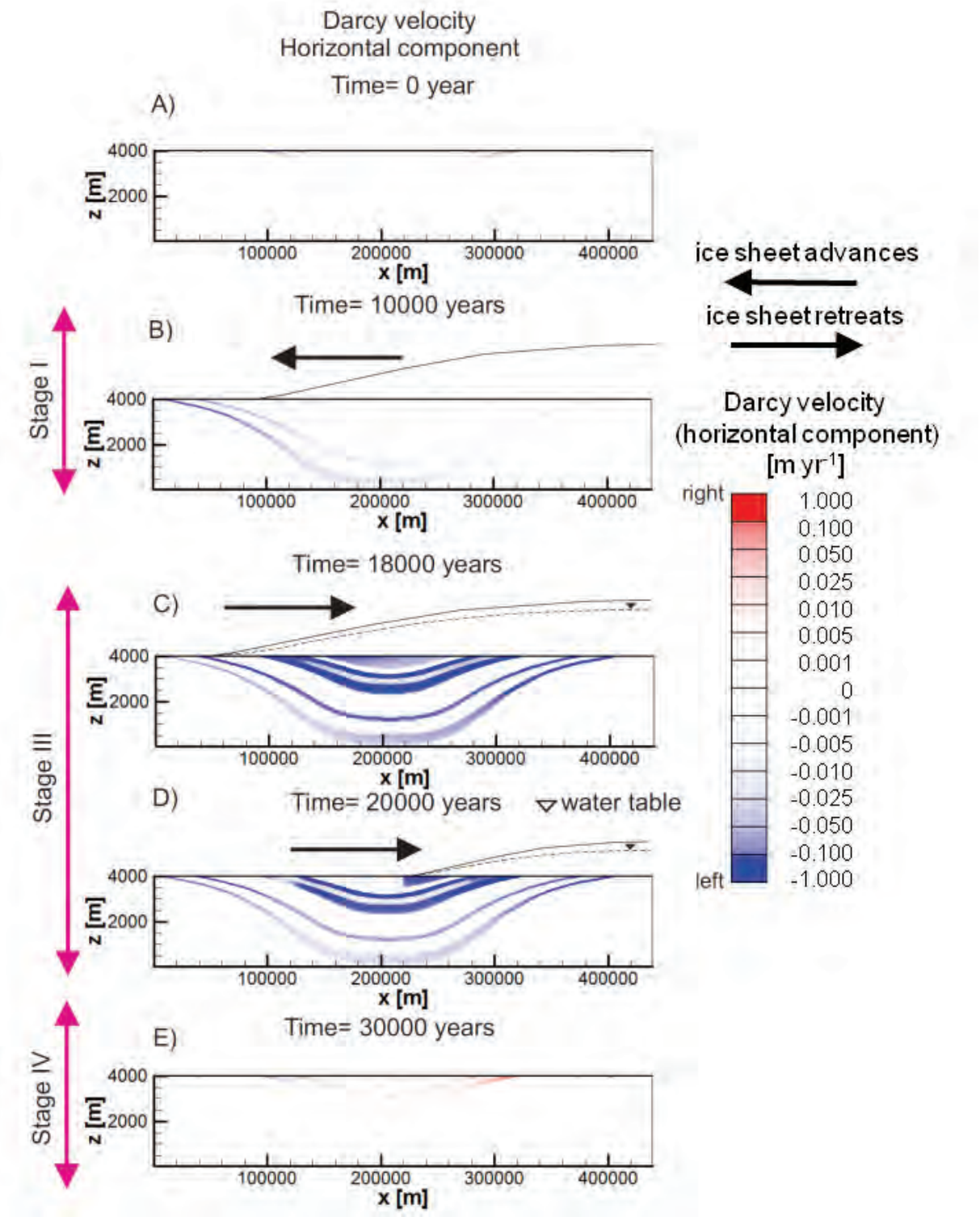

Figure 15: BASE-CASE simulation results - horizontal components of specific discharge (Darcy velocity) at different times: A) Initial condition. B) 10000 years. C) 18000 years. D) 20000 years. E) 30000 years

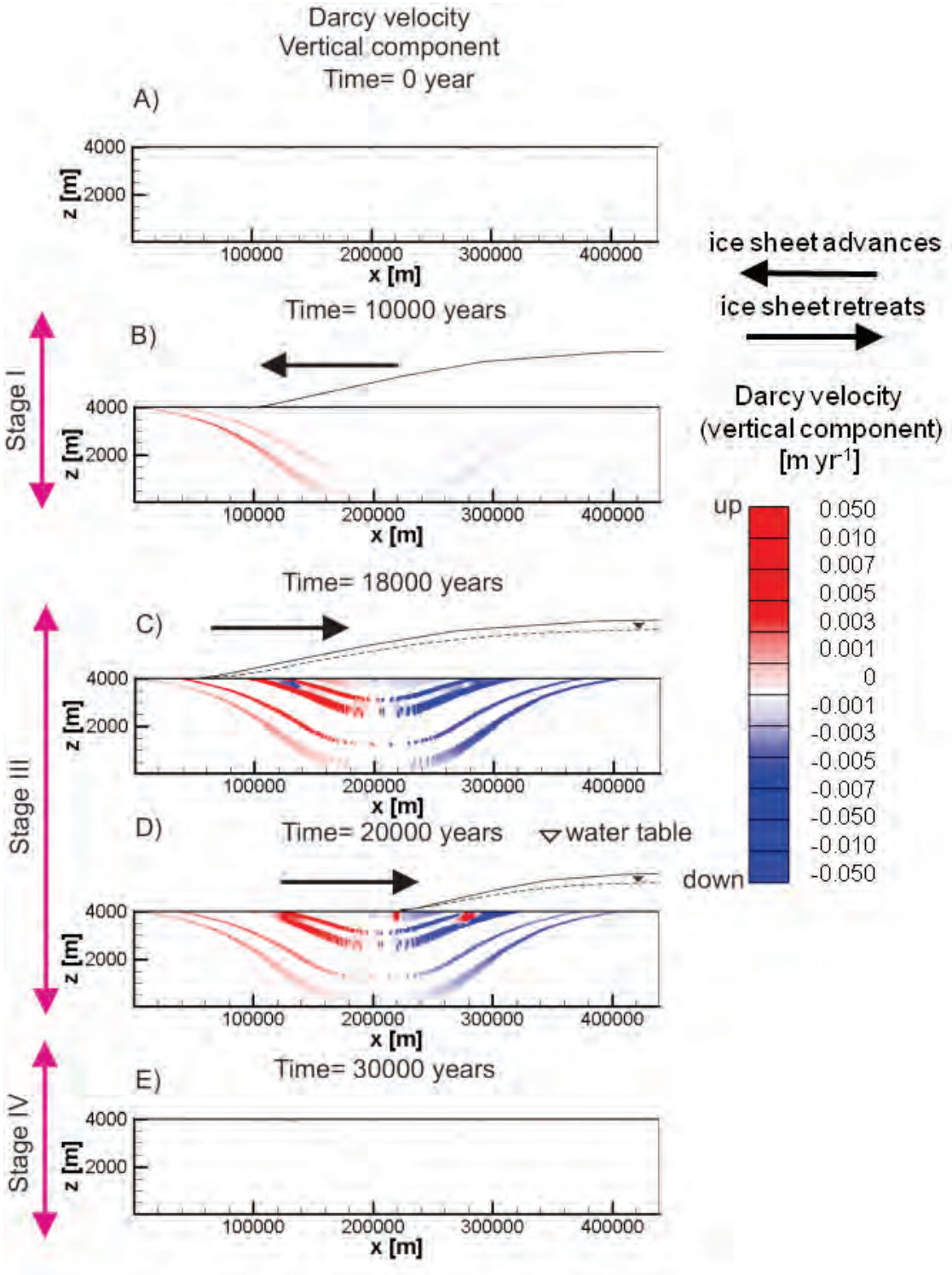

Figure 16: BASE-CASE simulation results - vertical components of specific discharge (Darcy velocity) at different times: A) Initial condition. B) 10000 years. C) 18000 years. D) 20000 years. E) 30000 years

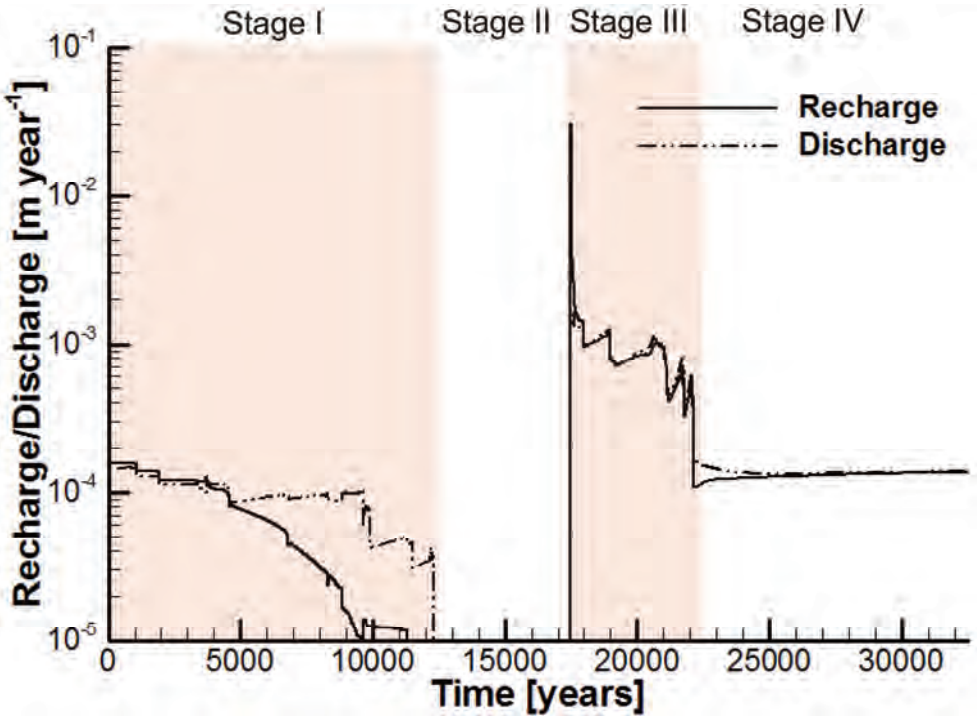

Figure 17: BASE-CASE simulation results - temporal evolution of the recharge and discharge rates in the sedimentary basin

8.2 MINERAL DISSOLUTION/PRECIPITATION

Mineral dissolution and precipitation are expected to be the most important geochemical processes occurring in the basin during a glaciation event. As was discussed in Section 4.4, mineral dissolution/precipitation may occur due to displacement of groundwater into a region with a different mineral assemblage than present at its origin, or when waters with different chemical compositions mix. For example, mineral dissolution may be induced by the infiltration of fresh water undersaturated with respect to mineral phases present in the rock matrix (i.e. calcite ($CaCO_3$), dolomite ($CaMg(CO_3)_2$), anhydrite ($CaSO_4$) and halite (NaCl)). For the current simulation, there are three potential zones where reactions are expected to occur:

1) In the pre-existing transition zone between fresh water and brine as a consequence of groundwater displacement;
2) At the boundary of aquitards/aquifers due to the differential response to glacial loading and diffusive exchange; and
3) At the basin margins as a result of the fresh water recharge.

As expected, simulated rock-water interaction processes vary in space and time during the evolution of the glaciation event. To visualize these processes, the spatial distribution of mineral dissolution/precipitation rates are presented for two times, 10000 yr (Stage I) and 21000 yr (Stage III). Average mineral dissolution/precipitation rates for each time have been computed based on the difference between the volume fractions at the presented simulation time, and the volume fraction present at the beginning of the particular glaciation stage (e.g. Stage III begins

at t= 17500 yr, Figure 6). For example, when calculating rates for Stage III, mineral volume fractions at 21000 yr are compared to those at 17500 yr.

Up to the simulation time of 10000 yr (i.e. during ice sheet loading), halite dissolution and calcite precipitation exhibit the largest average rates, and are the most spatially extensive mineral reactions in the basin (Figure 18). Halite dissolution is spatially restricted to the assumed initial location of this mineral phase (i.e. within the Ev unit, Figure 10A). Diffusive exchange between Dol1, which completely surrounds the Ev unit and in which groundwater is initially undersaturated with respect to halite (Table 5), is the most probable mechanism driving halite dissolution.

Calcite precipitation rates are greatest in the shallow flanks of the basin (Figure 18C), and are in part related to dedolomitization. Dedolomitization is indicated by the coincident spatial patterns of calcite precipitation and dolomite dissolution that occur, for example, at shallow depths near the boundary between units Sand2 and Sh1 (Figure 18C and D). Again, mixing of waters from these two units is likely responsible for driving these reactions.

Anhydrite exhibits relatively low rates of precipitation during Stage I (Figure 18B). As discussed when presenting the conceptual model, anhydrite was chosen as the calcium-sulfate mineral phase because of its noted importance in sedimentary basins; however, it is also possible that gypsum could precipitate under similar geochemical conditions.

At the simulation time of 21000 yr (i.e. 3500 yr into Stage III), the spatial extent and magnitude of the halite dissolution rates are essentially unchanged from those obtained during the first 10000 yr of Stage I, with maximum rates of approximately 10^{-4} mol m^{-3} yr^{-1} (Figure 19A).

Calcite precipitation and coincident dolomite dissolution (i.e. dedolomitization) are occurring in a larger portion of the basin during glacial retreat than during Stage I (Figure 19C and D); however, the highest reaction rates for calcite precipitation and dolomite dissolution remain restricted to the upper 500 m of the domain. The precipitation rates for calcite are about two times larger than the dissolution rates for dolomite because two moles of calcite are precipitated for each mole of dolomite that is dissolved. Interestingly, calcite dissolution is also occurring during Stage III where fresh meltwater has recharged the relatively high hydraulic conductivity Dol2 and Sand3 units near the toe of the receding ice sheet (x= 310000 m, Figure 19D).

The amount of each mineral dissolved or precipitated during the entire 32500 yr simulation is small relative to the initial volume fractions (i.e. Figure 10; Table 6). Over the entire simulation the maximum change in mineral volume fractions are: 0.26% for halite dissolution; 0.0006% for anhydrite precipitation; 0.033% and 0.0089% for calcite dissolution and precipitation, respectively; and 0.0046% for dolomite dissolution.

As might be expected, mineral dissolution and precipitation will influence porosity. However, the porosity is influenced not only by mineral reactions, but also by the hydromechanical coupling resulting from loading by the ice sheet. These two components, and the total porosity change during the simulation, are shown in Figure 20. The maximum porosity increase of approximately 0.004 occurs in the Ev unit because of halite dissolution; this unit had an initial porosity that varied with depth from approximately 0.08 to 0.02 (Figure 3). The results therefore indicate a porosity enhancement of approximately 5 to 20% in the Ev unit during the course of the simulation. The natural tendency of evaporates to compensate for dissolution-induced porosity changes by deformation and consolidation was not considered in the present simulations. Porosity decreases due to mineral precipitation are negligible (Figure 20B).

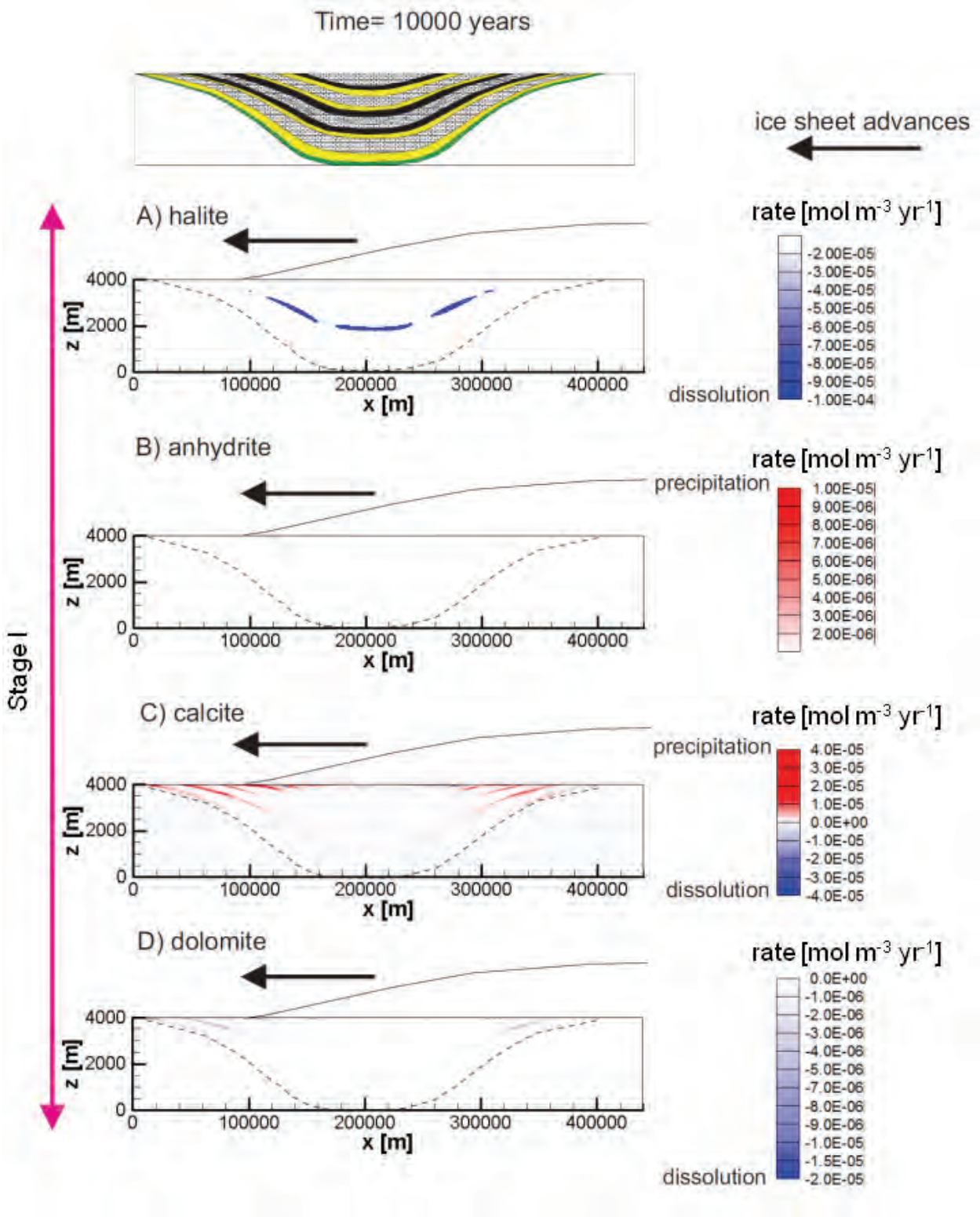

Figure 18: BASE-CASE mineral reaction rates at 10000 years: A) Distribution of halite dissolution rate. B) Distribution of anhydrite precipitation rate. C) Distribution of calcite dissolution/precipitation rates. D) Distribution of dolomite dissolution rate

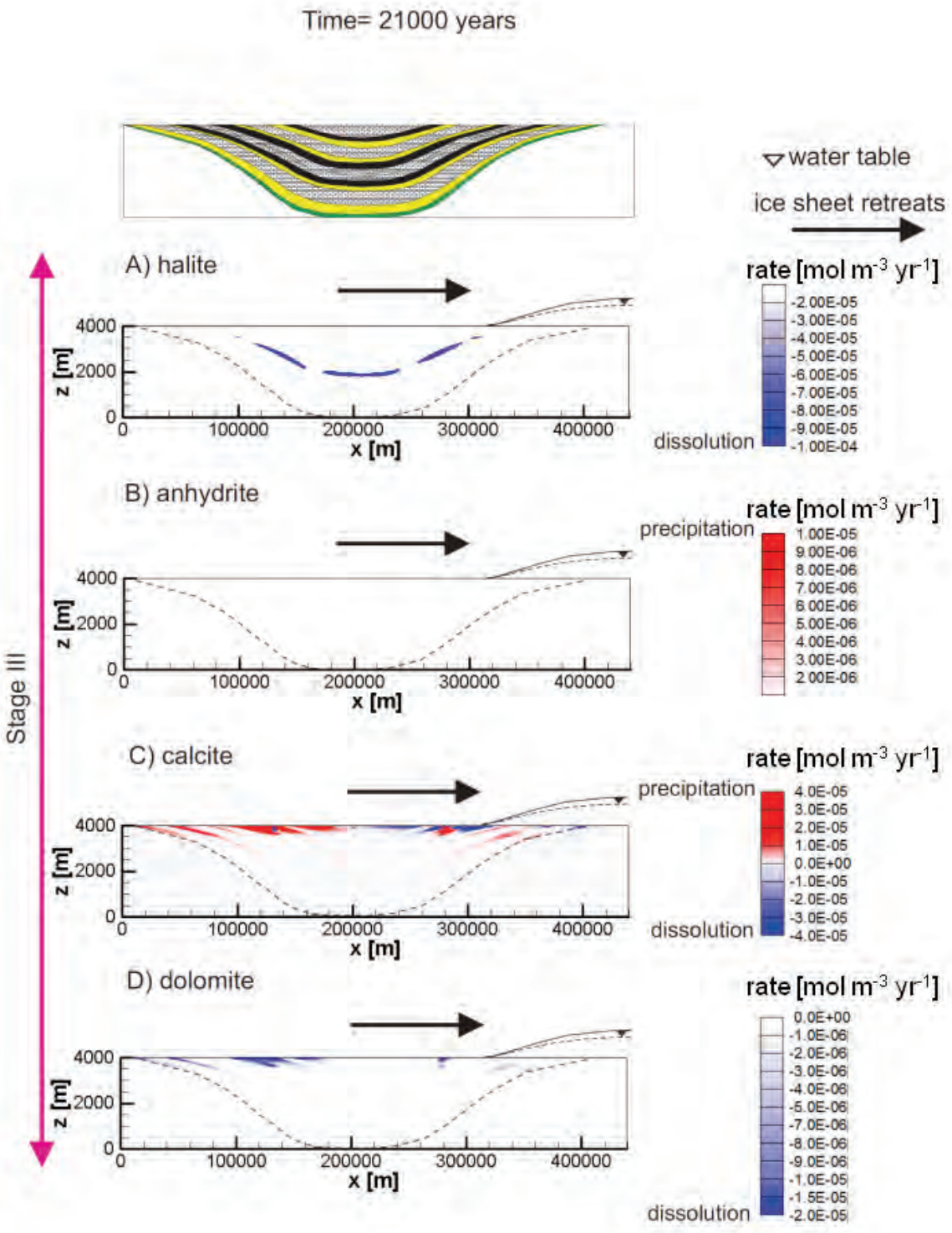

Figure 19: BASE-CASE mineral reaction rates at 21000 years: A) Distribution of halite dissolution rate. B) Distribution of anhydrite precipitation rate. C) Distribution of calcite dissolution/precipitation rates. D) Distribution of dolomite dissolution rate

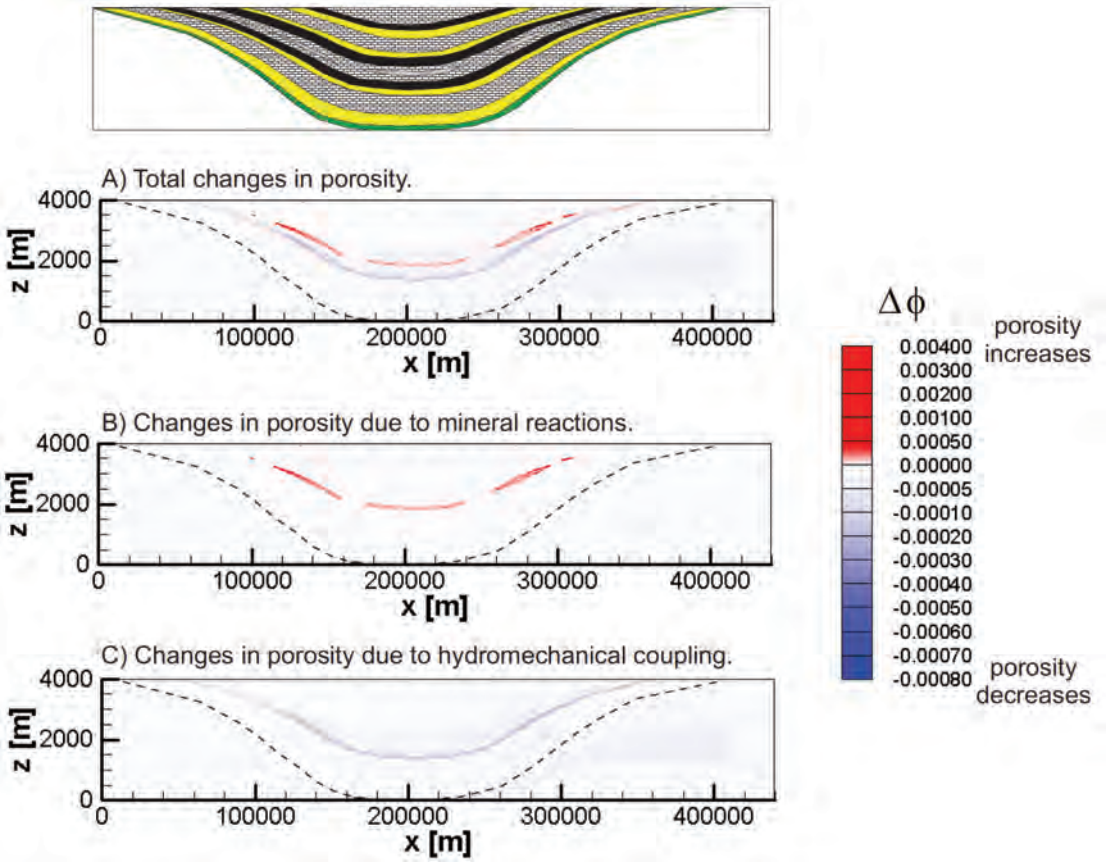

Figure 20: BASE-CASE simulation results for porosity change during the entire simulation (32500 years): A) Total porosity change. B) Porosity change due to mineral reactions. C) Porosity change due to hydromechanical coupling

8.3 CHEMICAL EVOLUTION IN THE BASIN

The distributions of pH and selected major ions at several simulation times are shown in Figure 21 through Figure 25. For pH, no substantial changes are predicted throughout the majority of the basin mainly due to the buffering provided by the presence of carbonate minerals (i.e. calcite and dolomite, see Figure 21). A minor area of pH increase is indicated where meltwater recharge occurs at shallow depths during glacial retreat (x=300000 m, Figure 21D).

The distribution of chloride is essentially coincident with that of density throughout the simulation (compare Figure 12 and Figure 22). During ice retreat, a region of low chloride concentration develops to depths of approximately 300 m in the more permeable aquifers (i.e. Sand3, Sand4, and Dol2) that sub-crop beneath the toe of the receding ice sheet (Figure 22D). Freshening of these shallow aquifers can also be detected by careful examination of the results for sulphate, calcium and magnesium (Figure 23-25). However, throughout the majority of the basin the major ion distributions are remarkably stable during the 32500 yr simulation.

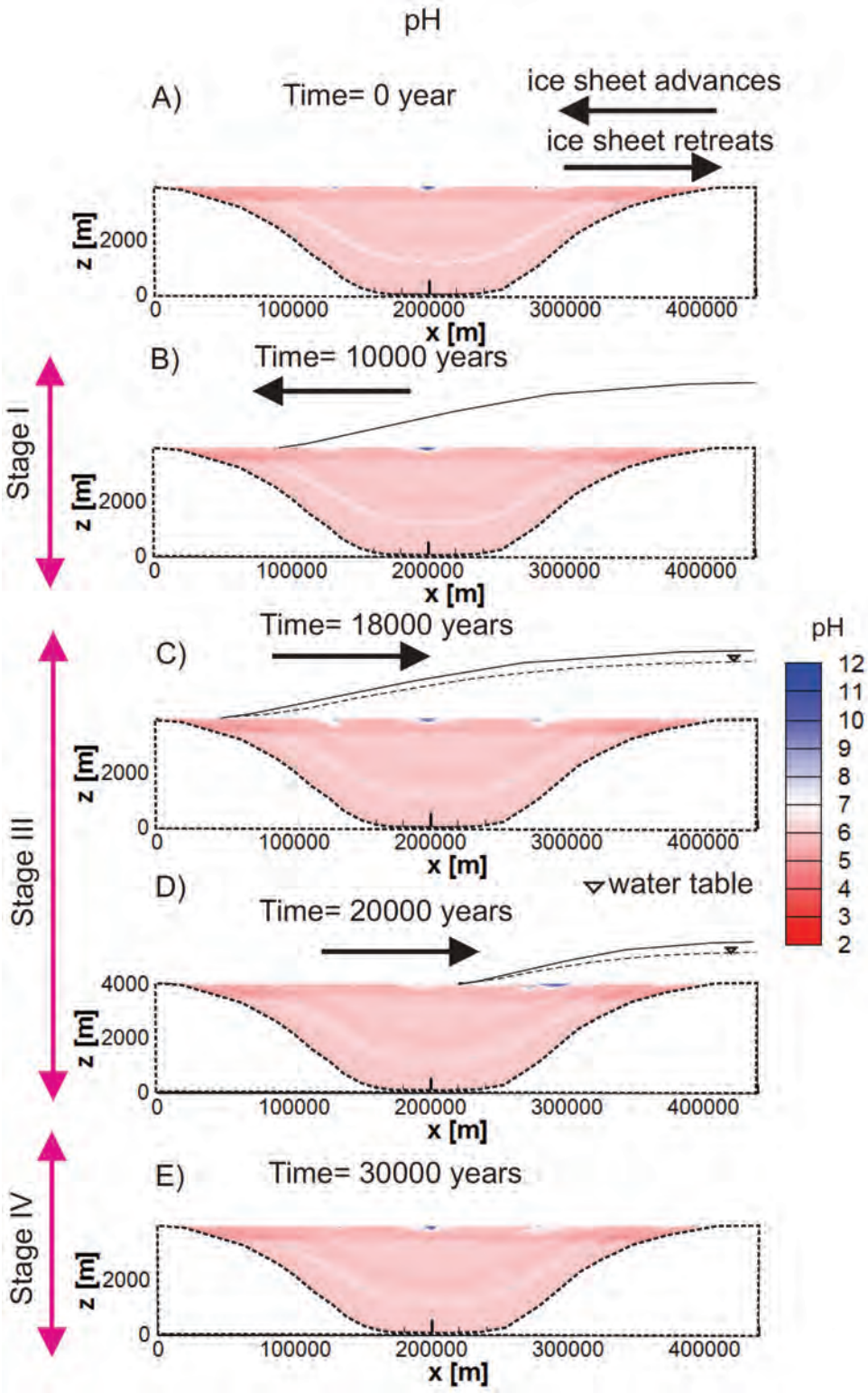

Figure 21: BASE-CASE simulation: pH distributions at different times. A) Initial condition. B) 10000 years. C) 18000 years. D) 20000 years. E) 30000 years

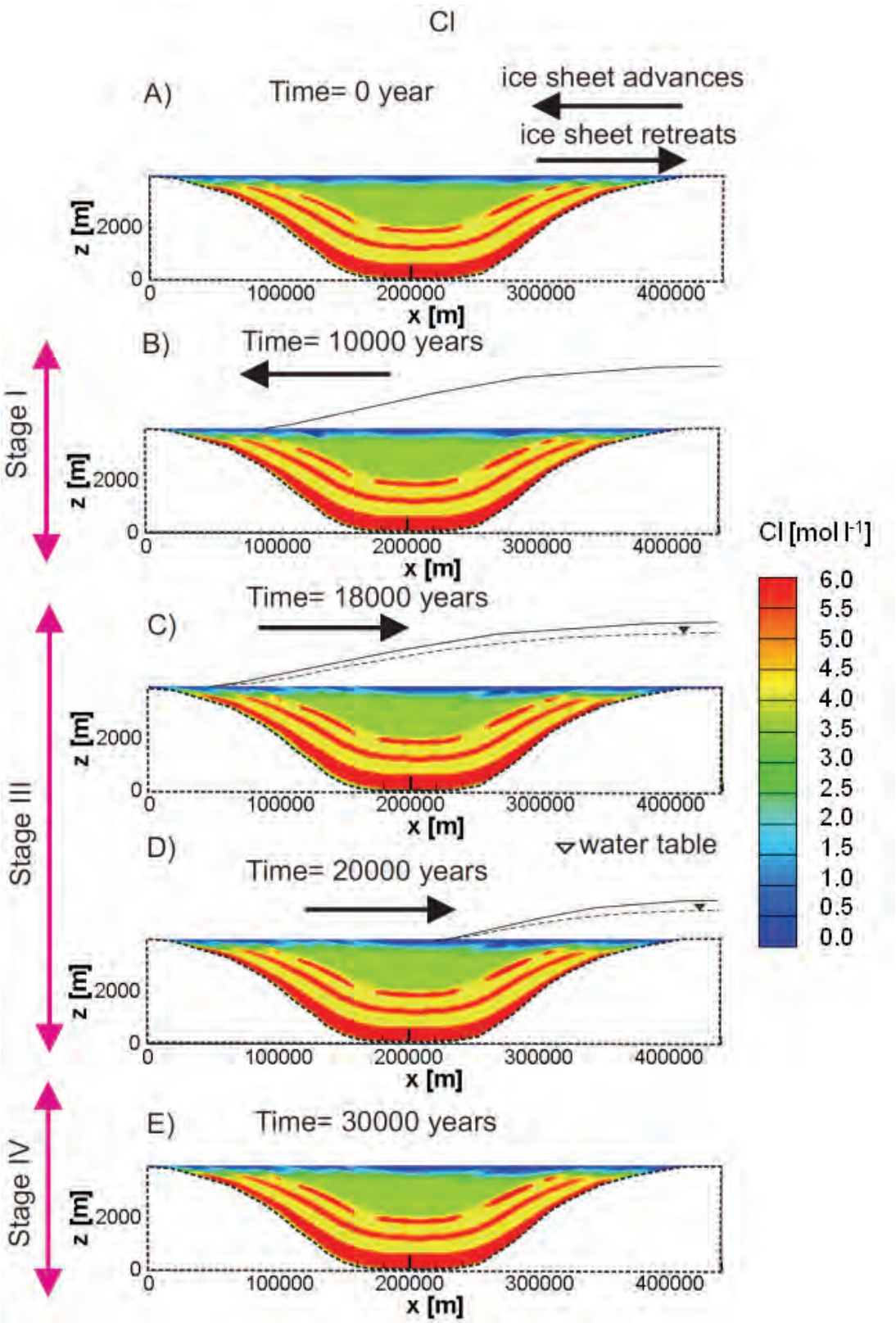

Figure 22: BASE-CASE simulation: Distribution of Cl total concentration at different times. A) Initial condition. B) 10000 years. C) 18000 years. D) 20000 years. E) 30000 years

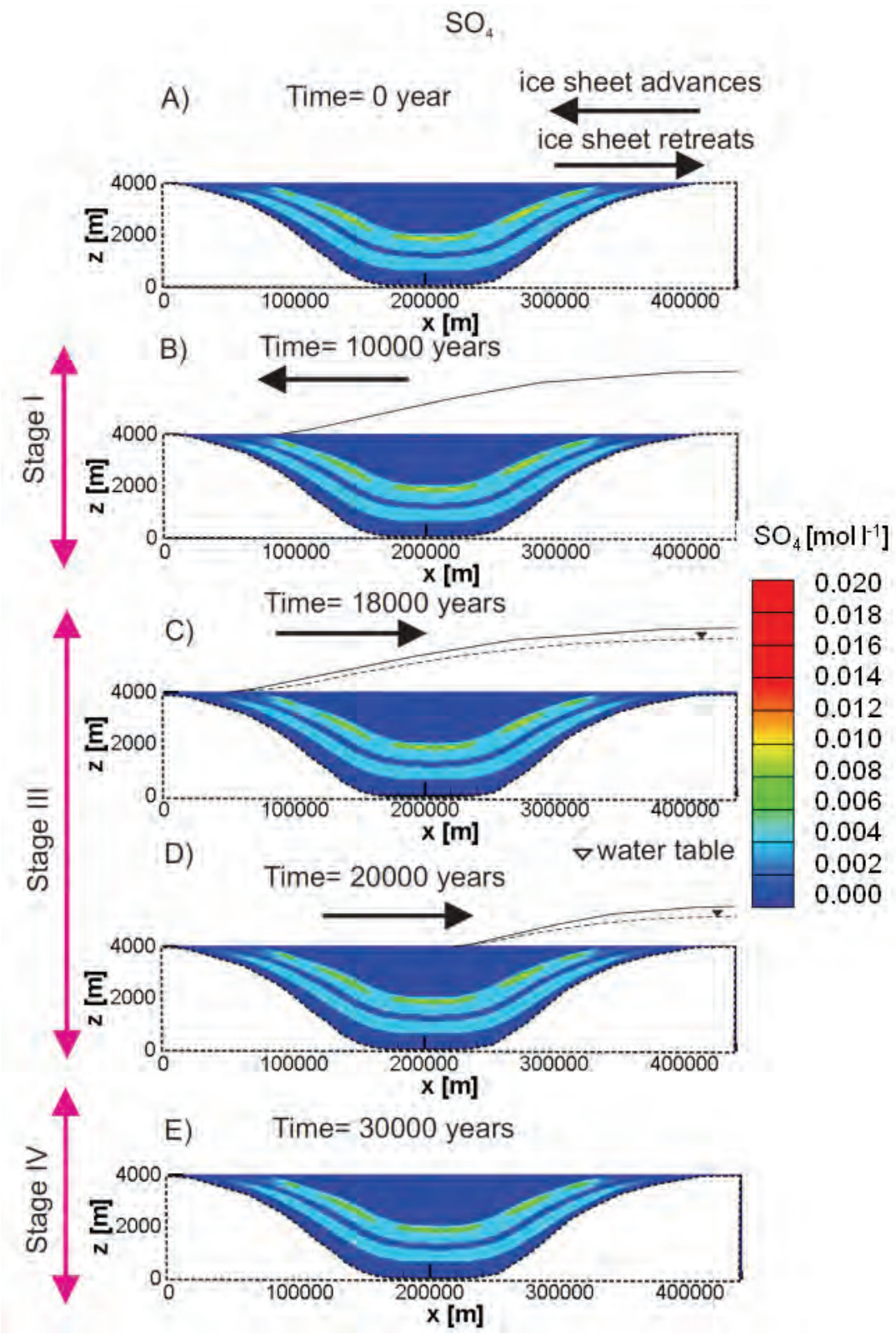

Figure 23: BASE-CASE simulation: Distribution of SO_4 total concentration at different times. A) Initial conditions. B) 10000 years. C) 18000 years. D) 20000 years. E) 30000 years

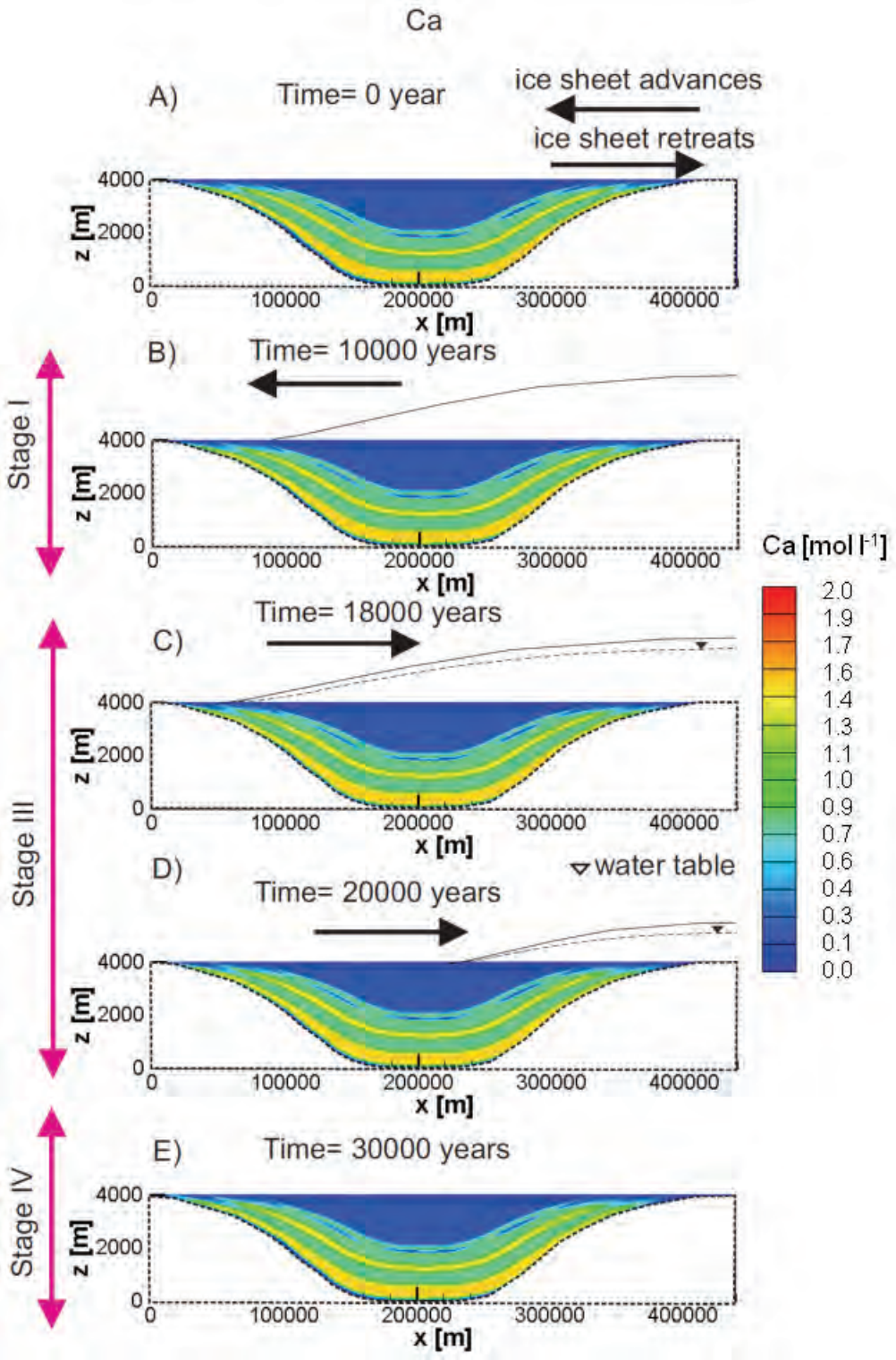

Figure 24: BASE-CASE simulation: Distributions of Ca total concentrations at different time. A) Initial condition. B) 10000 years. C) 18000 years. D) 20000 years. E) 30000 years

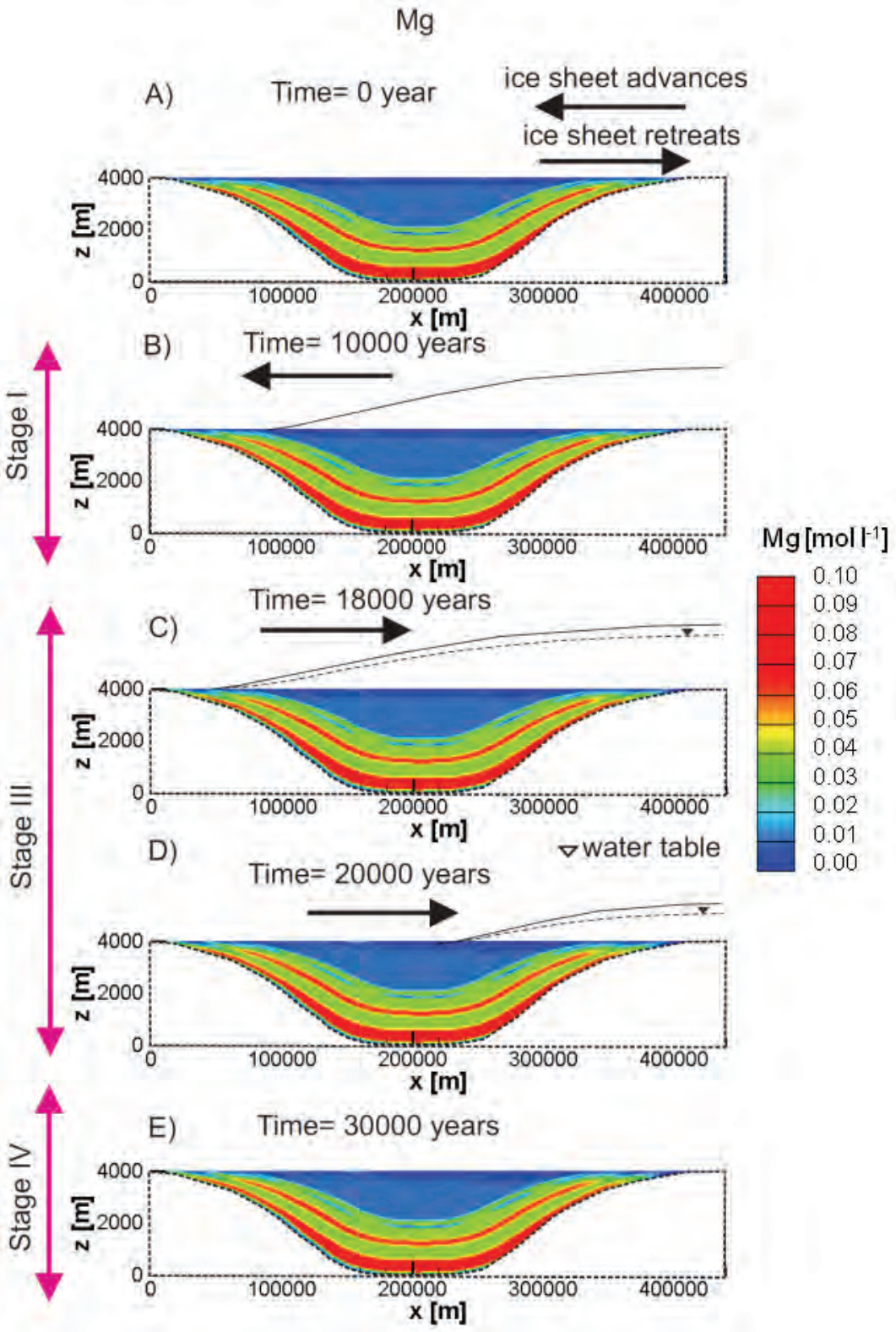

Figure 25: BASE-CASE simulation: Distribution of Mg total concentration at different times. A) Initial condition. B) 10000 years. C) 18000 years. D) 20000 years. E) 30000 years

9. ALTERNATIVE SCENARIOS

In this section several alterations to the BASE-CASE are considered. The objective of this set of simulations is to isolate a particular process, or conceptual model assumption, and examine its influence on groundwater flow, fluid density distribution, and the geochemical behaviour within the basin during a single cycle of ice sheet advance and retreat. Several of the alternative scenarios may appear unrealistic, for example assuming conservative solute transport in what is known to be a reactive system; however, such simulations are useful for improving the understanding of how sedimentary basins may respond to a glaciation event. The following alternative scenarios are considered:

- Permafrost in front of the advancing ice sheet;
- Enhanced vertical hydraulic conductivity in shallow aquitard units;
- A greater initial depth of fresh water;
- Constant porosity with depth in each hydrogeologic unit;
- Basin-scale heat transport;
- Exclusion of cation exchange reactions; and
- Exclusion of all heterogeneous reactions (conservative transport).

The key input parameters or boundary condtions that are different than the BASE-CASE, and the most relevant results of these simulations, are described in the following sections. The discussion focuses on the primary differences from the BASE-CASE results, rather than describing the full suite of results for each of the alternative simulations.

9.1 PERMAFROST IN FRONT OF THE ADVANCING ICE SHEET

The formation of permafrost in association with large-scale ice sheets can significantly reduce the hydraulic conductivity of porous media. Permafrost can have a hydraulic conductivity that is up to eight orders of magnitude lower than the unfrozen equivalent (e.g. Kleinberg and Griffin, 2005). Several previous numerical investigations of the response of hydrogeologic systems to glaciation have included consideration of permafrost (e.g. Person et al., 2007; Walsh and Avis, 2010).

This scenario (identified as PERM) is designed to provide preliminary insight into the impact of permafrost. As discussed previously, permafrost formation and dissipation are not coupled to the subsurface heat transport or solute transport equations. Permafrost propagation was simulated by assuming it was present to a constant distance of 140 km in front of the ice sheet during ice sheet advance (Stage I). No permafrost was included in the model during ice sheet melting (i.e. Stage III), and the transition between frozen and unfrozen conditions was assumed to be instantaneous. The maximum depth of the permafrost zone was 100 m and the hydraulic conductivity in this zone was reduced by five orders of magnitude.

The simulated temporal evolution of the recharge and discharge in the basin is shown in Figure 26. Permafrost formation affects the recharge and discharge in the basin during Stage I due to the hydraulic conductivity reduction in the periglacial areas; recharge and discharge are reduced to near zero approximately 2000 yr earlier than in the BASE-CASE simulation (Figure 17). This

is due to the development of permafrost conditions ahead of the advancing ice sheet, leading to a closed flow system at an earlier time.

Because of the assumption of no permafrost during Stage III, the recharge and discharge patterns evolve in the same manner as for the BASE-CASE during this stage. Horizontal Darcy velocities in Sand1 and Sand2 at the center of the basin at 18000 yr are 9.3 x 10^{-2} m yr^{-1} and 3.8 x 10^{-1} m yr^{-1}, respectively, which are only slightly larger (a factor of 2.2 or less) than for the BASE-CASE.

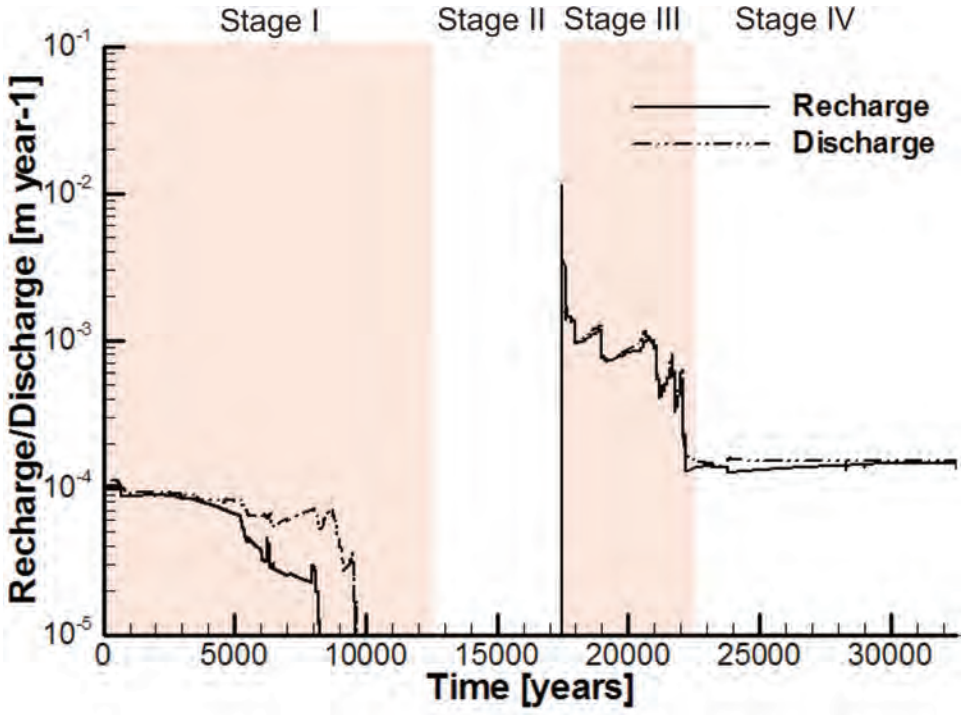

Figure 26: Scenario PERM results - temporal evolution of the recharge and discharge rates in the sedimentary basin.

The mineral reaction rates for calcite and dolomite at 10000 yr (Stage I) and 21000 yr (Stage III) are used to illustrate the impact of hydraulic conductivity reduction due to permafrost on the geochemical processes. The spatial patterns and magnitudes of the calcite and dolomite reaction rates at 10000 yr are indistinguishable from those of the BASE-CASE at the same time (i.e. compare Figure 27A and B with Figure 18C). The same similarity is also noted for the results at 21000 yr (i.e. compare Figure 27C and 27D with Figure 19C and 19D).

The amount of each mineral dissolved or precipitated during the entire 32500 yr simulation is again small relative to the initial volume fractions. Over the entire simulation time the maximum change in mineral volume fractions are: 0.35% for halite dissolution; 0.0013% for anhydrite precipitation; 0.012% and 0.026% for calcite dissolution and precipitation, respectively; and 0.0073% for dolomite dissolution. These are all within a factor of three of the results obtained for the BASE-CASE; however, the results also suggest a shift in the relative importance of dissolution and precipitation of calcite, with a decline of dissolution and an increase of calcite formation.

Overall, it appears that the presence of permafrost during the advance of the cold-based ice sheet has little impact on the geochemical stability of the basin. Additional simulations would be required to examine the importance of permafrost for a scenario involving more gradual development and dissipation of frozen subsurface sediments during both ice sheet advance and retreat.

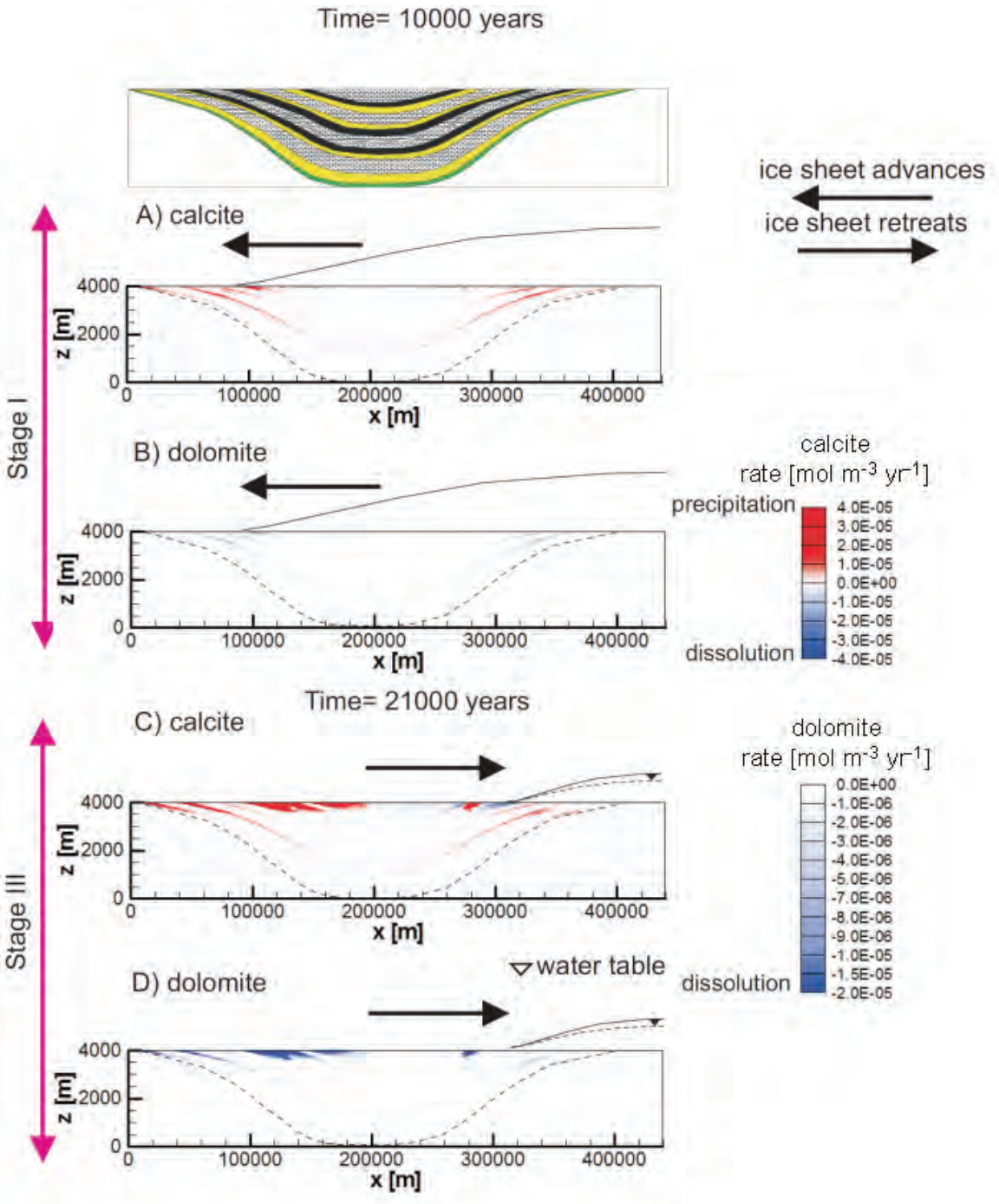

Figure 27: Scenario PERM mineral reaction rates: A) Dissolution/precipitation of calcite at 10000 years. B) Dissolution of dolomite at 10000 years. C) Dissolution/precipitation of calcite at 21000 years. D) Dissolution of dolomite at 21000 years

9.2 ENHANCED VERTICAL HYDRAULIC CONDUCTIVITY IN SHALLOW AQUITARDS

There have been several suggestions in the literature that vertical fractures may be present, or have been activated in the past, in shale aquitard units. Person et al. (2007) have suggested that glaciation may have promoted microbial gas production by diluting the salinity of formation waters and dilating fractures in Upper Devonian organic-rich shales. Based on data from several cores of the New Albany shale (Illinois basin), Strapoc et al. (2010) hypothesized that lower than expected gas content was related to postglacial relaxation of vertical fractures, which were also visually observed in one core sample obtained from a depth of approximately 830 m to 860 m. While the physical evidence supporting the occurrence of vertical fractures in shales is quite limited, if present, vertical fractures would be expected to enhance the bulk vertical hydraulic conductivity of such units. The potential influence of enhanced vertical hydraulic conductivity in shallow aquitards on groundwater evolution and stability is explored here using illustrative numerical modelling.

In this scenario (identified as FRAC), the same hydraulic conductivity distribution as used in the BASE-CASE simulation is applied during Stages I (i.e. ice sheet advance) and II (i.e. constant ice sheet thickness). However, during Stages III (i.e. ice sheet retreat) and IV, the vertical hydraulic conductivities for the shale units Sh1, Sh2 and Sh3 (Figure 28) are increased to represent the postglacial relaxation of fractures. The vertical hydraulic conductivity increase is assumed to be limited to an arbitrarily assigned depth of 500 m below the ground surface (Figure 28). The vertical hydraulic conductivity in the shale units reaches a maximum at the ground surface (a two order of magnitude increase relative to the BASE-CASE), and approaches BASE-CASE values (representing unfractured conditions) 500 m below the surface.

The distributions of specific discharge (Darcy velocity) during Stages III and IV, in direct comparison to the BASE-CASE results, are depicted in
Figure 29, Figure 30, and Figure 31. The results suggest that the increased vertical hydraulic conductivities in the upper 500 m of the shale units cause only a minor impact on the flow pattern. The horizontal Darcy velocities in the deep aquifer units Sand1 and Sand2 (at mid-basin) are 4.3×10^{-2} m yr^{-1} and 2.2×10^{-1} m yr^{-1} at 18000 yr for the FRAC simulation. This indicates that the horizontal Darcy velocity for Sand1 is the same as that of BASE-CASE, while the increase of the Darcy velocity in Sand2 is restricted to approximately 5% (Section 9.1). The vertical components of the Darcy velocities at the center of the basin in Sand1 and Sand2 for the FRAC simulation are the same (8.4×10^{-6} m yr^{-1} and 2.0×10^{-3} m yr^{-1}, respectively, at 18000 yr) as obtained for the BASE-CASE.

As expected, the vertical component of the Darcy velocities in the upper 500 m of the basin exhibit some changes relative to the BASE-CASE during ice retreat (Figure 31). This is most obvious in the shallowest shale, Sh3 (Figure 28), at 18000 yr (x= 150000 m, Figure 31A and C) where downward velocity is increased by approximately 3×10^{-3} m yr^{-1} relative to the BASE-CASE, and at 20000 yr (x= 260000 m, Figure 31B and D) where vertical velocities are increased by about 3×10^{-3} m yr^{-1} in the upward direction. These changes amount to less than 10% of the maximum Darcy velocities in the system.

The temporal variation of recharge and discharge for the entire basin for the FRAC scenario (results not shown) is not significantly different than that obtained for the BASE-CASE (Figure 17).

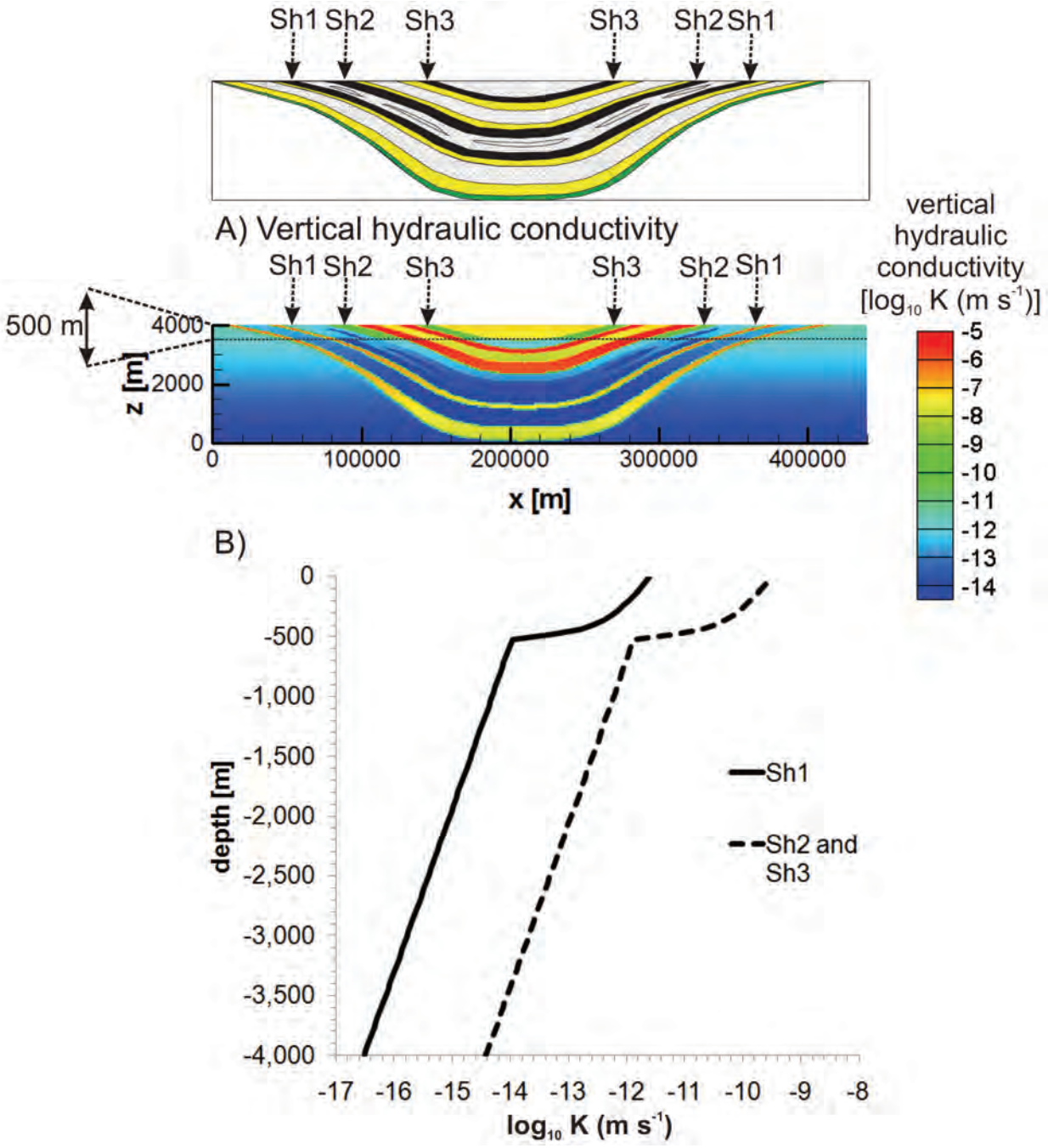

Figure 28: Scenario FRAC vertical hydraulic conductivity distribution: A) Two dimensional distribution. B) Vertical profile assigned for shale units Sh1, Sh2 and Sh3

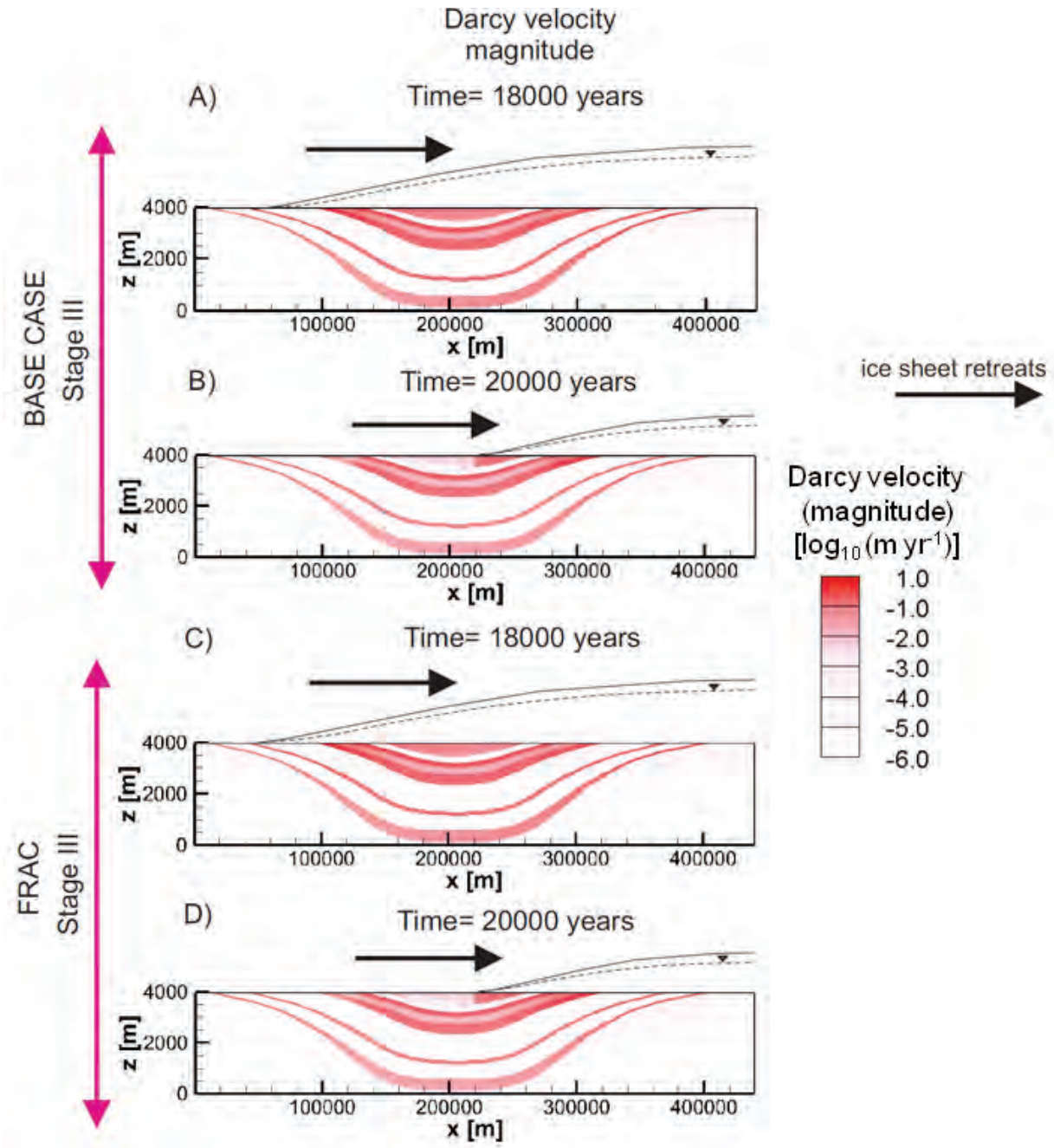

Figure 29: BASE-CASE and FRAC scenario results for Darcy velocity magnitude: A) and B) Results for the BASE-CASE simulation at 18000 years and 20000 years, respectively. C) and D) Results for the FRAC scenario at 18000 years and 20000 years, respectively

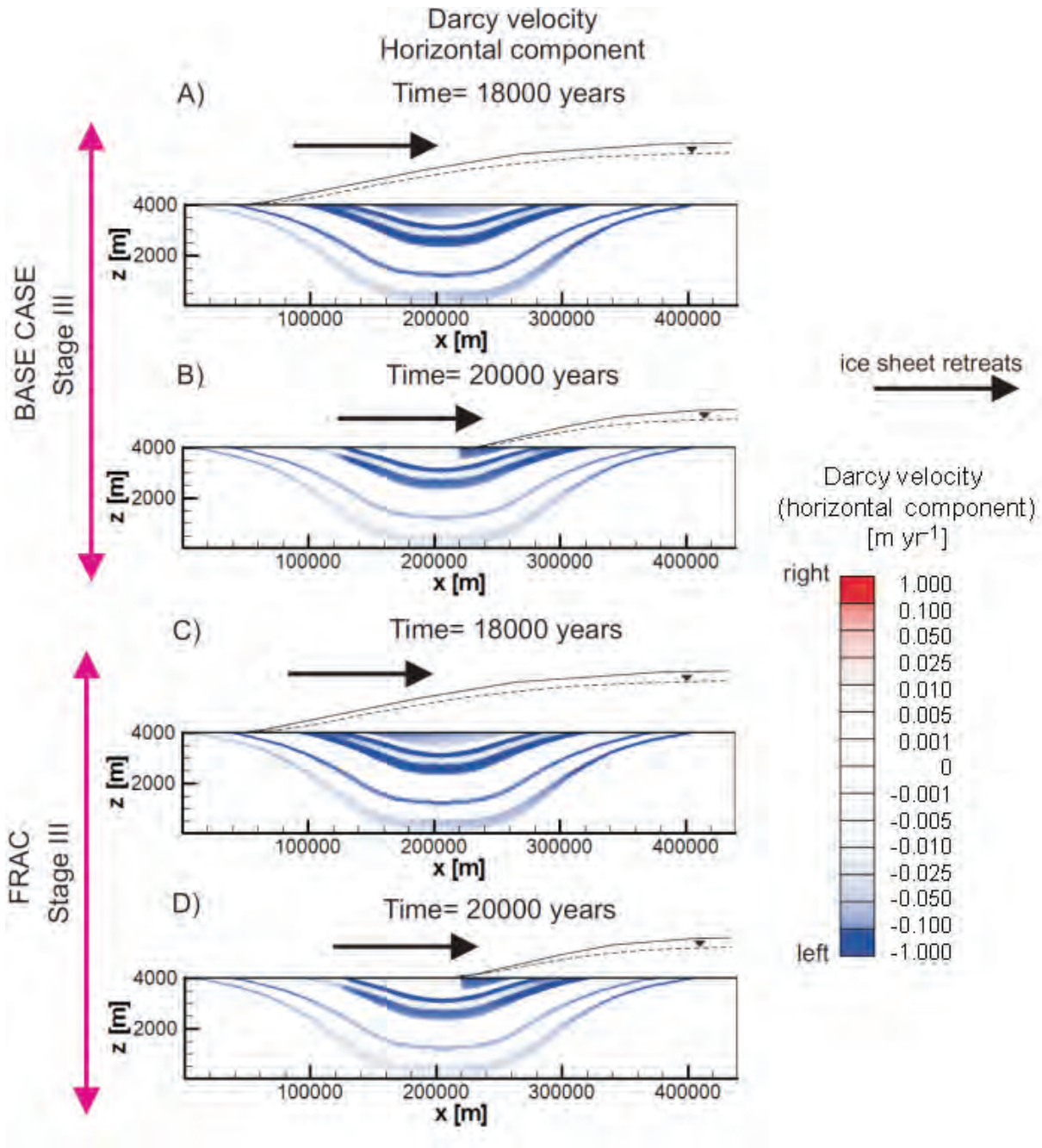

Figure 30: BASE-CASE and FRAC scenario results for the horizontal component of specific discharge (Darcy velocity): A) and B) Results for the BASE-CASE simulation at 18000 and 20000 years, respectively. C) and D) Results for the FRAC scenario at 18000 and 20000 years, respectively

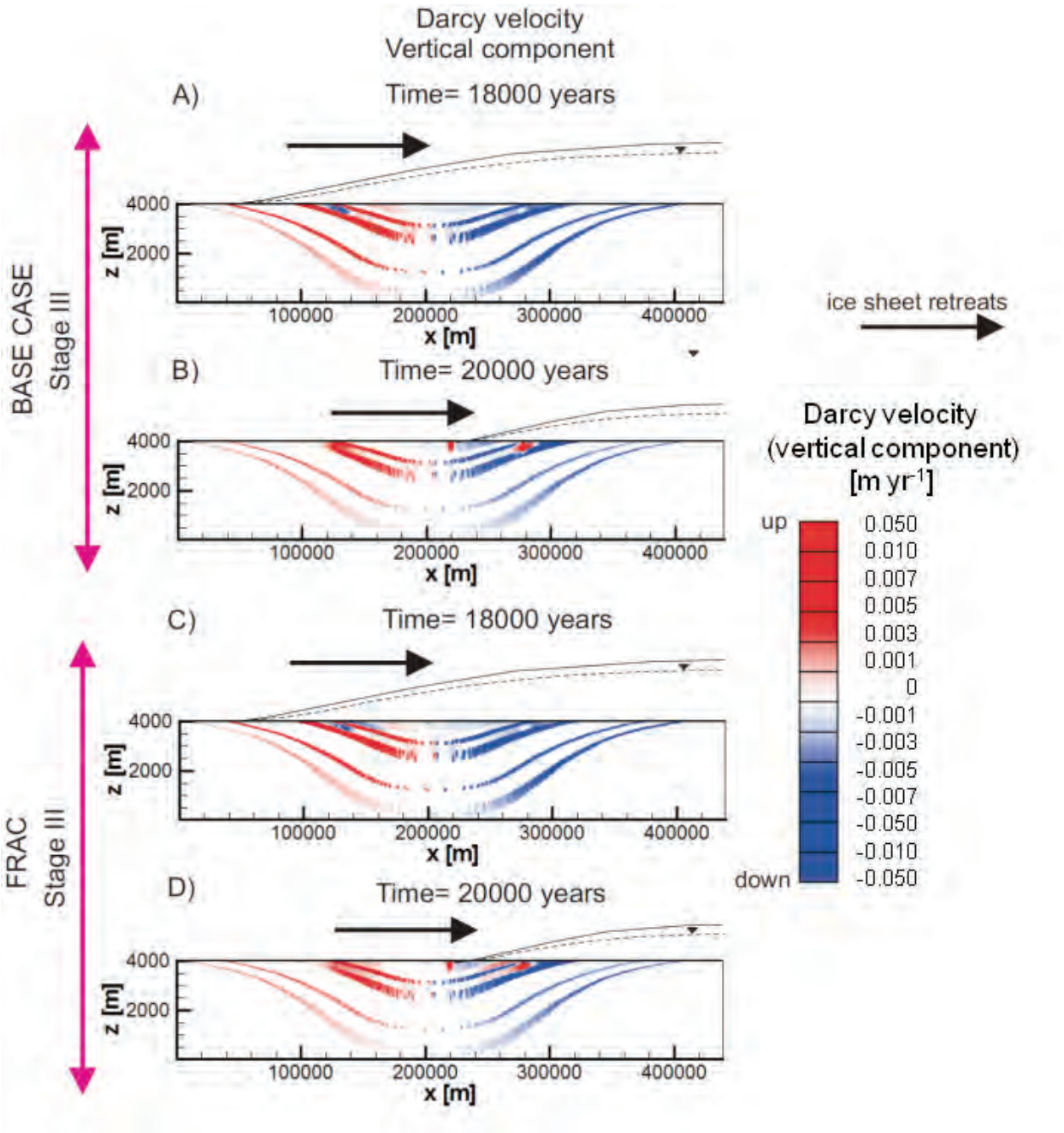

Figure 31: BASE-CASE and FRAC scenario results for the vertical component of specific discharge (Darcy velocity): A) and B) Results for the BASE-CASE simulation at 18000 and 20000 years, respectively. C) and D) Results for the FRAC scenario at 18000 and 20000 years, respectively

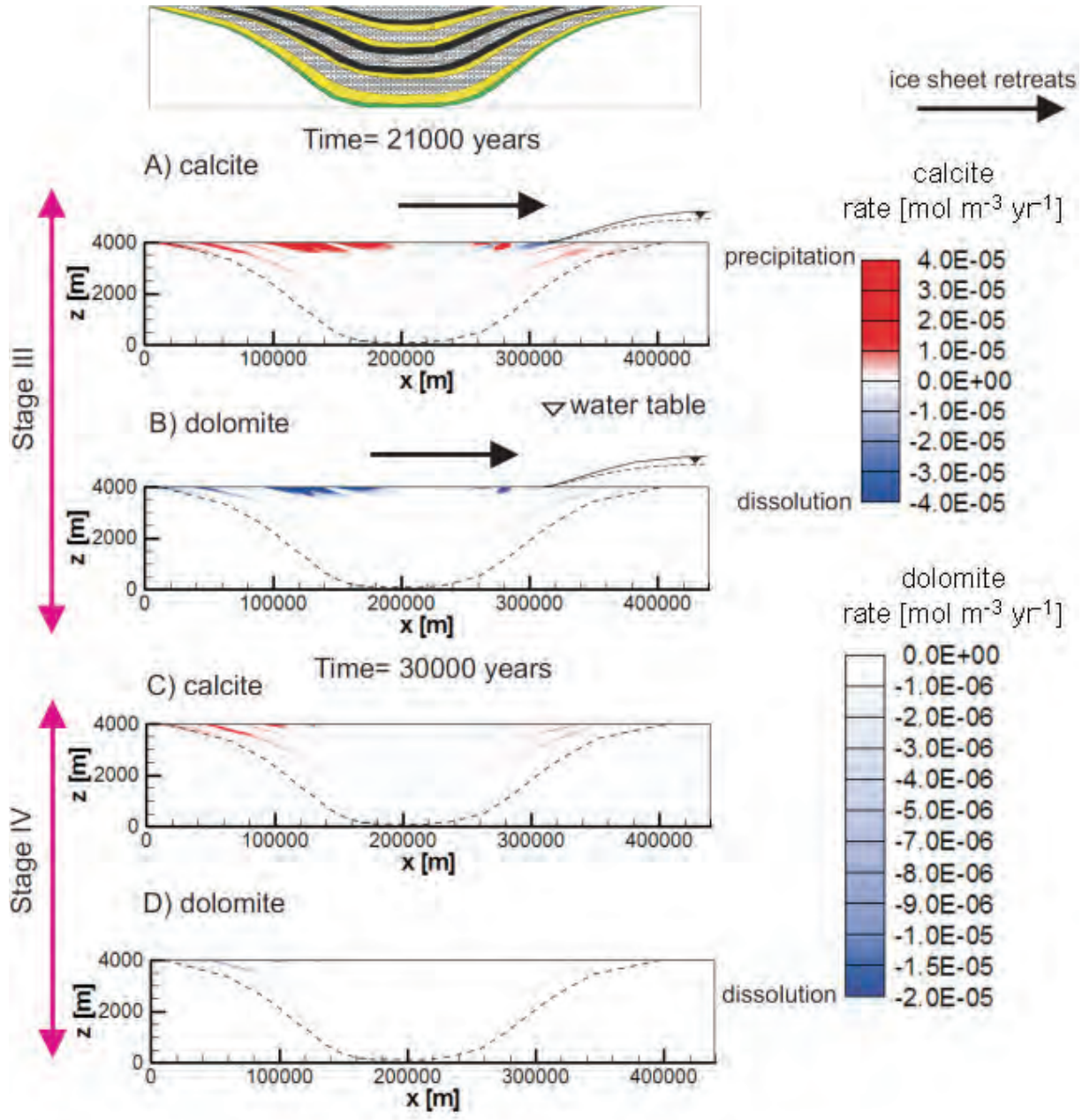

Figure 32: Scenario FRAC mineral reaction rates. A) Dissolution/precipitation of calcite at 21000 years. B) Dissolution of dolomite at 21000 years. C) Dissolution/precipitation of calcite at 30000 years. D) Dissolution of dolomite at 30000 years

Calcite and dolomite reaction rates at a simulation time of 10000 yr (not shown) are identical to the BASE-CASE results because the permeability increase due to the assumed reactivation of fractures has not yet taken place. Despite the permeability increase during the period of deglaciation (i.e. after 17500 yr), the calcite and dolomite reaction rates (Figure 32A and B) remain very similar in magnitude and spatial distribution compared to those obtained for the BASE-CASE (Figure 19C and D), with the minor exception of a localized increase in calcite precipitation and dolomite dissolution in the upper few hundred metres of Sh3 (x= 260000 m, Figure 32A and B). Reaction rates subsequently decline during the interglacial period due to limited fluid flow (Figure 32C and D).

9.3 GREATER INITIAL DEPTH OF FRESH WATER

The initial depth of fresh water in a sedimentary rock sequence, prior to imposing the effects of an ice sheet, will depend on the specific recharge and discharge conditions existing within the basin. To investigate the sensitivity to the depth of fresh water, from a hydrogeochemical perspective, a scenario (identified as FRESH) with increased initial fresh water depth was simulated. In this scenario the initial fresh water depth is approximately 200 m, compared to 100 m used in the BASE-CASE. The initial density and point pressure head distributions used in this scenario are shown in Figure 33. As discussed above for the BASE-CASE, the fluid density does not increase smoothly with depth because of the different initial chemical compositions assigned for the formation waters (Table 5).

The simulation results for Darcy velocities and the basin-wide variations of recharge and discharge (not shown) indicate that the increased fresh water thickness causes no measurable impact on fluid flow in the basin.

The mineral dissolution-precipitation rates (Figure 34 and Figure 35) are affected in the upper 500 m of the domain due to the deeper location of the freshwater-brine interface. This is especially noticeable for calcite precipitation and dolomite dissolution (i.e. dedolomitization) at 10000 yr (Stage I, Figure 34C and D), when the rates in the upper 300 m have been reduced to essentially zero compared to rates on the order of 10^{-5} mol m^{-3} yr^{-1} for the BASE-CASE (Figure 18C and D). During this time period, no recharge takes place; however, glacial loading introduces differential compression of the sedimentary units, enhancing flow and mixing. Although flow processes are most active near the surface, only very limited water-rock interaction takes place, due to the relatively uniform groundwater composition, which is already in equilibrium with the resident mineral phases (Figure 34). These results highlight that hydrodynamically induced mixing may be an important mechanism for mineral dissolution-precipitation in these systems, potentially rivalling the effect of freshwater recharge. The same general reduction in the reaction rates for calcite and dolomite in the upper several hundred metres of the basin also persists into Stage III (e.g. 21000 yr, compare Figure 35 C and D with Figure 19C and D), although dedolomitization is evident in isolated locations in shallow aquifers (e.g. Dol2, Sand4, x =270000 m, Figure 35 C and D) due to meltwater infiltration. Further comparing results to the BASE-CASE shows that there is little difference of mineral dissolution-precipitation rates at depths below 500 mbgs (compare Figure 19 and Figure 35). Reaction rates for halite and anhydrite are unchanged from the BASE-CASE because these minerals are not initially present in the upper few hundred metres of the domain (Figure 10).

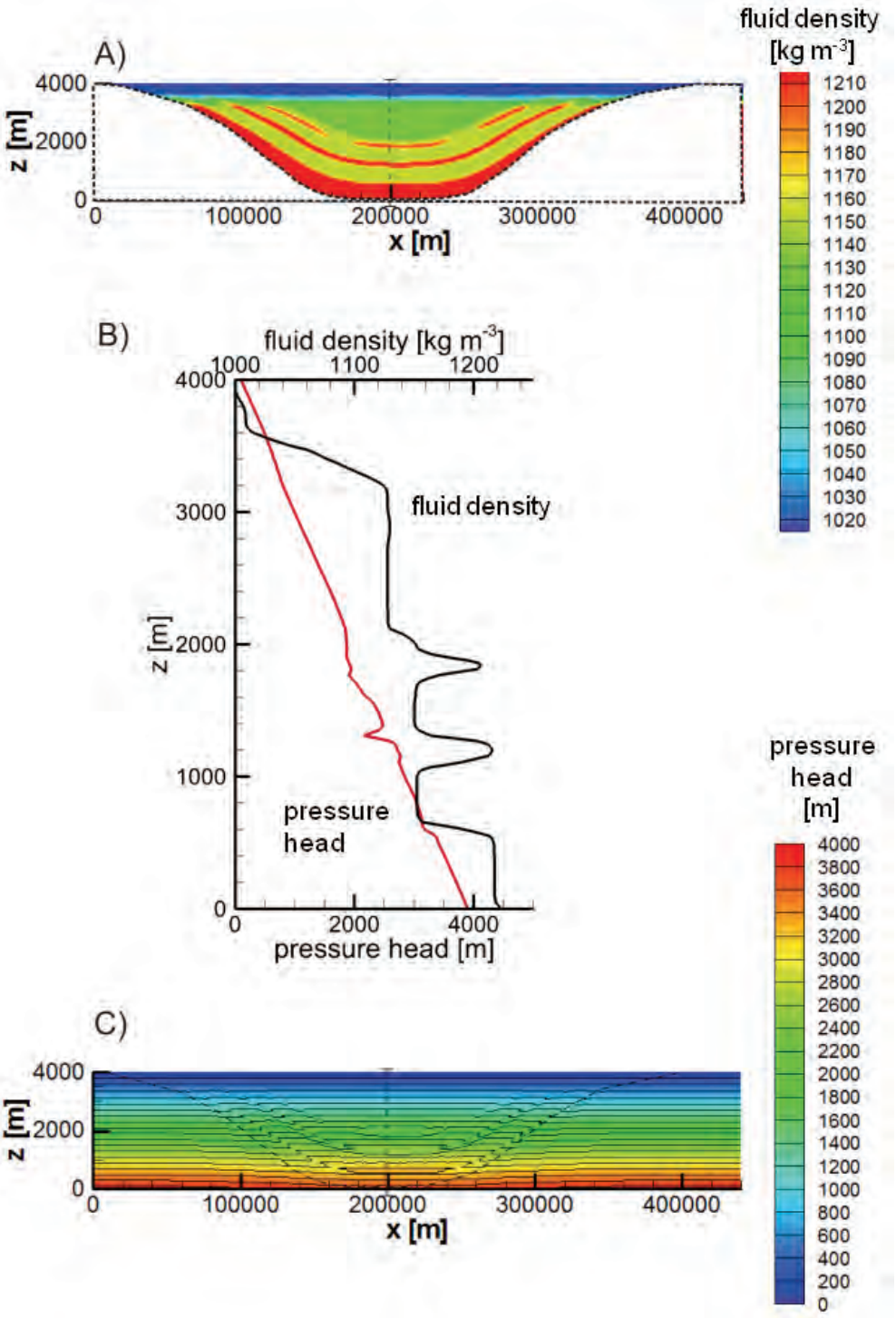

Figure 33: Initial conditions for the FRESH simulation: A) Fluid density distribution. B) Vertical point pressure head (red line) and density (black line) distributions at the center of the sedimentary basin. C) Spatial distribution of point pressure head

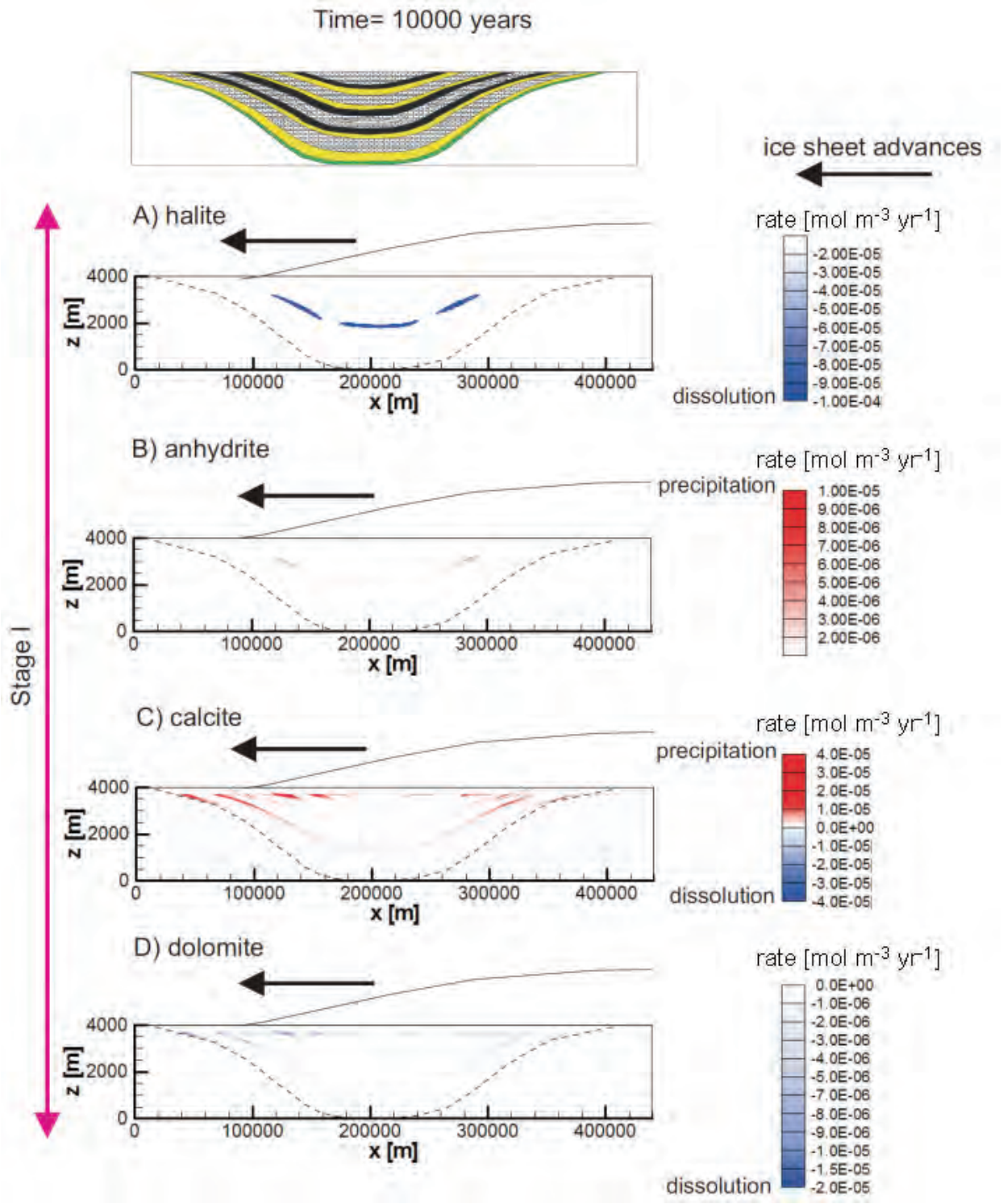

Figure 34: Scenario FRESH mineral reaction rates at 10000 years: A) Distribution of halite dissolution rate. B) Distribution of anhydrite precipitation rate. C) Distribution of calcite dissolution/precipitation rates. D) Distribution of dolomite dissolution rate

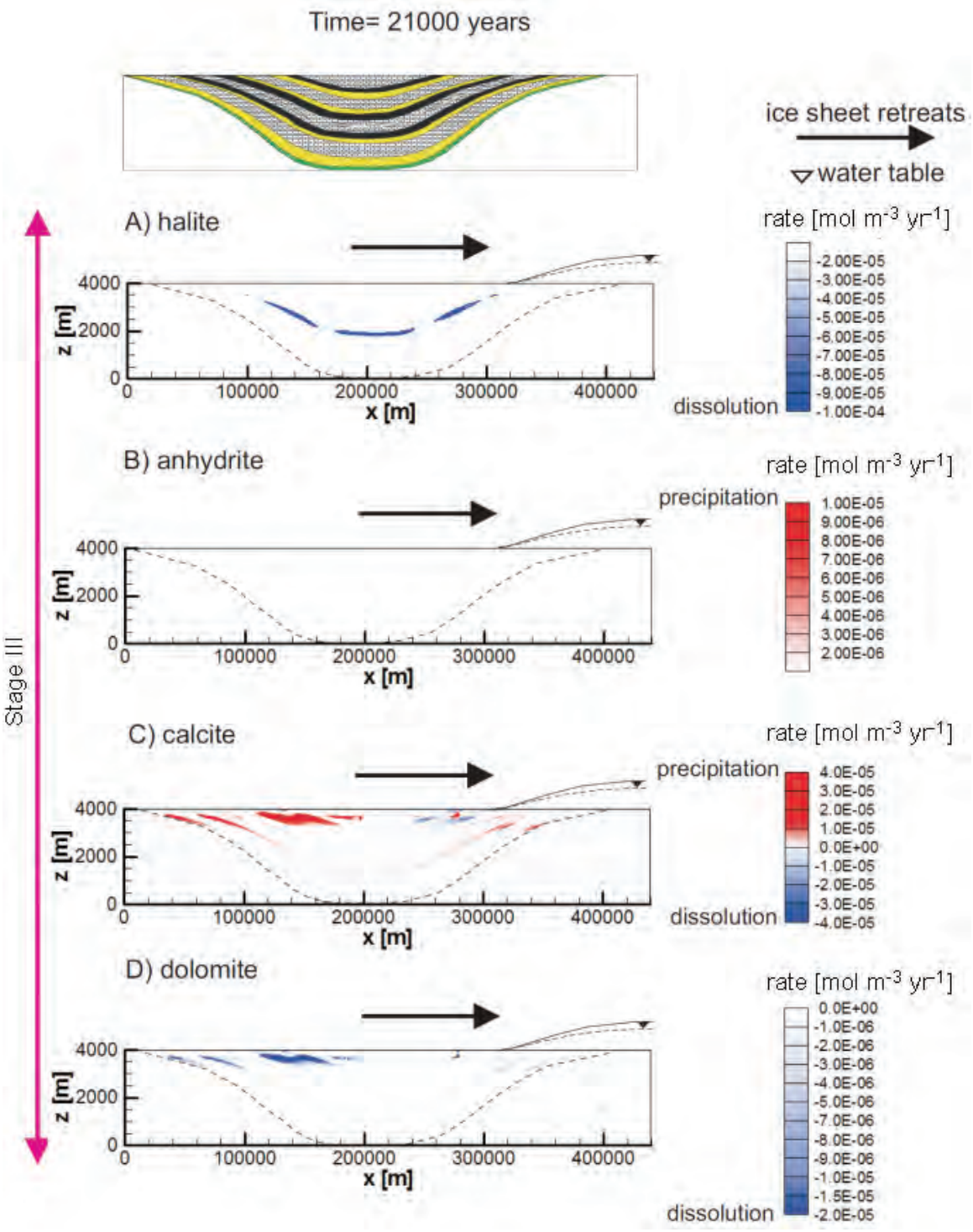

Figure 35: Scenario FRESH mineral reaction rates at 21000 years: A) Distribution of halite dissolution rate. B) Distribution of anhydrite precipitation rate. C) Distribution of calcite dissolution/precipitation rates. D) Distribution of dolomite dissolution rate

9.4 CONSTANT POROSITY WITH DEPTH IN EACH HYDROGEOLOGIC UNIT

As discussed above, porosity was decreased with depth in the BASE-CASE simulation and related parameters (e.g. hydraulic conductivity, specific storage) were scaled according to the porosity distribution (see sections 4.1-4.3). Such a basin-scale decline in porosity is supported by field evidence (e.g. Medina et al., 2011); however, several previous hydrogeologic simulations of sedimentary basins have not considered this general trend (e.g. Bense and Person, 2008, McIntosh et al., 2011). The present scenario (identified as POR) investigates the impact of neglecting porosity variations with depth and assumes a constant porosity for each sedimentary unit. The initial porosity distribution and related parameters, such as hydraulic conductivity, one-dimensional specific storage coefficient, and the one-dimensional loading efficiency coefficient for the POR simulation are shown in Figure 36. For this simulation, these parameters vary as a function of the sedimentary unit, but not with depth. The parameters E (Young's modulus) and ν (Poisson's ratio) required to calculate the specific storage coefficient and the loading efficiency coefficient are identical to the BASE-CASE simulation (see Table 2).

In general, assuming a constant porosity with depth implies an increase in the hydraulic connection within and between the hydrogeologic units relative to the BASE-CASE. The simulation results show that this effect is most significant in deeper portions of the aquifers Sand1 and Sand2 after meltwater generation begins (Figure 37-39). For example, at 18000 yr the horizontal Darcy velocities in the deepest section (i.e. center of the basin) of the Sand1 and Sand2 aquifers are 4.2×10^{-1} m yr^{-1} and 1.6 m yr^{-1}, respectively (Figure 38B). For the BASE-CASE simulation (Figure 15) the values for the corresponding locations and time were 4.3×10^{-2} m yr^{-1} (Sand1) and 2.3×10^{-1} m yr^{-1}(Sand2). The vertical Darcy velocities within the Sand1 and Sand2 units (Figure 39) are also generally elevated, by factors of approximately two to ten, relative to the BASE-CASE (Figure 16), except in the central portion of the basin where flow is predominately horizontal in both cases.

Mineral dissolution and precipitation rates at 10000 yr and 21000 yr are shown in Figure 40 and Figure 41, respectively. While the magnitude of halite dissolution is similar to the BASE-CASE, the spatial extent over which anhydrite precipitation occurs (Figure 40B and Figure 41B) is larger than that of the BASE-CASE (Figure 18B and Figure 19B). As a consequence of the increased hydraulic connection at depth in the basal sandstones (Sand1 and Sand2) dedolomitization is spatially more widespread, especially in the right-hand flank of the basin for the simulation time of 21000 yr (Figure 41C and D), than the BASE-CASE (Figure 19C and D). These findings are consistent with the expectation that increased Darcy velocities will tend to increase water-rock interaction.

The mineral volume fraction changes for the POR simulation also reflect the increase in reaction rates. Over the entire 32500 yr simulation the maximum change in mineral volume fractions are: 0.51% for halite dissolution; 0.0023% for anhydrite precipitation; 0.093% and 0.038% for calcite dissolution and precipitation, respectively; and 0.033% for dolomite dissolution. These changes are greater than those of the BASE-CASE by factors ranging from 1.9 (halite dissolution) to 7 (dolomite dissolution).

The results of the POR simulation suggest that fluid flow velocities, and to a lesser magnitude geochemical reactions involving minerals, will be impacted by the variation of hydraulic properties with depth. Neglecting the decrease of porosity with depth will generally lead to an overestimation of Darcy velocities and water-rock interaction.

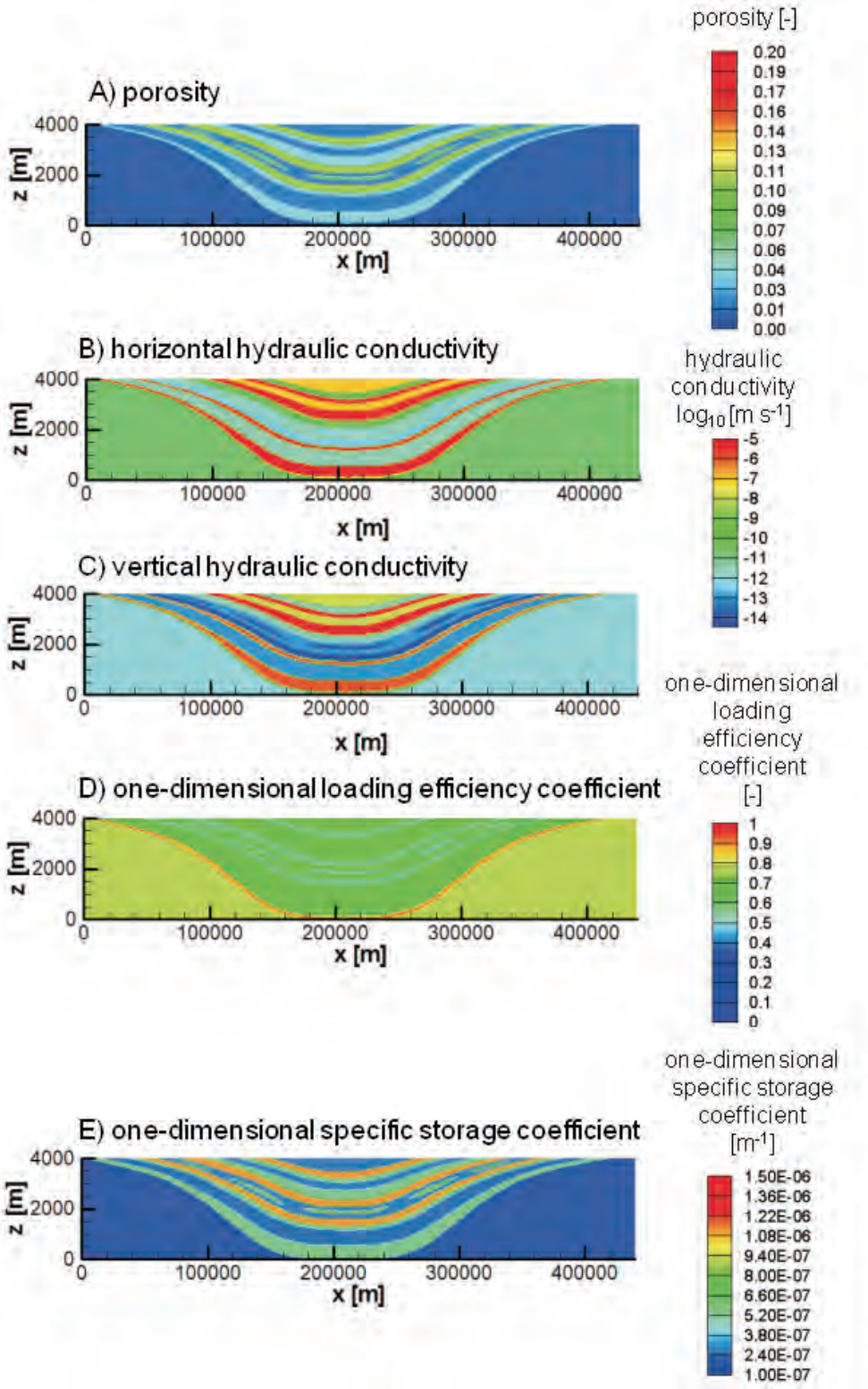

Figure 36: Spatial variation of porous medium parameters for the POR simulation: A) Porosity. B) Horizontal component of hydraulic conductivity. C) Vertical component of hydraulic conductivity. D) One-dimensional loading efficiency coefficient. E) One-dimensional specific storage coefficient

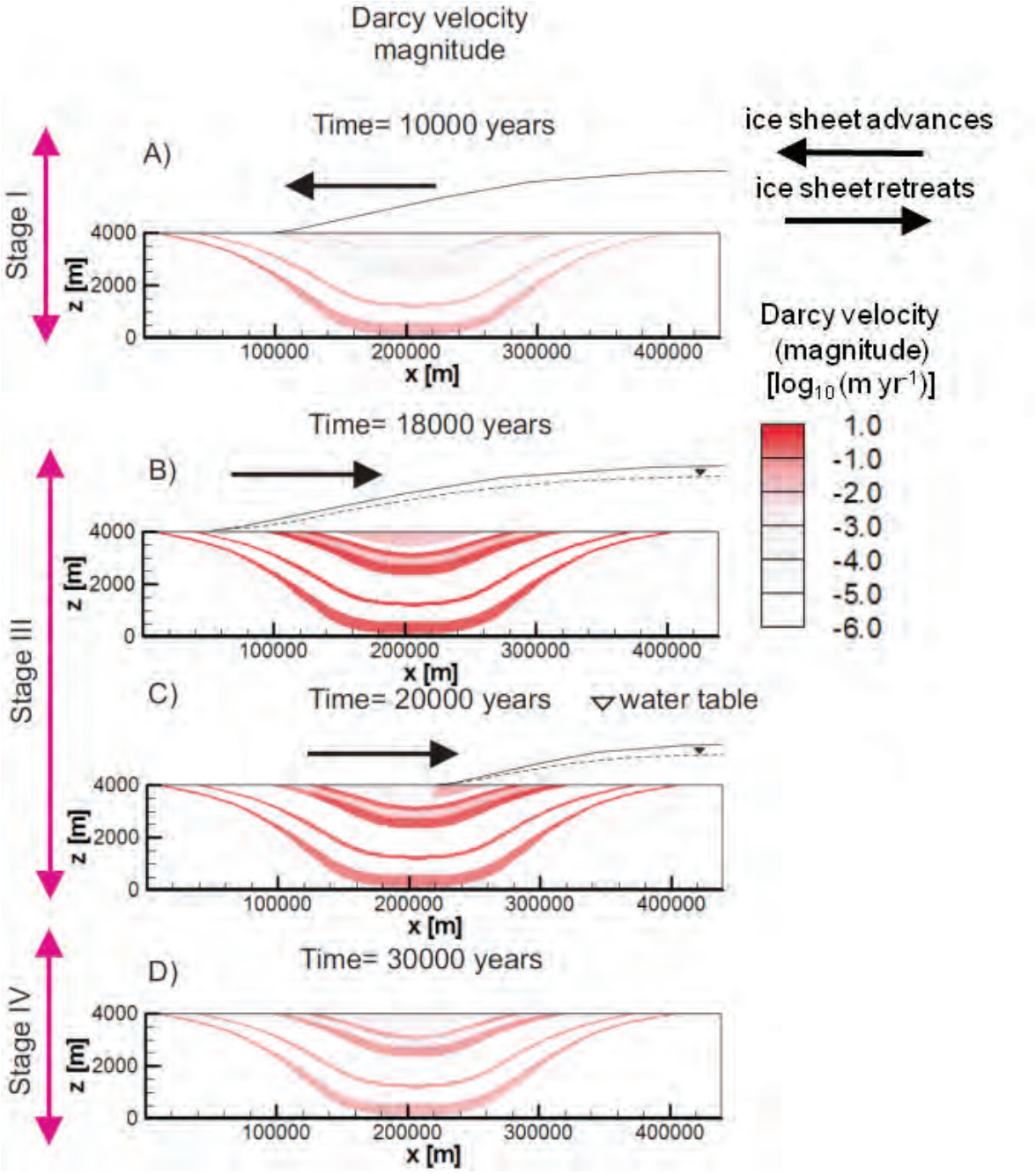

Figure 37: Scenario POR simulation results - magnitude of specific discharge (Darcy velocity) at different times: A) 10000 years. B) 18000 years. C) 20000 years. D) 30000 years

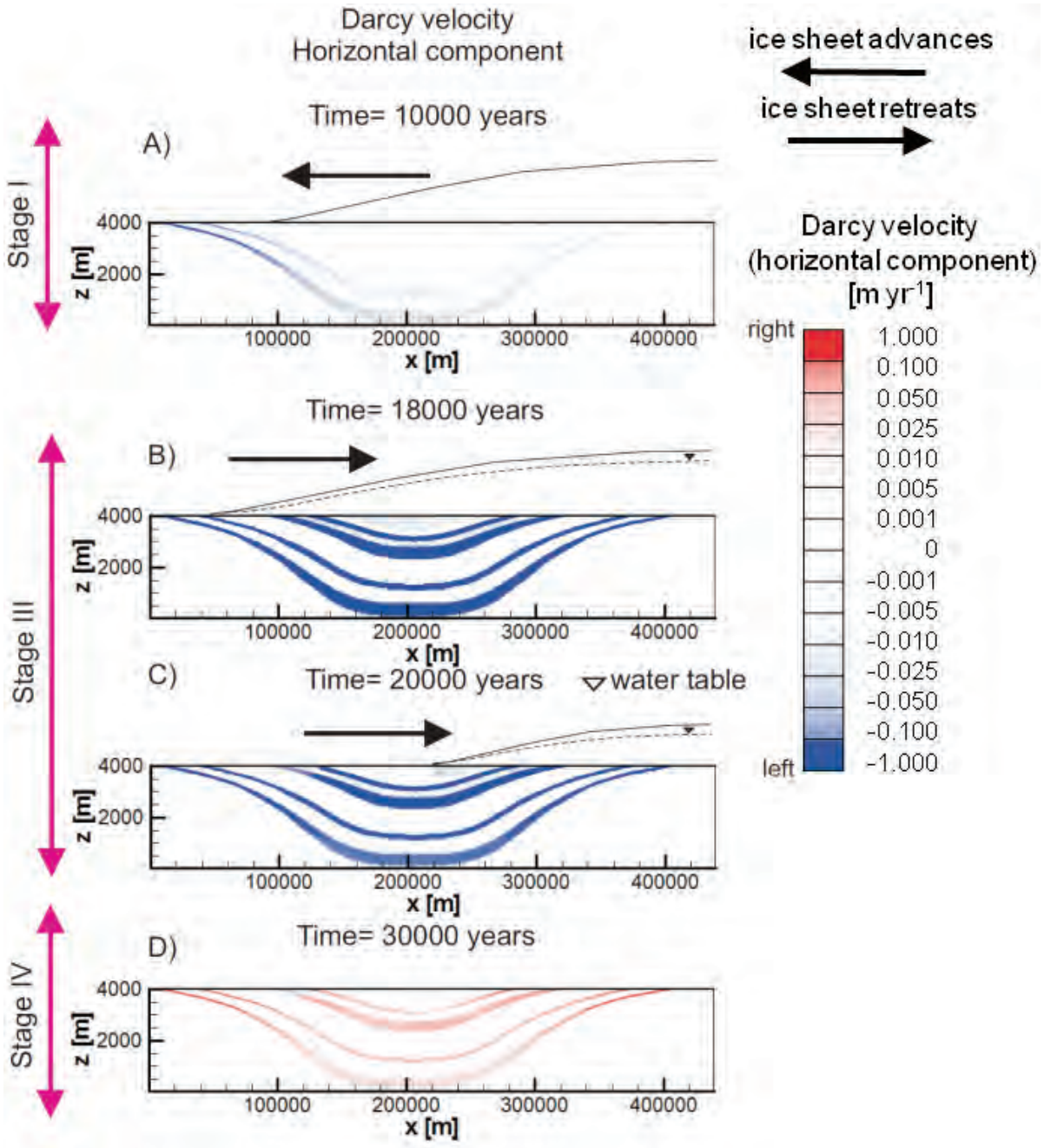

Figure 38: Scenario POR simulation results - horizontal components of specific discharge (Darcy velocity) at different times: A) 10000 years. B) 18000 years. C) 20000 years. D) 30000 years

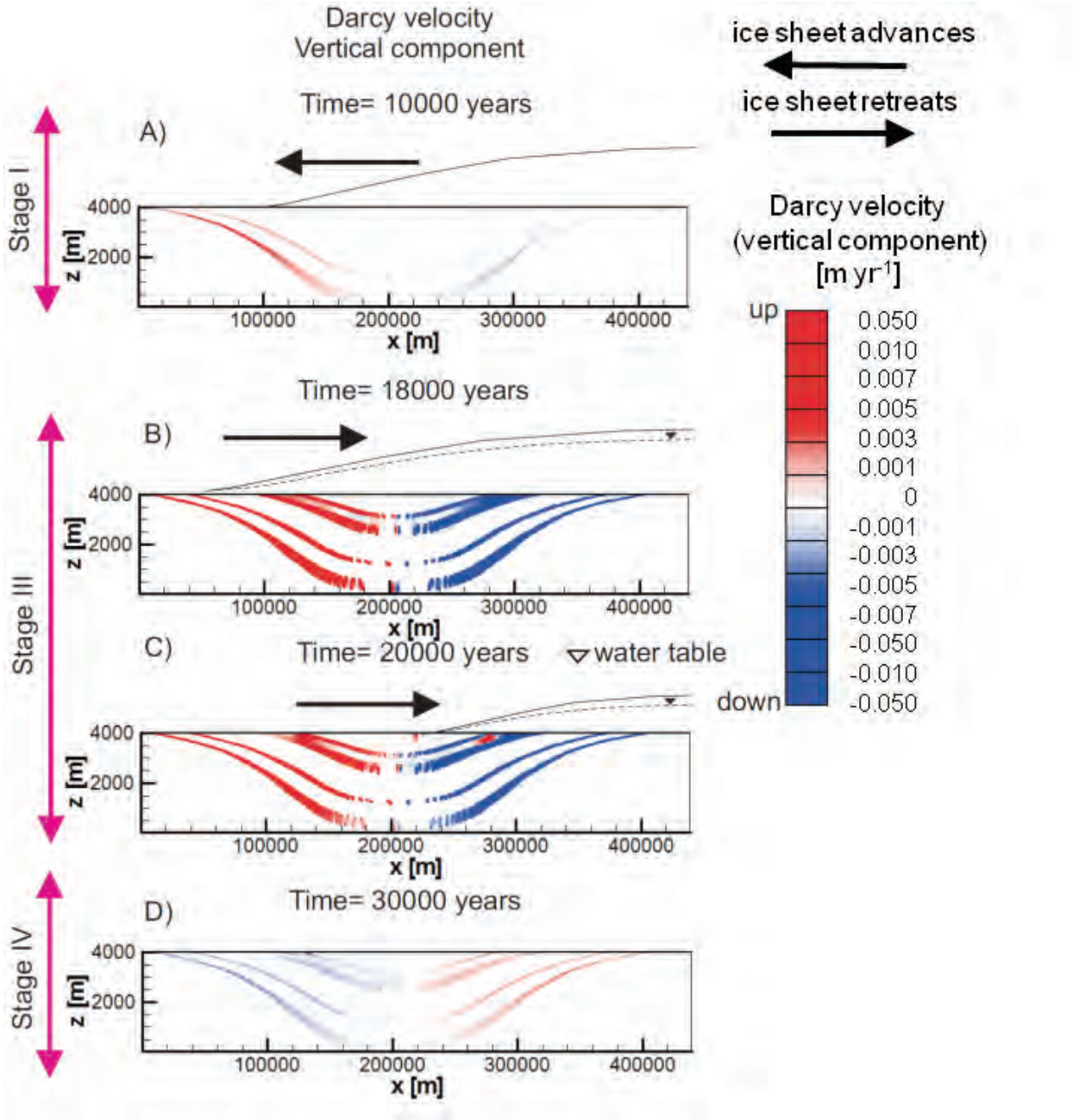

Figure 39: Scenario POR simulation results - vertical components of specific discharge (Darcy velocity) at different times: A) 10000 years. B) 18000 years. C) 20000 years. D) 30000 years

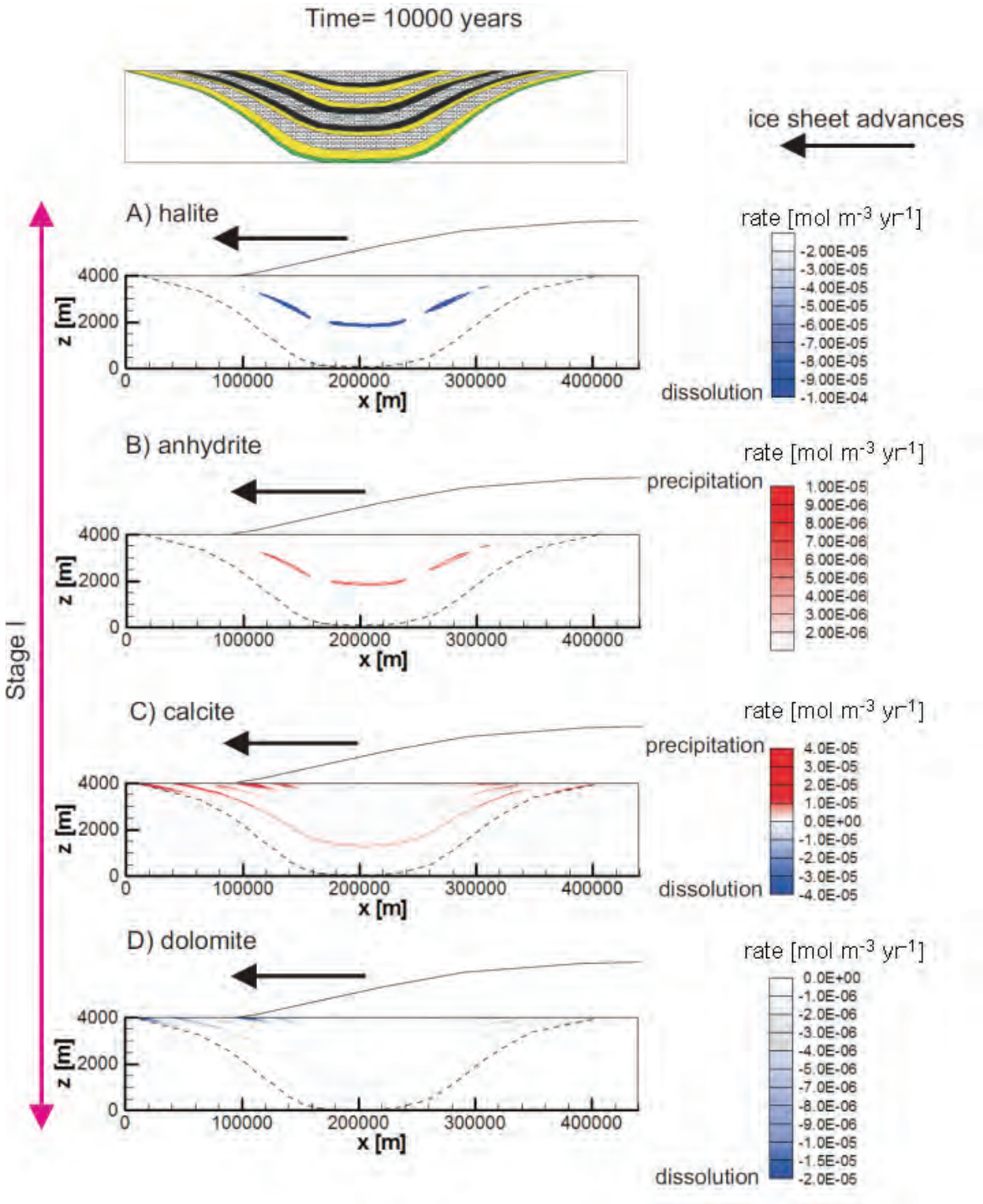

Figure 40: Scenario POR mineral reaction rates at 10000 years: A) Distribution of halite dissolution rate. B) Distribution of anhydrite precipitation rate. C) Distribution of calcite dissolution/precipitation rates. D) Distribution of dolomite dissolution rate

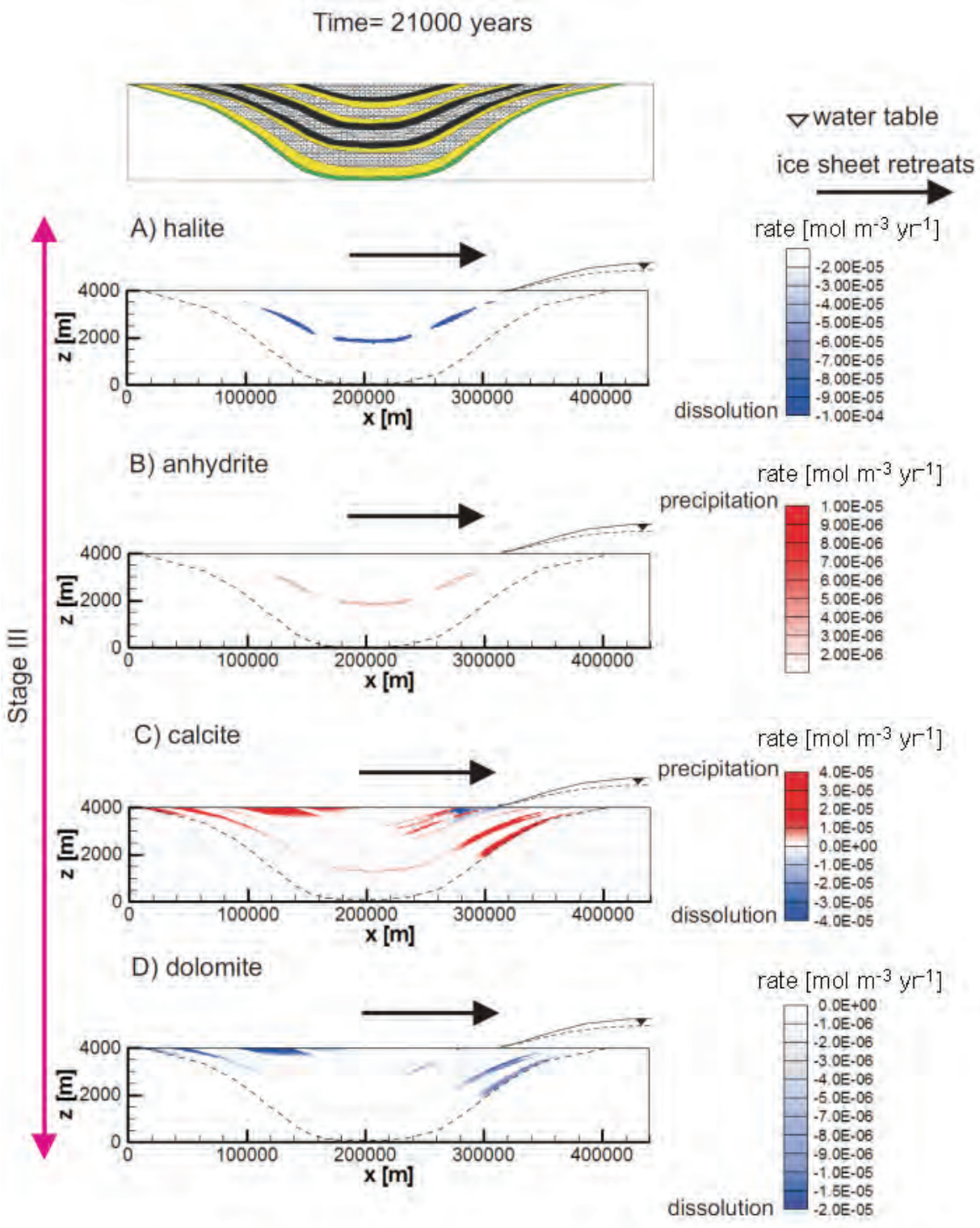

Figure 41: Scenario POR mineral reaction rates at 21000 years: A) Distribution of halite dissolution rate. B) Distribution of anhydrite precipitation rate. C) Distribution of calcite dissolution/precipitation rates. D) Distribution of dolomite dissolution rate

9.5 BASIN-SCALE HEAT TRANSPORT

Heat transport in sedimentary basins could modify the thermodynamic (e.g. equilibrium constants and dissolution/precipitation rates for chemical reactions) and physical properties of fluids (e.g. density and viscosity). In order to provide a preliminary evaluation of the importance of thermal effects on the hydrogeologic system considered here, a scenario that includes heat transport (identified as THERMAL) is simulated. For this simulation, a geothermal heat flux of 0.05 W m^{-2} (Bense and Person, 2008) is imposed at the base of the model (Figure 7). On the top surface of the domain the temperature is varied spatially during ice sheet advance (Stages I and II), with the temperature specified at a constant 0^{o}C beneath the ice sheet, and increasing linearly from 0^{o}C to a maximum of 10^{o}C (at the left boundary) over portions of the domain not covered by ice. The temperature on the top surface varies linearly from 0^{o}C to 10^{o}C (right to left) when the ice sheet is retreating (Stage III) or is entirely absent (Stage IV).

The spatial distributions of the key thermal properties (i.e. solid thermal conductivity and specific heat capacity) are shown in Figure 42; shale formations have lower thermal conductivities than limestone, dolostone, or sandstone formations. The solid thermal conductivities were obtained from Côté and Konrad (2005). It should be noted that because porosity varies with depth, the bulk thermal conductivity in a particular unit will also vary with depth according to Equation 3-14. However, the specific heat capacity (Figure 42B) does not vary greatly for the various units.

The initial conditions for fluid density, point pressure head and temperature are provided in Figure 43**.** The assumed linear increase in fluid temperature with depth causes the initial fluid density profile to decrease over specific intervals (e.g. z= 600 to 1100 m, Figure 43B) rather than remain constant as was the situation for the isothermal BASE-CASE (i.e. Figure 9B).

In general, the point pressure head distribution evolves in a manner similar to the BASE-CASE simulation (compare Figure 44 with Figure 11); however, the inclusion of a geothermal gradient affects the density and viscosity of the basal brines more substantially than the other alternative cases considered previously. For example, because of higher temperatures the fluid density in the lower most sandstone units (Sand1 and Sand 2) are reduced by approximately 3% compared with the BASE-CASE (compare Figure 43B and Figure 45 with Figure 9B and Figure 12). However, the initial density distribution below a depth of approximately 300 m remains unchanged during the ice sheet advance and retreat (Figure 45), which is consistent with the results of the BASE-CASE (Figure 12). Specific discharge also evolves in a manner similar to the BASE-CASE, with elevated specific discharge in the most permeable units during ice sheet retreat (e.g. Stage III, Figure 46C). The horizontal components of specific discharge (results not shown) in the Sand1 and Sand2 units at the center of the basin at 18000 yr are 9.3 x 10^{-2} m yr^{-1} and 3.8 x 10^{-1} m yr^{-1}, respectively, compared to corresponding values of 4.3 x 10^{-2} m yr^{-1} and 2.3 x 10^{-1} m yr^{-1}, respectively, for the BASE-CASE. The temperature distribution within the basin remains relatively unchanged throughout the simulation (Figure 47).

The presence of a thermal gradient in the basin results in relatively high reaction rates for calcite and dolomite in the upper 1 km of the domain where temperatures are lowest (Figure 48A and B). Maximum reaction rates for calcite precipitation, obtained from the calcite volume fraction change during the first 10000 yr of the simulation, are about 2 x 10^{-3} mol m^{-3} yr^{-1} compared to rates on the order of 10^{-5} mol m^{-3} yr^{-1} for the BASE-CASE (Figure 18C). During the simulation (i.e. from 17500 to 21000 yr) the reaction rates decrease and calcite dissolution occurs near the toe of the receding ice sheet (Figure 48C). The maximum change in mineral volume fractions over the entire 32500 yr simulation are: 0.0087% and 0.058% for calcite dissolution and

precipitation, respectively, and 0.052% for dolomite dissolution. Although the changes due to calcite precipitation and dolomite dissolution are larger than obtained for the BASE-CASE, these changes remain small compared to the initial volume fractions of these minerals (e.g. minimum volume fractions are 1% for dolomite and 4% for calcite; Table 6). The dissolution of halite and precipitation of anhydrite in the THERMAL scenario are not significantly different from the BASE-CASE simulation (results not shown).

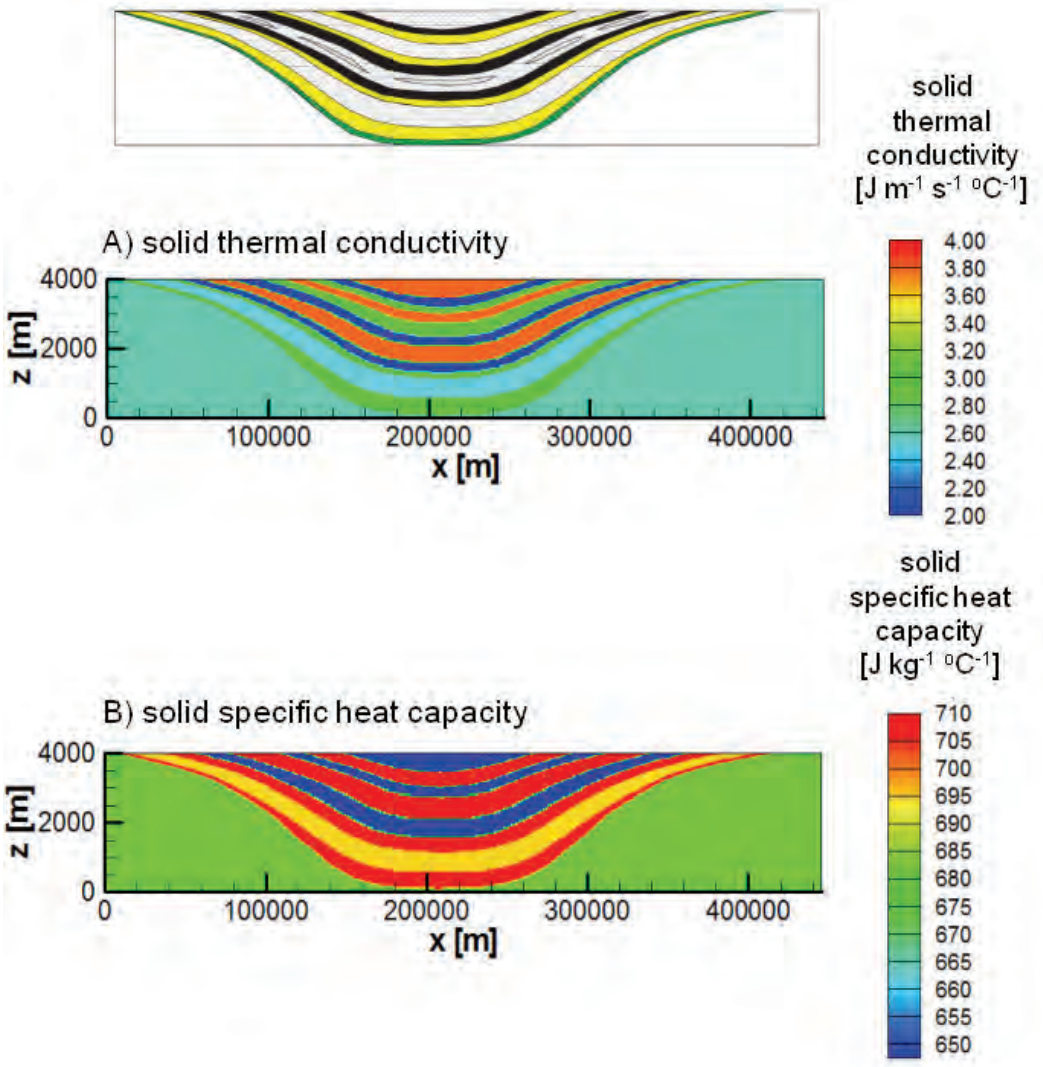

Figure 42: Scenario THERMAL heat transport parameters: A) Solid thermal conductivity distribution. B) Solid specific heat capacity distribution

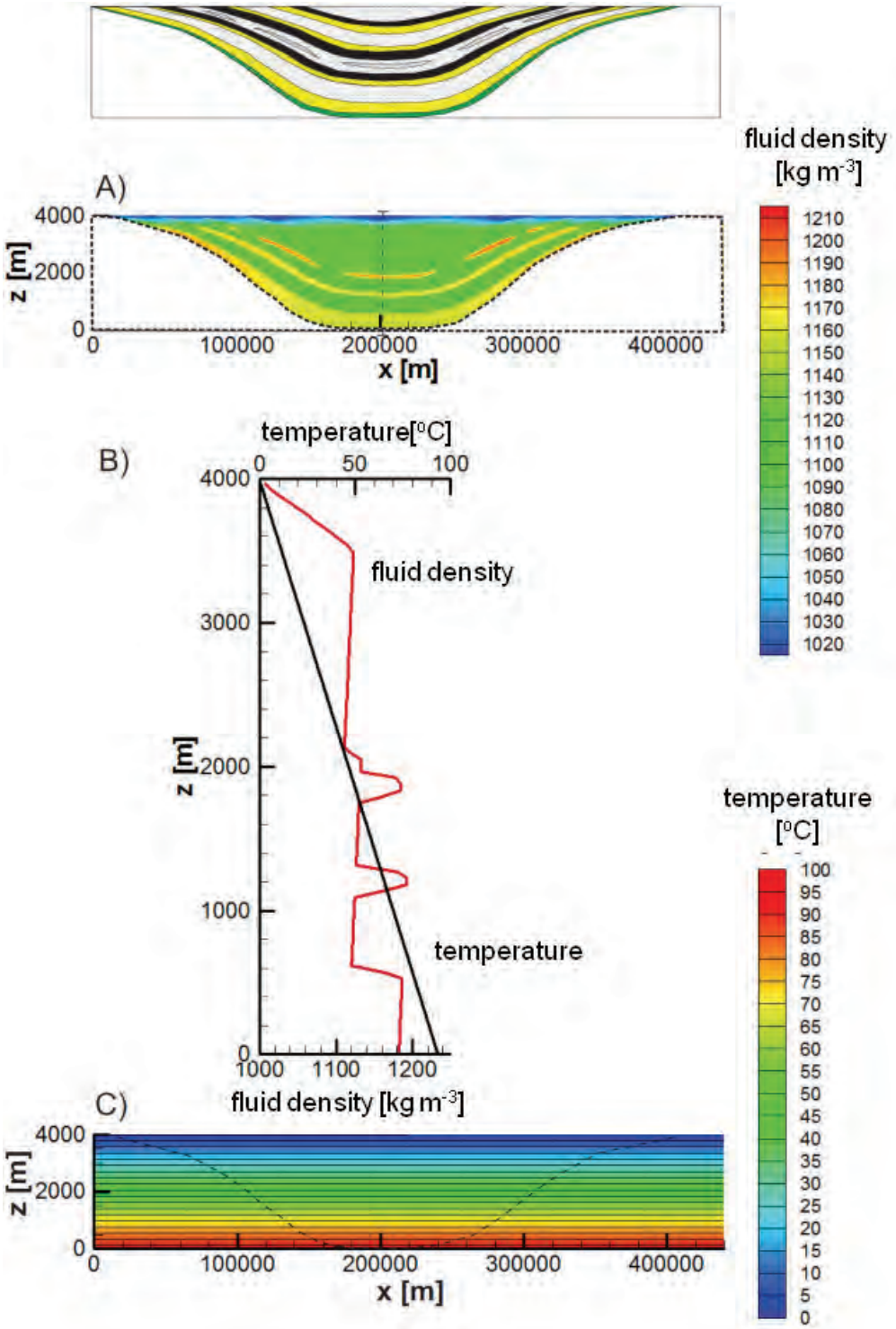

Figure 43: Initial conditions for the THERMAL scenario: A) Fluid density distribution. B) Fluid density (red) and temperature (black) profiles in the center of the sedimentary basin. C) Spatial distribution of temperature

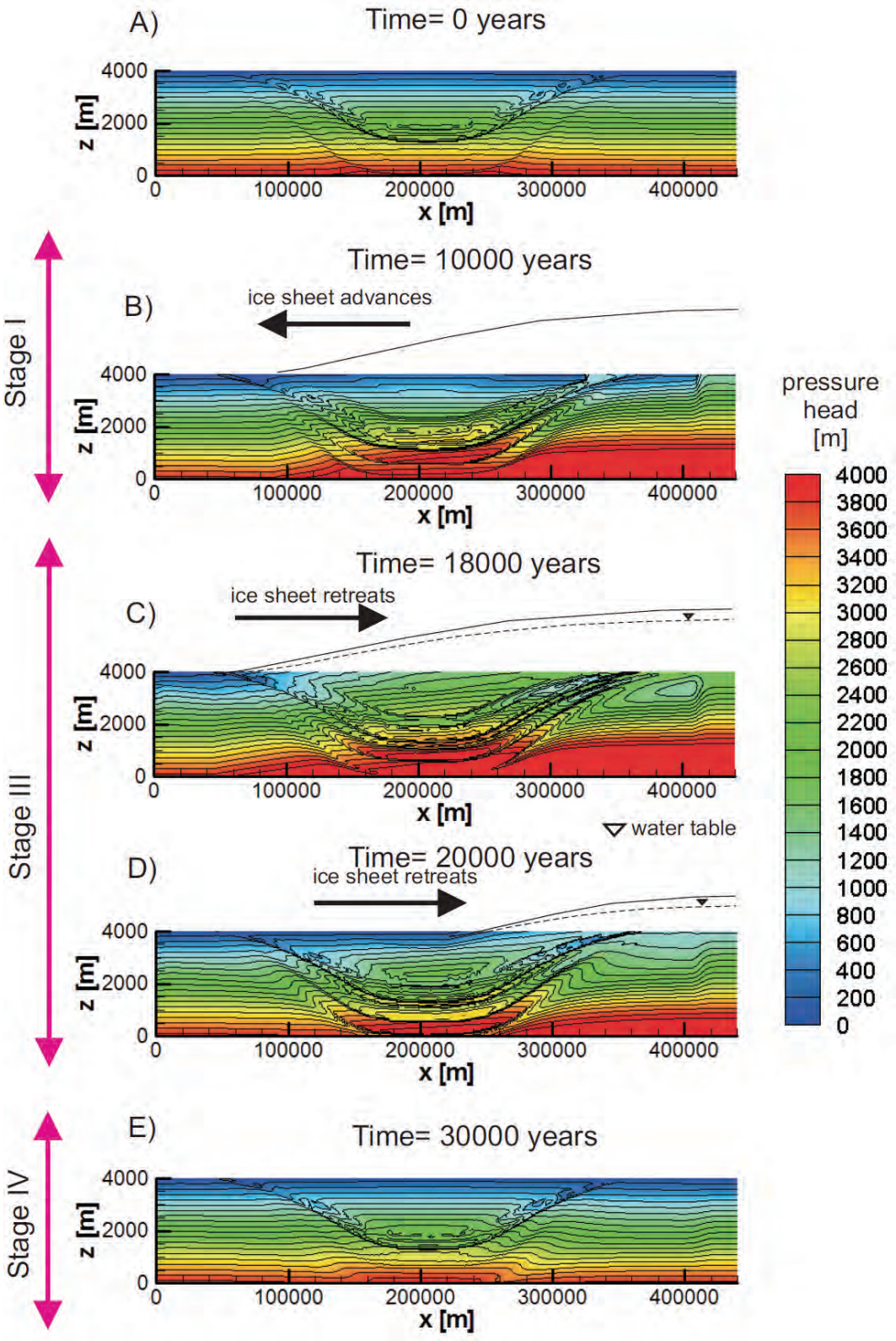

Figure 44: THERMAL simulation results - spatial distribution of point pressure head: A) Initial condition. B) 10000 years (Stage I). C) 18000 years (Stage III). D) 20000 years (Stage III). E) 30000 years (Stage IV)

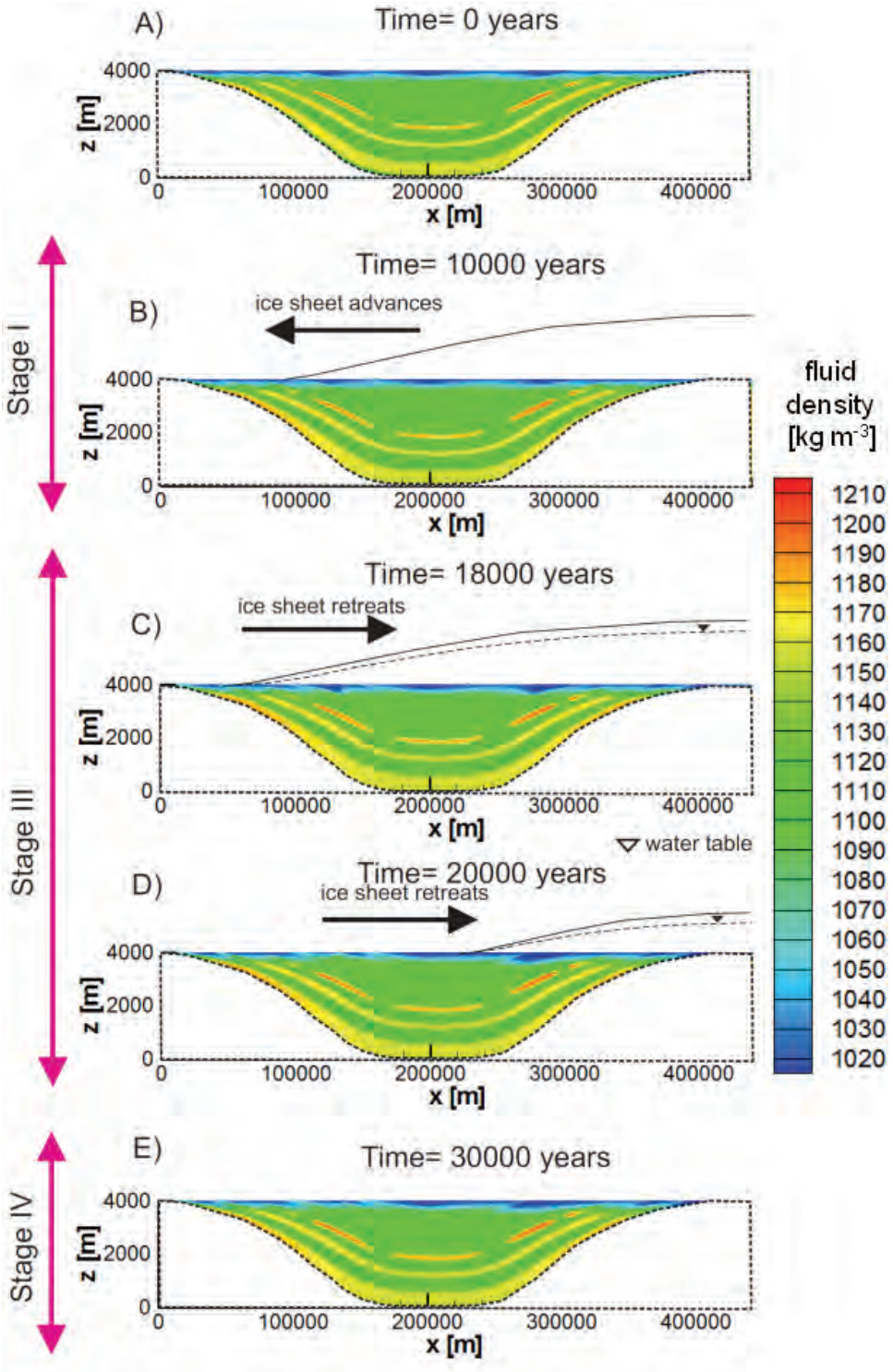

Figure 45: THERMAL simulation results - spatial distribution of fluid density: A) Initial condition. B) 10000 years (Stage I). C) 18000 years (Stage III). D) 20000 years (Stage III). E) 30000 years (Stage IV)

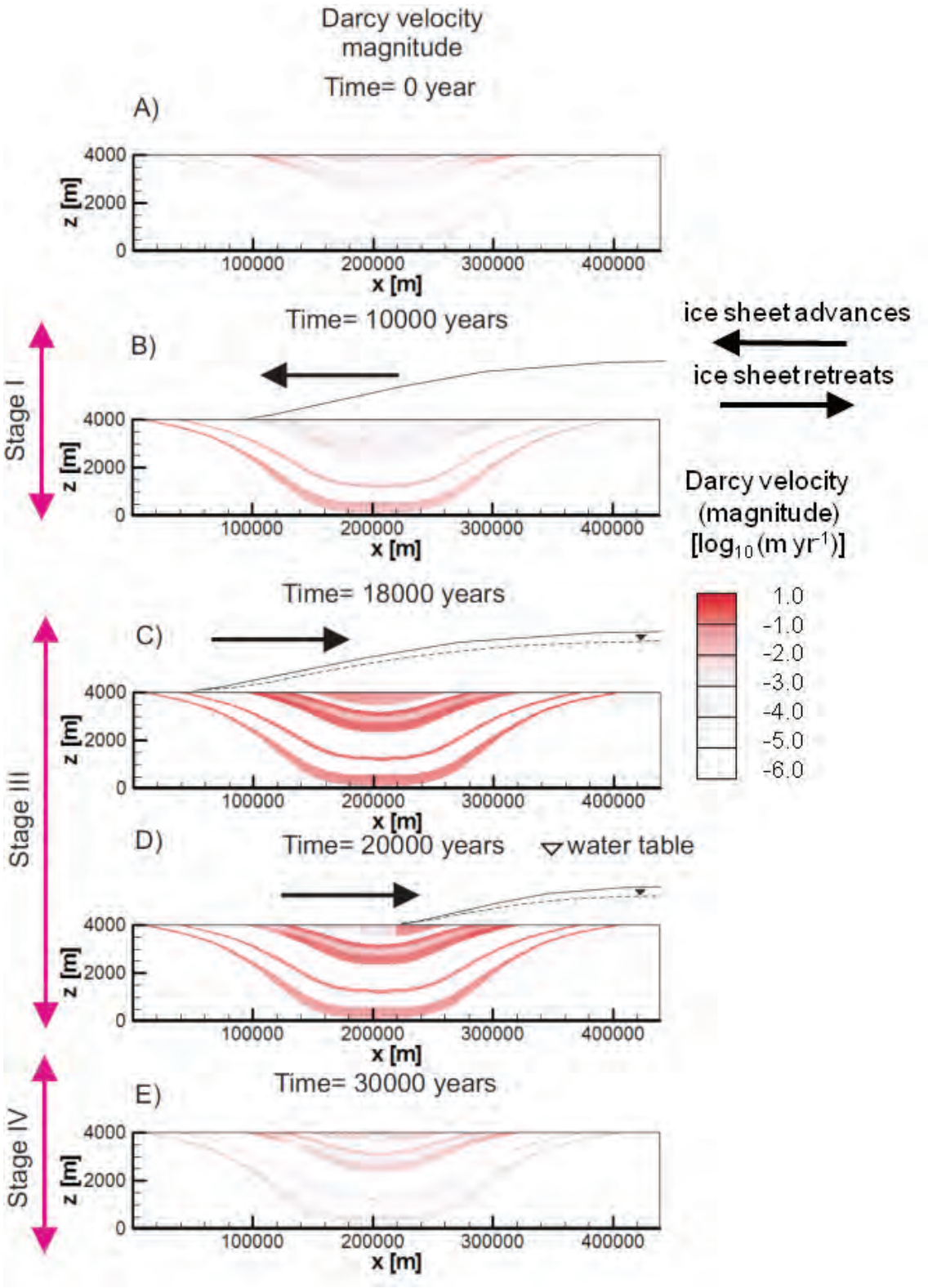

Figure 46: THERMAL simulation results – magnitude of specific discharge (Darcy velocity): A) Initial condition. B) 10000 years. C) 18000 years. D) 20000 years. E) 30000 years

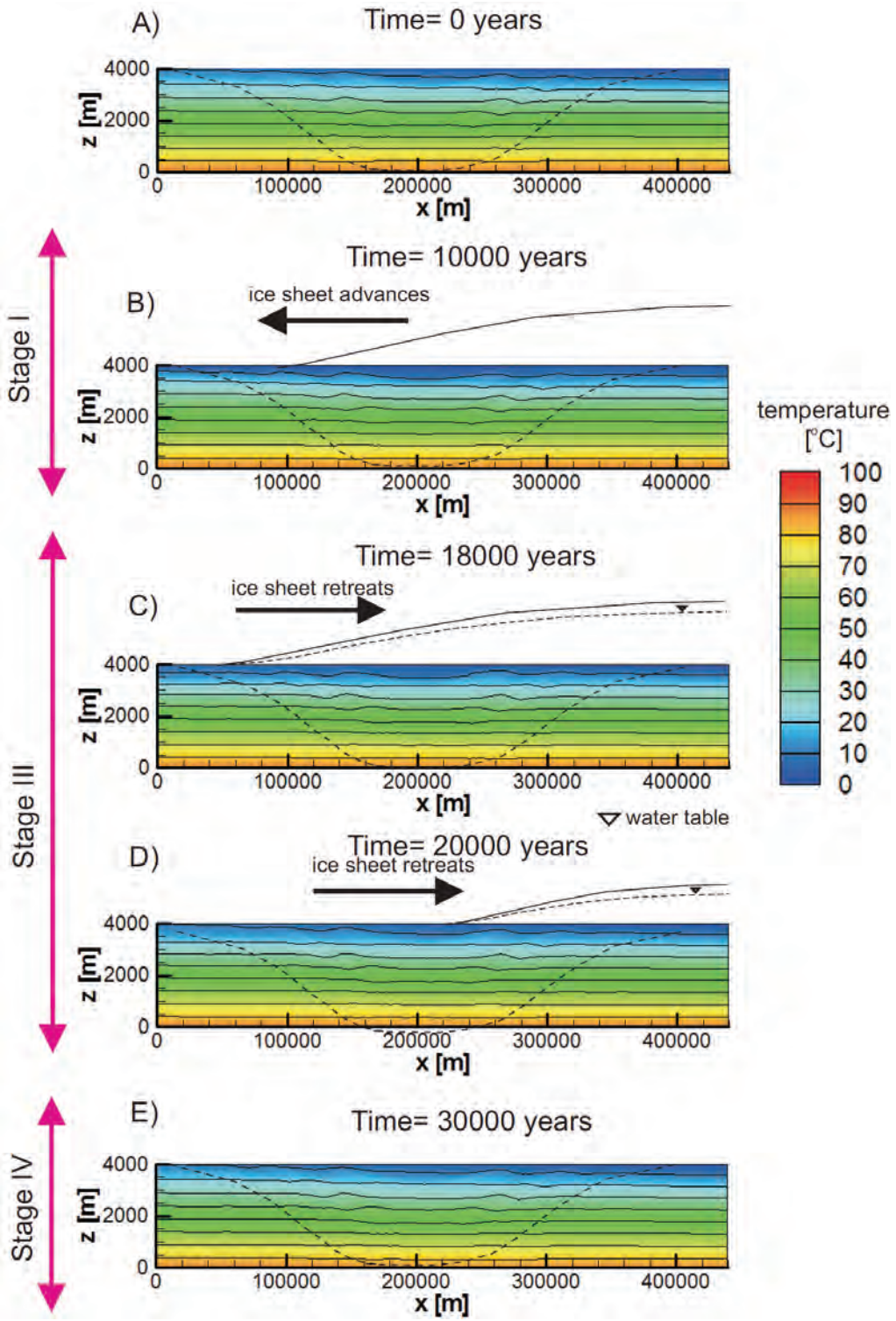

Figure 47: THERMAL simulation results - spatial distribution of temperature: A) Initial condition. B) 10000 years (Stage I). C) 18000 years (Stage III). D) 20000 years (Stage III). E) 30000 years (Stage IV)

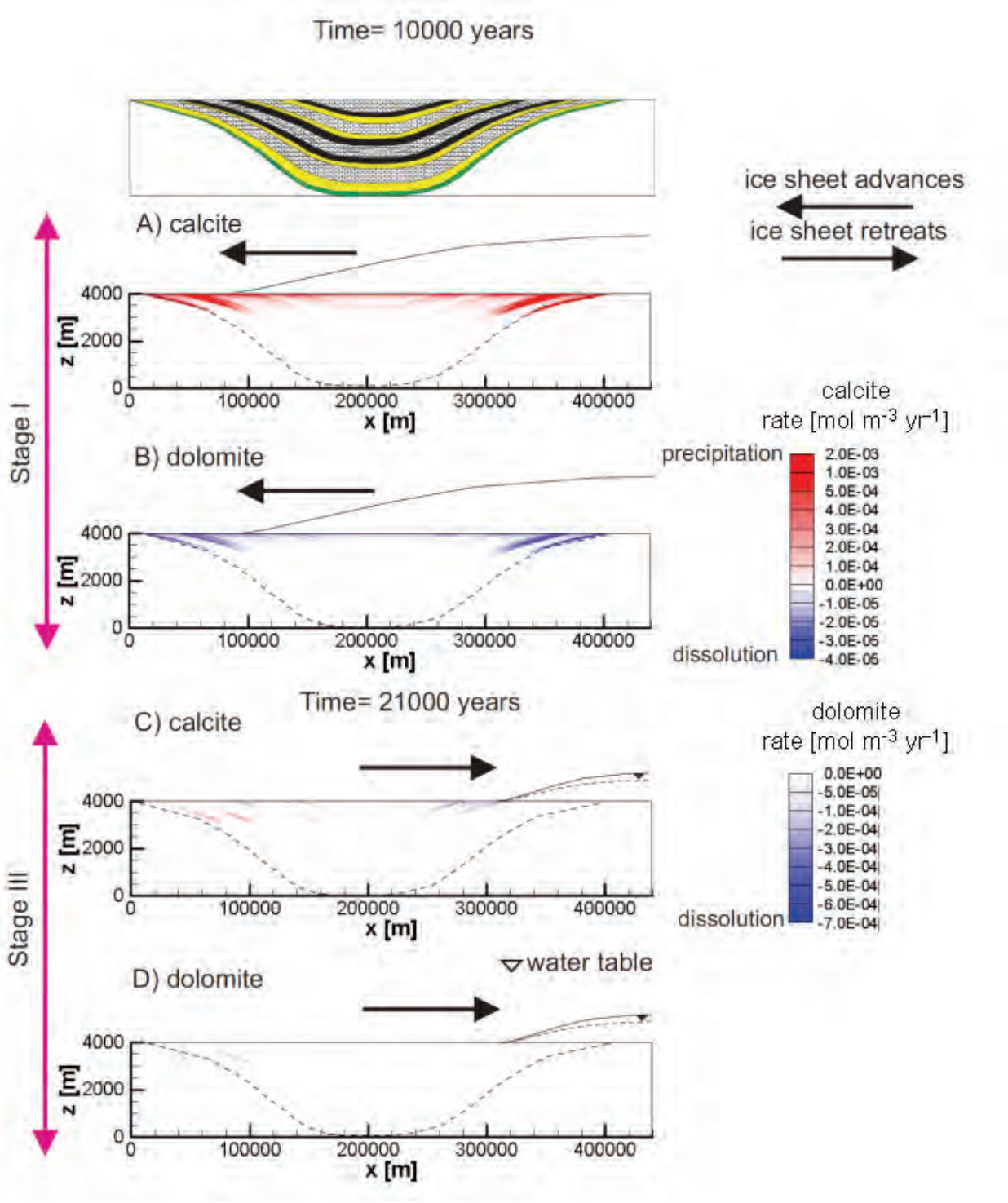

Figure 48: Scenario THERMAL mineral reaction rates: A) Dissolution/precipitation rate of calcite at 10000 years. B) Dissolution rate of dolomite at 10000 years. C) Dissolution/precipitation rate of calcite at 21000 years. D) Dissolution of dolomite rate at 21000 years

9.6 EXCLUSION OF CATION EXCHANGE REACTIONS

This scenario (identified as NO_EXCH) evaluates the effect of neglecting cation-exchange reactions on the evolution of flow patterns and mineral reaction rates. This scenario is unlikely to be representative of conditions in sedimentary basins because of the common occurrence of clay minerals in such settings in which cation exchange reactions are one of the important geochemical reactions; however, it is considered here in order to isolate the potential impact of cation exchange.

The simulation results for specific discharge, fluid density, and the evolution of recharge and discharge for the basin (results not shown) are very similar to those obtained for the BASE-CASE. The results for calcite and dolomite reaction rates suggest that neglecting cation-exchange reactions has an impact on the spatial extent of dedolomitization in the basin. For the BASE-CASE, calcite precipitation and dolomite dissolution are mainly restricted to depths less than 500 m and to the left and right flanks of the basin (Figure 18C, 18D and Figure 19C, 19D). For the NO_EXCH scenario, dedolomitization occurs mostly near the boundary between units Sand2 and Sh1 (Figure 49). The maximum changes in mineral volume fractions, over the simulation time of 32500 yr, for all reactive minerals are within a factor of three of values obtained for the BASE-CASE, indicating that cation exchange reactions have a relatively small overall impact on the geochemical evolution of the basin.

9.7 EXCLUSION OF MINERAL DISSOLUTION-PRECIPITATION AND CATION EXCHANGE REACTIONS

This scenario (identified as CONS) evaluates the effect of neglecting all the heterogeneous reactions (dissolution/precipitation and ion exchange) on the evolution of flow patterns and pore water chemistry in the basin. This scenario includes multicomponent transport, but corresponds to a conservative solute transport case (i.e. the total concentrations of the chemical components are not affected by water-rock interactions).

The simulated spatial distributions of point pressure head and fluid density at different times are shown in Figure 50 and Figure 51, respectively. There are no differences of note between these results and those of the BASE-CASE. The temporal variations in recharge and discharge for the basin are also similar to those of the BASE-CASE (results not shown, see Figure 17 for BASE_CASE). These findings indicate that, at least for this single 32500 yr cycle of ice sheet advance and retreat, the impact of heterogeneous reactions on fluid flow is relatively minor. Further work would be necessary to determine if such a finding holds over longer time periods, including for example, multiple repeated glaciation events.

The distributions of total concentrations for Ca and Mg are depicted in Figure 52 and Figure 53, respectively. Similar to the BASE-CASE (Figure 24 and Figure 25), some localized fresh water ingress is indicated by the decrease in the total Ca and Mg concentrations in the shallow permeable aquifers, particularly during ice sheet retreat (Figure 52C and Figure 53C). However, the distribution of the Ca and Mg concentrations below the depths of approximately 300 m are essentially unchanged compared to the BASE-CASE.

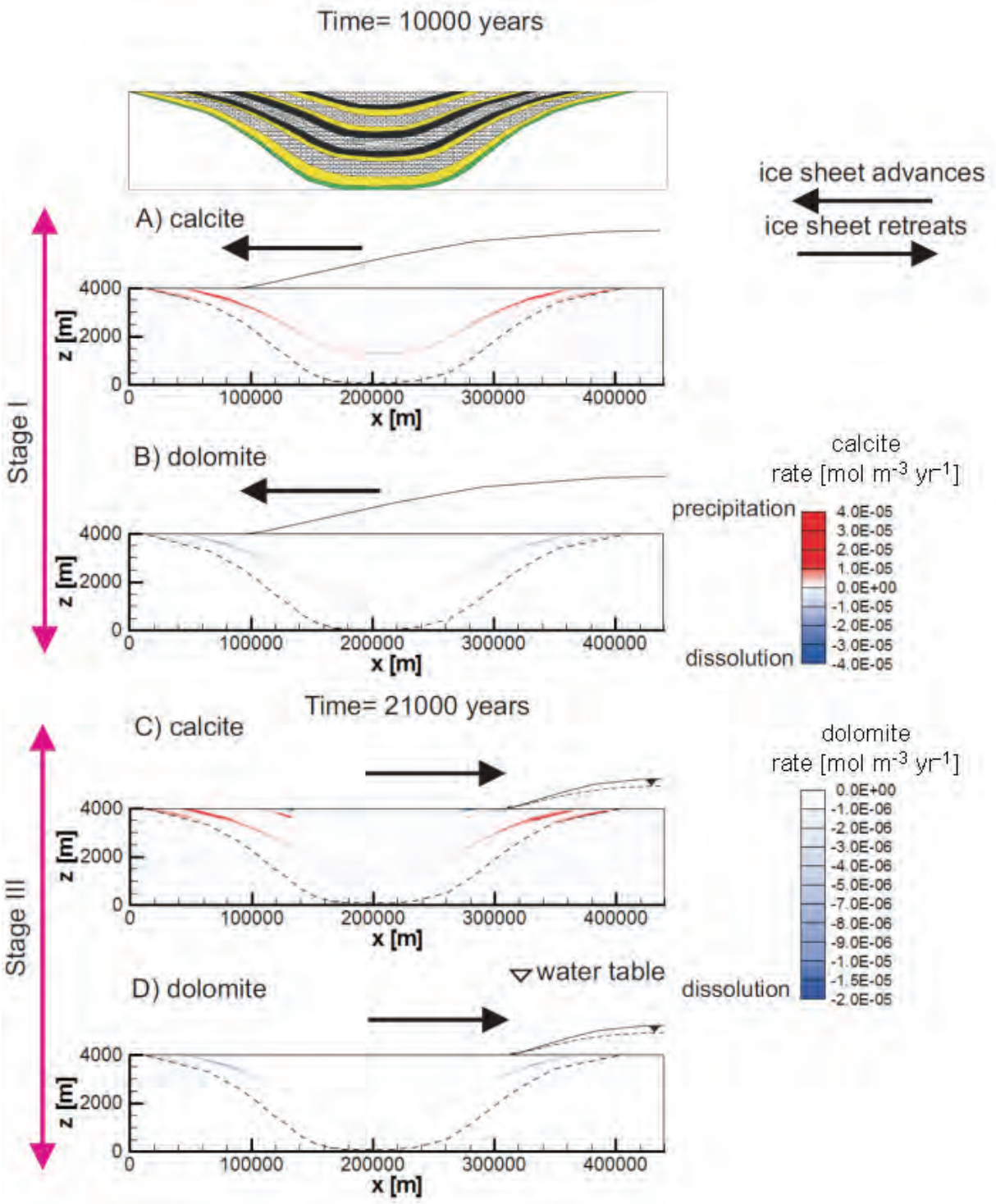

Figure 49: Scenario NO_EXCH mineral reaction rates: A) Dissolution/precipitation rate of calcite at 10000 years. B) Dissolution rate of dolomite at 10000 years. C) Dissolution/precipitation rate of calcite at 21000 years. D) Dissolution rate of dolomite at 21000 years

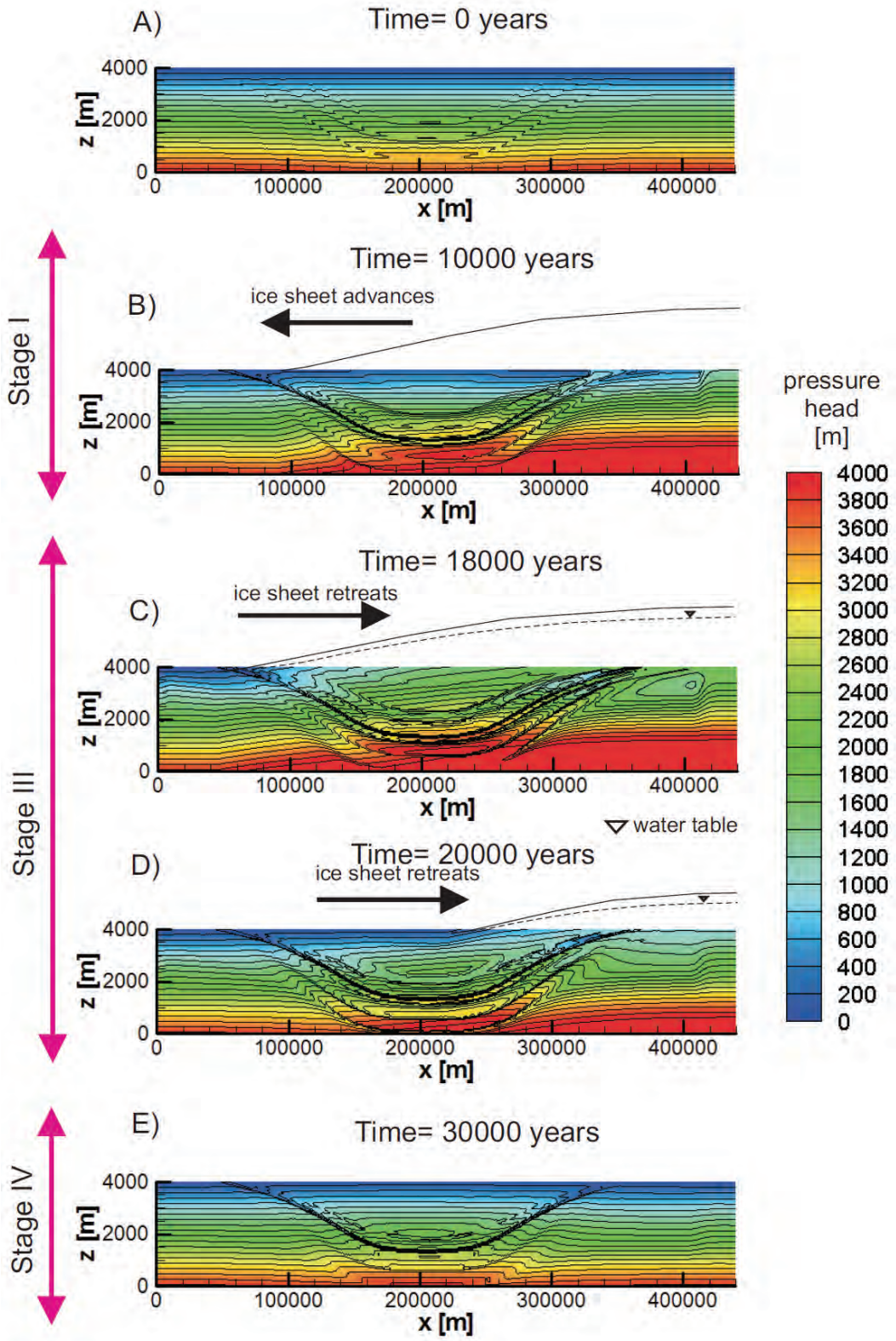

Figure 50: Scenario CONS simulation results - spatial distribution of point pressure heads: A) Initial condition. B) 10000 years (Stage I). C) 18000 years (Stage III). D) 20000 years (Stage III). E) 30000 years (Stage IV)

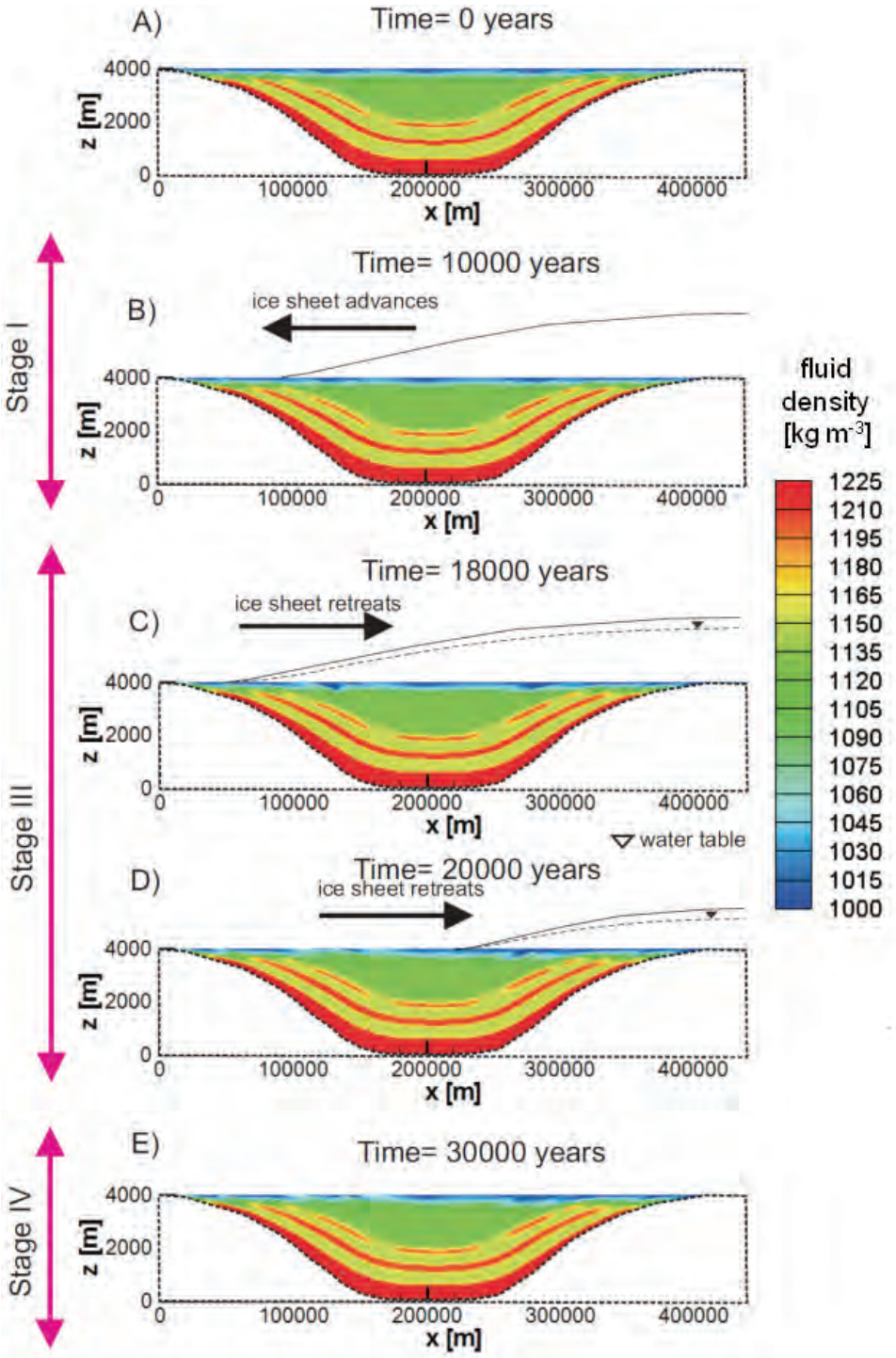

Figure 51: Scenario CONS simulation results - spatial distribution of fluid density: A) Initial condition. B) 10000 years (Stage I). C) 18000 years (Stage III). D) 20000 years (Stage III). E) 30000 years (Stage IV)

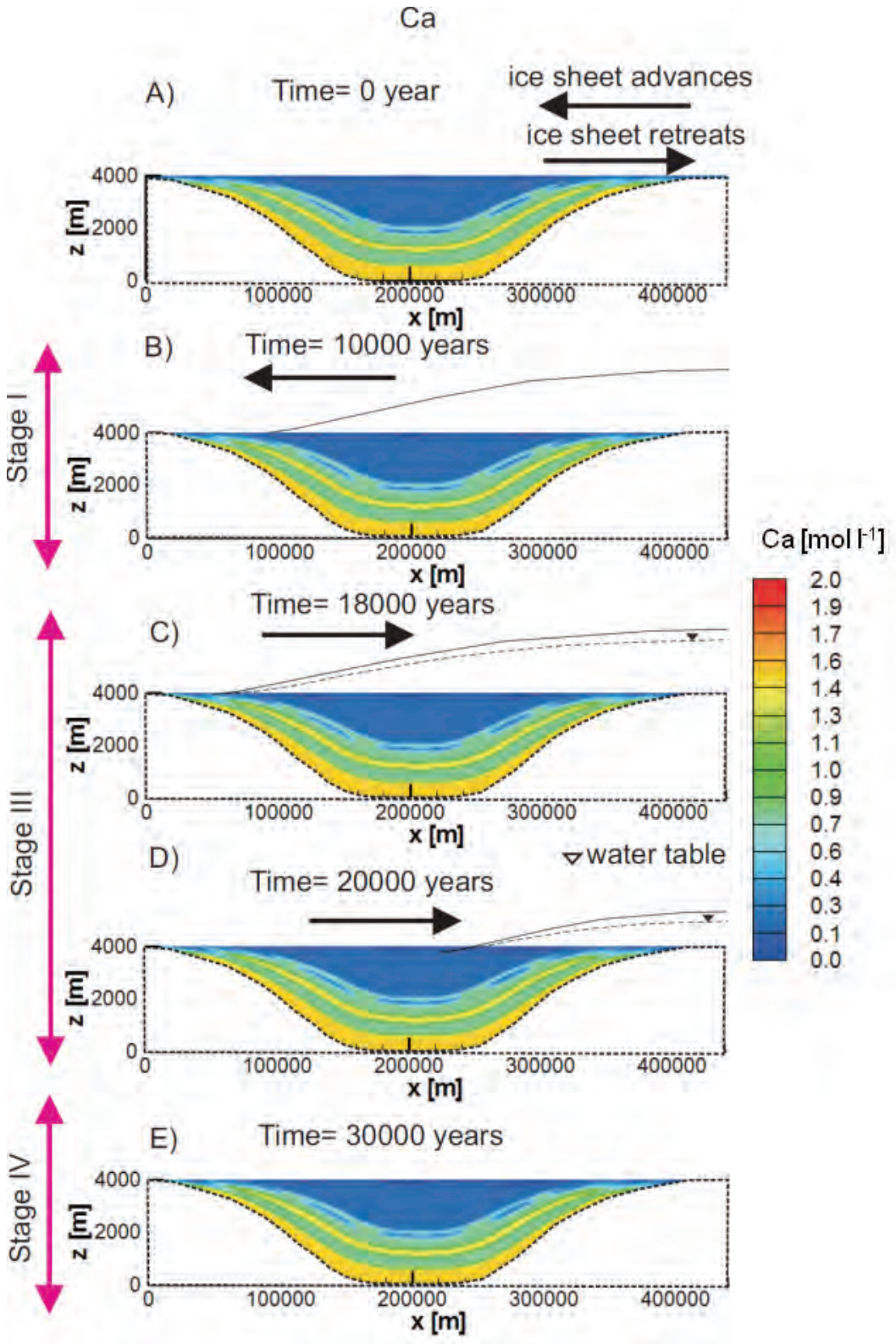

Figure 52: Scenario CONS simulation: Distributions of Ca total concentrations at different times. A) Initial conditions. B) 10000 years. C) 18000 years. D) 20000 years. E) 30000 years

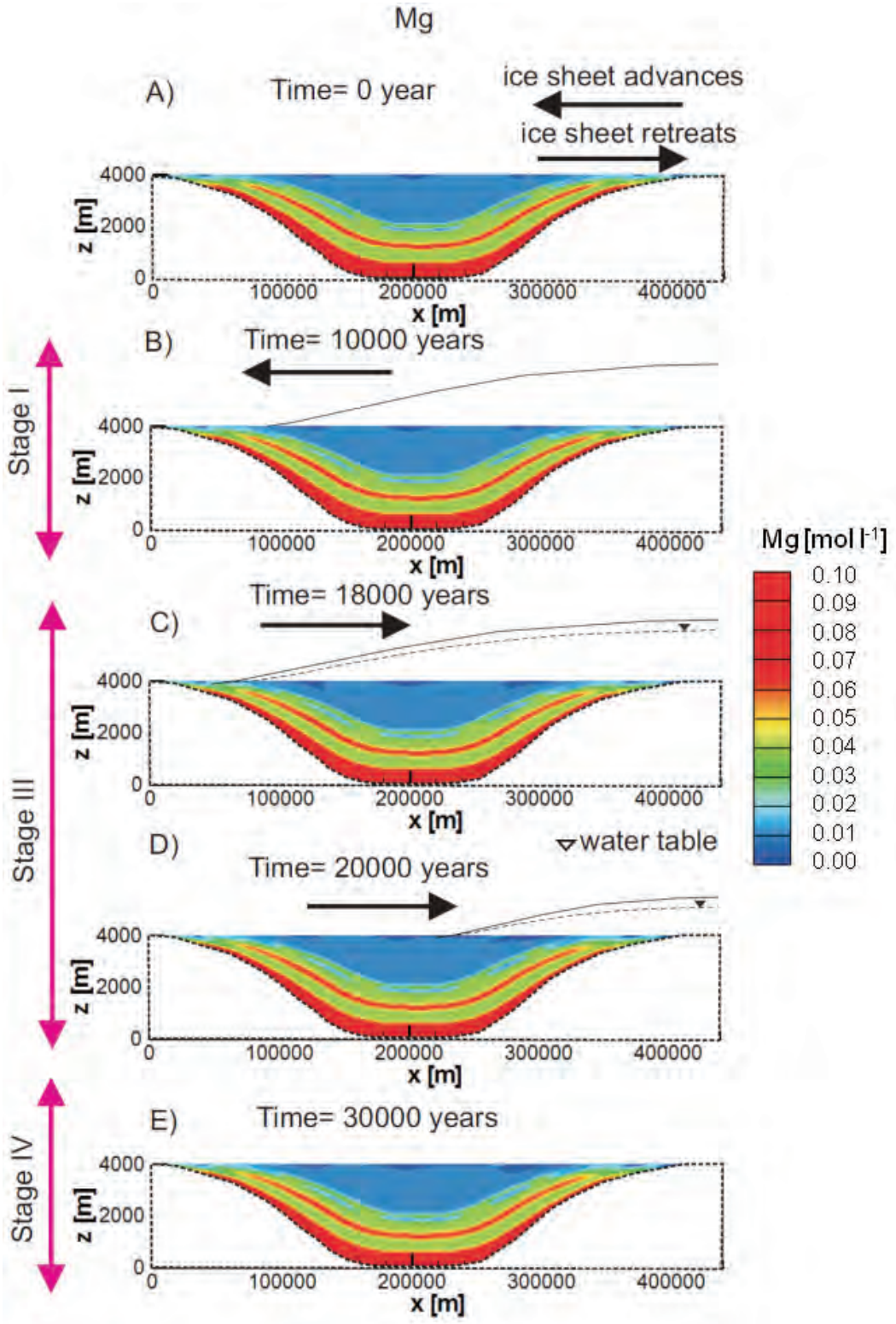

Figure 53: Scenario CONS simulation: Distributions of Mg total concentrations at different times. A) Initial conditions. B) 10000 years. C) 18000 years. D) 20000 years. E) 30000 years

10. SUMMARY AND CONCLUSIONS

The goal of this research was to advance the numerical simulation of fluid flow and geochemical processes in sedimentary basins, in order to improve the capability to assess how such systems may respond to long term changes in surface boundary conditions (e.g. glaciation). The main components of this research work included:

1. incorporating new simulation capabilities into the existing MIN3P-D code (Henderson et al., 2009), resulting in the version entitled MIN3P-NWMO, and verification of these new capabilities by benchmarking the solutions obtained for selected problems with independently derived solutions, or intercomparison with comparable simulation codes;

2. demonstrating the capabilities of the new code for simulating the response of a hypothetical large-scale sedimentary basin to ice sheet advance and retreat over time periods greater than 30,000 years; and

3. conducting a limited sensitivity analysis of geochemical stability in the hypothetical sedimentary basin as a function of selected model processes and parameters.

The new features included in MIN3P-NWMO are: fluid density and ion activity correction calculations for high ionic strength solutions (up to 20 mol l^{-1}); one-dimensional hydromechanical coupling due to ice sheet loading; and coupling of subsurface energy (heat) transport with fluid and solute transport. The mathematical formulations for these processes were based on previously published work (e.g. Harvie et al., 1984; Neuzil, 2003; Voss and Provost, 2008). Verification of MIN3P-NWMO was conducted by comparing simulation results to analytical solutions and published results obtained with other established numerical models designed to solve specific sub-problems. These benchmark problems included ones dealing with single processes (e.g. one-dimensional hydromechanical coupling) and multiple, coupled processes (e.g. flow and reactive transport in high ionic strength solutions; coupled flow, heat and solute transport). Overall, good agreement was obtained for these verification problems. While these new capabilities significantly improve the ability to simulate density-dependent flow and geochemical processes in sedimentary basins, it must be noted that several processes remain weakly coupled or have not been considered. For example, permafrost development is considered simply by reducing the hydraulic conductivity in preselected locations (i.e. not coupled to heat transport), while lithospheric flexure is not incorporated. Many of these limitations also exist in other recent models for sedimentary basins (e.g. McIntosh et al., 2011).

An illustrative scenario (BASE-CASE) was developed to investigate the hydrogeological and geochemical stability of a large-scale generic sedimentary basin (400 km in width, maximum 4 km depth) during a 32500 yr glaciation-deglaciation cycle. The surface boundary conditions were varied with time to represent cold-based ice sheet advance during a time of 12500 yr, followed by a stable glacial maximum (5000 yr duration), with subsequent warm-based ice sheet retreat (5000 yr duration). The final 10000 yr period represented interglacial conditions during which no ice sheet was present. The sedimentary basin was represented by a sequence of horizontally continuous carbonates interbedded with sandstones and shales; a weathered zone in the basement rocks and discontinuous evaporites were also considered. The model was hypothetical; however, to the extent possible, model parameters were based on published data or relationships.

The simulation results indicated that, during the period of ice sheet retreat, limited infiltration of glacial meltwater occurs into the higher hydraulic conductivity units. Based on changes in fluid density and solute concentrations (e.g. Cl), relatively fresh meltwater migrated to depths of approximately 300 to 400 m in the more permeable aquifers (i.e. Sand3, Sand4, and Dol2) that sub-crop beneath the toe of the receding ice sheet. Deeper in the basin, Darcy velocity (specific discharge) increases were also noted in the highest hydraulic conductivity units. For example, in a sandstone unit (Sand1) at a depth of approximately 3700 m, the horizontal component of specific discharge during glacial retreat was 4.3×10^{-2} m yr^{-1}, compared to a value of 1.4×10^{-2} m yr^{-1} during ice sheet advance. These specific discharge changes were not, however, significant enough to perturb the fluid density in the basin at depths greater than approximately 300 m. At the end of the simulation, point pressure heads in low hydraulic conductivity units (i.e. shales) and specific discharge values in aquifers were only slightly elevated (by less than a factor of 2) relative to the initial conditions.

From a geochemical perspective, the simulation results reveal that dedolomitization (i.e., dissolution of dolomite ($MgCa(CO_3)_2$) and precipitation of calcite ($CaCO_3$)) is the most significant geochemical process during the deglaciation phase. Dedolomitization is mainly restricted to the shallow aquifers. Although dissolution of halite (NaCl) is more significant locally (i.e., at the margins of the evaporite units), it is not as widespread as dedolomitization. Porosity changes due to mineral dissolution-precipitation reactions are predicted to be very small, with a maximum porosity increase of approximately 0.004 occurring in the evaporite units because of halite dissolution. Major ion distributions remained remarkably stable during the 32500 yr simulation, except for localized freshening in shallow aquifers that received meltwater recharge. In general, the simulation results indicated a high degree of geochemical stability for this hypothetical basin.

Seven alternative scenarios, which were designed to investigate a particular process, or conceptual model assumption, were also simulated. In general, there were only minor differences between the BASE-CASE simulation results and these alternative scenarios. Of note were the scenarios that assumed constant porosity and hydraulic conductivity in individual hydrogeological units, and the one having non-isothermal conditions. In the situation where porosity and hydraulic conductivity was assumed not to decrease with depth, specific discharge in deeper aquifer units was typically higher than that in the BASE-CASE; for example, at 18000 yr (ice sheet retreat) the horizontal component of the specific discharge at a depth of 3700 m in Sand1 (the center of the basin) was 4.2×10^{-1} m yr^{-1}, which was about one order of magnitude greater than for the BASE-CASE. Maximum mineral volume fraction changes (for the entire 32500 yr simulation) were greater than those of the BASE-CASE by factors ranging from 1.9 (halite dissolution) to 7 (dolomite dissolution). In the presence of a thermal gradient, the calcite reaction rates were enhanced in the upper 1 km of the basin relative to the BASE-CASE; however, the mineral volume fraction changes remained small compared to the initial volume fractions of the carbonate minerals. Although alterations of the conceptual model or underlying processes resulted in changes to the rates of fluid flow and geochemical reactions, perturbations of the initial fluid density distribution and geochemical conditions due to ice sheet advance and retreat were essentially negligible below depths of approximately 300 m.

ACKNOWLEDGEMENTS

We would like to thank Thomas H. Henderson, the developer of MIN3P-D, for his assistance at the onset of this project and for providing the verification examples for density-dependent flow and solute transport. The authors greatly appreciate the constructive reviews by Tammy Yang, Eric Sykes, Monique Hobbs, and Mark Jensen.

REFERENCES

Appelo, C., and D. Postma. 1993. Geochemistry, Groundwater and Pollution. A.A. Balkema Publishers.

Avis, J., R. Roberts, D. Chace, N. Toll and R. Beauheim. 2009. Hydraulic testing to characterize low permeability sedimentary formations - proposed Deep Geologic Repository, Tiverton, Ontario. Proceedings GeoHalifax 2009, 62nd Canadian Geotechnical Conference & 10th Joint CGS/IAH-CNC Groundwater Conference, 1356-1361.

Ayora, C., J. Garcia-Veigas and J. Pueyo. 1994. The chemical and hydrological evolution of an ancient potash-forming evaporite basin as constrained by mineral sequence, fluid inclusion composition, and numerical simulation. Geochimica et Cosmochimica Acta , 58, 3379-3394.

Azaroual, M., C. Kervevan, M. Durance and P. Durst. 2004. SCALE2000: reaction-transport software dedicated to thermokinetic prediction and quantification of scales - Applicability to desalination problems. Desalination, 3rd Conference on Desalination Strategies in South Mediterranean Countries, 165, 409-419.

Bachler, D., and T. Kohl. 2005. Coupled thermal-hydraulic-chemical modelling of enhanced geothermal systems. Geophysical Journal International, 161, 533-548

Bahr, D.B., E.W.H. Hutton, J.P.M. Syvitski and L.F. Pratson. 2001. Exponential approximations to compacted sediment porosity profiles. Computers & Geosciences , 27, 691-700.

Baker, P., and M. Kastner. 1981. Constraints on the formation of sedimentary dolomite. Science, 213, 214-216.

Bea, S.A., J. Carrera, J.M. Soler, C. Ayora and M.W. Saaltink. 2004. Simulation of remediation alternatives for a ^{137}Cs contaminated soil. Radiochimica Acta, 92, 827-833.

Bea, S.A., J. Carrera, C. Ayora and F. Batlle. 2010. Pitzer Algortithm: Efficient implementation of Pitzer equations in geochemical and reactive transport models. Computers & Geosciences, 36, 526-538.

Benbow, S., R. Metcalfe and J. Wilson. 2008. Pitzer databases for use in thermodynamic modelling. Nuclear Waste Management Organization Technical Memorandum (QRS-3021A-TM1) Version: 1.0. Toronto, Canada.

Bense, V.F. and M.A. Person. 2008. Transient hydrodynamics within intercratonic sedimentary basins during glacial cycles. Journal of Geophysical Research-Earth Surface, 113, Article No. F04005, 1-17.

Birkholzer, J. and Q. Zhou. 2009. Basin-scale hydrogeologic impacts of CO_2 storage: Capacity and regulatory implications. International Journal of Greenhouse Gas Control, 3, 745-756.

Brennan, S.T. and T.K. Lowenstein. 2002. The major-ion composition of Silurian seawater. Geochimica et Cosmochimica Acta, 66, 2683-2700.

Calderhead, A.I. and K.U. Mayer. 2004. Comparison of the suitability of the global implcit method and the sequential non-iterative approach for multicomponent reactive transport modelling. Proceedings GeoQuebec 2004, 57th Canadian Geotechnical Conference & 4th Joint CGS/IAH-CNC Groundwater Conference, 32-39.

Christov, C. and N. Moller. 2004. A chemical equilibrium model of solution behavior and solubility in the H-Na-K-Ca-OH-Cl-HSO_4-SO_4-H_2O system to high concentration and temperature. Geochimica et Cosmochimica Acta, 68, 3717-3739.

Côté, J. and J. Konrad. 2005. Thermal conductivity of base-course materials. Canadian Geotechnical Journal, 42, 61-77.

Diersch, H. and O. Kolditz. 1998. Coupled groundwater flow and transport: 2. Thermohaline and 3D convection systems. Advances in Water Resources, 21, 401-425.

Diersch, H. and O. Kolditz. 2002. Variable-density flow and transport in porous media: approaches and challenges. Advances in Water Resources, 25, 899-944.

Eugster, H.P., C.E. Harvie and J.H. Weare. 1980. Mineral equilibria in a six-component seawater system, Na-K-Mg-Ca-SO_4-Cl-H_2O, at 25°C. Geochimica et Cosmochimica Acta, 44, 1335-1347.

Frind, E. 1982. Simulation of long-term transient density-dependent transport in groundwater. Advances in Water Resources, 5, 73-88.

Frolkovic, P. 1999. Discretization. In: Fein E, editor. d3f - a simulator for density-driven flow. Gesellschaft fuer Anlagen-und Reaktorsicherheit, Braunschweig .

Frolkovic, P. and H.D. Schepper. 2001. Numerical modeling of convection dominated transport with density driven flow in porous media. Advances in Water Resources, 24, 63-72.

Geiger, S., T. Driesner, C. Heinrich and S. Matthai. 2006. Multiphase thermohaline convection in the Earth's crust: II. Benchmarking and application of a finite element-finite volume solution technique with a NaCl-H_2O equation of state. Transport In Porous Media, 63, 435-461.

Gelhar, L. and M. Collins. 1971. General analysis of longitudinal dispersion in nonuniform flow. Water Resources Research, 7, 1511-1521.

Grasby, S., K. Osadetz, R. Betcher and F. Render. 2000. Reversal of the regional-scale flow system of the Williston basin in response to Pleistocene glaciation. Geology, 28, 635-638.

Grasby, S. and Z. Chen. 2005. Subglacial recharge into the Western Canada Sedimentary Basin. Impact of Pleistocene glaciation on basin hydrodynamics. GSA Bulletin, 117, 500-514.

Greenberg, J.P. and N. Möller. 1989. The prediction of mineral solubilities in natural-waters - A chemical-equilibrium model for the Na-K-Ca-Cl-SO_4-H_2O system to high-concentration from 0^o to 250^oC. Geochimica et Cosmochimica Acta, 53, 2503-2518.

Guo, W. and C. Langevin. 2002. User's Guide to SEAWAT: A Computer program for simulation of three-dimensional variable-density ground-water flow. U.S. Geological Survey, Techniques of Water-Resources Investigations Book 6, Chapter A7, 77p.

Hanor, J. 1987. Origin and migration of subsurface sedimentary brines. Soc. Sediment. Geol. Short Course 21, Soc. of Econ. Paleontol. and Mineral., Tulsa, Okla.

Hanor, J.S. 2001. Reactive transport involving rock-buffered fluids of varying salinity. Geochimica et Cosmochimica Acta, 65, 3721-3732.

Hardie, L. 1987. Dolomitization: A critical view of some current views. Journal of Sedimentary Petrology, 57, 166-183.

Harrison, W., G. Grammer and D. Barnes. 2009. Reservoir characteristics of the Bass Islands dolomite in Otsego County, Michigan: Results for a saline reservoir CO_2 sequestration demonstration. Environmental Geosciences, 16, 139-151.

Harvie, C.E., H.P. Eugster and J.H. Weare. 1982. Mineral equilibria in the six-component seawater system, Na-K-Mg-Ca-SO_4-Cl-H_2O at 25^oC. II: Compositions of the saturated solutions. Geochimica et Cosmochimica Acta, 46, 1603-1618.

Harvie, C.E., N. Moller and J.H. Weare. 1984. The prediction of mineral solubilities in natural waters: The Na-K-Mg-Ca-H-Cl-SO_4-OH-HCO_3-CO_3-CO_2-H_2O system to high ionic strengths at 25^oC. Geochimica et Cosmochimica Acta, 48, 723-751.

Haung, H.H. 1989. Estimation of Pitzer ion interaction parameters for electrolytes involved in complex-formation using a chemical-equilibrium model. Journal of Solution Chemistry, 18, 1069-1084.

He, S. and J.W. Morse. 1993. Prediction of halite, gypsum, and anhydrite solubility in natural brines under subsurface conditions. Computers & Geosciences, 19, 1-22.

Henderson, T., K.U. Mayer, B. Parker and T. Al. 2009. Three-dimensional density-dependent flow and multicomponent reactive transport modeling of chlorinated solvent oxidation by potassium permanganate. Journal of Contaminant Hydrology, 106, 195-211.

Henry, H.R. 1964. Effects of dispersion on salt encroachment in coastal aquifers. U.S. Geological Survey Water Supply Paper, 1613-C, 70-84.

Henry, H. and J. Hilleke. 1972. Exploration of multiphase fluid flow in a saline aquifer system affected by geothermal heating. Bureau of Engineering Research, Report No. 150-118, University of Alabama, U.S. Geological Survey Contract No. 14-08-0001-12681, National Technical Information Service Publication No. PB234233, 105 pp.

Hobbs, M., S. Frape, O. Shouakar-Stash and L. Kennell. 2011. Regional Hydrogeochemistry, Southern Ontario. Nuclear Waste Management Organization Report. NWMO DGR-TR-2011-12 R000. Toronto, Canada.

Hughes, J. D. and W.E. Sanford. 2005. SUTRA-MS a Version of SUTRA Modified to Simulate Heat and Multiple-Solute Transport. U.S. Geological Survey Open-File Report 2004-1207, 141 pp.

Kharaka, Y., W. Gunter, P. Aggarwal, E. Perkins and J. Debraal. 1988. SOLMINEQ.88: A computer program for geochemical modeling of water-rock interactions. U.S. Geological Survey Report 88-4227.

Kleinberg, R. and D. Griffin. 2005. NMR measurements of permafrost: Unfrozen water assay, pore-scale distribution of ice, and hydraulic permeability of sediments. Cold Regional Science Technology, 42, 63-77.

Krumgalz, B.S. 2001. Application of the Pitzer ion interaction model to natural hypersaline brines. Journal of Molecular Liquids, 91, 3-19.

Lemieux, J.M., E.A. Sudicky, W.R. Peltier and L. Tarasov. 2008. Simulating the impact of glaciations on continental groundwater flow systems: 1. Relevant processes and model formulation. Journal of Geophysical Research-Earth Surface, 113, Article No. F03017, 12 p.

Lever, D.A. and C. Jackson. 1985. On the equations for the flow of concentrated salt solution through a porous medium. U.K. DOE Report No. DOE/RW/85.100.

Magaritz, M. and L. Goldenberg. 1980. Dolomite formation in the seawater-freshwater interface. Nature, 287, 622-624.

Marion, G.M. 2002. A molal-based model for strong acid chemistry at low temperatures (< 200 to 298 K). Geochimica et Cosmochimica Acta, 66, 2499-2516.

Marion, G.M., D.C. Catling and J.S. Kargel. 2003. Modeling aqueous ferrous iron chemistry at low temperatures with application to Mars. Geochimica et Cosmochimica Acta, 67, 4251-4266.

Mayer, K.U., E.O. Frind and D.W. Blowes. 2002. Multicomponent reactive transport modeling in variably saturated porous media using a generalized formulation for kinetically controlled reactions. Water Resources Research, 38, 1174.

Mayer, K.U. and K. MacQuarrie. 2007. Reactive transport modelling in sedimentary rock: State-of-science review. Nuclear Waste Management Organization Technical Report NWMO TR-2007-12. 39p. Toronto, Canada. (Available at www.nwmo.ca)

Mazurek, M. 2004. Long-term used fuel waste management - Geoscientific review of the sedimentary sequence in southern Ontario. Background Paper 6-12 prepared by Rock-Water Interactions, Institute of Geological Sciences, University of Bern for the Nuclear Waste Management Organization. (Available at www.nwmo.ca)

McIntosh, J.C. and L.M. Walter. 2005. Volumetrically significant recharge of Pleistocene glacial meltwaters into epicratonic basins: Constraints imposed by solute mass balances. Chemical Geology, 222, 292-309.

McIntosh, J.C. and L.M. Walter. 2006. Paleowaters in Silurian-Devonian carbonate aquifers: Geochemical evolution of groundwater in the Great Lakes region since the Late Pleistocene. Geochimica et Cosmochimica Acta, 70, 2454-2479.

McIntosh, J.C., G. Garven and J. Hanor. 2011. Impacts of Pleistocene glaciation on large-scale groundwater flow and salinity in the Michigan Basin. Geofluids, 11, 18-33.

Medina, C.R., J.A. Rupp and D.A. Barnes. 2011. Effects of reduction in porosity and permeability with depth on storage capacity and injectivity in deep saline aquifers: A case study from the Mount Simon Sandstone aquifer. International Journal of Greenhouse Gas Control, 5, 146-156.

Millero, F.J. 1982. The effect of pressure on the solubility of minerals in water and seawater. Geochimica et Cosmochimica Acta, 46, 11-22.

Monnin, C. 1994. Density calculation and concentration scale conversions for natural waters. Computers & Geosciences, 20, 1435-1445.

Neuzil, C. 2003. Hydromechanical coupling in geologic processes. Hydrogeology Journal, 11, 41-83.

Normani, S. 2009. Paleoevolution of pore fluids in glaciated geologic settings. PhD dissertation, University of Waterloo, Waterloo, Ontario, Canada.

Oldenburg, C. and K. Pruess. 1999. Plume separation by transient thermohaline convection in porous media. Geophysical Research Letters, 26, 2997-3000.

Oldenburg, C. and K. Pruess. 1995. Radionuclide Transport for TOUGH2. Lawrence Berkeley National Laboratory Report LBL-34868.

Park, Y., E. Sudicky and J. Sykes. 2009. Effects of shield brine on the safe disposal of waste in deep geologic environments. Advances in Water Resources, 32, 1352-1358.

Parkhurst, D., K. Kipp, P. Engesgaard and S. Charlton. 2005. PHAST-A program for simulating ground-water flow, solute transport, and multicomponent geochemical reactions. Geochimica et Cosmochimica Acta, 69, A156-A156.

Parkhurst, D. and C. Appelo. 1999. User's Guide to PHREEQC (Version 2). A computer program for speciation, batch-reaction, one-dimensional transport, and inverse geochemical calculations. U.S. Geological Survey Water-Resources Investigations Report 99-4259, 312 p.

Peltier, W.R. 2011. Long-term Climate Change. Nuclear Waste Management Organization Report NWMO DGR-TR-2011-14 R000. Toronto, Canada.

Person, M., J. McIntosh, V. Bense and V.H. Remenda. 2007. Pleistocene hydrology of North America: The role of ice sheets in reorganizing groundwater flow systems. Reviews of Geophysics, 45, RG3007.

Person, M., J. Raffensperger, S. Ge and G. Garven. 1996. Basin-scale hydrogeologic modeling. Reviews of Geophysics, 34, 61-87.

Pitzer, K.S. 1973. Thermodynamics of electrolytes. I. Theoretical basis and general equations. Journal of Physical Chemistry, 77, 268-277.

Post, V., H. Kooi and C. Simmons. 2007. Using hydraulic head measurements in variable-density ground water flow analyses. Ground Water, 45, 664-671.

Raven, K., K. Novakowski, R. Yager and R. Heystee. 1992. Supernormal fluid pressures in sedimentary rocks of southern Ontario-western New York State. Canadian Geotechnical Journal, 29, 80-93.

Reardon, E.J. 1988. Ion interaction parameters for $AlSO_4$ and application to the prediction of metal sulfate solubility in binary salt systems. Journal of Physical Chemistry, 92, 6426-6431.

Risacher, F. and A. Clement. 2001. A computer program for the simulation of evaporation of natural waters to high concentration. Computers & Geosciences, 27, 191-201.

Saaltink, M.W., J. Carrera and C. Ayora. 2001. On the behavior of approaches to simulate reactive transport. Journal of Contaminant Hydrology, 48, 213-235.

Simpson, M.J, and T.P. Clement. 2003. Theoretical analysis of the worthiness of Henry and Elder problems as benchmarks of density-dependent groundwater flow models. Advances in Water Resources, 26, 17-31.

Simpson, M.J. and T.P. Clement. 2004. Improving the worthiness of the Henry problem as a benchmark for density-dependent groundwater flow models. Water Resources Research, 40, W01504, doi:10.1029/2003WR002199.

Simunek, J. and D.L. Suarez. 1994. 2-Dimensional transport model for variably saturated porous-media with major ion chemistry. Water Resources Research, 30, 1115-1133.

Strąpoć, D., M. Mastalerz, A. Schimmelmann, A. Drobiniak and N.R. Hasenmueller. 2010. Geochemical constraints on the origin and volume of gas in the New Albany Shale (Devonian-Mississippian), eastern Illinois Basin. AAPG Bulletin, 94, 1713-1740.

Sykes, J., E. Sykes, S. Normani and Y. Yin. 2011. Hydrogeologic Modelling. Nuclear Waste Management Organization Report NWMO DGR-TR-2011-16-R00, Toronto, Canada.

Tosca, N., S. McLennan, B. Clark, J. Grotzinger, J. Hurowitz, A. Knoll, C. Schroder and S. Squyres. 2005. Geochemical modeling of evaporation processes on Mars: Insight from the sedimentary record at Meridiani Planum. Earth and Planetary Science Letters, Sedimentary Geology at Meridiani Planum, Mars, 240, 122-148.

USDOE (United States Department of Energy). 2007. In-drift precipitates/salts model. Argonne National Laboratory Report EBS-MD-000045 REV 03. Chicago, USA.

Van der Veen, C. J. 1999. Fundamentals of Glacier Dynamics. A.A. Balkema, Rotterdam, the Netherlands. 462p.

Voss, C. 1984. A finite-element simulation model for saturated-unsaturated, fluid-density-dependent ground-water flow with energy transport or chemically-reactive single-species

solute transport. U.S. Geological Survey Water-Resources Investigations Report 84-4369, 409p.

Voss, C. and A. Provost. 2008. SUTRA-A model for saturated-unsaturated, variable-density ground-water flow with solute or energy transport. U.S. Geological Survey Water-Resources Investigations Report 02-4231, 250p.

Voss, C. and W. Souza. 1987. Variable density flow and solute transport simulation of regional aquifers containing a narrow freshwater-saltwater transition zone. Water Resources Research, 23, 1851-1866.

Walsh, R. and J. Avis. 2010. Glaciation scenario: Groundwater flow and radionuclide transport studies, Nuclear Waste Management Organization Technical Report NWMO TR-2010-09. 126p. Toronto, Canada. (Available at www.nwmo.ca)

Westjohn, D.B. and T.L. Weaver. 1998. Hydrogeologic framework of the Michigan Basin regional aquifer system. U.S. Geological Survey Professional Paper PP 1418.

Wolery, T. and R. Jarek. 2003. Software user's manual. EQ3/6, Version 8.0. Sandia National Laboratories. U.S. Dept. of Energy Report.

Zhang, G. X., Z.P. Zheng and J.M. Wan. 2005. Modeling reactive geochemical transport of concentrated aqueous solutions. Water Resources Research, 41, W02018, doi:10.1029/2004WR003097.

THIS PAGE HAS BEEN LEFT BLANK INTENTIONALLY

APPENDIX A: NUMERICAL FORMULATION FOR VERTICAL STRESS

CONTENTS

Page

A.1 INTRODUCTION

The implementation of vertical stress in MIN3P-NWMO follows the formulation by Neuzil (2003). A hydrodynamic term ($\zeta\, \partial\sigma_{zz}/\partial t$) acts as a fluid source/sink term to effectively increase or decrease the fluid pore pressure based on the temporal rate of change of vertical stress $\partial\sigma_{zz}/\partial t$, the pressure-based specific storage coefficient S_p, and the one-dimensional loading efficiency coefficient ζ. This formulation does not account for the geometric deformation of the spatial grid as a mechanical load is applied.

A.2 GOVERNING EQUATIONS AND IMPLEMENTATION

The fluid mass conservation is defined as:

$$\frac{\partial \phi \rho}{\partial t} = -\nabla \cdot \rho \frac{\mathbf{K}}{\mu}\left(\nabla P_a + \rho g\right) + \rho Q \qquad \text{Equation A-1}$$

where ϕ is the porosity [-], ρ is the fluid density [M L^{-3}], t is time [T], **K** is the permeability tensor [L^2], μ is the dynamic fluid viscosity [M L^{-1} T^{-1}], P_a is the fluid pressure [M L^{-1} T^{-2}], g is the gravity constant [L T^{-2}], and Q is the volumetric fluid source/sink term [T^{-1}].

The storage term in Equation A-1 (left hand side) can be expanded as:

$$\frac{\partial \phi \rho}{\partial t} = \phi \frac{\partial \rho}{\partial t} + \rho \frac{\partial \phi}{\partial t} = \rho \frac{\partial \phi}{\partial \sigma_e} \frac{\partial \sigma_e}{\partial t} + \phi \frac{\partial \rho}{\partial P_a} \frac{\partial P_a}{\partial t} + \phi \left.\frac{\partial \rho}{\partial t}\right|_{C,T} \qquad \text{Equation A-2}$$

where $\frac{\partial \rho}{\partial P_a}$ [L^2 T^2], accounts for density changes induced by fluid pressure, whereas $\left.\frac{\partial \rho}{\partial t}\right|_{T,C}$ [M L^{-3} T^{-1}] accounts for temporal density changes by temperature and concentrations.

In the vertical stress formulation, effective stress (σ_e, [M L^{-1} T^{-2}]) is defined as the difference between liquid pressure (P_a) and total vertical stress (σ_v, [M L^{-1} T^{-2}]):

$$\sigma_e = \sigma_v - P_a \qquad \text{Equation A-3}$$

Its derivative with respect to time is:

$$\frac{\partial \sigma_e}{\partial t} = \frac{\partial \sigma_v}{\partial t} - \frac{\partial P_a}{\partial t} \qquad \text{Equation A-4}$$

Rock and fluid compressibilities are defined as (Bear, 1979):

$$\frac{\partial \phi}{\partial \sigma_e} = -\left[\frac{1}{K} - \frac{1}{K_S}\right] \qquad \text{Equation A-5}$$

$$\frac{\partial \rho}{\partial P_a} = \rho\left[\frac{1}{K_f} - \frac{1}{K_s}\right] \qquad \text{Equation A-6}$$

where K is the bulk modulus of the porous medium [$M\ L^{-1}\ T^{-2}$], K_s is the bulk modulus of the solid grains [$M\ L^{-1}\ T^{-2}$], and K_f is the fluid bulk modulus [$M\ L^{-1}\ T^{-2}$]. By substituting Equation A-4, Equation A-5 and Equation A-6 into Equation A-2, we obtain:

$$\frac{\partial \phi \rho}{\partial t} = \rho\left(\left[\frac{1}{K} - \frac{1}{K_s}\right] + \phi\left[\frac{1}{K_f} - \frac{1}{K_s}\right]\right)\frac{\partial P_a}{\partial t} - \rho\left[\frac{1}{K} - \frac{1}{K_s}\right]\frac{\partial \sigma_v}{\partial t} + \phi\frac{\partial \rho}{\partial t}\bigg|_{C,T} \qquad \text{Equation A-7}$$

We can now define the three-dimensional pressure-based specific storage coefficient (S_{p3}, [$M^{-1}\ L\ T^2$]) and the three-dimensional loading efficiency coefficient (i.e. Skempton's coefficient β,[-]):

$$S_{p3} = \left[\frac{1}{K} - \frac{1}{K_S}\right] + \phi\left[\frac{1}{K_f} - \frac{1}{K_S}\right] \qquad \text{Equation A-8}$$

$$\beta = \frac{\left[\frac{1}{K} - \frac{1}{K_s}\right]}{S_{p3}} \qquad \text{Equation A-9}$$

By substituting Equation A-8 and A-9 into Equation A-7, we obtain:

$$\frac{\partial \phi \rho}{\partial t} = \rho S_{p3}\left(\frac{\partial P_a}{\partial t} - \beta\frac{\partial \sigma_v}{\partial t}\right) + \phi\frac{\partial \rho}{\partial t}\bigg|_{C,T} \qquad \text{Equation A-10}$$

For the simplifying assumption of purely vertical stress (σ_{zz}), Equation A-10 can be approximated as (Neuzil, 2003):

$$\frac{\partial \phi \rho}{\partial t} = \rho S_p\left(\frac{\partial P_a}{\partial t} - \zeta\frac{\partial \sigma_{zz}}{\partial t}\right) + \phi\frac{\partial \rho}{\partial t}\bigg|_{T,C} \qquad \text{Equation A-11}$$

where S_p [M^{-1} L T^2] is the one-dimensional pressure-based specific storage coefficient (see Henderson et al., (2009) for the relationship between pressure-based specific storage coefficient S_p and specific storage coefficient S_s) and ζ [-] is the one-dimensional efficiency loading coefficient. For details on the derivation of this simplification we refer to Neuzil (2003). The full fluid mass conservation equation implemented in MIN3P-NWMO is obtained by substituting Equation A-11 into Equation A-1:

$$\rho S_p\left(\frac{\partial P_a}{\partial t}-\zeta\frac{\partial \sigma_{zz}}{\partial t}\right)+\phi\left.\frac{\partial \rho}{\partial t}\right|_{T,C}=-\nabla\cdot\rho\frac{K}{\mu}\left(\nabla P_a+\rho g\right)+\rho Q \qquad \text{Equation A-12}$$

Under equilibrium conditions when $\sigma_e=\sigma_{zz}-P_a=0$, the one-dimensional efficiency loading coefficient (ζ) in Equation A-12 can be arranged as:

$$\frac{\partial P_a}{\partial t}-\zeta\frac{\partial \sigma_{zz}}{\partial t}=0 \qquad \text{Equation A-13}$$

with

$$\zeta=\frac{\dfrac{\partial P_a}{\partial t}}{\dfrac{\partial \sigma_{zz}}{\partial t}}\approx\frac{\Delta P_a}{\Delta \sigma_{zz}} \qquad \text{Equation A-14}$$

The one-dimensional efficiency loading coefficient (ζ) is now expressed as the ratio of the change in fluid pressure to the change in vertical load under conditions of lateral confinement. As shown above, ζ is a function of the mechanical properties of the porous medium, and under the same vertical load, significant changes in P_a are to be expected in geological units with ζ close to one (i.e. deformable units), whereas small changes are expected in units with a low potential for deformation (i.e. ζ close to zero).

A.3 REFERENCES

Bear, J. 1979. Hydraulics of Groundwater. New York, McGraw-Hill Book Company.

Henderson, T., K.U. Mayer, B. Parker and T. Al. 2009. Three-dimensional density-dependent flow and multicomponent reactive transport modeling of chlorinated solvent oxidation by potassium permanganate. Journal of Contaminant Hydrology, 106, 195-211.

Neuzil, C. 2003. Hydromechanical coupling in geologic processes. Hydrogeology Journal, 11, 41-83.

APPENDIX B: NUMERICAL FORMULATION FOR SIMULATING FLOW AND MULTICOMPONENT REACTIVE TRANSPORT IN BRINES

CONTENTS

Page

LIST OF TABLES

Page

B.1 INTRODUCTION

The calculation of aqueous speciation and mineral solubilities in brines requires the evaluation of activity coefficients that are valid under high ionic strength conditions. In addition, empirical relationships to calculate fluid densities as a linear function of Total Dissolved Solids (TDS) break down for these concentrated solutions, and more sophisticated approaches are needed. This appendix describes the formulations used to calculate activity coefficients and the solution density based on the Pitzer equations (1973) and documents the Pitzer database as implemented in MIN3P-NWMO.

B.2 ACTIVITY COEFFICIENT CALCULATIONS BASED ON PITZER EQUATIONS

This section describes the HMW model (Harvie et al., 1984), an implementation of the Pitzer (1973) equations, as it is formulated in MIN3P-NWMO. The HMW model consists of a set of polynomial equations for water activity (a_w), the osmotic coefficient (ϕ), the activity coefficients of cations (γ_C), anions (γ_A), and neutral species (γ_N). These equations are expressed in compact matrix form, which eliminates the need to discriminate between cations, anions, and neutral species (see Bea et al., 2010).

The vector of species molalities ($\mathbf{m}$) is the input for this algorithm. The vector of activity coefficients ($\boldsymbol{\gamma}$) is computed according to:

$$\ln\boldsymbol{\gamma} = \left(\ln\gamma_{DH} + q'\right)\mathbf{z^2} + q^c\mathbf{z} + \left(2\mathbf{Q} + Z\mathbf{C}\right)\mathbf{m} + \mathbf{m}^t\mathbf{T}\mathbf{m} \qquad \text{Equation B-1}$$

$\mathbf{z}$ and $\mathbf{z^2}$ are the vectors of electric charge and squared electric charge, respectively. The modified Debye-Hückel terms (γ_{DH}), in Equation B-1, are defined according to Harvie et al. (1984):

$$\ln\gamma_{DH} = -A^{\phi}\left[\frac{\sqrt{I}}{1+b\sqrt{I}} + \frac{2}{b}\ln\left(1+b\sqrt{I}\right)\right] \qquad \text{Equation B-2}$$

where A^{ϕ} is the one third Debye-Hückel slope (A^{ϕ}=0.392 at 25^{o}C, Pitzer and Mayorga, 1973), I is ionic strength, and b is a Debye-Hückel parameter (for all electrolytes b=1.2).

The activity of water (a_W) is computed from the osmotic coefficient ϕ (Felmy and Weare, 1986):

$$\ln a_W = -\phi MW \qquad \text{Equation B-3}$$

where W is the molecular weight of water [kg mol^{-1}]. The osmotic coefficient is defined as:

$$\phi = \frac{2}{M}\left(f'(I) + q^{\phi} + Zq^{c} + q^{L} + t\right) + 1$$ Equation B-4

Ionic strength (I) and Z account for the effect of the electric charge in the electrolytic solution and are computed according to:

$$I = \frac{1}{2}\mathbf{z}_{\mathbf{2}}^{\mathbf{t}}\mathbf{m}$$ Equation B-5

$$Z = \mathbf{z}_{\mathbf{abs}}^{\mathbf{t}}\mathbf{m}$$ Equation B-6

where $\mathbf{z}_{\mathbf{2}}^{\mathbf{t}}$ and $\mathbf{z}_{\mathbf{abs}}^{\mathbf{t}}$ are the transpose of the square and absolute electric charge vectors, respectively. The total molar mass of solutes (M) in the water activity expression in Equation B-3 is calculated as:

$$M = \mathbf{1}_{\mathbf{N_{aq}}}^{\mathbf{t}}\mathbf{m}$$ Equation B-7

where $\mathbf{1}_{\mathbf{N_{aq}}}^{\mathbf{t}}$ is the unity vector of dimension N_{aq}. Scalars q', q^{ϕ}, q^{c} and q^{L} in Equation B-1 and Equation B-4 represent the contributions of binary interactions. They are computed from:

$$q' = \mathbf{m}^{\mathbf{t}}\mathbf{Q'}\mathbf{m}$$ Equation B-8

$$q^{\phi} = \mathbf{m}^{\mathbf{t}}\mathbf{Q}^{\phi}\mathbf{m}$$ Equation B-9

$$q^{c} = \mathbf{m}^{\mathbf{t}}\mathbf{C}\mathbf{m}$$ Equation B-10

$$q^{L} = \mathbf{m}^{\mathbf{t}}\mathbf{Q}^{\mathbf{L}}\mathbf{m}$$ Equation B-11

The last term in Equation B-1 and the scalar t in Equation B-4 account for ternary interactions. The scalar t is given by:

$$t = \mathbf{m}^{\mathbf{t}}\mathbf{m}^{\mathbf{t}}\mathbf{T}\mathbf{m}$$ Equation B-12

Matrices $\mathbf{Q}$, $\mathbf{Q'}$, $\mathbf{Q}^{\phi}$, $\mathbf{Q}^{\mathbf{L}}$ and $\mathbf{C}$ are square and symmetric [$N_{aq} \times N_{aq}$].These matrices include submatrices for interactions between cations (c), anions (a) and neutral species (n):

$$\mathbf{Q}(I)=\begin{bmatrix} \mathbf{\Phi_{cc`}} & \frac{1}{2}\mathbf{B^{t}_{ca}} & \frac{1}{2}\mathbf{L^{t}_{nc}} \\ \frac{1}{2}\mathbf{B_{ca}} & \mathbf{\Phi_{aa`}} & \frac{1}{2}\mathbf{L^{t}_{na}} \\ \frac{1}{2}\mathbf{L_{nc}} & \frac{1}{2}\mathbf{L_{na}} & 0 \end{bmatrix}$$ Equation B-13

$$\mathbf{Q'}(I)=\begin{bmatrix} \mathbf{\Phi'_{cc`}} & \frac{1}{2}\mathbf{B^{t}_{ca}} & 0 \\ \frac{1}{2}\mathbf{B'_{ca}} & \mathbf{\Phi'_{aa`}} & 0 \\ 0 & 0 & 0 \end{bmatrix}$$ Equation B-14

$$\mathbf{Q^{\phi}}(I)=\begin{bmatrix} \mathbf{\Phi}^{\varphi}_{cc'} & \frac{1}{2}\mathbf{B^{\varphi t}_{ca}} & 0 \\ \frac{1}{2}\mathbf{B}^{\varphi}_{\mathbf{ca}} & \mathbf{\Phi}^{\phi}_{aa'} & 0 \\ 0 & 0 & 0 \end{bmatrix}$$ Equation B-15

$$\mathbf{Q^{L}}=\begin{bmatrix} 0 & 0 & \frac{1}{2}\mathbf{L^{t}_{nc}} \\ 0 & 0 & \frac{1}{2}\mathbf{L^{t}_{na}} \\ \frac{1}{2}\mathbf{L_{nc}} & \frac{1}{2}\mathbf{L_{na}} & 0 \end{bmatrix}$$ Equation B-16

$$\mathbf{C}=\begin{bmatrix} 0 & \mathbf{C^{t}_{ca}} & 0 \\ \mathbf{C_{ca}} & 0 & 0 \\ 0 & 0 & 0 \end{bmatrix}$$ Equation B-17

Submatrices **B** in Equation B-13, Equation B-14, and Equation B-15 account for ionic interactions between ions of opposite charge. Submatrices **Φ** represent interactions between ions with the same electric charge. **L** accounts for interactions between neutral and charged species, while submatrices **C** account for ternary interactions (Pitzer and Mayorga, 1973).

The elements of submatrices **B** in Equation B-13, Equation B-14, and Equation B-15 are defined as (Pitzer, 1973):

$$\mathbf{B_{ca}} \Rightarrow B_{ij}=\beta^{(0)}_{ij}+\beta^{(1)}_{ij}g\left(\alpha_1\sqrt{I}\right)+\beta^{(2)}_{ij}g\left(\alpha_2\sqrt{I}\right)$$ Equation B-18

$$\mathbf{B'_{ca}} \Rightarrow B'_{ij}=\beta^{(1)}_{ij}\frac{g'\left(\alpha_1\sqrt{I}\right)}{I}+\beta^{(2)}_{ij}\frac{g'\left(\alpha_2\sqrt{I}\right)}{I}$$ Equation B-19

$$\mathbf{B}_{\mathbf{ca}}^{\varphi} \Rightarrow B_{ij}^{\phi} = \beta_{ij}^{(0)} + \beta_{ij}^{(1)} e^{-\alpha_1 \sqrt{I}} + \beta_{ij}^{(2)} e^{-\alpha_2 \sqrt{I}}$$ Equation B-20

where $\beta_{ij}^{(0)}$, $\beta_{ij}^{(1)}$, $\beta_{ij}^{(2)}$ are experimental coefficients. They are read from the virial coefficients database.

The functions g and g' in Equation B-18 and B-19 are a function of the ionic strength:

$$g(x) = 2\frac{\left(1-(1+x)e^{-x}\right)}{x^2}$$ Equation B-21

$$g'(x) = -2\frac{\left(1-\left(1+x+\frac{x^2}{2}\right)e^{-x}\right)}{x^2}$$ Equation B-22

with $x = \alpha_1\sqrt{I}$ or $x = \alpha_2\sqrt{I}$. When either ion in the couple ij is monovalent $\alpha_1 = 2$. For 2−2 or higher valence pairs, $\alpha_1 = 1.4$. For all electrolytes $\alpha_2 = 12$.

Higher-order ionic interactions are accounted by the submatrices $\mathbf{\Phi}$ in Equation B-13, Equation B-14 and Equation B-15. These matrices account for the effect of unsymmetrical mixing solutions between ions of the same charge (i.e. + + or − −) and are computed according to Pitzer (1975):

$$\mathbf{\Phi}_{\mathbf{cc'}}^{\phi}, \mathbf{\Phi}_{\mathbf{aa'}}^{\phi} \Rightarrow \phi_{ij}^{\phi} = \theta_{ij} + \theta_{ij}^{E}(I) + I\theta_{ij}^{E'}(I)$$ Equation B-23

$$\mathbf{\Phi}_{\mathbf{cc'}}, \mathbf{\Phi}_{\mathbf{aa'}} \Rightarrow \phi_{ij} = \theta_{ij} + \theta_{ij}^{E}(I)$$ Equation B-24

$$\mathbf{\Phi}_{\mathbf{cc'}}^{'}, \mathbf{\Phi}_{\mathbf{aa'}}^{'} \Rightarrow \phi_{ij}^{'} = \theta_{ij}^{E'}(I)$$ Equation B-25

where θ_{ij} are experimentally determined parameters, and $\theta_{ij}^{E}(I)$ and $\theta_{ij}^{E'}(I)$ are a function of ionic strength and the electrolyte pair type:

$$\theta_{ij}^{E}(I) = \left(\frac{z_i z_j}{4I}\right)\left(J(X_{ij}) - \frac{1}{2}J(X_{ii}) - \frac{1}{2}J(X_{jj})\right)$$ Equation B-26

$$\theta_{ij}^{E'}(I) = -\left(\frac{\theta_{ij}^{E}(I)}{I}\right) + \left(\frac{z_i z_j}{8I^2}\right)\left(J'(X_{ij}) - \frac{1}{2}J'(X_{ii}) - \frac{1}{2}J'(X_{jj})\right)$$ Equation B-27

where $X_{ij} = 6 z_i z_j A^{\phi} \sqrt{I}$ and z_i and z_j are the electric charge of i^{th} and j^{th} ion, respectively. To evaluate the functions J in Equation B-26, we can use two polynomial approximations presented by Pitzer (1975) for a broad range of X_{ij} values ($0.1 \le X_{ij} \le 80$):

$$J(X_{ij}) = -\frac{1}{6} X_{ij}^2 \ln(X_{ij}) e^{-10 X_{ij}^2} + \frac{1}{\sum_{k=1}^{6} \frac{C_k}{X_{ij}^k}}$$ Equation B-28

For $X_{ij} > 80$, Pitzer (1975) suggests:

$$J(X_{ij}) = \frac{X_{ij}}{4 + \frac{C_1}{X_{ij}^{C_2}} e^{-C_3 X_{ij}^{C_4}}}$$ Equation B-29

For the definition of the parameters C_k, we refer to Pitzer (1975). $J'(X_{ij})$ in Equation B-27 is the derivative of $J(X_{ij})$ as defined by Equation B-28 and Equation B-29 ($J'(X_{ij}) = dJ(X_{ij}) / dX_{ij}$).

The elements of submatrix $\mathbf{C_{ca}}$ in Equation B-17 do not depend on ionic strength and are defined as (Pitzer and Mayorga, 1973):

$$\mathbf{C_{ca}} \Rightarrow C_{ij} = \frac{C_{ij}^{\phi}}{2\sqrt{|z_i z_j|}}$$ Equation B-30

where C_{ij} are experimentally determined coefficients. **T** in Equation B-1 is a third order tensor $[N_{aq} \times N_{aq} \times N_{aq}]$ with the following structure:

$$\mathbf{T} = \begin{bmatrix} \mathbf{T_c} \\ \mathbf{T_a} \\ \mathbf{T_n} \end{bmatrix} = \begin{bmatrix} 0 & 0 & 0 \\ 0 & \Psi_{aa'ci} & 0 \\ 0 & 0 & 0 \\ . & . & . \\ . & . & . \\ \Psi_{cc'ai} & 0 & 0 \\ 0 & 0 & 0 \\ 0 & 0 & 0 \\ . & . & . \\ . & . & . \\ \Psi_{cc'ni} & 0 & 0 \\ 0 & \Psi_{aa'ni} & 0 \\ 0 & 0 & 0 \end{bmatrix} \qquad \text{Equation B-31}$$

Submatrices $\mathbf{\Psi}$ contain experimental information and are read from a virial coefficient data base.

B.3 SCALED MACINNES CONVENTION

Individual ion activities and activity coefficients cannot be determined separately. Individual ion activities and activity coefficients have a meaning only in a relative sense and individual values depend on a particular choice of scale convention. A common approach is the MacInnes convention (MacInnes, 1919). For example, the activity coefficient of Cl^- in KCl solution is defined as being equal to the mean activity coefficient of KCl in a KCl solution of equivalent ionic strength, $\gamma^M_{Cl} \equiv \gamma^M_{\pm KCl}$. The scaling factor ($f_i^M$) for the i^{th} ion in KCl solution is computed from:

$$f_i^M = \left[\frac{\gamma_{\pm KCl}}{\gamma_{\pm KCl}{}^M} \right]^{\frac{1}{z_i}} \qquad \text{Equation B-32}$$

The scaled activity coefficient for the i^{th} species (γ_i^M) is computed as:

$$\gamma_i^M = \gamma_i f_i^M \qquad \text{Equation B-33}$$

where γ_i is the activity coefficient for the i^{th} species.

B.4 DENSITY CALCULATIONS BASED ON PITZER EQUATIONS

The density of the aqueous phase is a key parameter in the modelling of mass transfer processes in a sedimentary basin. Solution density is commonly estimated by empirical relationships that derive the fluid density as a function of ionic strength, but independent of the fluid composition (e.g. Henderson et al., 2009). A more rigorous alternative that is based on the Pitzer equations is provided by Monnin (1994). Monnin (1994) determined the solution density based on the concentrations of the major ions in natural waters: Na, K, Ca, Mg, Cl, SO_4, HCO_3, and CO_3.

The total volume of the solution (which contains 1000 g of water) is:

$$V = V_{id} + V_{ex} = 1000\upsilon_w + \sum_i m_i \overline{V}_i^o + V_{ex} \qquad \text{Equation B-34}$$

where υ_w is the specific volume of pure water ($cm^3\ g^{-1}$), and $\overline{V}_i^o$ is the standard partial volume of the solute i ($cm^3\ mol^{-1}$). The term V_{ex} in Equation B-34 represents the total excess volume of a multicomponent electrolyte solution. It can be expressed as a virial expansion of the solute molalities:

$$\frac{V_{ex}}{RT} = f_{DH}^v(I) + 2\sum_c \sum_a m_c m_a \left(B_{ca}^v + \left(\sum_c m_c z_c \right) C_{ca}^v \right) \qquad \text{Equation B-35}$$

In this expression, R is the ideal gas constant and T the absolute temperature, m_c is the molality of cation c (of charge z_c), and m_a that of anion a. $f_{DH}^v(I)$ is the Debye-Hückel term:

$$f_{DH}^v(I) = \frac{A_v}{RT}\frac{I}{1.2}\ln\left(1 + 1.2\sqrt{I}\right) \qquad \text{Equation B-36}$$

in which I is the ionic strength and A_v the Debye-Hückel slope. B_{ca}^v is the second virial coefficients for the volume, depending on ionic strength (equivalent to Equation B-18 with slightly modified notation):

$$B_{ca}^v = \beta_{ca}^{(0),v} + \beta_{ca}^{(1),v} g\left(\alpha_1\sqrt{I}\right) + \beta_{ca}^{(2),v} g\left(\alpha_2\sqrt{I}\right) \qquad \text{Equation B-37}$$

The parameters α_1 and α_2 depend on the type of the electrolyte and are equal to 2.0 and 0.0, respectively for 1-1, 1-2 and 2-1 salts, and to 1.4 and 12.0 for 2-2 salts. $\beta_{ca}^{(0),v}$, $\beta_{ca}^{(1),v}$, $\beta_{ca}^{(2),v}$ and C_{ca}^v are empirical parameters specific to each salt. The functions g within Equation B-37 are defined by Equation B-21. The density of the solution (ρ) is computed according to:

$$\rho = \frac{1000 + \sum_i m_i W_i}{V} \qquad \text{Equation B-38}$$

where m_i and W_i are the molality and molecular weight ($g\ mol^{-1}$) of the i^{th} solute, respectively.

.

B.5 PITZER VIRIAL COEFFICIENTS DATA BASE FOR MODEL VERIFICATION

This section presents the Pitzer virial coefficients used in the reactive transport verification example described in **Appendix D.6**. The coefficients are based on the work from Harvie et al. (1984) and Greenberg and Möller (1989).

Table B. 1: Pitzer Virial Coefficients Used for Model Verification – Part 1

Cation	Anion	$\beta^{(0)}$	$\beta^{(1)}$	$\beta^{(2)}$	C^{φ}
Na^+	Cl^-	0.0765	0.2664	-	0.00127
K^+	Cl^-	0.04835	0.2122	-	-0.00084
Mg^{2+}	Cl^-	0.35235	1.6815	-	0.00519
Ca^{2+}	Cl^-	0.3159	1.614	-	-0.00034
$MgOH^+$	Cl^-	-0.1	1.658	-	-
H^+	Cl^-	0.1775	0.2945	-	0.0008
Na^+	Br^-	0.0973	0.2791	-	0.00116
K^+	Br^-	0.0569	0.2212	-	-0.0018
H^+	Br^-	0.196	0.3564	-	0.00827
Mg^{2+}	Br^-	0.4327	1.753	-	0.00312
Ca^{2+}	Br^-	0.3816	1.613	-	-0.00257
Na^+	SO_4^{2-}	0.01958	1.113	-	0.00497
K^+	SO_4^{2-}	0.04995	0.7793	-	-
Mg^{2+}	SO_4^{2-}	0.221	3.343	-37.23	0.025
Ca^{2+}	SO_4^{2-}	0.2	3.1973	-54.24	-
H^+	SO_4^{2-}	0.0298	-	-	-
Na^+	HSO_4^-	0.0454	0.398	-	-
K^+	HSO_4^-	-0.0003	0.1735	-	-
Mg^{2+}	HSO_4^-	0.4746	1.729	-	-
Ca^{2+}	HSO_4^-	0.2145	2.53	-	-
H^+	HSO_4^-	0.2065	0.5556	-	-
Na^+	OH^-	0.0864	0.253	-	0.0044
K^+	OH^-	0.1298	0.32	-	0.0041
Ca^{2+}	OH^-	-0.1747	-0.2303	-5.72	-
Na^+	HCO_3^-	0.0277	0.0411	-	-
Mg^{2+}	HCO_3^-	0.329	0.6072	-	-
K^+	HCO_3^-	0.0296	-0.013	-	-
Ca^{2+}	HCO_3^-	0.4	2.977	-	-
Na^+	CO_3^{2-}	0.0399	1.389	-	0.0044
K^+	CO_3^{2-}	0.1488	1.43	-	-0.0015

Table B. 2: Pitzer Virial Coefficients Used for Model Verification – Part 2

Ion	Ion	θ
K^+	Na^+	-0.012
Mg^{2+}	Na^+	0.07
Ca^{2+}	Na^+	0.07
H^+	Na^+	0.036
Ca^{2+}	K^+	0.032
H^+	K^+	0.005
Ca^{2+}	Mg^{2+}	0.007
H^+	Mg^{2+}	0.1
H^+	Ca^{2+}	0.092
SO_4^{2-}	Cl^-	0.02
HSO_4^-	Cl^-	-0.006
OH^-	Cl^-	-0.05
HCO_3^-	Cl^-	0.03
CO_3^{2-}	Cl^-	-0.02
OH^-	Br^-	-0.065
OH^-	SO_4^{2-}	-0.013
HCO_3^-	SO_4^{2-}	0.01
CO_3^{2-}	SO_4^{2-}	0.02
CO_3^{2-}	OH^-	0.1
CO_3^{2-}	HCO_3^-	-0.04
K^+	Na^+	-0.012
Mg^{2+}	Na^+	0.07
Ca^{2+}	Na^+	0.07
H^+	Na^+	0.036
Ca^{2+}	K^+	0.032
H^+	K^+	0.005
Ca^{2+}	Mg^{2+}	0.007
H^+	Mg^{2+}	0.1
H^+	Ca^{2+}	0.092
SO_4^{2-}	Cl^-	0.02

Table B. 3: Pitzer Virial Coefficients Used for Model Verification – Part 3

Ion	Neutral species	λ
Cl^-	CO_2(aq)	-0.012
Na^+	CO_2(aq)	0.07
K^+	CO_2(aq)	0.07
Ca^{2+}	CO_2(aq)	0.036
Mg^{2+}	CO_2(aq)	0.032
SO_4^{2-}	CO_2(aq)	0.005
HSO_4^-	CO_2(aq)	0.007

Table B. 4: Pitzer Virial Coefficients Used for Model Verification – Part 4

Ion	Ion	Ion	ψ
Na^+	K^+	Cl^-	-0.0018
Na^+	K^+	Br^-	-0.0022
Na^+	K^+	SO_4^{2-}	-0.01
Na^+	K^+	HCO_3^-	-0.003
Na^+	K^+	CO_3^{2-}	0.003
Na^+	Ca^{2+}	Cl^-	-0.007
Na^+	Ca^{2+}	SO_4^{2-}	-0.055
Na^+	Mg^{2+}	Cl^-	-0.012
Na^+	Mg^{2+}	SO_4^{2-}	-0.015
Na^+	H^+	Cl^-	-0.004
Na^+	H^+	Br^-	-0.012
Na^+	H^+	HSO_4^-	-0.0129
K^+	Ca^{2+}	Cl^-	-0.025
K^+	Mg^{2+}	Cl^-	-0.022
K^+	Mg^{2+}	SO_4^{2-}	-0.048
K^+	H^+	Cl^-	-0.011
K^+	H^+	Br^-	-0.021
K^+	H^+	SO_4^{2-}	0.197
K^+	H^+	HSO_4^-	-0.0265
Ca^{2+}	Mg^{2+}	Cl^-	-0.012
Ca^{2+}	Mg^{2+}	SO_4^{2-}	0.024
Ca^{2+}	H^+	Cl^-	-0.015
Mg^{2+}	$MgOH^+$	Cl^-	0.028
Mg^{2+}	H^+	Cl^-	-0.011
Mg^{2+}	H^+	HSO_4^-	-0.0178
Cl^-	SO_4^{2-}	Na^+	0.0014
Cl^-	SO_4^{2-}	Ca^{2+}	-0.018
Cl^-	SO_4^{2-}	Mg^{2+}	-0.004
Cl^-	HSO_4^-	Na^+	-0.006
Cl^-	HSO_4^-	H^+	0.013
Cl^-	OH^-	Na^+	-0.006
Cl^-	OH^-	K^+	-0.006
Cl^-	OH^-	Ca^{2+}	-0.025
Cl^-	HCO_3^-	Na^+	-0.015
Cl^-	HCO_3^-	Mg^{2+}	-0.096
Cl^-	CO_3^{2-}	Na^+	0.0085
Cl^-	CO_3^{2-}	K^+	0.004
SO_4^{2-}	HSO_4^-	Na^+	-0.0094
SO_4^{2-}	HSO_4^-	K^+	-0.0677
SO_4^{2-}	HSO_4^-	Mg^{2+}	-0.0425
SO_4^{2-}	OH^-	Na^+	-0.009
SO_4^{2-}	OH^-	K^+	-0.05
SO_4^{2-}	HCO_3^-	Na^+	-0.005
SO_4^{2-}	HCO_3^-	Mg^{2+}	-0.161
SO_4^{2-}	CO_3^{2-}	Na^+	-0.005

Table B.4: Pitzer Virial Coefficients Used for Model Verification – Part 4 (continued)

Ion	Ion	Ion	ψ
SO_4^{2-}	CO_3^{2-}	K^+	-0.009
OH^-	CO_3^{2-}	Na^+	-0.017
OH^-	CO_3^{2-}	K^+	-0.01
OH^-	Br^-	Na^+	-0.018
OH^-	Br^-	K^+	-0.014
HCO_3^-	CO_3^{2-}	Na^+	0.002
HCO_3^-	CO_3^{2-}	K^+	0.012

B.6 PITZER VIRIAL COEFFICIENTS DATA BASE FOR BASIN SCALE SIMULATIONS

An important aspect for the thermodynamic simulation of brines is to use the appropriate thermodynamic database. The Yucca Mountain Pitzer database "data0.ypf.R2" is a publicly accessible database, which was developed as part of the Yucca Mountain project (USDOE, 2007). The database was converted from the original EQ3/6 format to PHREEQC format by Benbow et al. (2008). As part of the present work, this database was converted to the MIN3P-NWMO format and used for the basin scale simulations described in the main report. The implementation of the Pitzer equations in MIN3P-NWMO and the database conversion were verified by comparing simulation results for the speciation of Dead Sea water to results obtained with EQ3/6 and PHREEQC (see Appendix D.2).

B.7 REFERENCES

Bea, S.A., J. Carrera, C. Ayora and F. Batlle. 2010. Pitzer Algortithm: Efficient implementation of Pitzer equations in geochemical and reactive transport models. Computers & Geosciences, 36, 526-538.

Benbow, S., R. Metcalfe and J. Wilson. 2008. Pitzer databases for use in thermodynamic modelling. Nuclear Waste Management Organization Technical Memorandum (QRS-3021A-TM1) Version: 1.0. Toronto, Canada.

Felmy, A.R. and J.H. Weare. 1986. The prediction of borate mineral equilibria in natural waters: Application to Searles Lake, California. Geochimica et Cosmochimica Acta, 50, 2771-2783.

Greenberg, J.P. and N. Moller. 1989. The prediction of mineral solubilities in natural-waters - A chemical-equilibrium model for the Na-K-Ca-Cl-SO_4-H_2O system to high-concentration from 0^o to 250^oC. Geochimica et Cosmochimica Acta, 53, 2503-2518.

Harvie, C.E., N. Moller and J.H. Weare. 1984. The prediction of mineral solubilities in natural waters: The Na-K-Mg-Ca-H-Cl-SO_4-OH-HCO_3-CO_3-CO_2-H_2O system to high ionic strengths at 25^oC. Geochimica et Cosmochimica Acta, 48, 723-751.

Henderson, T.H., K.U. Mayer, B. Parker and T. Al. 2009. Three-dimensional density-dependent flow and multicomponent reactive transport modelling of chlorinated solvent oxidation by potassium permanganate. Journal of Contaminant Hydrology, 106, 195-211.

MacInnes, D.A. 1919. The activities of the ions of strong electrolytes. Journal American Chemical Society, 41, 1086-1092.

Monnin, C. 1994. Density calculation and concentration scale conversions for natural waters. Computers & Geosciences, 20, 1435-1445.

Pitzer, K.S. 1973. Thermodynamics of electrolytes. I. Theoretical basis and general equations. Journal of Physical Chemistry, 77, 268-277.

Pitzer, K.S. and G. Mayorga. 1973. Thermodynamics of electrolytes. II. Activity and osmotic coefficients for strong electrolytes with one or both ions univalent. Journal of Physical Chemistry, 77, 2300-2307.

Pitzer, K.S. 1975. Thermodynamics of electrolytes V. Effects of higher-order electrostatic terms. Journal of Solution Chemistry, 4, 249-265.

USDOE (United States Department of Energy). 2007. In-drift precipitates/salts model. Argonne National Laboratory Report EBS-MD-000045 REV 03. Chicago, USA.

THIS PAGE HAS BEEN LEFT BLANK INTENTIONALLY

APPENDIX C: MIN3P-NWMO SOLUTION STRATEGY AND DISCRETIZED EQUATIONS

CONTENTS

Page

LIST OF FIGURES

Page

C.1 MIN3P-NWMO SOLUTION STRATEGY AND DISCRETIZED EQUATIONS

Obtaining solutions to the governing equations describing the movement of variable density fluids in fully- or variably-saturated media requires discretization in space and time. The formulation of the discrete algebraic equations used to approximate the governing equations, and the procedures employed to solve the interdependent fluid flow and chemical transport equations, are described in the following sections.

C.1.1 NUMERICAL IMPLEMENTATION OF FLOW EQUATIONS

In MIN3P-NWMO, the fluid flow conservation and energy transport equations are solved using Newton's method. The coupling between fluid density and solute concentrations in MIN3P-NWMO is resolved using the Picard iterative approach. This method linearizes the combined set of flow and reactive transport equations by computing fluid density and solving the fluid conservation equations using chemical concentrations computed during the previous Picard iteration. The Picard approach is conceptually straightforward and is used in a number of computer programs that simulate variable density flow and transport problems (Voss, 1984; Kipp, 1986; Ackerer et al., 1999; Frolkovic, 1999; Diersch and Kolditz, 2002). The Picard approach has also been used to combine individual computer programs for simulating reactive transport problems (Prommer et al., 2003).

C.1.1.1 Discretized equations

The fluid mass conservation equations (Equation 3-1) are formulated using an implicit time weighting scheme. The following mass conservation equation is based on the formulation of Henderson et al. (2009) and Henderson, 2009), and has been extended to include one-dimensional vertical stress (see Appendix A):

$$V_{ivol}\left[S_p\rho^{N+1}\left(\frac{P_{ivol}^{N+1}-P_{ivol}^{N}}{\Delta t}-\zeta\frac{\sigma_{zz}^{N+1}-\sigma_{zz}^{N}}{\Delta t}\right)+\phi^{N+1}\frac{\rho^{N+1}-\rho^{N}}{\Delta t}\right]+$$

$$\sum_{jvol=1}^{ncon} k^{N}\frac{\rho_{ups}^{N+1}}{\mu_{ups}^{N+1}}\frac{A}{\Delta l}\left[P_{jvol}^{N+1}-P_{ivol}^{N+1}+\rho_{av}^{N+1}g\left(z_{jvol}-z_{ivol}\right)\right]-\rho Q_{ivol}=0 \qquad \text{Equation C-1}$$

where the superscripts N and N+1 refer to the previous and current time steps, respectively, V is the cell volume [L^3], Δt is the time step length [T], Δl is the distance between connected control volumes [L], A is the cross-sectional area between connected volumes [L^2], and z refers to elevation [L]. The subscript *ivol* identifies the control volume under consideration, connected control volumes are identified by the subscript *jvol*, and *ncon* is the total number of connected control volumes. The subscript *ups* indicates that upstream-weighting is employed to define the parameters at the interface between a pair of connected control volumes, and the subscript *av* denotes use of the arithmetic average (Henderson, 2009).

The permeability values assigned to calculate fluxes between connected control volumes are computed using cell volume-weighted harmonic means. Upstream weighting of fluid density and viscosity is employed in the computation of fluid fluxes to promote a numerically stable solution (Forsyth et al., 1995). For fluid densities in the gravity term of Equation C-1, there is no physical reason to preferentially weight the density of either control volume, and the arithmetic average is used. This approach for calculating both upstream and average fluid densities at boundaries between model cells is similar to the approach used by Guo and Langevin (2002).

C.1.1.2 Initial and Boundary Conditions

Initial hydrologic conditions and boundary conditions may be assigned in units of fluid pressure, pressure heads, hydraulic heads, or freshwater heads. Initial fluid pressures are assigned to the model grid using the following relationships:

$$P_{ivol} = \psi_{ivol}|g|\rho_{ivol} \qquad \text{Equation C-2}$$

$$P_{ivol} = (h_f - z_{ivol})|g|\rho_f \qquad \text{Equation C-3}$$

$$P_{ivol} = (h_{ivol} - z_{ivol})|g|\rho_{ivol} \qquad \text{Equation C-4}$$

where ψ is the pressure head [L], $|g|$ is the magnitude of gravitational acceleration [L T^{-2}], h_f and h represent freshwater and hydraulic heads [L], ρ_f is the freshwater density [M L^{-3}] and the density ρ [M L^{-3}] is calculated using Equation 3-3.

Initial and boundary conditions specified for the geochemical system are read and assigned to the model grid before initial and boundary conditions are assigned to the flow system. This order of execution allows the density of fluids at assigned model boundaries to be computed, and facilitates the calculation of internal initial fluid pressures. A hydrostatic fluid pressure profile may be assigned to a vertical interval in the model domain containing a uniform solute concentration using the following relationship (Henderson, 2009):

$$P_{ivol} = P_0 + |g|\rho_{ivol}[z_0 - z_{ivol}] \qquad \text{Equation C-5}$$

where P_0 [M L^{-1} T^{-2}] and z_0 [L] represent the fluid pressure and the elevation at the top of the interval. This calculation provides an efficient mechanism to assign initial fluid pressures when dense fluids are present and ensures that their distribution is consistent with solute concentrations and fluid densities.

Specified fluid head, pressure or Darcy flux boundary conditions may be assigned to the exterior boundaries of the model domain. The seepage boundary algorithm developed in MIN3P (Mayer et al., 2002) was modified for variable density fluids to maintain the generality of the MIN3P-D program (Henderson, 2009), and is also available in MIN3P-NWMO.

C.1.2 NUMERICAL IMPLEMENTATION OF REACTIVE TRANSPORT EQUATIONS

In MIN3P-NWMO the global implicit approach (see e.g. Mayer, 1999; Saaltink et al., 2000; Mayer et al., 2002) is used to solve the set of reactive transport equations. A modified Newton-Raphson method is used to linearize the system of equations.

C.1.2.1 Discretized Equations

N_c mass conservation equations (Equation 3-15) are discretized in space using the finite volume technique and by applying fully implicit time weighting. The discretized equations for the j^{th} component can be written as:

$$\frac{V_k}{\Delta t}\left[\phi_k^{N+1}T_{j,k}^{a,N+1}-\phi_k^{N}T_{j,k}^{a,N}\right]+\frac{V_k}{\Delta t}\left[T_{j,k}^{s,N+1}-T_{j,k}^{s,N}\right]= -\sum_{l\in\eta_k}\nu_{a,kl}T_{j,kl}^{a,N+1}-\sum_{l\in\eta_k}\gamma_{a,kl}^{d}\left[T_{j,l}^{a,N+1}-T_{j,k}^{a,N+1}\right]+ V_k\left(Q_{j,k}^{a,a,N+1}+Q_{j,k}^{a,m,N+1}+Q_{j,k}^{a,ext}\right) \qquad \text{Equation C-6}$$

where V_k [L^3] is the volume of the k^{th} cell, Δt is the time increment [T], ϕ is the porosity [-], $\nu_{a,kl}$ [$L^3\ T^{-1}$] is the aqueous phase flux between control volumes *k* and *l*, and $\gamma_{a,kl}^{d}$ [$L^3\ T^{-1}$] is the influence coefficient for the dispersive flux in the aqueous phase. $T_{j,kl}^{a,N+1}$ [$M\ L^{-3}$] defines the total aqueous component concentration used for the advective flux calculations across the interface between the control volumes *k* and *l*.

C.1.2.2 Initial and Boundary Conditions

Boundary conditions for solutes include Dirichlet (specified concentration), Cauchy (specified mass flux), and free exit conditions. In the Dirichlet formulation, concentrations are specified at the boundary or internal nodes. In the Cauchy formulation, fluids entering the model domain are assigned user-specified chemical concentrations. Concentrations can be specified as total concentrations. In addition, pH, Eh, and partial gas pressures can be defined. The latter option is useful to define the saturation state of recharge with respect to oxygen.

Regarding the initial chemical composition in the domain, aqueous concentrations can be defined in a similar manner as the boundary conditions. In addition, the initial assemblage of reactive minerals must be specified. For adsorption reactions, the appropriate input parameters have to be provided for each simulation. For example, for cation-exchange reactions, it is necessary to provide the cation exchange capacity (CEC) and the bulk density of the porous medium.

C.1.3 NUMERICAL IMPLEMENTATION OF ENERGY BALANCE EQUATIONS

In MIN3P-NWMO, the fluid mass conservation equations are coupled with the energy balance equations and solved at the same time. Thus, the Newton-Raphson method is used to linearize the system of equations. Coupling among fluid flow, solute and energy transport is made through density, viscosity and Darcy velocities.

C.1.3.1 Discretized Equations

The energy conservation equations (Equation 3-13) are discretized in space using the finite volume technique and by applying fully implicit time weighting. The discretized equations can be written as:

$$\frac{c_w V_k}{\Delta t}\left[\phi_k^{N+1}\rho_k^{N+1}T^{N+1}-\phi_k^{N}\rho_k^{N}T^{N}\right]+ \frac{c_{s,k}\rho_{s,k}V_k}{\Delta t}\left[(1-\phi_k^{N+1})T^{N+1}-(1-\phi_k^{N})T^{N}\right]= -c_w\sum_{l\in\eta_k}\rho_{kl}^{N+1}\nu_{a,kl}T_{kl}^{N+1}-\sum_{l\in\eta_k}\gamma_{kl}^{c,N+1}\Delta T_{kl}^{N+1}+ \sum_{l\in\eta_k}\phi_{kl}^{N+1}\rho_{kl}^{N+1}\gamma_{kl}^{d,N+1}\Delta T_{kl}^{N+1}+c_w\rho^{*}A_kQ^{*}T^{*} \qquad \text{Equation C-7}$$

where c_w is the heat capacity for water [$L^2\ T^{-2}\ {}^oC^{-1}$], V_k is the volume of the k^{th} cell [L^3], Δt is the time increment [T], ϕ [-] is the porosity [-], ρ [$M\ L^{-3}$] is the fluid density, and T is temperature [Θ]. $c_{s,k}$ and $\rho_{s,k}$ are the heat capacity [$L^2\ T^{-2}\ \Theta^{-1}$] and density [$M\ L^{-3}$] of the solid, respectively. $\nu_{a,kl}$ is the volumetric fluid flux between control volumes *k* and *l* [$L^3\ T^{-1}$] used for the advective flux calculations across the interface between the control volumes *k* and *l* with T_{kl}^{N+1}[°C] and ρ_{kl}^{N+1}[$M\ L^{-3}$] defining the temperature and fluid density at the interface, respectively. γ_{kl}^{c} is the influence coefficient for the conduction flux [$M\ L^2\ T^{-3}\ {}^oC^{-1}$] and γ_{kl}^{d} is the influence coefficient for the dispersive flux [$L^5\ T^{-3}\ {}^oC^{-1}$]. ΔT_{kl}^{N+1} [Θ] represents the temperature difference between cells *k* and *l*. T^* and ρ^* is the external temperature [Θ] and fluid density [$M\ L^{-3}$] when fluid mass flux is entering the system, or the temperature and fluid density corresponding to an adjacent cell at the boundary when fluid mass exits the system. Q^* is the volumetric flux per unit of surface area at the boundary [$L^3\ L^{-2}\ T^{-1}$] and A_k is the surface area of the boundary cell [L^2].

The influence coefficient γ_{kl}^{c} for the conduction flux is defined by:

$$\gamma_{kl}^{c}=\frac{A_{kl}}{d_{kl}}\lambda_{kl} \qquad \text{Equation C-8}$$

where A_{kl}, d_{kl} and λ_{kl} [M L T^{-3} $^{o}C^{-1}$] are the interfacial area, distance and thermal conductivity of the porous medium between cells k and l, respectively. The thermal conductivity of the porous medium is computed according to:

$$\lambda = \phi_{kl}\lambda_w + (1-\phi_{kl})\lambda_s \qquad \text{Equation C-9}$$

where λ_w and λ_S are the thermal conductivities for water and solid, respectively.

λ_{kl} is the representative thermal conductivity used for the flux calculation between control volumes *k* and *l*, and can be calculated based on the distance-weighted harmonic mean:

$$\lambda_{kl} = \frac{\lambda_k \lambda_l d_{kl}}{\lambda_k d_k + \lambda_l d_l} \qquad \text{Equation C-10}$$

where λ_{kl} and λ_{kl} are the thermal conductivities of the control volumes *k* and *l*, respectively, perpendicular to the interfacial area A_{kl}.

The thermal dispersive term (γ^{d}_{kl}) is computed as:

$$\gamma^{d}_{kl} = \frac{A_{kl}}{d_{kl}} c_w \phi_{kl} D_{a,kl} \qquad \text{Equation C-11}$$

where $D_{a,kl}$ [L^2 T^{-1}] defines the effective dispersion coefficient in the aqueous phase between control volumes k and l.

C.1.3.2 Initial and Boundary Conditions

Boundary conditions for energy balance equations include Dirichlet (specified temperature), Cauchy (specified heat flux), and free exit conditions. In the Dirichlet formulation, temperature is specified at boundary or internal nodes. In the Cauchy formulation, heat fluxes entering the model domain are assigned by the user.

The initial conditions for temperature can be defined in a similar manner as the boundary conditions.

C.1.4 COUPLING OF FLOW, ENERGY AND REACTIVE TRANSPORT

Updates in fluid density provide the criteria to evaluate the convergence of the Picard iterations. Picard iterations continue until the maximum update in fluid density is reduced to a user-specified tolerance (Guo and Langevin, 2002). A non-iterative solution approach may be

employed by setting the convergence criteria to an arbitrarily high value, or setting the maximum number of Picard iterations to unity. In this case, fluid densities are computed using solute concentrations and temperature is computed from the previous time step.

A convergent model time step requires that the maximum updates for fluid pressures, temperature and solute concentrations fall below user-specified Newton convergence criteria, and that fluid density changes are less than the Picard convergence criteria. Following Picard convergence, mineral volume fractions and the porosity and permeability values are updated and the code proceeds to the next time step. These updates are lagged under the assumption that the changes in these properties in one time step are small enough to not significantly affect the accuracy of the simulation. The MIN3P-NWMO solution sequence is summarized in Figure C.1.

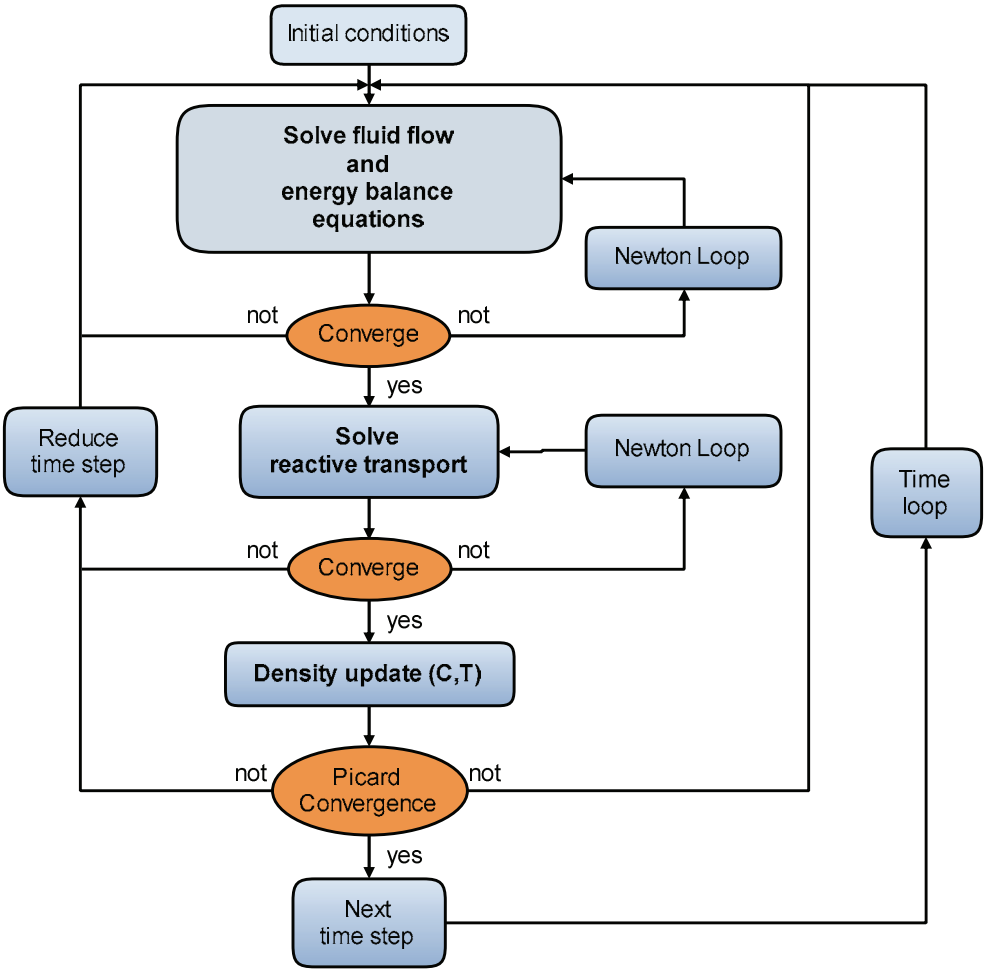

Figure C. 1: Flow diagram of the Picard iterative process implemented in the MIN3P-NWMO program execution structure. Time step reductions occur when the maximum number of Newton or Picard iterations have been reached and the convergence criteria have not been achieved

C.1.4.1 Adaptive Time Stepping Scheme

The MIN3P program computes time step lengths based on changes in the concentrations of aqueous components and the target number of Newton iterations (Mayer et al., 2002). In addition to these parameters, MIN3P-D (as well as MIN3P-NWMO) incorporates a Courant number target and the target number of Picard iterations to compute time step lengths (Henderson, 2009). The Courant number criterion was added in response to the use of the operator splitting approach for solving the coupled flow, energy transport and reactive transport equations.

C.2 REFERENCES

Ackerer, P., A. Younes and R. Mose. 1999. Modeling variable density flow and solute transport in porous medium: 1. Numerical model and verification. Transport in Porous Media , 35, 345-373.

Diersch, H. and O. Kolditz. 2002. Variable-density flow and transport in porous media: approaches and challenges. Advances in Water Resources, 25, 899-944.

Forsyth, P.A., Y.S. Wu and K. Pruess. 1995. Robust numerical methods for saturated-unsaturated flow with dry initial conditions in heterogeneous media. Advances in Water Resources, 18, 25-38.

Frolkovic, P. 1999. Discretization. In: Fein E, editor. d^3f - a simulator for density-driven flow. Gesellschaft fuer Anlagen-und Reaktorsicherheit, Braunschweig .

Guo, W. and C. Langevin. 2002. User's Guide to SEAWAT: A Computer program for simulation of three-dimensional variable-density ground-water flow. U.S. Geological Survey, Techniques of Water-Resources Investigations Book 6, Chapter A7, 77p.

Henderson, T.H. 2009, Density-dependent flow and reactive transport modeling of chlorinated solvent oxidation by permanganate, Ph.D.-Thesis, Dept. of Earth and Ocean Sciences, University of British Columbia, Vancouver, B.C., Canada.

Henderson, T.H., K.U. Mayer, B. Parker and T. Al. 2009. Three-dimensional density-dependent flow and multicomponent reactive transport modeling of chlorinated solvent oxidation by potassium permanganate. Journal of Contaminant Hydrology, 106, 195-211.

Kipp, K.L. 1986. HST3D-A computer code for simulation of heat solute transport in three-dimensional ground-water flow systems. U.S. Geological Survey Water-Resources Investigations Report 86-4095.

Mayer, K.U. 1999. A Numerical Model for Multicomponent Reactive Transport in Variably Saturated Porous Media. PhD dissertation, University of Waterloo, Waterloo, Ontario, Canada.

Mayer, K.U., E.O. Frind and D.W. Blowes. 2002. Multicomponent reactive transport modeling in variably saturated porous media using a generalized formulation for kinetically controlled reactions. Water Resources Research, 38, 1174.

Prommer, H., D.A. Barry and C. Zheng. 2003. MODFLOW/MT3DMS-based reactive multicomponent transport modeling. Ground Water, 41, 247-257.

Saaltink, M.W., J. Carrera and C. Ayora. 2000. A comparison of two approaches for reactive transport modelling. Journal of Geochemical Exploration, 69, 97-101.

Voss, C. 1984. A finite-element simulation model for saturated-unsaturated, fluid-density-dependent ground-water flow with energy transport or chemically-reactive single-species solute transport. U.S. Geological Survey Water-Resources Investigations Report 84-4369, 409p.

THIS PAGE HAS BEEN LEFT BLANK INTENTIONALLY

APPENDIX D: MODEL VERIFICATION

CONTENTS

Page

LIST OF TABLES

Page

LIST OF FIGURES

Page

D.1 VERIFICATION OF VERTICAL STRESS

The one-dimensional vertical stress implementation was verified by comparison to the exact analytical solution presented by Lemieux et al. (2008). The analytical solution was applied to a one-dimensional semi-infinite vertical column of fully saturated sand (Figure D. 1A). In this case, a load is applied to the top boundary at a constant rate (~ 0.32 m year^{-1}, e.g. it could represent the ice sheet loading in a glaciation scenario). The top of the column is drained and the bottom is a no-flow boundary condition. Model parameters are described in Lemieux et al. (2008). The analytical solution in space (z) and time (t) for the hydraulic head ($h(z,t)$) is (Lemieux et al. 2008, and personal communication)

$$h(z,t) = \frac{\zeta}{\rho_f g}\frac{\partial \sigma_{zz}}{\partial t}\left[t - \left(t + \frac{z^2}{2D} \right) \operatorname{erfc}\left(\frac{z}{2\sqrt{Dt}} \right) + z\sqrt{\frac{t}{\pi D}} \exp\left(-\frac{z^2}{4Dt} \right) \right] \qquad \text{Equation D-1}$$

where D is the hydraulic diffusivity defined as $D = k / S_S$ [$L^2\ T^{-1}$].

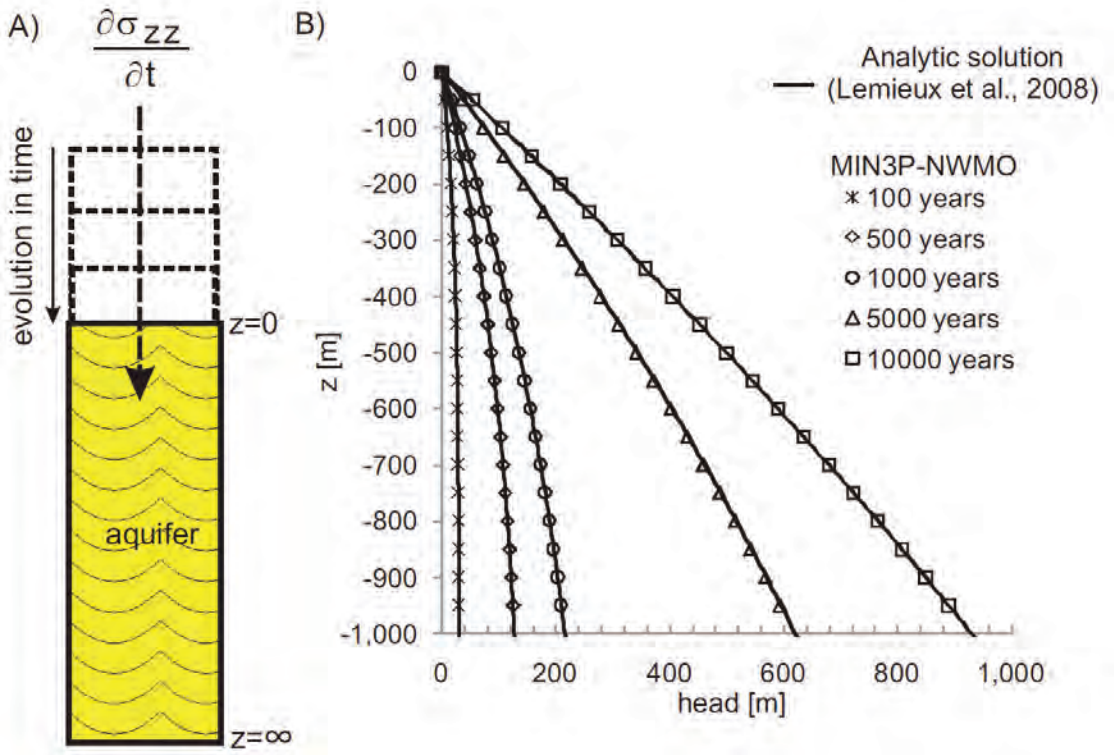

Figure D. 1: Verification of the one-dimensional vertical stress implementation in MIN3P-NWMO. A) Conceptual model depicting vertical loading on an aquifer with free drainage on surface. B) MIN3P-NWMO results (symbols) compared with the analytical solution (solid lines) presented by Lemieux et al. (2008)

The vertical distributions of pressure head at different times are shown in Figure D. 1B. The pressure heads increase with time as a consequence of the temporally constant loading. Note that the MIN3P-NWMO results agree well with the analytical results obtained using Equation D-1.

D.2 VERIFICATION OF PITZER EQUATIONS FOR ACTIVITY CALCULATIONS

In order to verify the implementation of the Pitzer equations (Appendix B.2) and to ensure that the thermodynamic database "data0.ypf.R2" (USDOE, 2007, Benbow et al., 2008) was converted correctly into the format required for MIN3P-NWMO (see Appendix B.6), the chemical speciation of Dead Sea Water was calculated with PHREEQC, EQ3/6 and MIN3P-NWMO. The results of chemical speciation calculations are in good agreement for all three codes and database implementations (Table D. 1 - Table D. 3).

Table D. 1: Speciation of Dead Sea water – Model input

Chemical parameters	
T(°C)	25
pH	7
P(bar)	1

Component	**Concentration (molality)**
Na	1.752
K	0.1739
Mg	1.555
Ca	0.4274
Cl	5.810
CO_3	$3.92\ 10^{-3}$
S	$6.3\ 10^{-3}$

Table D. 2: Speciation of Dead Sea Water – Aqueous Speciation

Speciation	EQ3	PHREEQC	MIN3P-NWMO
	Molality	molality	molality
Cl^-	5.809	5.809	5.809
Na^+	1.752	1.752	1.752
Mg^{2+}	1.551	1.551	1.551
Ca^{2+}	0.4239	0.4235	0.4239
K^+	0.1739	0.1739	0.1739
SO_4^{2-}	$4.038\ 10^{-3}$	$3.782\ 10^{-3}$	$4.106\ 10^{-3}$
$MgHCO_3^+$	$3.6\ 10^{-3}$	$3.648\ 10^{-3}$	$3.474\ 10^{-3}$
$CaSO_{4(aq)}$	$2.262\ 10^{-3}$	$2.518\ 10^{-3}$	$2.194\ 10^{-3}$
$CaCl^+$	$1.198\ 10^{-3}$	$1.366\ 10^{-3}$	$1.226\ 10^{-3}$
$MgOH^+$	$3.235\ 10^{-4}$	$2.692\ 10^{-4}$	$2.56\ 10^{-4}$
$MgCO_{3(aq)}$	$1.256\ 10^{-4}$	$1.042\ 10^{-4}$	$1.43\ 10^{-4}$
HCO_3^-	$9.756\ 10^{-5}$	$9.251\ 10^{-5}$	$1.974\ 10^{-4}$
CO_3^{2-}	$5.526\ 10^{-5}$	$3.918\ 10^{-5}$	$5.924\ 10^{-5}$
$CaCO_{3(aq)}$	$4.1\ 10^{-5}$	$3.494\ 10^{-5}$	$4.474\ 10^{-5}$
$CaOH^+$	$4.571\ 10^{-6}$	$3.804\ 10^{-6}$	$2.406\ 10^{-6}$
$CO_2(aq)$	$9.584\ 10^{-7}$	$1.195\ 10^{-6}$	$1.656\ 10^{-6}$
HSO_4^-	$2.048\ 10^{-10}$	$2.607\ 10^{-10}$	$2.792\ 10^{-10}$
$CaCl_{2(aq)}$	$1.142\ 10^{-15}$	$1.195\ 10^{-15}$	$1.073\ 10^{-15}$

Table D. 3: Speciation of Dead Sea Water – Mineral Saturation Indices

Minerals	Saturation Indices		
	EQ3	PHREEQC	MIN3P-NWMO
Anhydrite	0.02	0.02	0.01
Antarcticite	-3.31	-3.29	-3.33
Aragonite	0.62	0.56	0.66
Arcanite	-4.31	-4.33	-4.3
Bischofite	-2.75	-2.69	-2.75
Bloedite	-5.00	-5.02	-4.97
Calcite	0.80	0.67	0.83
Carnallite	-2.76	-2.69	-2.76
Dolomite	3.55	3.41	3.64
Epsomite	-2.37	-2.32	-2.35
Glauberite	-2.49	-2.46	-2.49
Gypsum	-0.03	-0.05	-0.04
Halite	-0.37	-0.35	-0.37
Hexahydrite	-2.54	-2.50	-2.52
Hydromagnesite	-2.43	-2.90	-2.38
Kainite	-3.79	-3.80	-3.78
Kieserite	-3.56	-3.53	-3.56
Lansfordite	-2.02	-2.11	-1.95
Leonhardtite	-2.93	-2.89	-2.91
Magnesite	1.16	1.08	1.21
Mirabilite	-3.41	-3.58	-3.38
Natron	-7.24	-7.33	-7.15
Nesquehonite	-1.92	-2.36	-1.86
Oxychloride-Mg	-2.65	-2.91	-2.93
Pentahydrite	-2.66	-2.62	-2.65
Pentasalt	-3.16	-2.55	-3.21
Polyhalite	-4.66	-4.69	-4.67
Sylvite	-1.06	-1.05	-1.06
Syngenite	-3.26	-3.19	-3.14
Thenardite	-3.13	-3.15	-3.11
Brucite	-1.97	-2.14	-2.16

D.3 VERIFICATION OF DENSITY-DRIVEN FLOW AND CONSERVATIVE SOLUTE TRANSPORT

This section describes the verification of the equations implemented in MIN3P-NWMO for simulating coupled density-driven flow and solute transport. Four benchmarking problems are presented to document the accuracy of MIN3P-NWMO. The emphasis is placed on benchmarking problems with solutions constrained by established mathematical or laboratory results.

Theoretical box problems were simulated to evaluate error-driven spreading of solutes in static and advecting fluids (Voss and Souza, 1987; Diersch and Kolditz, 2002). The Elder fluid convection benchmarking problem (Elder, 1967), for which an exact solution does not exist (Diersch and Kolditz, 2002), was included in the current evaluation due to its extensive use in model benchmarking (Oldenburg and Pruess, 1995; Ackerer et al., 1999; Oltean and Buès, 2001; Frolkovic and Schepper, 2001; Diersch and Kolditz, 2002; Simpson and Clement, 2003). MIN3P-NWMO results for the modified Henry seawater intrusion problem (Henry, 1964; Simpson and Clement, 2004) were benchmarked against a published solution. Additional benchmarking simulations were performed for the modified Horton-Rogers-Lapwood problem (Weatherill et al., 2004) and three-dimensional laboratory experiments of saltwater up coning and mixing with freshwater, as presented by Oswald and Kinzelbach (2004) (results not shown).

D.3.1 BOX PROBLEMS

These simulations are designed to detect spurious numerical results which may be generated in the vicinity of freshwater-saltwater interfaces. Two box problems were benchmarked, investigating stable density stratifications under hydrostatic conditions and in advecting fluids. A stable density stratification satisfies the following condition throughout the model domain:

$$\frac{\partial P_a}{\partial z} \geq \rho|g| \qquad \text{Equation D-2}$$

where P_a is the aqueous fluid pressure [M L^{-1} T^{-2}], ρ is the fluid density [M L^{-3}], and |g| is the magnitude of gravitational acceleration [L T^{-2}], and in this case, z [L] is positive downward.

D. 3.1.1 Hydrostatic Box Test

The hydrostatic box test (Diersch and Kolditz, 2002) compares solute diffusion in variable density fluids, with solute diffusion in a freshwater system in which fluid density is not a function of solute concentration. The implementation of hydrodynamic dispersion in MIN3P-NWMO should produce results for solute diffusion, from saltwater into freshwater, that are independent of the density contrast between the two fluids.

The hydrostatic box test was simulated in a 20 m horizontal by 40 m vertical domain, with a saltwater layer located below a freshwater layer. The two fluids were initially separated by a sharp horizontal interface in the middle of the domain (Diersch and Kolditz, 2002). The domain was surrounded by no flow boundaries for flow and transport. The decoupled (reference) case was simulated by setting the coefficient of density variation, ∂ρ/∂c, to zero, resulting in the

freshwater density being assigned to both fluids. The coupled variable density scenario was simulated by setting the coefficient of density variation to 0.7, resulting in a three percent density contrast between the saltwater and freshwater layers. The model was discretized using a 40200-node grid with Δx = 1.0 m and Δz = 0.2 m. The simulations were executed for a period of 1000 days. Flow and transport parameters are summarized in Table D. 4.

Table D. 4: Parameters for Hydrostatic Box Problem

Parameter	Symbol	Value	Units
Hydraulic conductivity	K	1.0×10^{-4}	$m\ s^{-1}$
Porosity	Φ	0.4	-
Specific storage	S_s	0.0	m^{-1}
Longitudinal dispersivity	α_L	5.0	m
Transverse dispersivity	α_T	0.5	m
Molecular diffusion coefficient	D_m	1.0×10^{-8}	$m^2\ s^{-1}$
Saltwater density	ρ_s	1030	$kg\ m^{-3}$
Freshwater density	ρ_0	1000	$kg\ m^{-3}$
Maximum density ratio	ρ_{max}	1.03	-
Coefficient of density variation	$\partial\rho/\partial c$	0.0/0.7	-
Saltwater concentration	C_s	43	$g\ L^{-1}$

Figure D. 2 compares the diffusive concentration distributions for the constant density and variable density cases at a simulation time of 1000 days. As shown in Figure D. 2, an excellent agreement was obtained for the two cases, indicating an absence of spurious fluid movement for the coupled case.

D. 3.1.2. Hydrodynamic Box Problem

The second box problem was simulated to investigate the potential for numerically-induced smearing of sharp concentration gradients in the direction normal to the direction of fluid movement (Voss and Souza, 1987). The domain dimensions were 2000 m in height and length, and the region was discretized using 21 control volumes in the x and z directions. Similar to the hydrostatic problem, a layer of freshwater was initially present above a layer of saltwater.

A constant groundwater seepage velocity of 5 m d^{-1} in the positive x-direction was simulated by assigning hydrostatic pressure profiles to the left and right sides of the model domain. Fixed solute concentrations were assigned to the influent (left) boundary of the domain, and these were set equal to the initial concentrations assigned to the model domain. A free exit solute boundary condition was assigned to the right side of the model domain. The molecular diffusion coefficient and the transverse dispersivity were both set to zero (Table D. 5). Given these values, no mechanism was present to cause the vertical spreading of solutes, except for potential numerical errors. The simulation was run for a total of 4000 days.

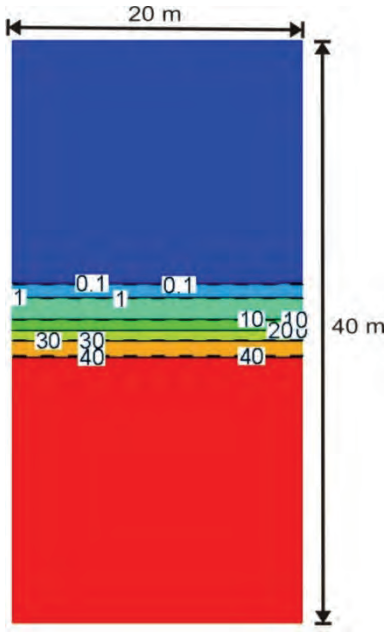

Figure D. 2: Concentration distributions at 1000 days for decoupled ($\partial\rho/\partial c = 0$; dashed lines) and coupled ($\partial\rho/\partial c = 0.7$; solid lines) hydrostatic simulations. Concentration contours have the units g L^{-1}

Table D. 5: Parameters for Hydrodynamic Box Problem

Parameter	Symbol	Value	Units
Hydraulic conductivity	K	1.16×10^{-3}	m s^{-1}
Porosity	Φ	0.01	-
Specific storage	S_s	0.0	m^{-1}
Longitudinal dispersivity	α_L	100.0	m
Transverse dispersivity	α_T	0.0	m
Molecular diffusion coefficient	D_m	0.0	m^2 s^{-1}
Saltwater density	ρ_s	1025	kg m^{-3}
Freshwater density	ρ_0	1000	kg m^{-3}
Maximum density ratio	ρ_{max}	1.025	-
Coefficient of density variation	$\partial\rho/\partial c$	0.71	-
Saltwater concentration	C_s	35	g L^{-1}

As Figure D. 3 indicates, the solute iso-concentration lines at the conclusion of the 4000 day simulation were identical to those of the initial solute distribution. The results indicate no numerically-induced solute spreading, or smearing of the solute concentration gradient.

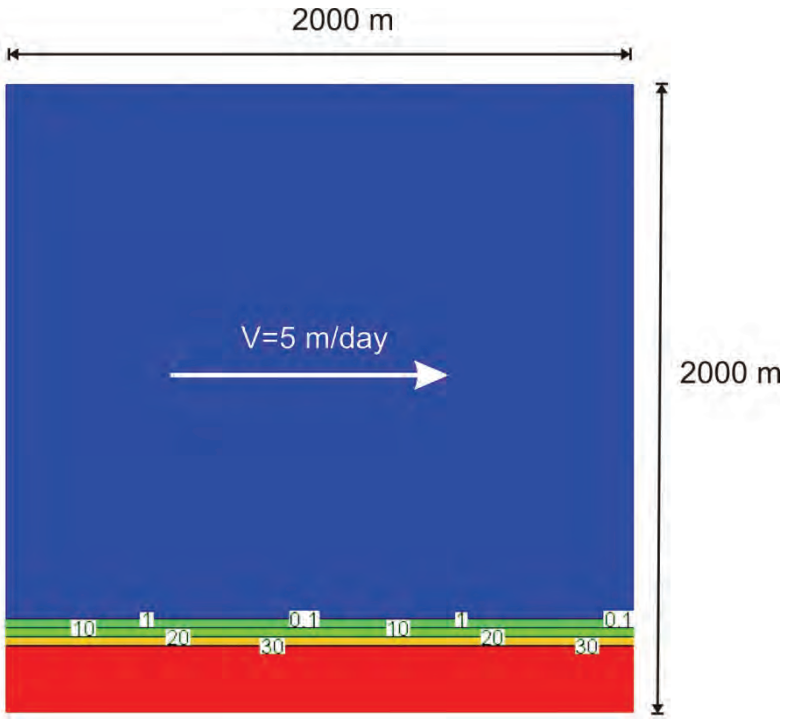

Figure D. 3: Concentration distributions for the hydrodynamic box simulations. Concentration contours (g L^{-1}) at 0 days (solid lines) and 4000 days (dashed lines) are coincident

D.3.2 ELDER PROBLEM

Voss and Souza (1987) utilized laboratory investigations of fluid convection driven by a thermal gradient (Elder, 1967) to develop a benchmarking problem involving fluid convection resulting from solute concentration gradients. In this problem, a dense fluid is present along a portion of the top of the model domain, which initially contains only freshwater. Convective fluid flow patterns develop during the simulation, which evolve into stationary zones of fluid upwelling and downwelling (Frolkovic and Schepper, 2001; Diersch and Kolditz et al., 2002). The problem depicts the interactions of fluids differing in density by a factor of 20%, consistent with the contrast between brines and freshwater (Millero, 1982). The non-linearity and sensitivity of this problem provide a rigorous test of numerical simulators (Simpson and Clement, 2003). Numerical simulation results are sensitive to the level of grid refinement (Oldenburg and Pruess, 1995; Kolditz et al., 1998; Oltean and Buès, 2001; Diersch and Kolditz, 2002) and other numerical parameters, such as the convergence criteria (Ackerer et al., 1999). Because there is no analytical solution to this problem, results for the Elder benchmarking problem must be compared to accepted numerical modelling results (Diersch and Kolditz, 2002).

The Elder problem domain consists of a two-dimensional vertical cross-section depicting a zone of freshwater underlying a source of brines. Initial investigations of the Elder problem simulated the entire domain (Voss and Souza, 1987), while recent investigations have simulated the left half of the symmetrical problem domain to facilitate grid refinement investigations (Oltean and Buès, 2001; Frolkovic and Schepper, 2001; Diersch and Kolditz, 2002). MIN3P-NWMO benchmarking has been conducted using the left half of the domain, with dimensions 300 m

horizontal by 150 m vertical, and discretized using a 8192-node grid with $\Delta x = \Delta z = 2.4$ m. A constant concentration of 0 g l^{-1} was assigned to the entire bottom boundary, and no flow boundaries were assigned to all four sides of the domain. A constant fluid pressure of 0 Pa was assigned to the upper left corner of the domain (Voss and Souza, 1987). The model domain and boundary conditions for the Elder problem are illustrated in Figure D. 4.

The Elder problem was simulated for a period of 20 years using the parameter values presented by Voss and Souza (1987). The Van Leer (1974) flux limiting scheme was used in MIN3P-NWMO to estimate interfacial solute concentrations. The flow and transport parameters are summarized in Table D. 6.

Table D. 6: Parameters for Elder Convection Problem

Parameter	Symbol	Value	Units
Hydraulic conductivity	K	4.75×10^{-6}	m s^{-1}
Porosity	Φ	0.1	-
Specific storage	S_s	0.0	m^{-1}
Longitudinal dispersivity	α_L	0.0	m
Transverse dispersivity	α_T	0.0	m
Molecular diffusion coefficient	D_m	0.0	m^2 s^{-1}
Saltwater density	ρ_s	1200	kg m^{-3}
Freshwater density	ρ_0	1000	kg m^{-3}
Maximum density ratio	ρ_{max}	1.2	-
Coefficient of density variation	$\partial\rho/\partial c$	0.7	-
Saltwater concentration	C_s	285.7	g L^{-1}

Figure D. 4 compares MIN3P-NWMO solute concentration results with published results of the d^3f simulator for the same level of grid discretization (Frolkovic and Schepper, 2001). The d^3f model was selected for the current comparison because it has provided the best agreement with published saltpool upconing experiments (Diersch and Kolditz, 2002; Oswald and Kinzelbach, 2004). Figure D. 5 shows the results for simulation times of 4, 7, and 20 years, during which density-driven flow causes the development and downward movement of dense brine fingers. The two sets of results are in close agreement, and the stationary solute distribution at 20 years is consistent with other published results for a comparable level of grid discretization (Oldenburg and Pruess, 1995; Kolditz et al., 1998; Ackerer et al., 1999; Oltean and Buès, 2001).

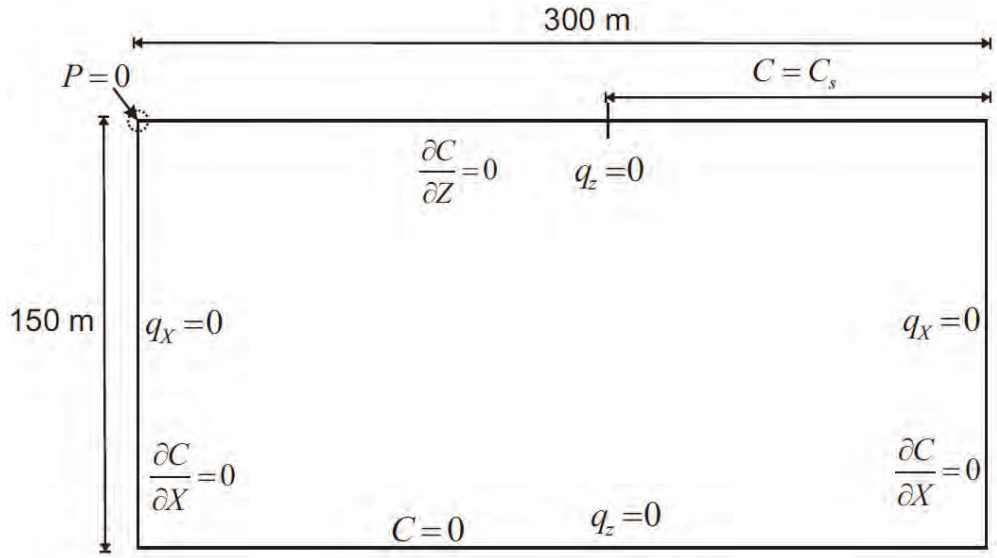

Figure D. 4: Elder problem domain and boundary conditions

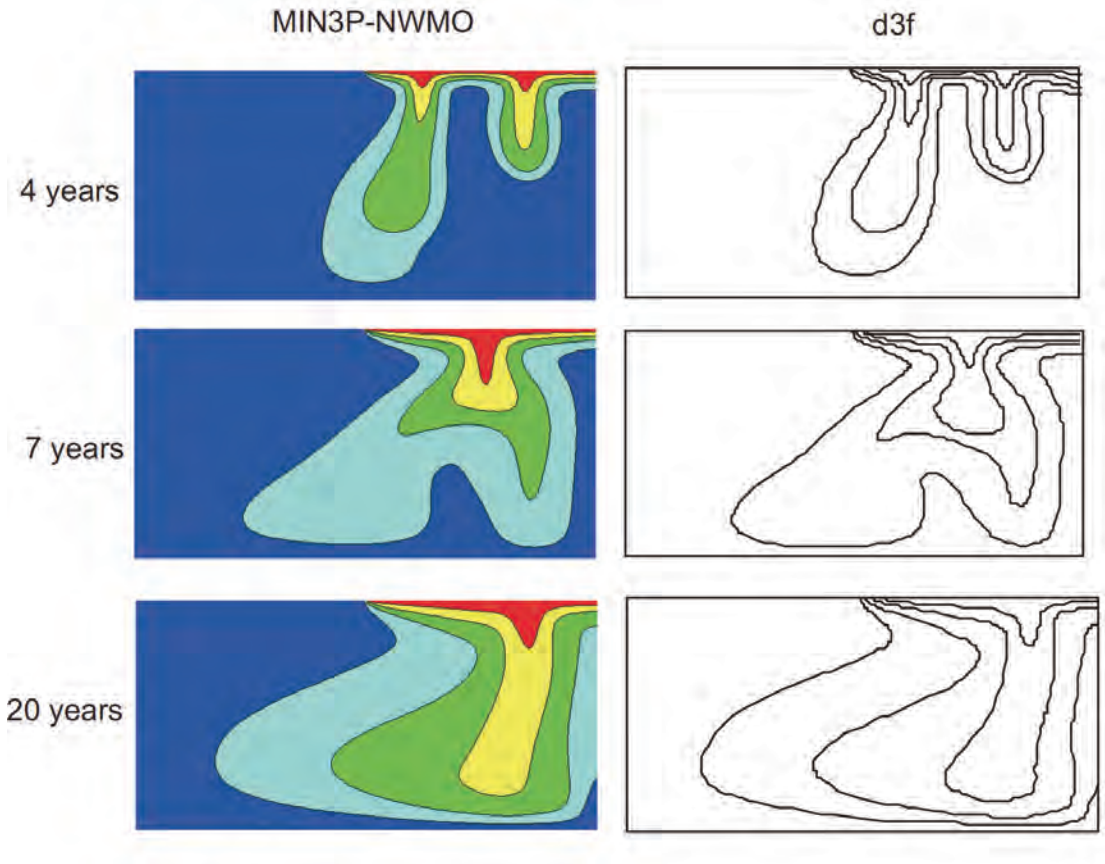

Figure D. 5: MIN3P-NWMO (left) and d^{3}f (right) solute concentration results for the Elder problem. The relative concentration contours are, from top to bottom, 0.8, 0.6, 0.4 and 0.2 of the saltwater source concentration

D.3.3 MODIFIED HENRY PROBLEM

The Henry problem (Henry, 1964) depicts lateral saltwater intrusion into a homogeneous confined aquifer and the development of a mixing zone between freshwater and saltwater. The Henry problem has been widely used as a test case of density-dependent groundwater flow models (e.g. Pinder and Cooper, 1970; Frind, 1982; Kipp, 1986; Voss and Souza, 1987; Ackerer et al., 1999; Guo and Langevin, 2002). However, the merits of this problem for code benchmarking have been scrutinized due to the weak coupling between flow and solute transport (Simpson and Clement, 2003). Simpson and Clement (2004) proposed a modification to the Henry problem, reducing the constant freshwater flux by 50%, to increase the coupling between fluid flow and solute transport and thus the numerical difficulty. This modified problem definition was used to benchmark MIN3P-NWMO.

The Henry problem domain consists of a two-dimensional vertical cross-section, bounded on the top and bottom by no flow boundaries (Figure D. 6A). A constant freshwater flux is applied to the left boundary, representing aquifer flow. The right model boundary represents a hydrostatic column of seawater, with a fixed concentration. The model domain is 2 m horizontal by 1 m vertical, and was discretized using a uniform grid with 861 control volumes with $\Delta x = \Delta z = 0.05$ m.

The MIN3P-NWMO simulation of the modified Henry problem was performed using the parameter values provided by Simpson and Clement (2004). The flow and transport parameters are summarized in Table D. 7. The Henry problem was simulated for a period of 0.833 days, representing the point at which a stationary solute distribution was achieved.

Table D. 7: Parameters for Modified Henry Saltwater Intrusion Problem

Parameter	Symbol	Value	Units
Hydraulic conductivity	K	10^{-2}	m s^{-1}
Porosity	Φ	0.35	-
Specific storage	S_s	0.0	m^{-1}
Longitudinal dispersivity	α_L	0.0	m
Transverse dispersivity	α_T	0.0	m
Molecular diffusion coefficient	D_m	1.89×10^{-5}	$m^2 s^{-1}$
Freshwater flux per unit width	q_x	3.3×10^{-5}	m s^{-1}
Saltwater density	ρ_s	1025	kg m^{-3}
Freshwater density	ρ_0	1000	kg m^{-3}
Maximum density ratio	ρ_{max}	1.025	-
Coefficient of density variation	$\partial\rho/\partial c$	0.7125	-
Saltwater concentration	C_s	35.0	g L^{-1}

Figure D. 6B compares the MIN3P-NWMO simulation results with results from the semi-analytical solution presented by Simpson and Clement (2004). The results show the encroachment of a wedge of saltwater into the freshwater aquifer, in the opposite direction of

groundwater flow. The MIN3P-NWMO results are in excellent agreement with the semi-analytical solution given by Simpson and Clement (2004).

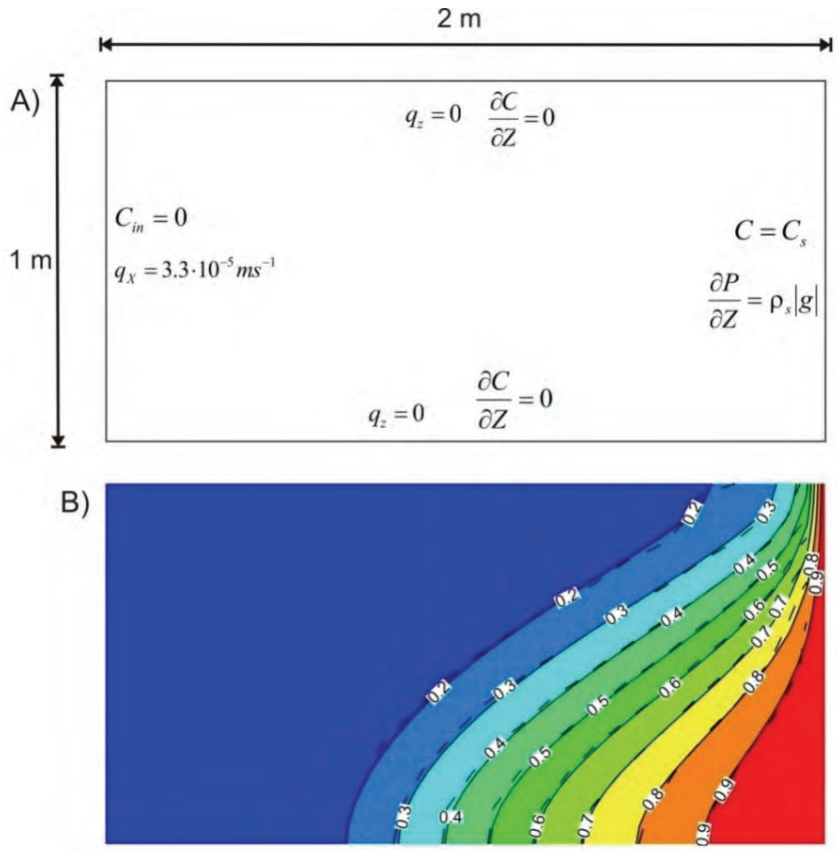

Figure D. 6: The modified Henry problem for lateral saltwater intrusion. (A) Simulation domain with flow and transport boundary conditions. (B) Relative solute concentration results at 0.833 d for MIN3P-NWMO (solid lines) and the semi-analytical solution of Simpson and Clement (2004) (dashed lines)

D.4 VERIFICATION OF ENERGY BALANCE EQUATIONS

The verification of the energy transport equations (and their coupling with the fluid and solute transport equations) implemented in MIN3P-NWMO was carried out using both analytical and numerical solutions for benchmark problems published in the literature (e.g. salt-dome thermo-haline convection).

D.4.1 RADIAL FLOW WITH ENERGY TRANSPORT (ANALYTICAL SOLUTION)

The first problem involves radial groundwater flow with energy transport as presented by Voss and Provost (2008). The problem domain consists of a confined aquifer of thickness b [L], with a fully penetrating injection well (see Figure D. 7B, and model parameters in Table D. 8). Fluid is injected at a rate Q, with a temperature of T*, into the aquifer which is initially at a uniform

temperature of T_0. For this problem, the fluid density and viscosity are approximately constant because the injected fluid temperature differs only slightly from the ambient fluid temperature; i.e., (T^*-T_0) is small.

MIN3P-NWMO results are compared with an approximate analytical solution from Gelhar and Collins (1971), as modified by Voss and Provost (2008):

$$\left(\frac{T-T_0}{T^*-T_0}\right)=\frac{1}{2}\text{erfc}\left[\frac{r^2-(r^*)^2}{2\sqrt{\left(\frac{4}{3}\alpha_L\right)(r^*)^3+\left(\frac{\lambda_{aq}}{A_T}\right)(r^*)^4}}\right] \qquad \text{Equation D-3}$$

where the parameter A_T is defined by:

$$A_T=\frac{\phi\rho c_w}{c_{aq}}A \qquad \text{Equation D-4}$$

with A given by:

$$A=\frac{Q}{2\pi\phi b\rho} \qquad \text{Equation D-5}$$

and c_{aq} defined as:

$$c_{aq}=\phi\rho c_w+(1-\phi)\rho_s c_s \qquad \text{Equation D-6}$$

The parameters λ_{aq} and r* in Equation D-3 are given by:

$$\lambda_{aq}=\phi\lambda_w+(1-\phi)\lambda_s \qquad \text{Equation D-7}$$

$$r^*=\sqrt{2A_T t} \qquad \text{Equation D-8}$$

where ρ is the fluid density [M L^{-3}], α_L is the longitudinal dispersivity [L], c_{aq}, c_w and c_s are the heat capacities for the aquifer, fluid and solid, respectively [L^2 T^{-2} Θ^{-1}], and λ_{aq}, λ_w and λ_s are the thermal conductivities for the aquifer, fluid and solid, respectively [L M T^{-3} Θ^{-1}].

As can be seen in Figure D. 7A, the MIN3P-NWMO and analytical solutions agree well. The MIN3P-NWMO solution is based on the complete set of governing equations, while simplifying assumptions are made for the analytical solution. The differences in formulation likely explain the slight deviations between the two solutions.

Table D. 8: Parameters for Radial Flow Problem with Energy Transport

Parameter	Value	Unit
Solid density	2650	[kg m^{-3}]
Fresh-water density	1000	[kg m^{-3}]
Q	312.15	[kg s^{-1}]
Porosity	0.2	[-]
Permeability	1.02×10^{-11}	[m^2]
Water specific thermal capacity	4182	[J kg^{-1} $^oC^{-1}$]
Solid specific thermal capacity	840	[J kg^{-1} $^oC^{-1}$]
Water thermal conductivity	0.6	[J s^{-1} m^{-1} $^oC^{-1}$]
Solid thermal conductivity	3.5	[J s^{-1} m^{-1} $^oC^{-1}$]
Heat capacity of water	4182	[J kg^{-1} $^oC^{-1}$]
T_0 (initial condition in aquifer)	0	[^oC]
T* (injected water)	1	[^oC]
$\frac{\partial \rho}{\partial TDS}$	0	[-]
$\frac{\partial \rho}{\partial T}$	0	[kg m^{-3} $^oC^{-1}$]
α_L	4	[m]
α_T	1	[m]

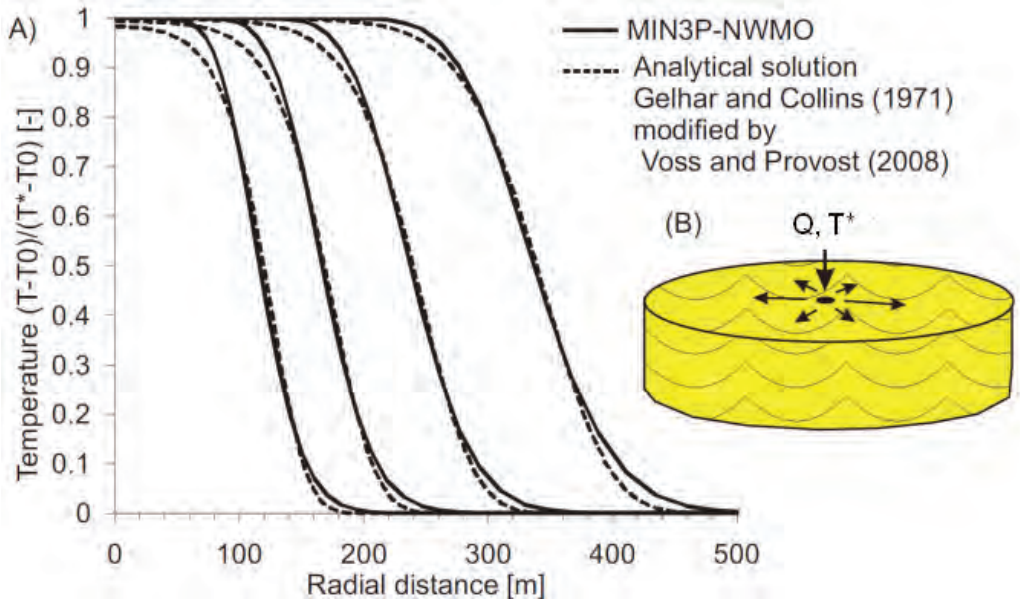

Figure D. 7: Radial flow with energy transport. A) MIN3P-NWMO results (solid lines) are compared with the analytical solution (dashed lines) presented by Gelhar and Collins (1971), as modified by Voss and Provost (2008). B) Idealized representation of the domain

D.4.2 DENSITY-DEPENDENT FLOW AND ENERGY TRANSPORT (AQUIFER THERMAL ENERGY STORAGE EXAMPLE)

This verification example includes density-dependent flow and energy transport (aquifer thermal energy storage). Hot water was injected into an aquifer for storage (injection stage for 90 days) and later withdrawn as an energy source (pumping for 90 days). Model parameters are provided in Table D. 9. The groundwater flow field was radial, similar to the previous example.

Simulation results at 30 and 90 days during the injection stage are shown in Figure D. 8. Results at 30 and 90 days into the pumping stage are shown in Figure D. 9. The MIN3P-NWMO results are compared with results obtained with the numerical model SUTRA (Voss and Provost, 2008), with equivalent spatial discretization. To test the influence of the density weighting in the Darcy flux terms, the MIN3P-NWMO simulations were conducted using both upstream and centered weighting.

Figure D. 8 and Figure D. 9 show that the centered weighting scheme produces less numerical dispersion in the thermal transition zone, and overall provides results which agree better with the SUTRA results. The thermal transition zone widens throughout the injection-production cycle, due to both dispersion and heat conduction. The top of the transition zone tips away from the well during the entire cycle, due to the buoyancy of the hotter water. The combination of these two effects causes cooler water to reach the bottom of the withdrawal well much earlier than if density differences had been ignored.

Table D. 9: Parameters for Aquifer Thermal Energy Storage Problem (Density-Dependent Flow and Energy Transport)

Parameter	Value	Unit
Solid density	2650	[kg m^{-3}]
Fresh-water density	1000	[kg m^{-3}]
Q_{in}	200	[kg s^{-1}]
Porosity	0.35	[-]
Permeability	1.02×10^{-10}	[m^2]
Water specific thermal capacity	4182	[J kg^{-1} $^oC^{-1}$]
Solid specific thermal capacity	840	[J kg^{-1} $^oC^{-1}$]
Water thermal conductivity	0.6	[J s^{-1} m^{-1} $^oC^{-1}$]
Solid thermal conductivity	3.5	[J s^{-1} m^{-1} $^oC^{-1}$]
Heat capacity of water	4182	[J kg^{-1} $^oC^{-1}$]
T_0	20	[^oC]
T_{in}	60	[^oC]
$\frac{\partial \rho}{\partial TDS}$	0	[-]
$\frac{\partial \rho}{\partial T}$	-0.375	[kg m^{-3} $^oC^{-1}$]
α_L	4	[m]
α_T	1	[m]

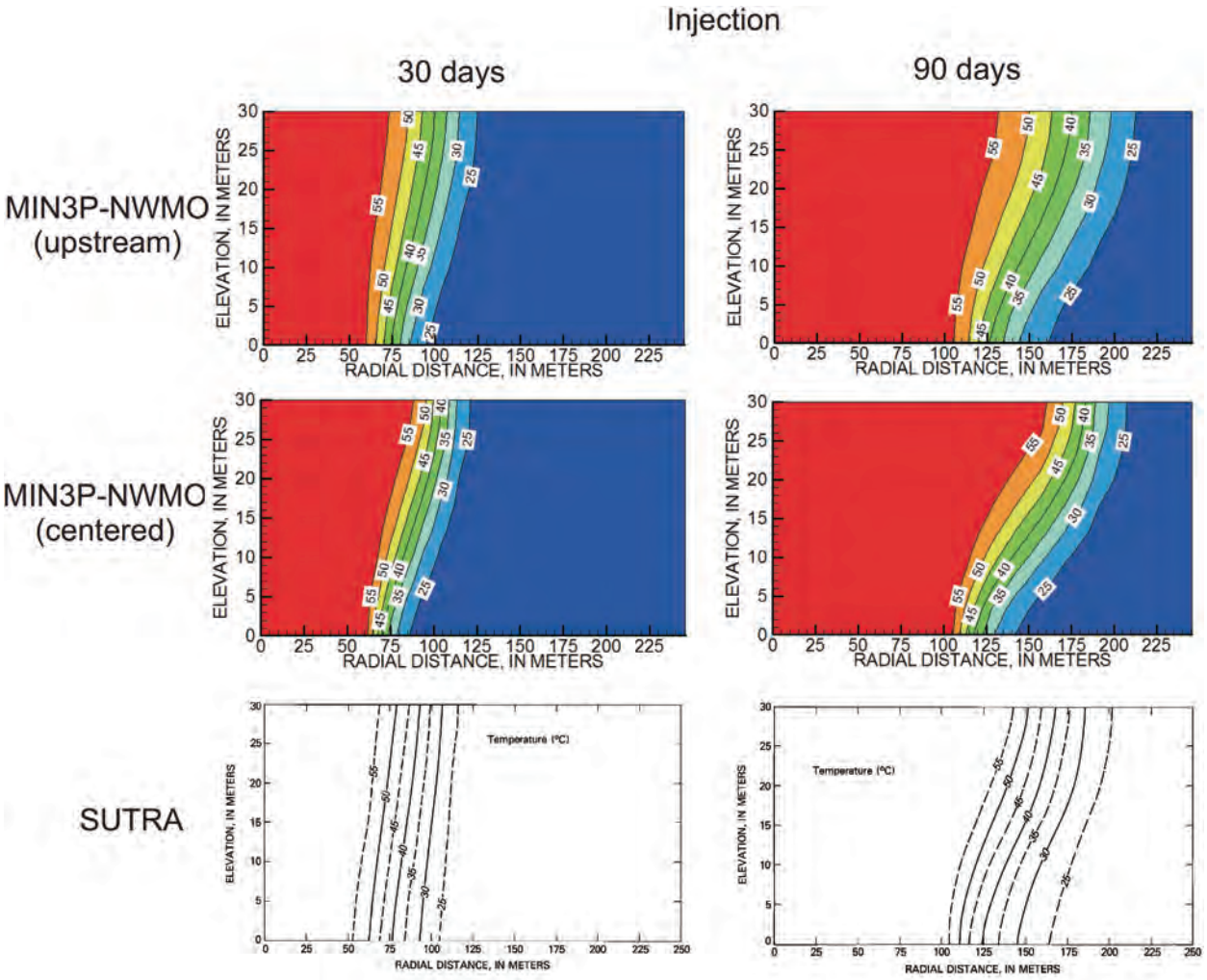

Figure D. 8: Verification of density-dependent radial flow and energy transport (aquifer thermal storage) during hot water injection. MIN3P-NWMO results using upstream and centered weighting are compared with SUTRA

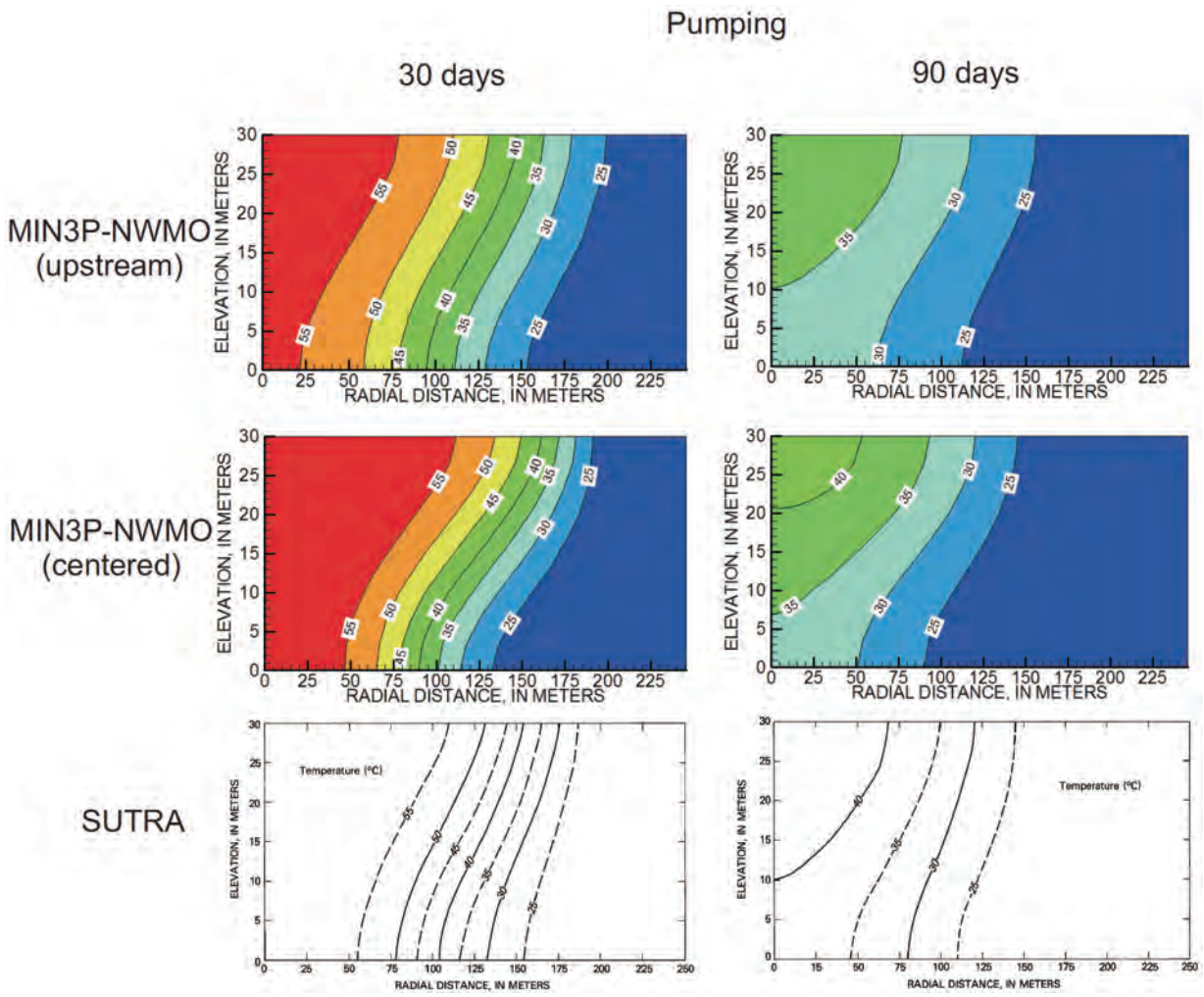

Figure D. 9: Verification of density-dependent radial flow and energy transport (aquifer thermal storage) during groundwater withdrawal. MIN3P-NWMO results using upstream weighting and centered weighting are compared with SUTRA

D.4.3 DENSITY-DEPENDENT FLOW, HEAT AND SOLUTE TRANSPORT (HENRY-HILLEKE PROBLEM)

This example considers seawater intrusion into a non-isothermal confined aquifer, simulated in a 2-dimensional cross section under steady-state conditions (Henry and Hilleke, 1972). Freshwater flows from an inland boundary over dense saline water, which enters from a seaward boundary, and discharges in the upper portions of the vertical seaward boundary. Initially, hydrostatic pressure conditions are present throughout the aquifer with linear variations of seawater concentrations and temperatures (see Figure D. 10A and Figure D. 10B). Model parameters are tabulated in Table D. 10. An aspect ratio equal to unity and a spatial discretization about 0.025 m for horizontal and vertical direction are used.

Results obtained with MIN3P-NWMO are compared with SUTRA-MS (Hughes and Sanford, 2004) and HST3D (Kipp, 1986) and are shown in Figure D. 10. The original results by Henry and Hilleke (1972) are also shown for 50% of seawater density and temperature increase

(continuous red line). The results show that at time zero, heat begins to be transported inward from the top, bottom, and left boundaries, and seawater begins to intrude the freshwater system by moving in laterally under the freshwater from the seawater boundary. Seawater intrusion in the aquifer is primarily the result of the greater density of the seawater. Lateral temperature variations at the top and bottom of the aquifer and vertical temperature variations at the freshwater boundary increase vertical freshwater fluid movement and intrusion of seawater at the base of the aquifer when compared to a similar isothermal case (not shown). As shown in Figure D. 10, simulated temperatures for MIN3P-NWMO, SUTRA-MS and HST3D compare favourably with each other. The MIN3P-NWMO results show more solute dispersion in comparison with the other models, which is likely due to the use of upstream weighting in the transport equations.

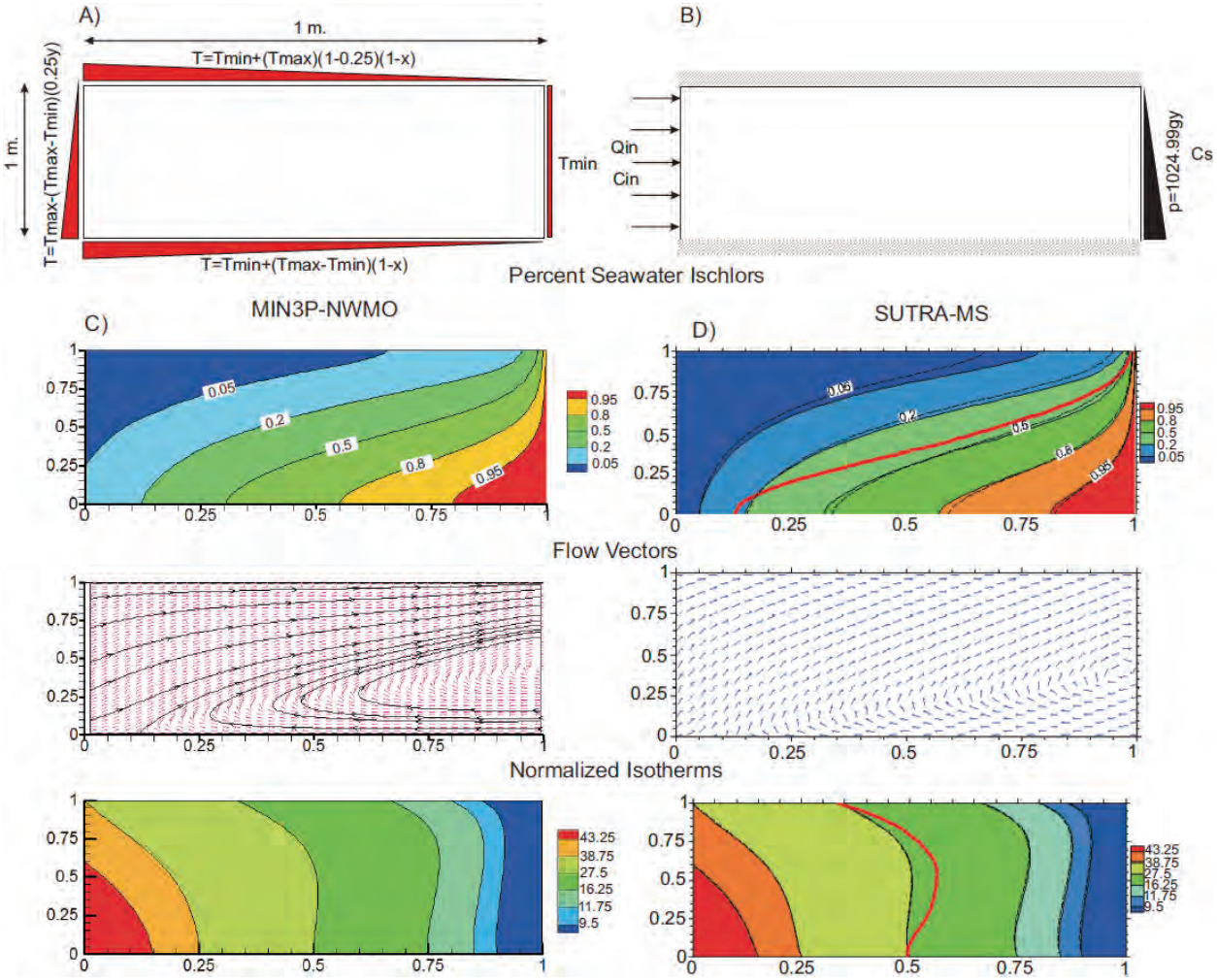

Figure D. 10: Verification of density-dependent flow, heat transport and solute transport (Henry-Hilleke problem). A) Domain and energy transport boundary conditions. B) Flow and solute transport boundary conditions. C) and D) Percent seawater isochlors, flow vectors, and normalized isotherms. Results obtained by MIN3P-NWMO, SUTRA-MS and HST3D, respectively. SUTRA-MS results are represented as continuous lines. The continuous red line corresponds to the Henry and Hilleke numerical solution (0.5 percent seawater concentration and isotherm only), the HST3D code solution is presented by the dashed black line.

Table D. 10: Parameters for Henry-Hilleke Problem (Density-Dependent Flow, Heat and Solute Transport)

Parameter	Value	Unit
Solid density	2600	[kg m^{-3}]
Fresh-water density	1000	[kg m^{-3}]
Sea-water density	1024.99	[kg m^{-3}]
Dynamic fluid viscosity	10^{-3}	[kg m^{-1} s^{-1}]
Cs	35.7	[kg m^{-3}]
Cin	0	[kg m^{-3}]
Qin	8.33×10^{-6}	[kg s^{-1}]
Porosity	0.35	[-]
Permeability	1.2×10^{-9}	[m^2]
Diffusion- dispersion (solute transport)	2.38×10^{-5}	[m^2 s^{-1}]
Diffusion- dispersion (energy transport)	2.38×10^{-4}	[m^2 s^{-1}]
Water thermal conductivity	995.73	[J s^{-1} m^{-1} $^oC^{-1}$]
Solid thermal conductivity	0	[J s^{-1} m^{-1} $^oC^{-1}$]
Specific heat capacity of water	4182	[J kg^{-1} $^oC^{-1}$]
Rock Density	2650	[kg m^{-3}]
Tmin	5	[^oC]
Tmax	50	[^oC]
$\frac{\partial \rho}{\partial TDS}$	0.7	[-]
$\frac{\partial \rho}{\partial T}$	-0.375	[kg m^{-3} $^oC^{-1}$]

D.4.4 THERMO-HALINE CONVECTION

Thermo-haline examples are commonly used in the validation of coupled thermal-hydraulic and transport models (e.g. Oldenburg and Pruess, 1998; 1999; Geiger et al., 2006). In these types of problems the flow and transport equations are strongly coupled through the temperature and salinity control on fluid density (ρ) and viscosity (μ). Here, a thermal convection example involving the separation of a thermal plume and a salt plume by transient thermo-haline double-advective convection, for a NaCl–$CaCl_2$-H_2O system, was simulated. Although this problem was initially studied numerically by Oldenburg and Pruess (1999), results are compared with more recent work (Geiger et al., 2006).

In the present work, different equations of state for the NaCl-$CaCl_2$-H_2O system are used (i.e. HWM (Harvie et al., 1984) model based on Pitzer (1973) equations), but the differences with respect to the equations of state presented by Oldenburg and Pruess (1999) and Geiger et al. (2006) are small. The domain and boundary conditions for this example are shown in Figure D. 11. In this case, the domain was uniformly discretized using 64 cells resulting with a grid spacing of about 39 m, which is similar to the discretization used by Geiger et al. (2006). Key parameter values are provided in Table D. 11.

Results for two different initial conditions (i.e. either positive or negative initial buoyancy in the central region of the domain) are shown in Figure D. 12 and Figure D. 13. Overall there is good agreement between the two sets of numerical simulations for both fluid density and temperature. For the initially negatively buoyant case (see Figure D. 12), the thermal and brine plumes separate, and the high-density zone that evolves below the initial parcel location moves downward while the warm water plume rises after plume separation. For the initially positive buoyancy brine parcel (see Figure D. 13), the overall motion of fluid is upward. In this case, because the temperature front is thermally retarded, a high fluid density zone is predicted to develop above a low-density region.

Table D. 11: Parameters for Thermohaline Convection Problems

Parameter	Value	Unit
Positive initial buoyancy		
Initial parcel temperature	300	^{o}C
Initial parcel brine mass fraction	0.14	[-]
Initial parcel density	831	[kg m^{-3}]
Negative initial buoyancy		
Initial parcel temperature	250	^{o}C
Initial parcel brine mass fraction	0.47	[-]
Initial parcel density	919	[kg m^{-3}]
Reservoir temperature	200	^{o}C
Reservoir initial mass fraction	0	[-]
Reservoir liquid density	875	[kg m^{-3}]
Porosity	0.1	[-]
Permeability	$5x10^{-14}$	[m^2]
Molecular diffusion	10^{-8}	[m^2 s^{-1}]
Formation conductivity	1.8	[J s^{-1} m^{-1} $^{o}C^{-1}$]
Specific heat capacity of rock	1000	[J kg^{-1} $^{o}C^{-1}$]
Specific heat capacity of water	4184	[J kg^{-1} $^{o}C^{-1}$]
Density of rock	2650	[kg m^{-3}]

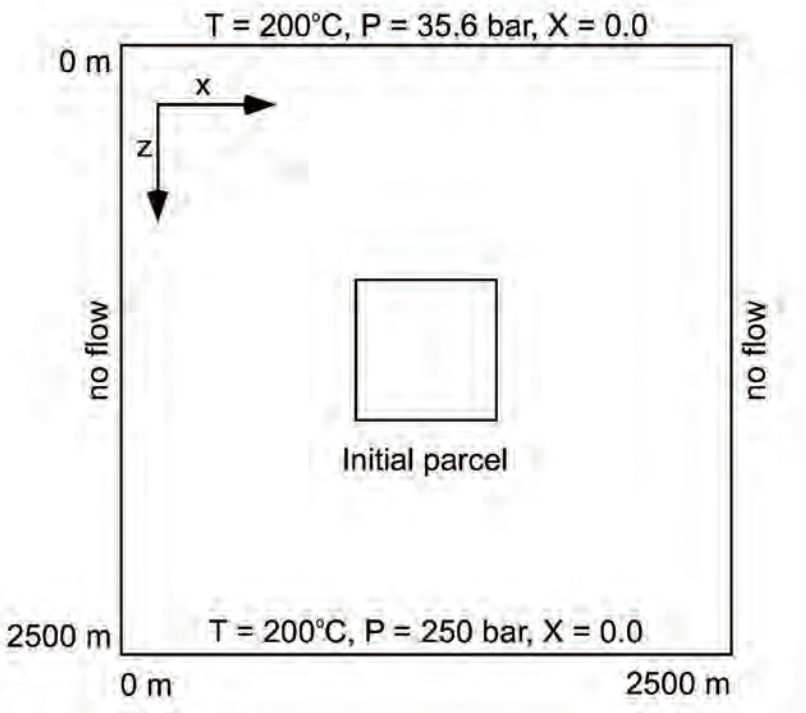

Figure D. 11: Domain and boundary conditions for the transient thermohaline convection problems as given in Oldenburg and Pruess (1999), X relates to the mass fraction of brine groundwater in relation to the source region (X = 1 in source)

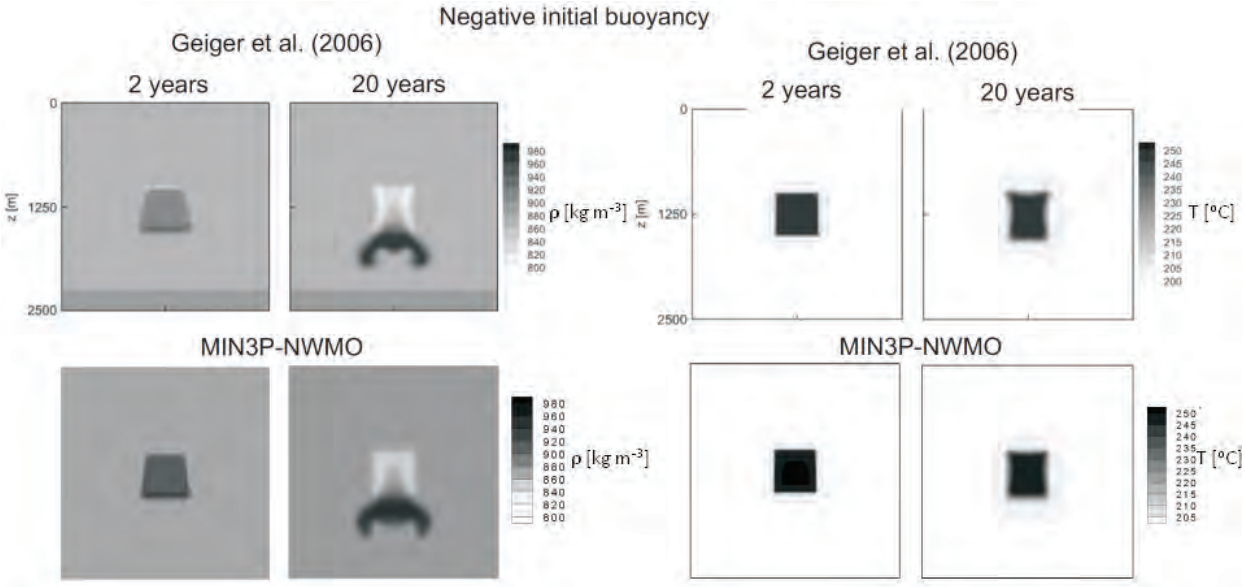

Figure D. 12: Verification of thermo-hydraulic coupling for negative initial buoyancy. MIN3P-NWMO results of density and temperature at 2 and 20 years are compared with the results from Geiger et al. (2006)

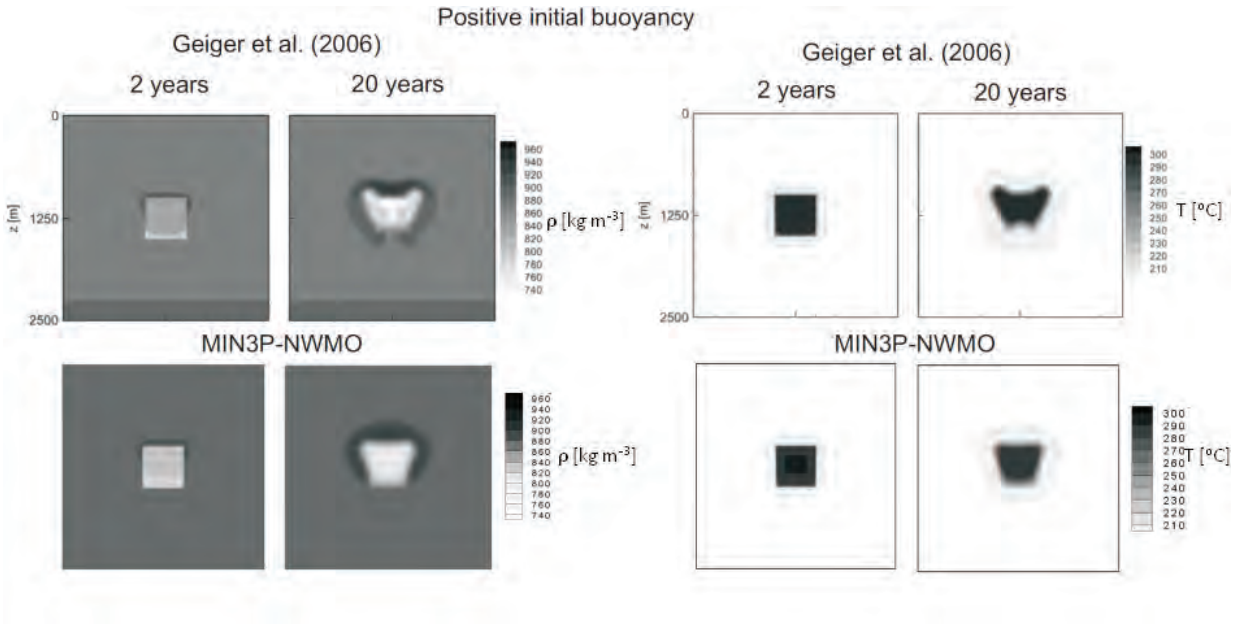

Figure D. 13: Verification of thermo-hydraulic coupling for positive initial buoyancy. MIN3P-NWMO results of density and temperature at 2 and 20 years are compared with the results from Geiger et al. (2006)

D.4.5 SALT-DOME PROBLEM

Another verification example that was simulated is an idealization of flow over a salt dome. In this case, fluid flow, energy, and solute transport are coupled through density because density is treated as a function of temperature as well as solute concentrations. This relationship can be expressed in form of the buoyancy ratio B as:

$$B = \frac{\frac{\partial \rho}{\partial TDS}\Delta TDS}{\frac{\partial \rho}{\partial T}\Delta T} \qquad \text{Equation D-9}$$

The geometry and boundary conditions for the problem are shown in Figure D. 14A. The domain extends 900 m horizontally and 300 m vertically (i.e. the aspect ratio about 3). The aquifer is considered homogeneous and isotropic and the hydraulic head varies linearly along the top boundary. All remaining boundaries are impervious to flow. Key parameter values for flow and transport are provided in Table D. 12.

The thermohaline extension of the salt dome problem involves the superposition of an upward thermal gradient, which tends to destabilize the brine plume due to the resulting buoyant forces. Accordingly, the bottom of the aquifer is assigned a constant normalized temperature (i.e. T=1), while the top boundary is assigned a normalized temperature of zero (i.e. T=0). The upper boundary is additionally constrained by a heat flux of zero. The side walls of the domain are assumed impervious for solute mass and adiabatic (insulated) for heat.

Results obtained with MIN3P-NWMO and FEFLOW at a simulation time of 100 years for three different buoyancy ratios are shown in Figure D. 14B. Although these two codes use different

numerical approaches (finite volumes and finite elements, respectively), the results are comparable. The differences that are noticed, particularly for the lowest buoyancy ratio of 2, may be attributable to different spatial interpolation of temperature-dependent variables (i.e. density and viscosity). In the finite volume method (MIN3P-NWMO), density is only interpolated between the center of adjacent cells, whereas it is interpolated at Gauss points, for instance, in the finite element method.

Table D. 12: Parameters for Salt-Dome Problem

Parameter	Value	Unit
Solid density	2600	[kg m^{-3}]
Fresh-water density	1000	[kg m^{-3}]
Sea-water density	1024.99	[kg m^{-3}]
Dynamic fluid viscosity	10^{-3}	[kg m^{-1} s^{-1}]
Cs	35.7	[kg m^{-3}]
Cin	0	[kg m^{-3}]
Qin	8.33×10^{-6}	[kg s^{-1}]
Porosity	0.35	[-]
Permeability	1.2×10^{-9}	[m^2]
Difussion- dispersion (solute transport)	2.38×10^{-5}	[m^2 s^{-1}]
Difussion- dispersion (energy transport)	2.38×10^{-4}	[m^2 s^{-1}]
Water thermal conductivity	995.73	[J s^{-1} m^{-1} $^oC^{-1}$]
Solid thermal conductivity	0	[J s^{-1} m^{-1} $^oC^{-1}$]
Specific heat capacity of water	4182	[J kg^{-1} $^oC^{-1}$]
Density of rock	2650	[kg m^{-3}]
Tmin	5	[^{o}C]
Tmax	50	[^{o}C]
$\frac{\partial \rho}{\partial \mathrm{TDS}}$	0.7	[-]
$\frac{\partial \rho}{\partial \mathrm{T}}$	-0.375	[kg m^{-3} $^oC^{-1}$]

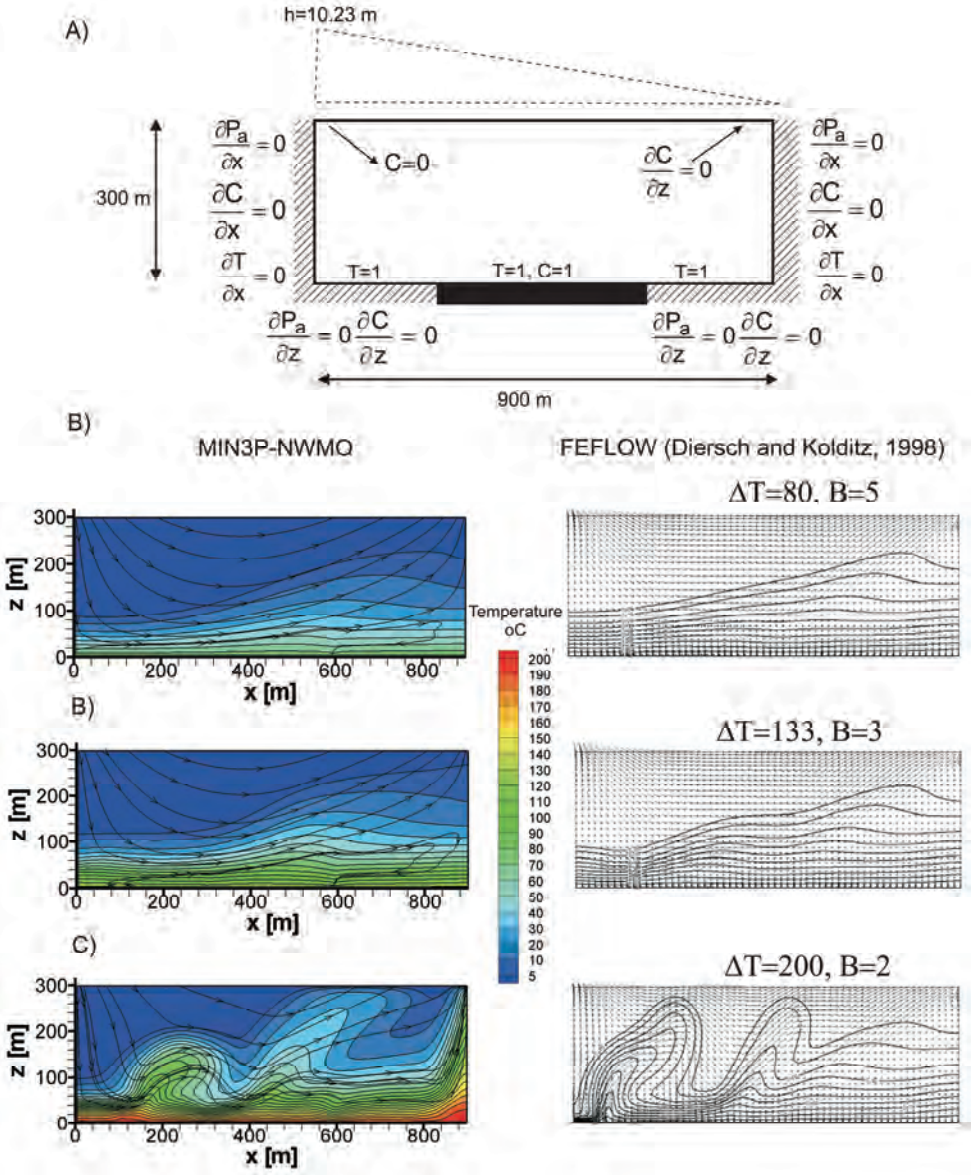

Figure D. 14: Salt dome verification example. A) Domain geometry and boundary conditions for flow, energy and solute transport. B) Results obtained with MIN3P-NWMO (left) are compared with FEFLOW (right) at different buoyancy ratios

D.5 VERIFICATION OF REACTIVE TRANSPORT

This section describes the verification of the main reactive transport capabilities of MIN3P-NWMO. Three examples are presented focusing on geochemical processes that are relevant in sedimentary rock formations. The simulations are designed to simulate dedolomitization (as an example for the dissolution/precipitation of mineral phases), cation exchange, and aerobic degradation of toluene (as an example for dissolved organic matter degradation). Simulation results are compared to results obtained with the reactive transport code PHAST (Parkhurst et al., 2005).

D.5.1 DEDOLOMITIZATION

The replacement of dolomite by calcite was simulated by the infiltration of Ca-rich acidic water, undersaturated with respect to calcite and dolomite, into an aquifer that initially only contains dolomite. The initial volumetric content of dolomite in the aquifer was 0.2. The chemical compositions of the initial and boundary waters are presented in Table D. 13. Physical and chemical parameters for the simulation domain are depicted in Figure D. 15A.

The simulation results show the replacement of dolomite by calcite, and subsequent dissolution of calcite (see Figure D. 15B and Figure D. 15C). The results obtained with MIN3P-NWMO are virtually identical to the results obtained using PHAST (Parkhurst et al., 2005). Small differences may be attributed to the different solution algorithms used by the codes, for example, MIN3P-NWMO uses a global implicit method, while PHAST uses an operator splitting method, which is known to introduce an operator splitting error (Calderhead and Mayer, 2004).

Table D. 13: Dedolomitization Problem: Composition of Initial and Boundary Waters

Parameter	Boundary water	Initial Water	Unit
pH	3	7	[-]
Ca^{2+}	4.15×10^{-3}	1.19×10^{-3}	[mol l^{-1}]
Mg^{2+}	7.12×10^{-5}	8.85×10^{-4}	[mol l^{-1}]
Cl^{-}	2.4×10^{-4}	1.44×10^{-3}	[mol l^{-1}]
Na^{+}	9.9×10^{-5}	10^{-4}	[mol l^{-1}]
CO_3^{2-}	5.5×10^{-5}	1.11×10^{-4}	[mol l^{-1}]
SO_4^{2-}	4.82×10^{-3}	8.5×10^{-4}	[mol l^{-1}]
Ionic strength	1.5×10^{-2}	6×10^{-3}	[mol l^{-1}]

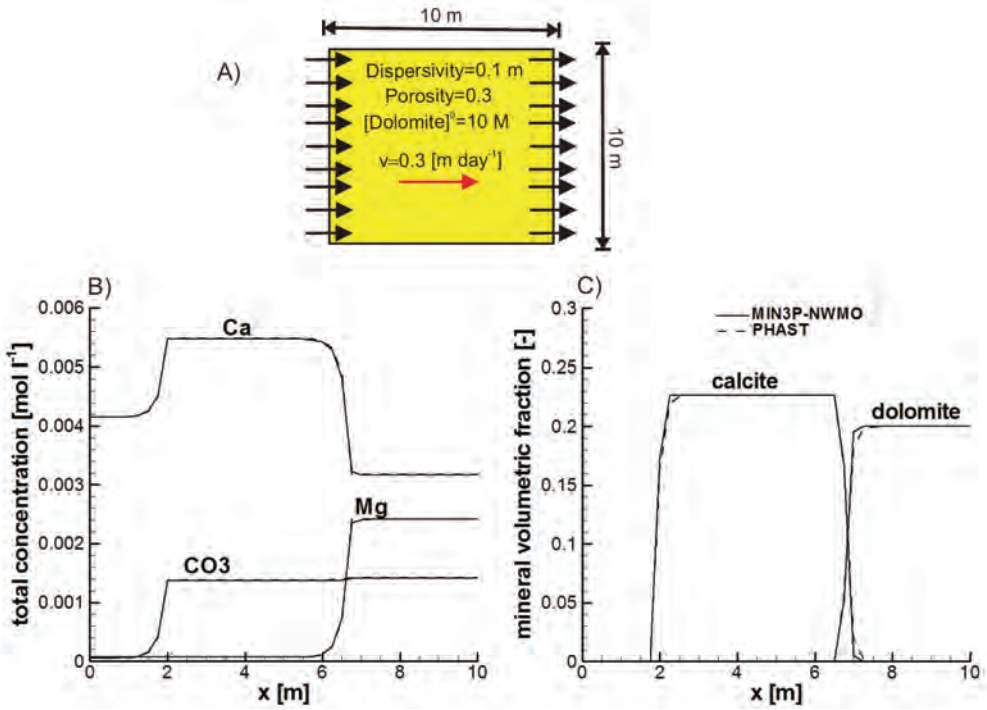

Figure D. 15: Dedolomitization problem. A) Physical and chemical properties of the domain. B) Spatial distribution of total concentrations at 30000 days. C) Volumetric fractions of calcite ($CaCO_3$) and dolomite ($CaMg(SO_4)_2$) at 30000 days. MIN3P-NWMO results (solids lines) are compared with PHAST (dashed lines)

D.5.2 CATION EXCHANGE

Cation exchange is an important geochemical process in formations containing clay minerals. The following example evaluates cation exchange processes under advective-dispersive transport conditions. The domain was initially dominated by a sodium-potassium-nitrate (Na-K-NO_3) solution in equilibrium with a cation exchanger, and was then flushed by a solution rich in calcium and chloride (Ca-Cl) (Table D. 14 and Figure D. 16A).

Table D. 14: Cation Exchange Problem: Composition of Initial and Boundary Waters and Chemical Parameters of the Domain

Parameter	Boundary water	Initial Water	Unit
pH	7	7	[-]
Ca^{2+}	$6x10^{-4}$	10^{-9}	[mol l^{-1}]
Cl^-	$1.2x10^{-3}$	$6x10^{-9}$	[mol l^{-1}]
K^+	10^{-9}	$2x10^{-4}$	[mol l^{-1}]
Na^+	10^{-9}	10^{-3}	[mol l^{-1}]
NO_3^-	10^{-9}	$1.2x10^{-3}$	[mol l^{-1}]
Ionic strength	$1.8x10^{-3}$	$1.2x10^{-3}$	[mol l^{-1}]
CEC	N/A	17.5	[mol l^{-1}]

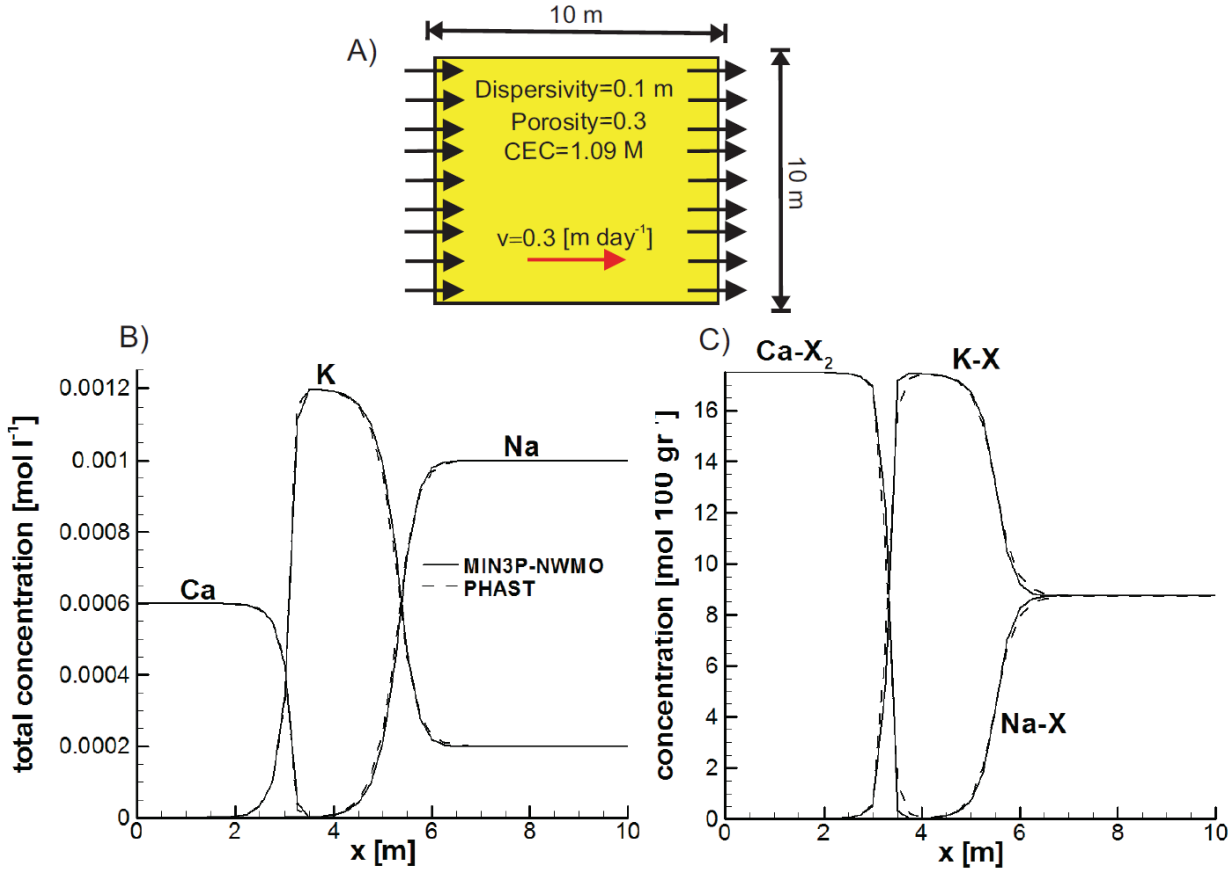

Figure D. 16: Cation-exchange problem. A) Physical and chemical properties of the domain. B) Spatial distribution of total concentrations at 3000 days. C) Concentration of exchanged species at 3000 days. The MIN3P-NWMO results (solid lines) are compared with PHAST (dashed lines)

The spatial distributions of total concentrations of the major cations at 3000 days are presented in Figure D. 16B. The spatial distributions of exchanged species are presented in Figure D. 16C. Simulation results demonstrate the replacement of Na and K by Ca. Similar to the example on dedolomitization, the results obtained with MIN3P-NWMO agree very well with the solution obtained using PHAST (Figure D. 16B, and 16C). Because the spatial and temporal discretization was the same for both numerical solutions, it is believed that the slightly more dispersed concentration profiles for the PHAST model are due to operator-splitting errors introduced by the solution algorithm.

D.5.3 AEROBIC DEGRADATION OF TOLUENE

This example simulates an aquifer that initially contains groundwater with substantial dissolved oxygen, and which is infiltrated by strongly reducing groundwater containing toluene ($C_6H_5CH_3$). Under these conditions, $C_6H_5CH_3$ is degraded using O_2(aq) as the electron acceptor according to the following reaction:

$$C_6H_5CH_3 + 9O_2(aq) + 3H_2O \rightarrow 7CO_3^{2-} + 14H^+$$ Equation D-10

The degradation of toluene in the mixing zone of the two solutions leads to a decrease in dissolved oxygen and an increase of total dissolved inorganic carbon.

Table D. 15: Toluene Degradation Problem: Composition of Initial and Boundary Waters

Parameter	Boundary water	Initial Water	Unit
pH	7	7	[-]
$C_6H_5CH_3$	10^{-3}	10^{-10}	[mol l^{-1}]
O_2(aq)	10^{-10}	10^{-3}	[mol l^{-1}]
Cl^-	10^{-3}	10^{-10}	[mol l^{-1}]
Na^+	10^{-3}	10^{-10}	[mol l^{-1}]
CO_3^{2-}	10^{-10}	10^{-10}	[mol l^{-1}]
Ionic strength	10^{-3}	10^{-7}	[mol l^{-1}]

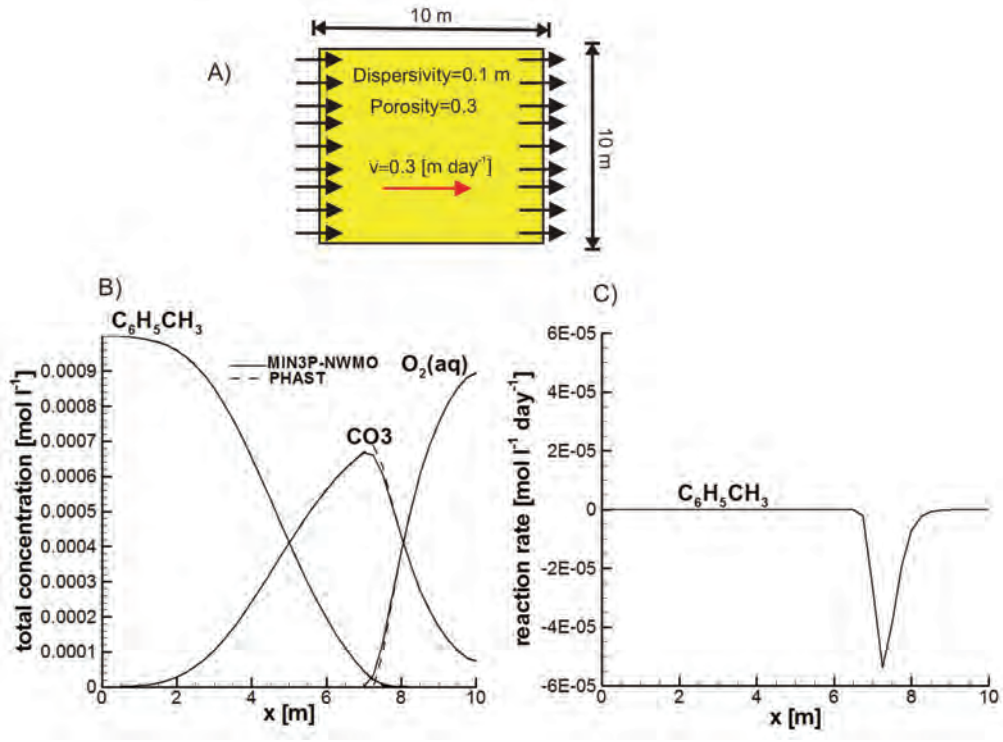

Figure D. 17: Toluene verification problem. (A) Physical and chemical properties of the domain. (B) Spatial distribution of total concentrations at 5 days. (C) Spatial distribution of aerobic degradation rate of toluene ($C_6H_5CH_3$) at 5 days. The results for MIN3P-NWMO (solid lines) are compared with PHAST (dashed lines)

The chemical compositions of the initial and boundary waters are presented in Table D. 15. Physical properties of the domain are illustrated in Figure D. 17A. Simulation results for total concentrations of carbonate, toluene and oxygen, and the rate of toluene oxidation in the dispersive mixing zone, are shown for MIN3P-NWMO and PHAST in Figure D. 17B. The spatial distribution of the aerobic degradation rate for toluene at 5 days is shown in Figure D. 17C. The results of MIN3P-NWMO are essentially identical with the PHAST results.

D.6 VERIFICATION OF REACTIVE TRANSPORT IN HIGHLY SALINE SOLUTIONS: REPLACEMENT OF GYPSUM BY POLYHALITE

This verification problem was simulated to evaluate the capabilities of MIN3P-NWMO for reactive transport at high solute concentrations. The test consists of a one-dimensional reactive transport simulation in which a K-enriched solution in equilibrium with halite (NaCl) and polyhalite ($Ca_2MgK_2(SO_4)_4.2H_2O$) migrates through a column initially in equilibrium with halite and gypsum ($CaSO_4.2H_2O$) (see Bea et al., 2010).

The compositions of initial and boundary solutions are detailed in Table D. 16. Physical and chemical parameters of the problem are presented in Figure D. 18A. The length of the domain is 1 m (porosity and dispersivity are 0.4 and 0.01 m, respectively) and the domain initially contains gypsum and halite. The Pitzer equations are used to calculate the activities of aqueous species. For major components, the virial coefficients are taken from Harvie et al. (1984) and Greenberg and Möller (1989), as tabulated in Appendix B.5. The problem was also solved with PHAST (Parkhurst et al., 2005), allowing for a direct comparison between the results.

Table D. 16: Replacement of Gypsum by Polyhalite: Composition of Initial and Boundary Waters of the Domain

Parameter	Boundary water	Initial water	Unit
pH	7.3	8.1	[-]
Ca^{2+}	$3.8x10^{-3}$	$1.1x10^{-2}$	[mol l^{-1}]
Mg^{2+}	2.2	$6.3x10^{-1}$	[mol l^{-1}]
Cl^-	6.48	5.94	[mol l^{-1}]
K^+	7.43	$1.2x10^{-1}$	[mol l^{-1}]
Na^+	2.72	5.178	[mol l^{-1}]
Br^-	10^{-6}	$1.0x10^{-9}$	[mol l^{-1}]
CO_3^{2-}	$5.1x10^{-5}$	$1.7x10^{-5}$	[mol l^{-1}]
SO_4^{2-}	$5.6x10^{-1}$	$2.3x10^{-1}$	[mol l^{-1}]
Ionic strength	13.83	7.35	[mol l^{-1}]

The spatial distributions of Ca, Na, K and SO_4 and the volumetric content of mineral phases at 10 and 30 years are shown in Figure D. 18. Gypsum was completely dissolved from the domain at the end of the simulation (total simulated time was approximately 100 years). The precipitation/dissolution of halite is controlled by the precipitation of polyhalite. When polyhalite starts to precipitate, halite is partially re-dissolved (results not shown). The results obtained with

MIN3P-NWMO and PHAST are in good agreement for both aqueous species and mineral phases.

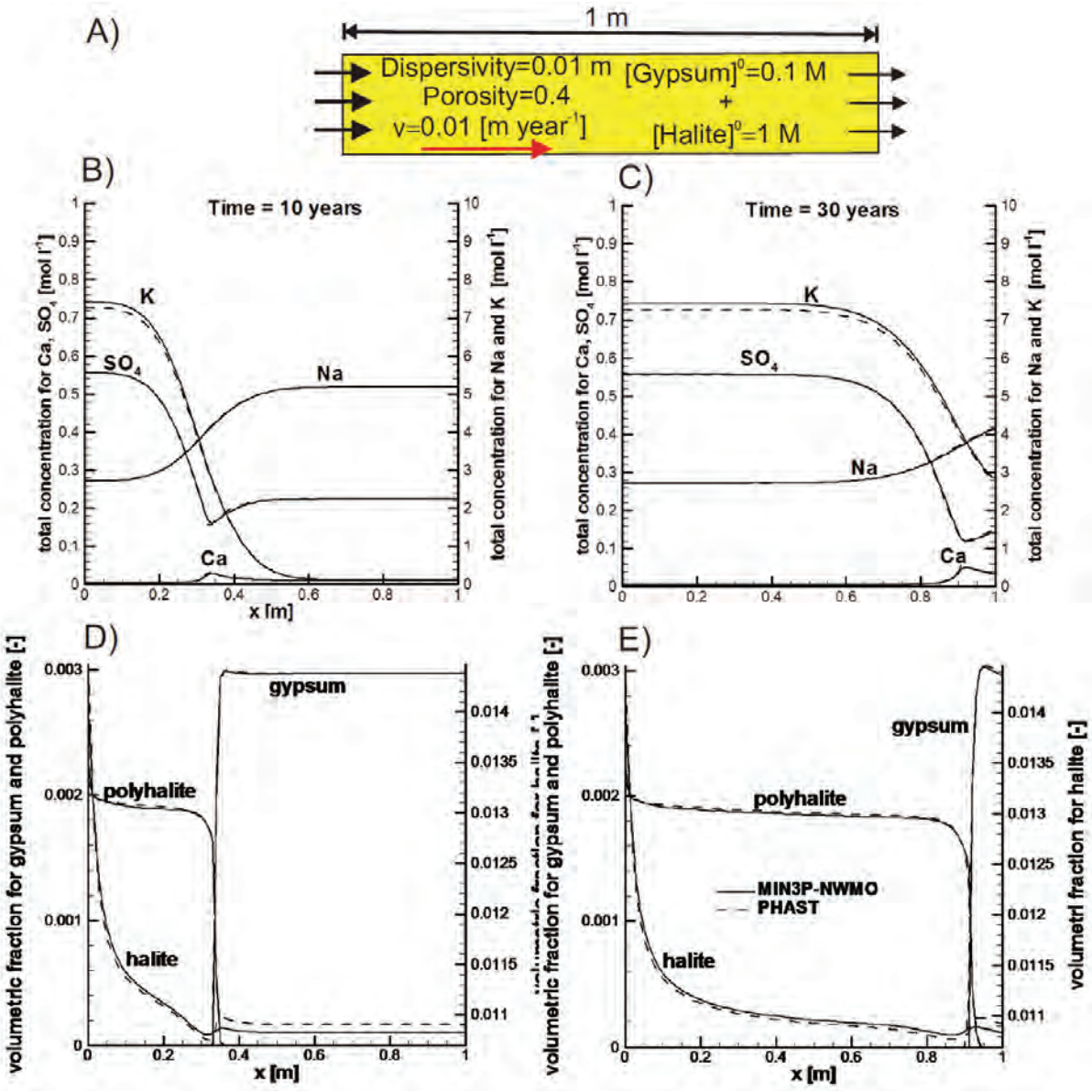

Figure D. 18: Replacement of gypsum by polyhalite. (A) Physical and chemical properties of the domain. (B) and (C) Spatial distribution of total concentrations at 10 and 30 years, respectively. (D) and (E) Volumetric fractions of halite (NaCl), gypsum ($CaSO_4.2H_2O$), and polyhalite ($Ca_2MgK_2(SO_4)_4.2H_2O$), at 10 and 30 years, respectively. The MIN3P-NWMO results (solid lines) are compared with PHAST (dashed lines)

D.7 REFERENCES

Ackerer, P., A. Younes and R. Mose. 1999. Modeling variable density flow and solute transport in porous medium: 1. Numerical model and verification. Transport in Porous Media , 35, 345-373.

Bea, S.A., J. Carrera, C. Ayora and F. Batlle. 2010. Pitzer Algortithm: Efficient implementation of Pitzer equations in geochemical and reactive transport models. Computers & Geosciences, 36, 526-538.

Benbow, S., R. Metcalfe and J. Wilson. 2008. Pitzer databases for use in thermodynamic modelling. Nuclear Waste Management Organization Technical Memorandum (QRS-3021A-TM1) Version: 1.0. Toronto, Canada.

Calderhead, A.I. and K.U. Mayer. 2004. Comparison of the suitability of the global implcit method and the sequential non-iterative approach for multicomponent reactive transport modelling. Proceedings GeoQuebec 2004, 57th Canadian Geotechnical Conference & 4th Joint CGS/IAH-CNC Groundwater Conference, 32-39.

Diersch, H. and O. Kolditz. 1998. Coupled groundwater flow and transport: 2. Thermohaline and 3D convection systems. Advances in Water Resources, 21, 401-425.

Diersch, H. and O. Kolditz. 2002. Variable-density flow and transport in porous media: approaches and challenges. Advances in Water Resources, 25, 899-944.

Elder, J.W. 1967. Transient convection in a porous medium. Journal of Fluid Mechanics, 27, 609-623.

Frind, E. 1982. Simulation of long-term transient density-dependent transport in groundwater. Advances in Water Resources, 5, 73-88.

Frolkovic, P. and H.D. Schepper. 2001. Numerical modeling of convection dominated transport with density driven flow in porous media. Advances in Water Resources, 24, 63-72.

Geiger, S., T. Driesner, C. Heinrich and S. Matthai. 2006. Multiphase thermohaline convection in the Earth's crust: II. Benchmarking and application of a finite element-finite volume solution technique with a NaCl-H_2O equation of state. Transport In Porous Media, 63, 435-461.

Gelhar, L. and M. Collins. 1971. General analysis of longitudinal dispersion in nonuniform flow. Water Resources Research, 7, 1511-1521.

Greenberg, J.P. and N. Moller. 1989. The prediction of mineral solubilities in natural-waters - A chemical-equilibrium model for the Na-K-Ca-Cl-SO_4-H_2O system to high-concentration from 0^o to 250^oC. Geochimica et Cosmochimica Acta, 53, 2503-2518.

Guo, W. and C. Langevin. 2002. User's Guide to SEAWAT: A Computer program for simulation of three-dimensional variable-density ground-water flow. U.S. Geological Survey, Techniques of Water-Resources Investigations Book 6, Chapter A7, 77p.

Harvie, C.E., N. Moller and J.H. Weare. 1984. The prediction of mineral solubilities in natural waters: The Na-K-Mg-Ca-H-Cl-SO_4-OH-HCO_3-CO_3-CO_2-H_2O system to high ionic strengths at 25^oC. Geochimica et Cosmochimica Acta, 48, 723-751.

Henry, H.R. 1964. Effects of dispersion on salt encroachment in coastal aquifers. U.S. Geological Survey Water Supply Paper, 1613-C, 70-84.

Henry, H. and J. Hilleke. 1972. Exploration of multiphase fluid flow in a saline aquifer system affected by geothermal heating. Bureau of Engineering Research, Report No. 150-118, University of Alabama, U.S. Geological Survey Contract No. 14-08-0001-12681, National Technical Information Service Publication No. PB234233, 105 pp.

Hughes, J. and W. Sanford. 2004. SUTRA-MS: A Version of SUTRA Modified to Simulate Heat and Multiple-Solute Transport U.S. Department of the Interior. U.S. Geological Survey.

Kipp, K.L. 1986. HST3D-A computer code for simulation of heat solute transport in three-dimensional ground-water flow systems. U.S. Geological Survey Water-Resources Investigations Report 86-4095.

Kolditz, O., R. Ratke, H.J.G. Diersch and W. Zielke. 1998. Coupled groundwater flow and transport: 1. Verification of variable density flow and transport models. Advances in Water Resources, 21, 27-46.

Lemieux, J.M., E.A. Sudicky, W.R. Peltier and L. Tarasov. 2008. Simulating the impact of glaciations on continental groundwater flow systems: 1. Relevant processes and model formulation. Journal of Geophysical Research-Earth Surface, 113, Article No. F03017, 12 p.

Millero, F.J. 1982. The effect of pressure on the solubility of minerals in water and seawater. Geochimica et Cosmochimica Acta, 46, 11-22.

Oldenburg, C. and K. Pruess. 1998. Layered thermohaline convection in hypersaline geothermal systems. Transport in Porous Media, 39, 29-63.

Oldenburg, C. and K. Pruess. 1999. Plume separation by transient thermohaline convection in porous media. Geophysical Research Letters, 26, 2997-3000.

Oldenburg, C. and K. Pruess. 1995. Radionuclide Transport for TOUGH2. Lawrence Berkeley National Laboratory Report LBL-34868.

Oltean, C. and A. Buès. 2001. Coupled groundwater flow and transport in porous media. A conservative or non-conservative form? Transport in Porous Media, 44, 219-246.

Oswald, S.E. and W. Kinzelbach. 2004. Three-dimensional physical benchmark experiments to test variable-density flow models. Journal of Hydrology, 290, 22-42.

Parkhurst, D., K. Kipp, P. Engesgaard and S. Charlton. 2005. PHAST-A program for simulating ground-water flow, solute transport, and multicomponent geochemical reactions. Geochimica et Cosmochimica Acta, 69, A156-A156.

Pinder, G.F. and H.H. Cooper. 1970. A numerical technique for calculating the transient position of the saltwater front. Water Resources Research, 3, 875-882.

Pitzer, K.S. 1973. Thermodynamics of electrolytes. I. Theoretical basis and general equations. Journal of Physical Chemistry, 77, 268-277.

Simpson, M. J. and T.P. Clement. 2003. Theoretical analysis of the worthiness of Henry and Elder problems as benchmarks of density-dependent groundwater flow models. Advances in Water Resources, 26, 17-31.

Simpson, M.J. and T.P. Clement. 2004. Improving the worthiness of the Henry problem as a benchmark for density-dependent groundwater flow models. Water Resources Research, 40(1), W01504, doi:10.1029/2003WR002199.

USDOE (United States Department of Energy). 2007. In-drift precipitates/salts model. Argonne National Laboratory Report EBS-MD-000045 REV 03. Chicago, USA.

Van Leer, B. 1974. Towards the ultimate conservative scheme. II Monotonicity and conservation combined in a second order scheme. Journal of Computational Physics, 14, 361-370.

Voss, C. and A. Provost. 2008. SUTRA-A model for saturated-unsaturated, variable-density ground-water flow with solute or energy transport. U.S. Geological Survey Water-Resources Investigations Report 02-4231, 250p.

Voss, C. and W. Souza. 1987. Variable density flow and solute transport simulation of regional aquifers containing a narrow freshwater-saltwater transition zone. Water Resources Research, 23, 1851-1866.

Weatherill, D., C.T. Simmons, C. Voss and N. Robinson. 2004. Testing density-dependent groundwater models: Two-dimensional steady state unstable convection in infinite, finite and inclined porous layers. Advances in Water Resources, 27, 547-562.